CAVITATION INCEPTION ON SHIP PROPELLER MODELS

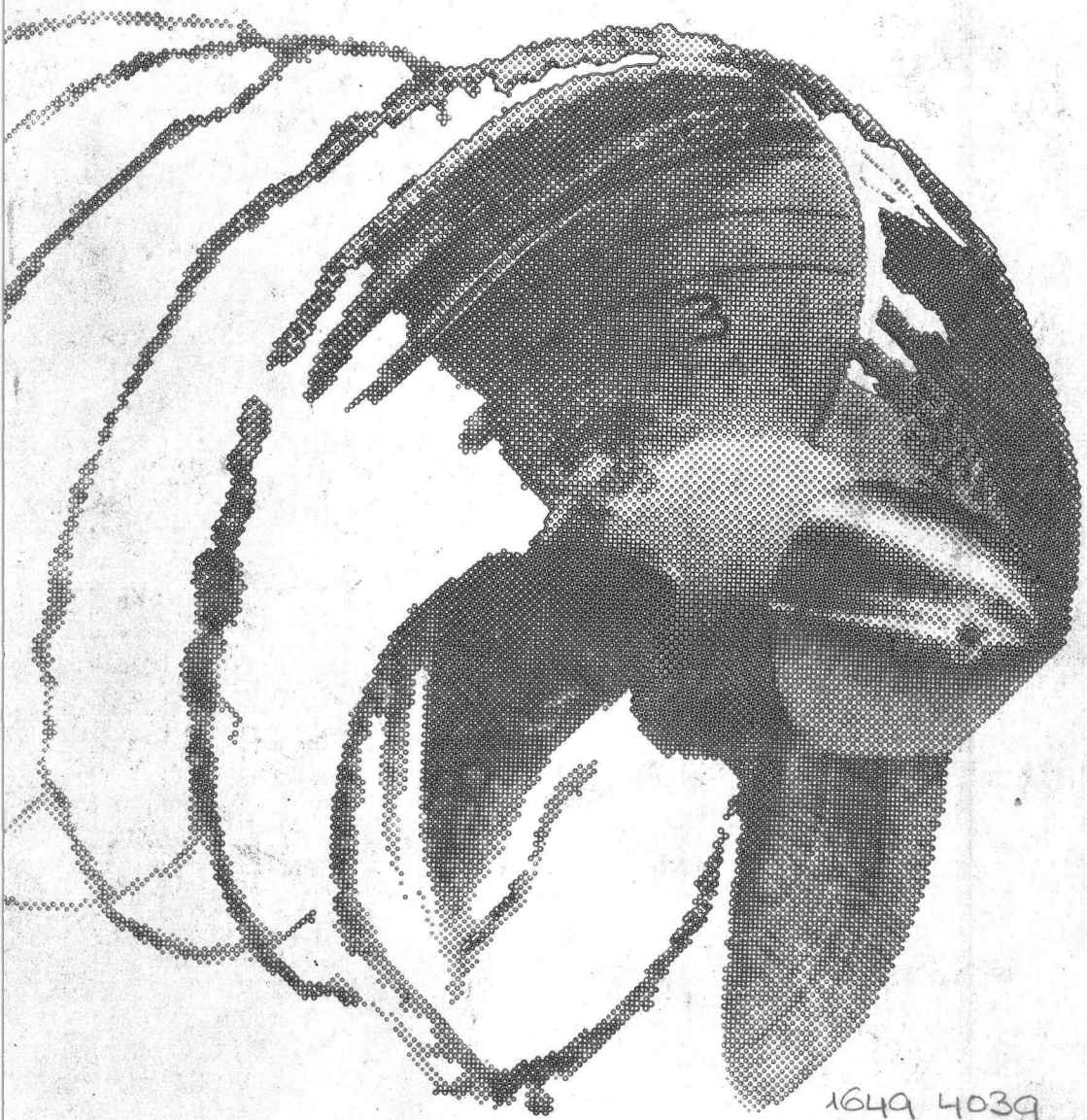

G. KUIPER

CAVITATION INCEPTION ON SHIP PROPELLER MODELS

CAVITATION INCEPTION ON SHIP PROPELLER MODELS

PROEFSCHRIFT

TER VERKRIJGING VAN DE GRAAD VAN DOCTOR IN DE TECHNISCHE WETENSCHAPPEN AAN DE TECHNISCHE HOGESCHOOL DELFT OP GEZAG VAN DE RECTOR MAGNIFICUS, PROF. IR. B. P. TH. VELTMAN VOOR EEN COMMISSIE AANGEWEZEN DOOR HET COLLEGE VAN DEKANEN TE VERDEDIGEN OP WOENSDAG 11 MAART 1981 TE 16.00 UUR

DOOR

GERRIT KUIPER

SCHEEPSBOUWKUNDIG INGENIEUR
GEBOREN TE ROTTERDAM

H. VEENMAN EN ZONEN B.V. – WAGENINGEN – 1981

Dit proefschrift is goedgekeurd
door de promotoren

Prof. Dr. Ir. J. D. van Manen
Prof. Dr. Ir. L. van Wijngaarden

Aan mijn ouders

CONTENTS

1. Introduction

Cavities are volumes filled with vapor in a local low pressure region in a fluid flow. The beginning or inception of cavitation is important for scaling of cavitation. In this section the mechanism of cavitation inception is discussed and a simple theoretical model of bubble equilibrium is described. Arguments are given why diffusion and bubble dynamics can be neglected in cavitation inception. The parameters for scaling cavitation on ship propellers are given and the facilities used in this investigation are described.

1.1. CAVITATION

When in a fluid flow high velocities occur locally, the pressure will consequently drop and when the pressure decrease is large enough part of the fluid will become vapor. The regions in which vapor exists are called cavities.

The volume increase due to vaporization limits the pressure decrease to about the equilibrium vapor pressure at the local temperature. At room temperature the temperature of the fluid is hardly affected by this process of cavitation. This distinguishes cavitation from boiling, which occurs when the temperature is raised to the boiling-point and where the vaporization is controlled by heat transfer (Plesset and Prosperetti, 1969).

In cavitation the dynamic behaviour of the vapor "bubbles" is decisive. Because low pressures and high velocities go together the time during which a fluid particle is in a low pressure region is generally short and the motions of the cavities are mostly violent, resulting in detrimental effects such as erosion, vibrations and excessive noise production, while large amounts of cavitation will cause a loss of performance of e.g. hydrofoils, ship propellers or pumps.

Cavitation is a widespread phenomenon in fluids engineering. Everywhere where high fluid velocities are required or where bodies move through a fluid with high speed there is a risk of cavitation. Cavitation occurs from

rocket fuel systems to normal taps, from river dam overflows to sluice-gates. Cavitation is common in marine propulsion, but also occurs on fins, domes, rudders, bossings, hydrofoils, torpedo's, etc. But also in unexpected cases as in the medical use of ultrasonics cavitation is suspected to occur.

Especially where reliability is very important, e.g. in reactor coolant systems, cavitation poses unacceptable risks. Sometimes cavitation can be made use of, such as in the case of supercavitating propellers and rock-cutting.

1.2. CAVITATION INCEPTION

Although the pressure in a cavity is close to the vapor pressure it sometimes requires very low pressures to create a cavity, because the fluid can withstand high tensions. An extreme example was given by Briggs (1950), who found a maximum tension in pure, standing water at $10^{\circ}C$ of 277 bars !

The pressure at which cavities are formed is called the inception pressure. In most cases the deviation of the inception pressure from the vapor pressure is below 1 bar, but certainly not negligible. A possible consequence of this deviation of the inception pressure from the vapor pressure is cavitation hysteresis, which means that the disappearance of cavitation occurs at a higher pressure than the appearance or inception of cavitation.

The deviation of the inception pressure from the vapor pressure causes serious problems when cavitation is scaled, that is when the cavitation behaviour of a device is investigated on model scale, as is e.g. common in the case of ship propellers. Correct scaling of cavitation inception to model scale is important not only for the correct prediction of the occurrence of cavitation, but also for a proper representation of propeller induced vibrations, which has become very important. Improper scaling of cavitation inception can strongly affect the hydrodynamic forces on the hull, especially the higher harmonics. Here scale effects can occur, which can be mistakenly attributed to scale effects in the wake of a ship model.

These problems triggered the present investigation and its purpose therefore is to investigate the parameters which control cavitation inception on model propellers and to devise test techniques which improve the prediction of cavitation inception on the prototype from model tests.

1.3. THE MECHANISM OF CAVITATION INCEPTION

1.3.1. The bubble equilibrium approach

Since pure liquids can withstand high tensions some additional mechanism is required to break the bond between the water molecules at cavitation inception. Elements able to do this are called nuclei, and one form of a nucleus is a free gas bubble. Knapp and Hollander (1948) visualized the growth and collapse of cavitation bubbles in their classical high speed film of bubble cavitation on a 1.5 caliber ogive headform. Plesset (1949) showed that the observed behaviour of the cavities could remarkably accurately be described by the somewhat modified Rayleigh equation:

$$\rho R\ddot{R} + \frac{3}{2}\rho\dot{R}^2 = -p+p_v - \frac{2s}{R} + \frac{K}{R^3} \qquad (1.1)$$

where: R = bubble radius

$\dot{R}$, $\ddot{R}$ = time derivatives of the bubble radius

p = pressure in the fluid surrounding the bubble

p_v = vapor pressure at the local temperature

s = surface tension

K = constant representing the amount of gas in the bubble, assuming isothermal expansion.

Plesset did not need the gas pressure to obtain a good correlation with the observations since the bubbles had already grown significantly before becoming visible, which made the gas pressure very low. Initially, however, such a gas bubble existed in the fluid with a radius R_o which can be found from the equilibrium equation:

$$p_o-p_v + \frac{2s}{R_o} - \frac{K}{R_o^3} = 0 \qquad (1.2)$$

with p_o as the pressure at infinity. When the equilibrium of eq. 1.2 exists

the bubble growth with decreasing pressure is small. Below a certain critical pressure equilibrium is, however, no longer possible and the bubble will grow rapidly. This critical pressure can be considered as the inception pressure, which is (Blake, 1949):

$$p_i = p_v - \frac{4s}{3R_{crit}} \tag{1.3}$$

in which

$$R_{crit} = (\frac{3}{2}\frac{K}{s})^{\frac{1}{2}} \tag{1.4}$$

The inception pressure p_i in eq. 1.3 is smaller than the vapor pressure and depends on the largest gas bubbles in the flow.

The growth rate of the bubble after inception can be approximated by:

$$\frac{3}{2}\dot{R}^2 = p_v - p \tag{1.5}$$

which is an asymptotic solution of eq. 1.1.

The definition of cavitation inception when a gas-vapor bubble becomes unstable coincides with the acoustical detection of cavitation inception, since a violent collaps occurs only when the bubble is unstable. Generally, however, cavitation inception is detected visually by observing bubbles which exceed a certain minimum size, and when the initial bubble diameter is not too small a gas-vapor bubble can grow to visible dimensions without being unstable. When the bubble is visible the effect of surface tension can be neglected and the inception pressure can be written from eq. 1.2 as:

$$p_i = p_v + \frac{K}{R_i^3} \tag{1.6}$$

where R_i is the radius of a bubble just visible. In such a case the inception pressure depends on the gas content K of the initial bubble and the inception pressure is higher than the vapor pressure. Holl (1960)called this type of cavitation "gaseous cavitation" and he suggested that K/R^3 remains constant due to gas diffusion into the bubble.

1.3.2. Viscous effects on cavitation inception

The radial motions of a gas-vapor bubble are determined by the pressure it experiences. Since the bubbles are generally small this pressure is not necessarily the local mean pressure. Daily and Johnson (1956) observed gas bubbles of about 0.25 mm diameter in a turbulent boundary layer. Arndt and Ippen (1968) did the same in the boundary layer above a roughened surface. They observed a critical radius when the bubbles arrived in a low pressure region and also determined the growth rate. Both the critical pressure, calculated from eq. 1.3 and the local pressure, calculated from eq. 1.5 were lower than the measured wall pressure, which is the mean pressure in the boundary layer. This pressure difference was much larger than could be explained by the rms-value of the turbulent pressure fluctuations, so apparently local low pressure regions occur in a turbulent boundary layer with a pressure considerably below the mean pressure. These low pressure regions occur in the center of the turbulent boundary layer since the bubbles mainly expanded in that region.

Kermeen et al (1955) experimentally verified on a hemispherical headform that negative pressures occurred in the minimum pressure region without cavitation inception. They observed microscopic bubbles growing into cavities at a position downstream of the minimum pressure point. Since these bubbles grew while attached to the body the attention was focussed on diffusive growth of microbubbles which are immersed in a boundary layer (v.d. Walle, 1962; Holl, 1960; Oshima, 1961; v. Wijngaarden, 1967; Holl and Kornhauser, 1970). Visualization of the boundary layer by Arakeri and Acosta (1973), however, revealed the existence of a laminar separated region in the boundary layer of the hemispherical headform and they related the inception pressure with the pressure at the separation point. Similar findings were made by Casey (1974) on two-dimensional headforms. Alexander (1974) hypothesized that diffusive bubble growth occurred due to a longer residence time of the bubbles in the separated region, but Arakeri (1975) and Huang and Hannan (1975) measured strong wall-pressure fluctuations in the reattachment region of the separation bubble. (The separated region is called a separation "bubble", which should not be confused with actual bubbles in the flow). These wall-pressure fluctuations were an order of magnitude larger than those in a fully established turbulent boundary layer.

Similar pressure fluctuations, but somewhat less strong, were measured by Huang and Hannan (1975) in the transition region of a body without laminar separation, while Arakeri and Acosta (1973) found a remarkable correlation between the mean pressure at transition and the vapor pressure at cavitation inception. Actually Huang (1979) observed that the transition region was the location of cavitation inception, as was also measured by Holl and Carroll (1979).

Since these pressure fluctuations were recognized as the cause of cavitation inception a kind of dualistic prediction of inception has prevailed. On the one hand the bubble equilibrium theory is used to describe cavitation inception at the minimum pressure point, resulting in transient bubble cavitation, on the other hand the strong pressure fluctuations in the boundary layer are used to predict inception at reattachment or transition, assuming inception at the vapor pressure (Huang and Peterson, 1976). Still it can be expected that also when inception is controlled by viscous effects nuclei are still necessary for inception, and when no sensitivity for their initial size is found the mechanism causing this should be identified.

1.3.3. Additional effects on cavitation inception

1.3.3.1. Turbulence

The turbulence level of the inflow can affect cavitation inception indirectly by changing transition in the boundary layer (Gates, 1977; Keller, 1979). Probably this occurs when the turbulence provides initial disturbances, which are amplified in the laminar boundary layer (Mack, 1977).

A ship propeller generally operates in a highly turbulent wake and it is therefore sometimes assumed that this fact offsets, as least partially, the effect of a low Reynolds number on model scale. Little information is available, but some observations made with paint streaks on model propellers in behind condition revealed that laminar boundary layer flow persisted despite the high turbulence levels, which is possible when the turbulence frequencies do not match with the unstable frequencies on the propeller blades.

1.3.3.2. Bubble response in a pressure field.

The bubble equilibrium approach of cavitation inception is a strongly simplified approach and it requires some more arguments to make clear that it is a good approximation for cavitation inception. The pressure gradient, experienced by a bubble passing through a low pressure region, can be too large for the bubble to be in static equilibrium. The radial motion of the bubble is then governed by the Rayleigh-Plesset equation, eq. 1.1. In water the effect of viscosity on the bubble motion can be neglected.

An extreme case of a rapid pressure drop is a pressure step. When the pressure step is small and negative the bubble will grow dynamically and perform an oscillation around a new equilibrium radius. Above a critical value of the pressure step the bubble will remain unstable and grow indefinitely with a growth rate as given in eq. 1.5. Persson (1973) calculated this critical pressure and showed that it differed less than 10% from the critical pressure obtained from static equilibrium. Oldenziel (1979) formulated an explicit expression for the bubble wall velocity, neglecting the vapor pressure and viscosity and using a polytropic gas constant of 4/3. The critical pressures derived from this expression were also within 10% of those from the equilibrium approach. These deviations occurred for large initial radii, and therefore we may conclude that eq. 1.3 can also be used in this case of a strong pressure gradient.

A dynamic behaviour of the radial bubble motion can also occur when the bubble is subjected to fluctuating pressures, as for example, occur in the reattachment region of a laminar separation bubble. When the frequency of the pressure fluctuations is high the threshold pressure amplitude becomes frequency dependent (e.g. Flynn, 1964). This occurs only at frequencies higher than resonance frequency, which in the isothermal linear case can be written as:

$$\omega_o^2 = \frac{1}{\rho R^2} \{3(p_o - p_v + \frac{2s}{R}) - \frac{2s}{R}\} \qquad (1.7)$$

For frequencies much lower than the resonance frequency eq. 1.3 can also be used with good accuracy, as was shown by Neppiras and Noltink (1951) for an ultrasonic pressure field and by Flynn (1964) for a single pressure pulse. Flynn also showed that for frequencies up to about one tenth of the resonance frequency the bubble expansion is isothermal. When the bubble interior is

not considered as homogeneous the expansion process remains isothermal up to much higher frequencies (Plesset and Hsieh, 1960).

It must be mentioned that the assumption that pressure fluctuations act on microscopic bubbles is related with the way in which turbulence is considered. In the stochastic description of the turbulent motion the bubbles experience pressure fluctuations. In a more deterministic description, however, it is possible that a certain frequency or coherent structure dominates the flow and the bubble can travel at the same velocity as the wave or coherent structure. In such a case the pressure experienced by a bubble in the boundary layer can be lower than the lowest wall pressure, and the time scale during which this low pressure is experienced can be longer than that of the wall pressure fluctuations.

1.3.3.3. Diffusion.

In the bubble equilibrium approach the amount of gas in the bubble is considered constant and diffusion has been neglected. Diffusion can increase the amount of gas in the bubble when the fluid is supersaturated, thus stimulating inception because the critical pressure is reached sooner.

The mass flow into a bubble can be written as:

$$\frac{dm}{dt} = 4\pi r^2 \, D\left(\frac{\partial C}{\partial r}\right)_R \tag{1.8}$$

in which D is the diffusion coefficient, C is the gas concentration in the fluid and R is the bubble radius. Due to this mass flow the bubble radius changes as:

$$\frac{dR}{dt} = \frac{D}{\rho_g} \left(\frac{\partial C}{\partial r}\right)_R \tag{1.9}$$

where ρ_g is the specific mass of the gas. Epstein and Plesset (1950) gave a solution for the concentration gradient:

$$\left(\frac{\partial C}{\partial r}\right)_R = \left(\frac{1}{R} + \frac{1}{(\pi Dt)^{\frac{1}{2}}}\right)(C_\infty - C_o) \tag{1.10}$$

in which the length $(\pi Dt)^{\frac{1}{2}}$ can be regarded as a diffusion boundary layer thickness. For small bubbles this thickness is larger than the radius R.

Neglecting the term $(\pi Dt)^{-\frac{1}{2}}$ in eq. (1.10) this leads to

$$\left(\frac{R}{R_o}\right)^2 = 1 + \frac{2DC_\infty}{\rho_g R_o^2}\, t \qquad (1.11)$$

The gas concentration at the bubble wall C_o has been neglected in this case, since the gas pressure in an expanding bubble will be very low. The time, needed for a 20 μm diameter bubble to double its diameter in a five times saturated fluid can be calculated from eq. (1.11) to be 0.75 seconds, using the data :

$$\begin{aligned} &D = 2x19^{-9} \quad m^2/sec \\ &C_\infty/\rho_g = 0.1 \\ &R = 10^{-5} \\ &R/R_o = 2 \end{aligned} \qquad (1.12)$$

The diffusion boundary layer thickness $\sqrt{\pi Dt}$ is $1.1x10^{-4}$ in this case, which is indeed larger than R_o and the approximation of eq. 1.11 is therefore allowed.

The time of 0.75 seconds needed to double the bubble size in this highly supersaturated condition is too long to have an effect on cavitation inception. It is therefore justified to neglect diffusion effects in cavitation inception.

1.3.3.4. Convective diffusion

A significant increase in the growth velocity of a bubble occurs when the bubble is in motion relative to the fluid and convective diffusion takes place. The diffusion boundary layer thickness is of the order $(RD/U)^{\frac{1}{2}}$, where U is the relative bubble velocity, R the bubble radius and D the diffusion coefficient. (see Levich, 1962). For a 20 μm diameter bubble, moving at 1 cm/sec through the fluid, this boundary layer thickness is 10^{-6} m, which is an order of magnitude less than the radius R, used in eq. 1.11 and the doubling time will therefore be shorter.

Van Wijngaarden (1967) derived the time needed for the growth of a bubble from R_1 to R_2 to be:

$$t = \frac{\pi^{\frac{1}{2}} \rho_g}{(2UD)^{\frac{1}{2}} C} \int_{R_o}^{R_1} r^{\frac{1}{2}} dr \qquad (1.13)$$

In this relation the influence of the vapor pressure and of the surface tension has been neglected. When again the values (1.12) are used the doubling time reduces from 0.75 seconds for diffusion to 0.11 seconds for convective diffusion when the relative bubble velocity U=0.01 m/sec.

A relative bubble velocity can be caused by the pressure gradients along a propeller section. Assuming that the bubble resistance is that of a solid sphere the relation between the bubble velocity and the pressure gradient is

$$U_b = \frac{2}{9} \frac{R^2}{\mu} \frac{\partial p}{\partial x} \qquad (1.14)$$

Steep adverse pressure gradients occur behind a sharp low pressure peak at the leading edges of a propeller. As an example: the maximum pressure gradients, calculated on a propeller with such low pressure peaks at the leading edge (Propeller S, as will be described in section 1.6) were between 10^5 (at an advance ratio of 0.6) and 10^6 (at an advance ratio of 0.4). The relative velocity U_b of a 20 μm diameter bubble is between 0.002 and 0.02 m/sec. However, the time during which these steep pressure gradients act on the bubble is less than 10^{-4} seconds and during this time the bubble growth due to convective diffusion can be neglected.

Also turbulent velocity fluctuations can cause a bubble motion relative to the flow. The time scale of the bubble motion can be estimated as (Oldenziel, 1979):

$$t = \frac{10\ R_o^2}{\nu} \qquad (1.15)$$

For a bubble of 20 μm diameter in water ($\nu=10^{-6}$ m^2/sec) this time scale is 10^{-3} sec and a possibility of convective diffusion will occur for such a bubble in turbulence frequencies above 1 kHz. The length scale of the turbulence has to be large relative to the bubble size and this possibility of convective diffusion is therefore restricted to very small bubbles. Experimental verifications of this mechanism in the boundary layer of a body are not available.

Strong radial bubble growth can also cause convective diffusion (Oldenziel, 1979) which is the reason why cavitation generates free gas bubbles in the flow. This only occurs, however, when the bubbles are unstable and beyond inception.

1.3.3.5. Rectified diffusion

When a gas bubble is subjected to an oscillating pressure field the oscillatory bubble motion increases diffusion. When the diffusion length scale $\sqrt{D\omega}$ is small (ω is the circumferential frequency) relative to the bubble size R_o the gas inflow becomes independent of the frequency ω. For this case Hsieh and Plesset (1960) derived the following expression for the doubling time of a gas bubble due to rectified diffusion:

$$t = \frac{9R_o^2 \rho_g}{4C_\infty D\, p_a^2} \qquad (1.16)$$

where p_a is the relative pressure amplitude $\frac{p_{max}-p_o}{p_o}$ with $p_a \ll 1$.

Even if $p_a=0.5$ in a five times supersaturated flow ($C_\infty/\rho_g=0.1$) the doubling time for a 20 μm diameter gas bubble is still 4.5 seconds and again this is too long a time to be important for cavitation inception.

1.4. SCALING OF CAVITATION INCEPTION

1.4.1. Scaling parameters

As to the modelling of cavitation inception on foils and headforms the bubble equilibrium approach, although it is strongly simplified, is the only approach available and no improvements are to be expected without further quantitative knowledge about the nuclei distributions and the local pressures in the boundary layer, experienced by the nuclei. The following physical parameters govern the inception problem according to the equilibrium theory:

V	Flow velocity	$m\ sec^{-1}$
p_o-p_v	Difference between local pressure and vapor pressure	$kgm^{-1}sec^{-2}$
s/R_{crit}	Pressure increase due to the surface tension	$kgm^{-1}sec^{-2}$
ρ	Fluid density	kgm^{-3}
ν	Kinematic viscosity	m^2sec^{-1}
D	Body diameter	m

These six physical parameters in three dimensions lead to three non-dimensional parameters which completely describe the problem. These parameters are generally formulated as:

$$\sigma = \frac{p_o - p_v}{\frac{1}{2}\rho V^2} \qquad \text{cavitation index} \qquad (1.17)$$

$$Re = \frac{V.D}{\nu} \qquad \text{Reynolds number} \qquad (1.18)$$

$$We = \frac{\rho V^2 R_{crit}}{s} \qquad \text{Weber number} \qquad (1.19)$$

The Weber number is often related with the body diameter instead of with the critical bubble radius, but it should be kept in mind that this is only possible when the ratio R_{crit}/D is entered as a fourth dimensionless parameter.

1.4.2. Examples of scaling cavitation inception

For a correct scaling of the inception condition these three dimensionless parameters should be maintained. The effects of variations of each of these parameters were investigated extensively on foils and headforms, as e.g. summarized by Holl and Wislicenus (1961). A general problem in such tests is that the nuclei distribution, and consequently the critical bubble radius R_{crit}, is not known. It is, however, still important that interpretation of the results in terms of the bubble equilibrium theory is possible.

Two examples of results, given by Holl and Wislicenus, are shown in Figs. 1.1a and 1.1b for a hemispherical headform and a Joukowsky hydrofoil respectively. The inception index increases with increasing Reynolds number, but decreases with increasing body diameter. In terms of the bubble equilibrium theory the decrease of the inception index by an increase of body diameter at a constant Reynolds number (from A to C in Figs. 1.1) can only be caused by a change in Weber number. This change in inception index is therefore indicated as $\Delta\sigma_w$.

The decrease of the inception index is plausible since an increase of the body diameter at constant Reynolds number implies a decrease in tunnel velocity. Unless the critical bubble radius increases rapidly with decreasing

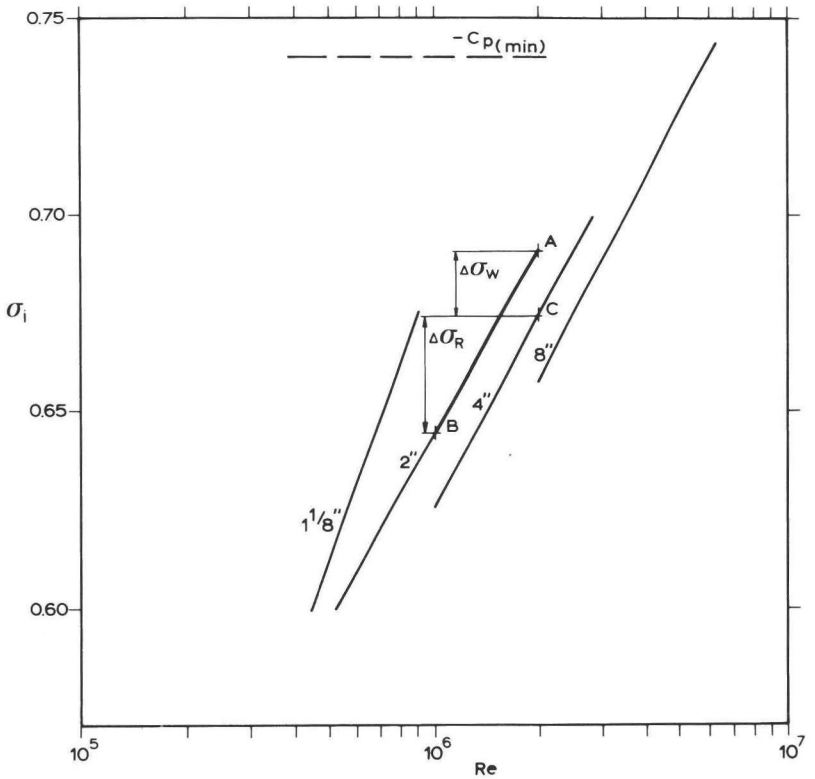

Fig. 1.1a. Inception index as a function of Reynolds number on a hemispherical headform. (Data from Parkin and Holl, 1954. Tunnel: 48" A.R.L.).

tunnel velocity and pressure, the Weber number will decrease and so will the inception index.

The effect of the variation of Reynolds number at constant Weber number can be seen from the difference in inception index $\Delta\sigma_R$ between conditions C and B in Figs. 1.1. The Weber number does not change between these two conditions since the tunnel velocity and pressure are approximately the same.

From these considerations it follows that the decrease of the inception index on the 2" bodies in Figs. 1.1 due to a decrease of Reynolds number (from condition A to B) is completely caused by a change in the nuclei content in the case of the Joukowski airfoil (Fig. 1.1b), while in the case of the hemispherical headform the Reynolds effect dominates (Fig. 1.1a).

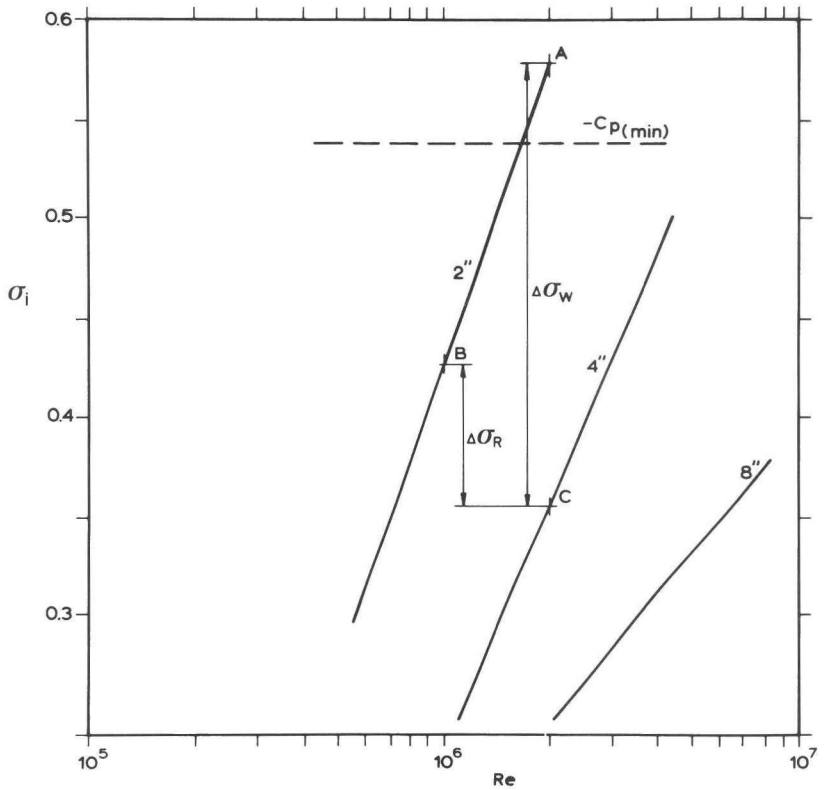

Fig. 1.1b. Inception index as a function of Reynolds number on a 12% Joukowski hydrofoil at 0^o angle of attack. (Data from Parkin, 1952. Tunnel: 14" C.I.T.).

The Reynolds dependency of the hemispherical headform was examined closely by many investigators and cavitation inception on this body indeed proved to be controlled by viscous effects (Arakeri and Acosta, 1973; van der Meulen, 1976; Holl and Carroll, 1979; Keller, 1979). The inception behaviour of the Joukowski airfoil has not been considered so closely, but probably inception of bubble cavitation occurred in the midchord region. These examples illustrate that a detailed description of the type and location of the cavities at inception as well as a detailed description of the tunnel conditions and properties is necessary for a proper interpretation of cavitation inception. This was elegantly illustrated by Johnsson (ITTC, 1969) who reported a wide range of inception pressures with a corresponding wide range of cavitation patterns obtained on the same headform in a variety of

cavitation tunnels. Reproducability of inception is still a problem, as was again illustrated by inception measurements on one body reported by the ITTC Cavitation Committee (ITTC, 1978).

1.4.3. Scaling of propeller cavitation inception

In the case of propellers a second velocity scale is present: the rotational speed, expressed as the number of revolutions per second. A propeller also generally operates in a vertical plane, which means that gravity influences the pressure distribution. These two parameters add two non-dimensional parameters to the three of eqs. 1.17 to 1.19. They are formulated in this investigation as:

$$\sigma_n = \frac{p_o - p_v}{\frac{1}{2}\rho n^2 D^2} \qquad \text{propeller cavitation index} \qquad (1.20)$$

$$Re_n = \frac{nD^2}{\nu} \qquad \text{propeller Reynolds number} \qquad (1.21)$$

$$We = \frac{\rho\, U^2 R_{crit}}{s} \qquad \text{Weber number} \qquad (1.22)$$

$$Fr = \frac{U}{\sqrt{g.D}} \qquad \text{Froude number} \qquad (1.23)$$

$$J = \frac{U}{nD} \qquad \text{Advance ratio} \qquad (1.24)$$

The velocity U is the forward speed of the propeller. The pressure p_o is the static pressure at shaft height, which in the Depressurized Towing Tank is found from the tank pressure p_t by $p_o = p_t + \rho g h$.

The propeller cavitation index and the propeller Reynolds number are parameters for the propeller. The relevant velocity for the propeller sections is the rotational inflow velocity at that radius, which in the far field is:

$$V(r) = \{U + (\frac{r}{R}\,\pi nD)^2\}^{\frac{1}{2}} \qquad (1.25)$$

The cavitation index for the propeller section is therefore written as:

$$\sigma(r) = \frac{p_o - p_v - \rho g h}{\frac{1}{2}\rho V^2} \tag{1.26}$$

where h is the height of the propeller section above the shaft. In most cases the propeller blade is in upright position and h=r.

The pressure coefficient on the blade section, which has to be related with σ, is defined as:

$$C_p(r,s) = \frac{p(s) - (p_o - \rho g h)}{\frac{1}{2}\rho V^2} \tag{1.27}$$

in which the pressure $p_o - \rho g h$ is the pressure at infinity at the same height and p(s) is the local pressure at chordwise position s.

Generally Reynolds-and Weber number are not accounted for in scaling cavitation, provided they both exceed some minimum value. Cavitation inception is then assumed at a certain radius if:

$$-C_p(r,s)_{min} = \sigma(r) \tag{1.28}$$

if this is not the case cavitation on the model is no longer a correct representation of the cavitation on full scale and so-called scale effects occur. These scale effects will be investigated and this is done by using propeller models in a uniform axial flow to avoid the difficult problem of interaction between the propeller and the inflow velocity distribution. The tests were carried out in two test facilities: a cavitation tunnel, in which much experience in cavitation testing exists, and a Depressurized Towing Tank, in which the conditions are different from those in a tunnel. The investigations will be carried out for three specific types of cavitation (bubble, sheet and vortex cavitation) for which purpose three special propellers were designed.

1.5. TEST FACILITIES

Tests were carried out in the N.S.M.B.* Depressurized Towing Tank at

*Netherlands ship model Basin

Ede, the Netherlands. The use of a towing tank has specific advantages, mainly because the nuclei contents of the water is very low and independent of the propeller velocity. A description of the tank is given by Kuiper (1974) and only some relevant data will be mentioned.

The tank consists of a water basin of 240x18x8 meters, which is covered by a cylindrical roof. The air pressure inside the tank can be lowered to a minimum pressure of about 40 mbar. The tank is filled with tap water and the total air contents is generally ppm. The air contents of the water can be changed by a circulation system along the length of the tank: one tube near the surface at one side, one tube near the bottom at the other side. Deaeration of the water can be done by blowing water out of the upper pipe through small holes at low tank pressure. The cavitating jets which are formed at the holes deaerate the water. Aeration is done at atmospheric pressure by blowing air into the circulation circuit and pumping this air-water mixture through the lower pipe into the tank. To obtain a significant change in the air content several hours of aerating or deaerating are necessary. The total air contents of the water is measured at atmospheric pressure by a van Slyke apparatus, using a water sample taken from the center of the tank at 1 meter below the surface. The characteristics of the total and free gas contents of the tank will be discussed in Section 2. The water temperature was about 10^{o}C for all tests.

The carriage has a maximum velocity of 4.6 m/sec and reaches this speed in a fixed time interval of 16 seconds. The constancy of the speed is very high to avoid accelerations and the accuracy of the speed is better than 0.5%. A sketch of the tank is given in Fig. 1.2.

The ship models are brought into the tank through a pressure lock. To test open-water characteristics of a propeller this requires a special floating platform. Therefore a catamaran-type vessel was used, as shown in Fig. 1.3. Propellers were mounted on a right angle drive and the rate of revolutions could be kept within 0.5% of the required propeller revolutions. Observations of the suction side of the propeller were made through windows in the hull of the catamaran by remotely controlled camaras. The stroboscopes for illumination were also placed in the catamaran. For the application of electrolysis a grid of wires was mounted at 1.6 meter in front of the propellers. This grid was not removed for tests without electrolysis.

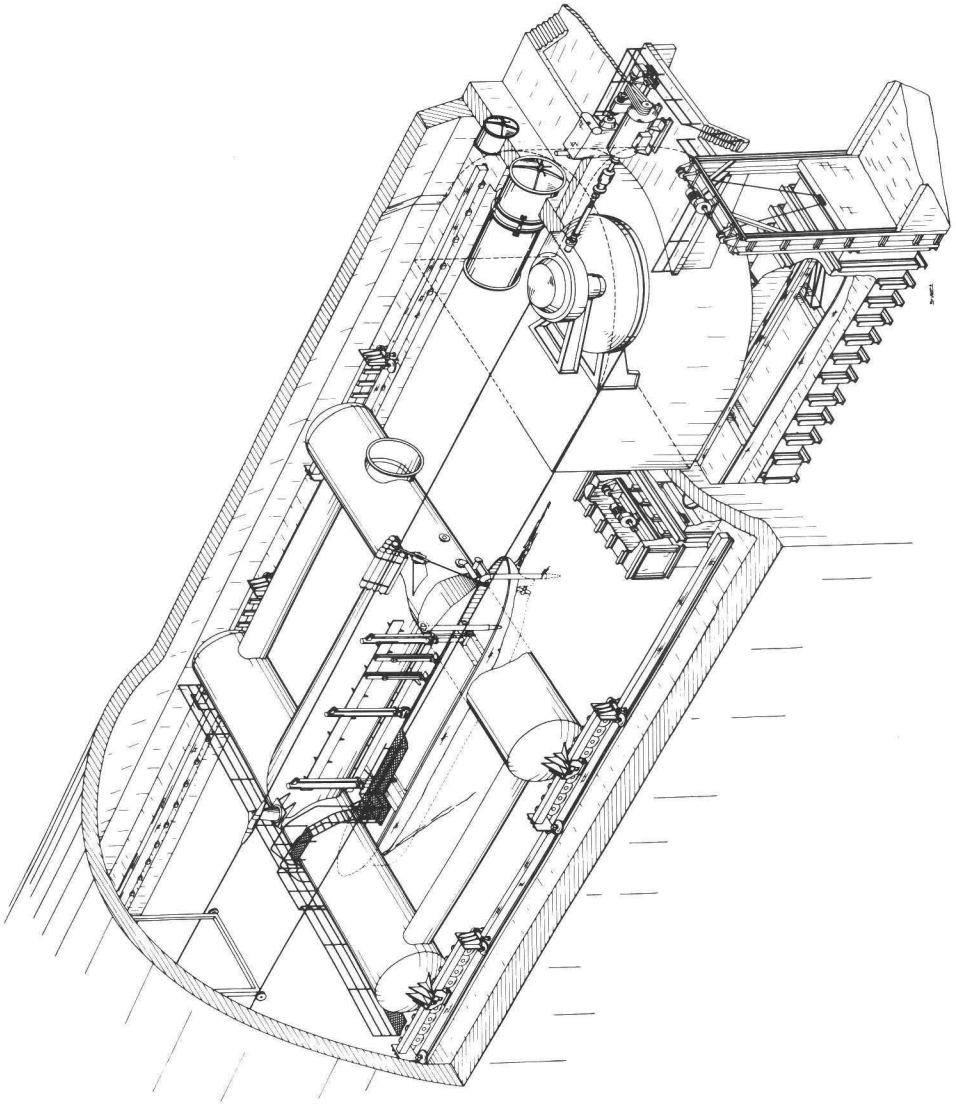

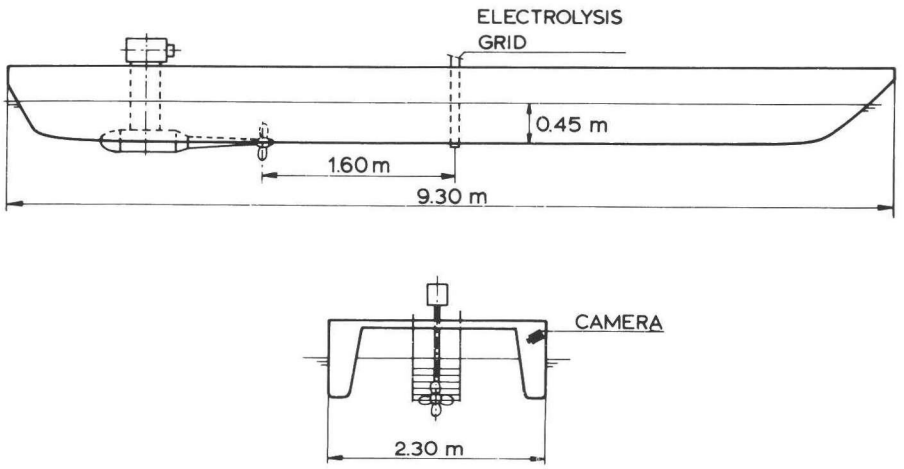

Fig. 1.3. Test arrangement in the Depressurized Towing Tank.

Small disturbances in the propeller inflow were caused by the catamaran at the propeller location. These disturbances were dependent on the carriage speed and could grow to 3% of the carriage speed, which determined the accuracy of the chosen advance ratio. These catamaran induced disturbance velocities were fairly uniform over the propeller disk and reproduced good as a function of the carriage velocity. When the propeller Reynolds number is varied, implying a variation in carriage speed, the inaccuracy of the advance ratio is consequently 3% maximum.

The propellers were also tested in the N.S.M.B. Cavitation Tunnel in Wageningen. A sketch of this tunnel is given in Fig. 1.4. The dimensions of the test section are 0.9x0.9 meter with rounded corners. The minimum pressure is about 200 mbar.

Electrolysis was applied in this tunnel using a pair of stainless steel strips, glued on top of a profile which was mounted in the test section at 1.6 meter in front of the propeller. The total air contents was 6.5 ppm and the temperature of the tunnel water was always near $20^{o}C$.

For observation reasons the propeller blades in the tunnel were observed in the downward position.

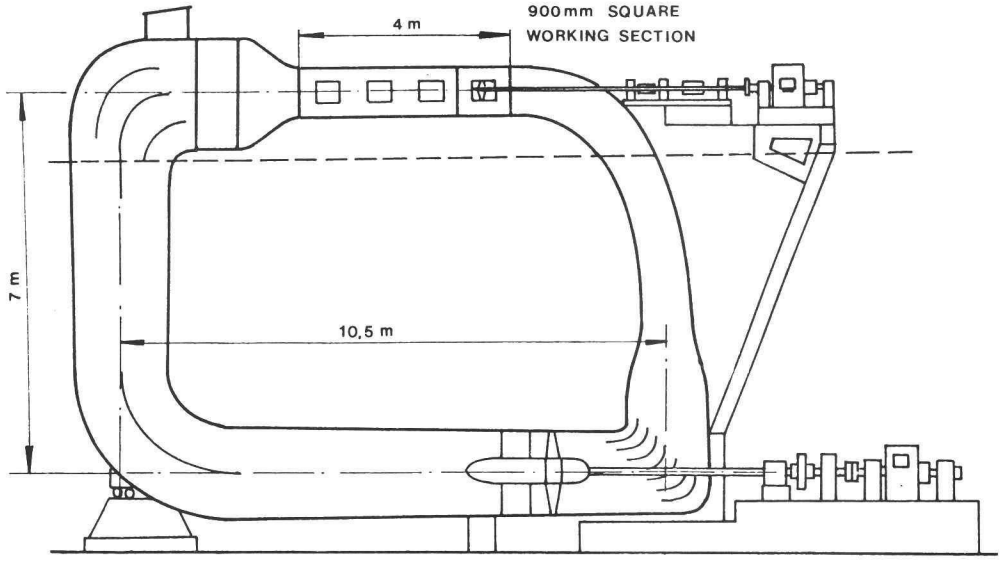

Fig. 1.4. The N.S.M.B. Large Cavitation Tunnel.

1.6. PROPELLERS FOR SPECIFIC TYPES OF CAVITATION

It has been observed on headforms that different types of cavitation have different inception indices. So it is necessary to distinguish the types of cavitation occurring on a propeller carefully. Cavitation can assume many shapes, the most distinctive of which are bubble cavitation, sheet cavitation and vortex cavitation.

Bubble cavitation occurs when distinct vapor bubbles are formed, which travel with the fluid.

Sheet cavitation occurs when a vapor region, attached to the wall, is formed. This vapor region displaces the streamlines of the fluid flow.

Vortex cavitation occurs in the center of a vortex and makes this vortex visible as a long tube of vapor, which moves with the flow.

Cavitation, has, however, generally a multitude of appearances. One of them is cloud cavitation, which, for example, occurs in a free shear layer. It consists of vapor regions which are very irregularly shaped and this is connected with violent turbulent motions in the fluid. Excellent pictures of this type of cavitation were made by Hoyt and Taylor (1979). Cloud cavitation is also typical behind an unsteady sheet cavity.

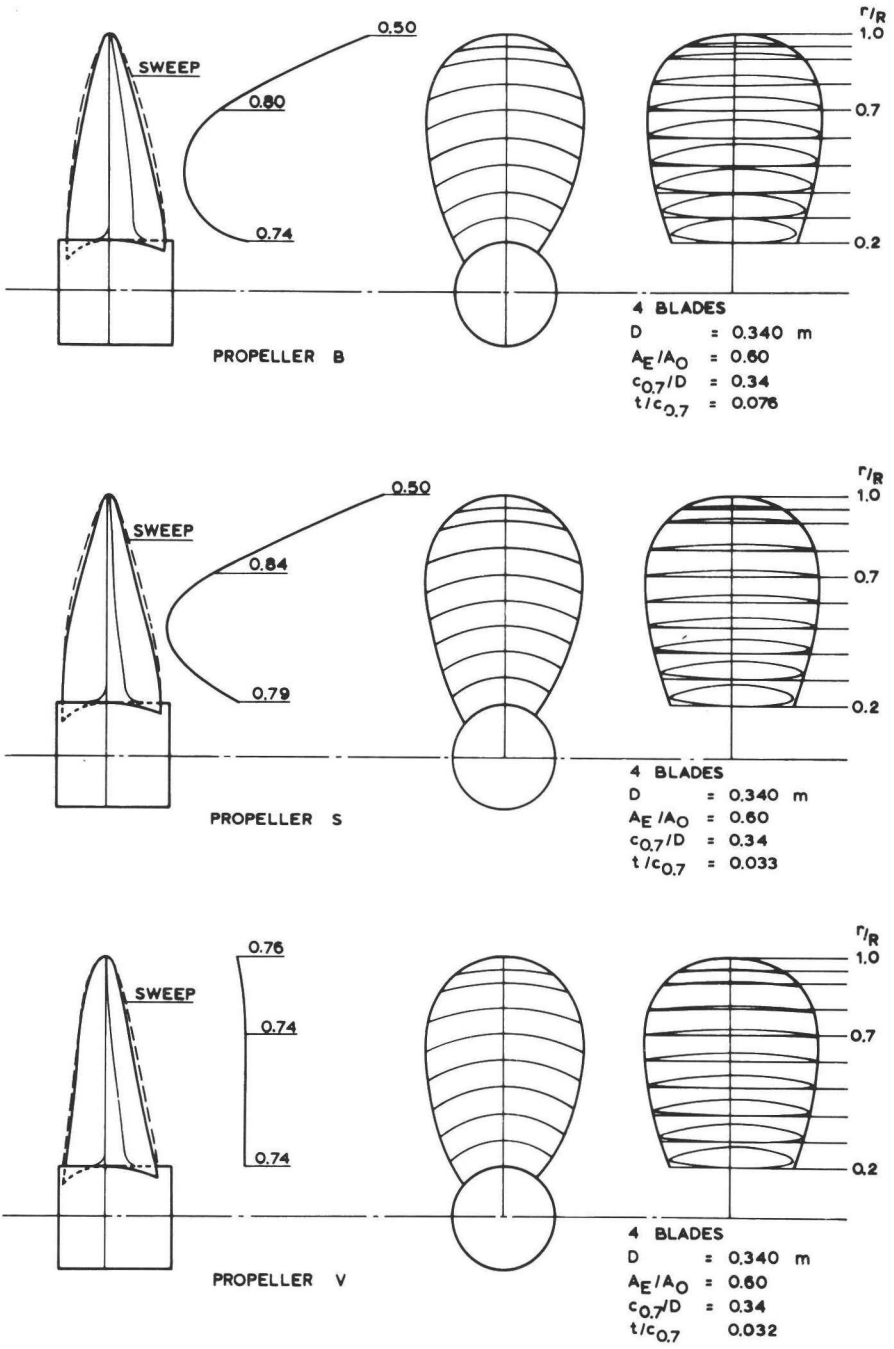

Fig. 1.5. Geometry of propellers B, S and V.

Also descriptions as spots, streaks or patches are used to describe the form of a cavity, while the surface of a sheet can be bubbly, glassy, foamy, streaky, etc. In general, it requires a good photograph to document properly what type of cavitation is involved. Much attention has therefore been paid to document the appearance of cavities in the present study.

Three propellers were designed to exhibit the three "basic" types of cavitation: bubble, sheet and tip-vortex cavitation. Each of these propellers was designed to exhibit one type of cavitation only. The propeller geometry given in Fig. 1.5, was made as simple as possible: no rake, no skew, an elliptic blade contour and one type of sections over the whole radius. The differences between the three propellers are in the radial distribution of the maximum thickness, of the maximum camber and of the pitch.

The propeller with bubble cavitation, designated as propeller B, has thick, cambered profiles to avoid sheet cavitation. The propeller with sheet cavitation, designated propeller S, has thin profiles with small cambers Both propellers have a strongly reduced pitch at the tip to avoid tip vortex cavitation.

The propeller with tip vortex cavitation, designated propeller V, has a constant pitch over the radius and thick, cambered profiles.

The geometry of these propellers is given in Fig. 1.5 and the detailed geometry is given in Appendix I.

Propellers B, S and V were also made with diameters of 0.48 m and 0.24 m. These propellers were not yet used frequently, but will be mentioned occasionally. They will be indicated by one dot for the 0.24 m diameter propellers and by two dots for the 0.48 m diameter propellers.

Propellers B and S were tested at two advance ratios : J=0.4 and J=0.6. Because propeller V exhibited pressure-side cavitation at J=0.6 this propeller was tested at J=0.4 and J=0.5. The pressure distributions on the blades in these conditions will be calculated in the next section.

2. The calculation of the pressure distribution

Knowledge about the pressure distributions on the blades is indispensable for the interpretation of cavitation phenomena. The lifting surface theory combined with a two-dimensional approach to include the blade thickness, is used to calculate the pressure distribution. The assumptions, made in the calculations, are discussed and the sensitivity of the results for these assumptions is investigated to determine the accuracy of the calculations. Some comparisons with data from literature are made.

For the prediction and interpretation of cavitation, knowledge of the pressure distribution on the blades is necessary. It is, however, extremely difficult to measure this pressure distribution on propeller blades. A number of attempts have been made. (Mavludoff (1966), Hoïby (1970), Kato (1977), Takahashi and Oku (1977), Yamasaki (1978), Dohrendorf et al (1978), Takei et al (1979)). Until now no measurements have emerged which are generally accepted as a check for calculations. The availability of very small pressure pick-ups as e.g. used by Takei et al (1979) should make it possible to arrive at such a set of data in the near future.

Calculations remain necessary since measurements are too elaborate and also since the pressure peak at the leading edge of the propeller blade, which, if present, controls cavitation, is mostly too sharp to measure. The calculation of the pressure distribution is not a straightforward process. Due to simplifications and approximations and the subsequent application of corrections a wide variety of calculation procedures is possible. It is therefore necessary to document these calculation procedures carefully

In the following the calculation procedure, used to arrive at the calculated pressure distributions, will be discussed and the sensitivity of the results for various approximations will be investigated. The mathematical formulation of the problem and its solution will not be given, since that has been done elsewhere (Van Gent, 1975, 1977).

2.1. THE LIFTING SURFACE THEORY

In all calculation methods a potential theory is used, which implies two simplifications, viz., the viscosity of the fluid is neglected and the vorticity of the incoming flow is assumed to be zero. This assumption, although often ignored when a wake field is considered, is correct in uniform flow.

The velocity field around a propeller can be represented by a source or vortex distribution on the propeller surface, which leads after discretization to the so-called panel method. This method, formulated by Hess and Smith (1972) is used for airplane configurations. A disadvantage for propeller application is that for a proper representation of the sharp pressure peak at the leading edge a large number of panels are needed. resulting in long computer runs. An effort to apply this method to propellers was made at Twente Technical University (Roodbergen, 1976). Although promising results were obtained for the non-lifting condition the program has not been made operational.

The problem is considerably simplified when it is linearized, which leads to the lifting surface theory. This method will be used in this investigation. First the flow field with reference to the rotating propeller is divided into a far field with incoming velocity V, and a near-field with incoming velocity V_E, as shown in Fig. 2.1. The difference between these two velocities is the propeller induced velocity V_i. Both V_E and V_i are averaged over the propeller chordlength. The linearization is applied by assuming the

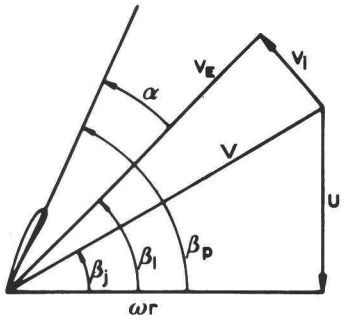

Fig. 2.1. Velocity diagram on a propeller section.

perturbations of V_E due to the propeller blades small relative to V_E. It must be mentioned that V_i is only small when the propeller is lightly loaded. At a moderate or heavy propeller loading V_i becomes large, which keeps the effective angle of attack α small. Linearization is therefore also possible for higher propeller loadings.

The sensitivity of the results for various parameters will be investigated using the "standard" program. Each of the "standard" parameters will be defined.

2.2. AN ESTIMATE OF THE LINEARIZATION ERROR

The error, made by the linearization, can be estimated using Bernoulli's equation along a streamline (see Fig. 2.2).

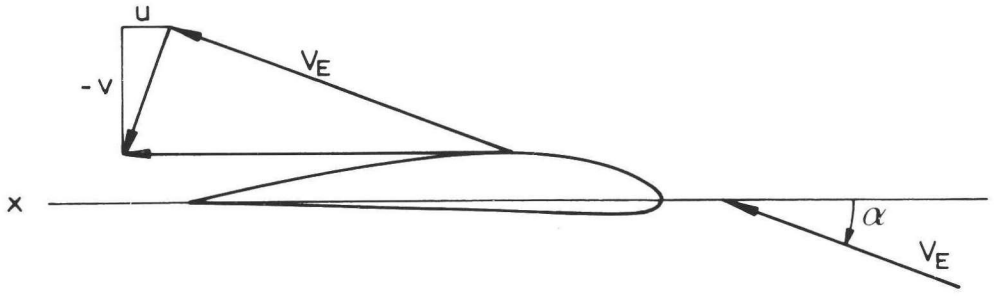

Fig. 2.2. Velocities on a propeller section.

$$p_o+\tfrac{1}{2}\rho\,\bar{V}_E^2 = p+\tfrac{1}{2}\rho\,(\bar{V}_E+\bar{v})^2 \qquad (2.1)$$

where p is the local pressure at a point on the propeller surface. Neglecting third orders of the angle of attack α eq. 2.1 can be written as:

$$C_p^* = \frac{p_o-p}{\tfrac{1}{2}\rho V_E^2} = 2\frac{u}{V_E} + \{\frac{u^2}{V_E^2} + \frac{v^2}{V_E^2} + \frac{w^2}{V_E^2} + \frac{2v\alpha}{V_E^2}\} \qquad (2.2)$$

where u, v and w are the components of the local perturbation velocity $\bar{v}$ (u in the direction of the chord and w in radial direction).

From the condition of tangential flow it follows that to the first order:

$$\frac{v}{V_E} = \alpha - \left(\frac{\partial f}{\partial x} \pm \tfrac{1}{2}\frac{\partial t}{\partial x}\right) \tag{2.3}$$

where f(x) is the camber and t(x) the thickness distribution. The magnitude of $\frac{u}{V_E}$ can be approximated in hindsight as $\frac{C_p^*}{2}$.

Except in the leading and trailing edge region (where u and v are not small) and in the tip region (where w is not small) and provided that the slope of the profile surface $\frac{\partial f}{\partial x} \pm \frac{1}{2}\frac{\partial t}{\partial x}$ is of order α, the error in the calculated linearized pressure coefficient is of the order:

$$\varepsilon = O\left(\alpha^2 + \frac{C_p^{*2}}{4}\right) \tag{2.4}$$

The region of interest for cavitation inception is the minimum pressure region, while the angles of attack generally remain small. As a result the second term mostly dominates the error.

Close to the leading edge the perturbation velocity becomes of the same order as the incoming velocity V_E, which leads to the well-known leading edge singularity, since the pressure coefficient becomes infinite. This is one of the main drawbacks of the linearized theory, because it makes it impossible to calculate the minimum pressure near the leading edge, which can be a measure for cavitation inception. This problem has to be overcome with a non-linear calculation, as will be discussed in section 2.9.

2.3. THE POSITION OF THE BOUND VORTICES

The linearization makes it possible to describe the propeller induced velocities by a distribution of vortices (or pressure dipoles) and sources in the propeller pitch plane. Only the vortices or pressure dipoles are considered in the lifting surface theory. The effect of propeller thickness will be discussed in sections 2.6 and 2.9.

In the lifting surface program the bound vortices are positioned in a helical plane with a constant pitch over the radius. In case of a propeller with a constant pitch over the radius the helical pitch is chosen equal to

the propeller pitch. When the propeller has a strongly varying pitch distribution over the radius the choice of the helical pitch is less obvious. This is e.g. the case with propellers S and B.

The standard helical pitch in the program is chosen as the propeller pitch at 0.7R. This choice is rather arbitrary, but is unimportant as long as the angle ϕ between the helical plane and the pitch plane remains of order α. In Fig. 2.3 the squares of the induced angles of attack α^2 are compared with the squares of the deviation angles ϕ^2 between the propeller pitch and the helical pitch. According to eq. 2.4 these values should be compared with $C_p^{*2}/4$, which value at midchord has also been plotted in Fig. 2.3. Only at radii larger than 0.9 the deviation of the helical pitch dominates. The data in Fig. 2.3 are for propeller S. The data of propeller

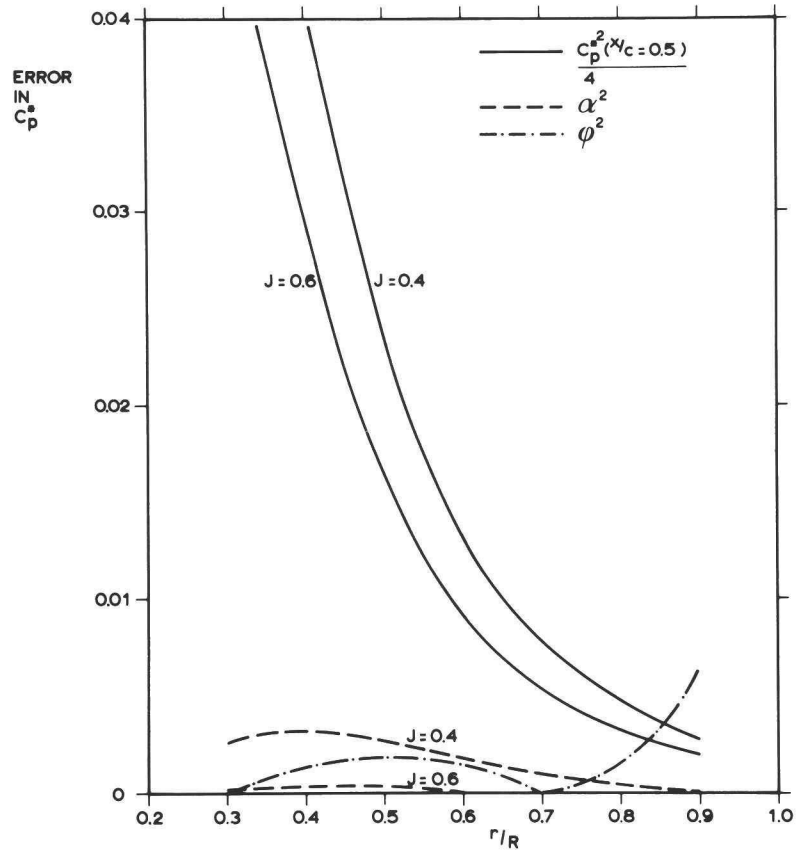

Fig. 2.3. A comparison of error components on propeller S.

B are very similar.

So even in this case of extreme propeller pitch variations the use of a constant pitch for the singular plane is within the accuracy of the linearization.

2.4. THE POSITIONS OF THE TRAILING VORTICES

The positions of the trailing vortices are difficult to establish since contraction of the race and roll-up of the vortex sheet occur. The influence of the trailing vortices on the propeller blades decreases with the distance from the blades, so a reasonable estimate for the pitch of the trailing vortex sheet is in between the propeller pitch angle β_p and the pitch angle of the incoming velocity β_ℓ (see Fig. 2.1). Since β_ℓ cannot be determined beforehand, while the difference with β_p is small, the pitch of the trailing vortex sheet is taken as the propeller pitch angle. Bound and trailing vortices are therefore located in the same helical plane. In case of a varying pitch distribution the pitch at r/R=0.7 is again taken as the helical pitch.

The sensitivity of the pressure distribution to the choice of the pitch of the helical plane is shown in Fig. 2.4 and 2.5. The variation of the pitch

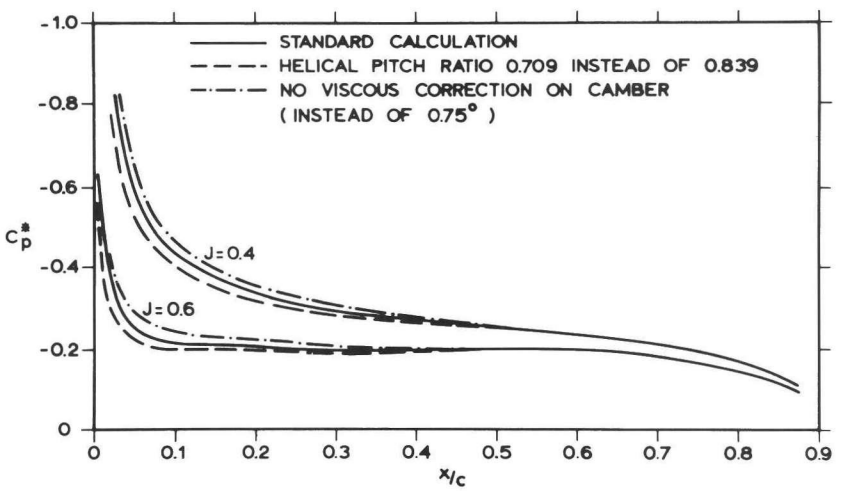

Fig. 2.4. Effect of variation of the helical pitch and of viscous corrections on the calculated pressure distribution. (Propeller S at r/R=0.6).

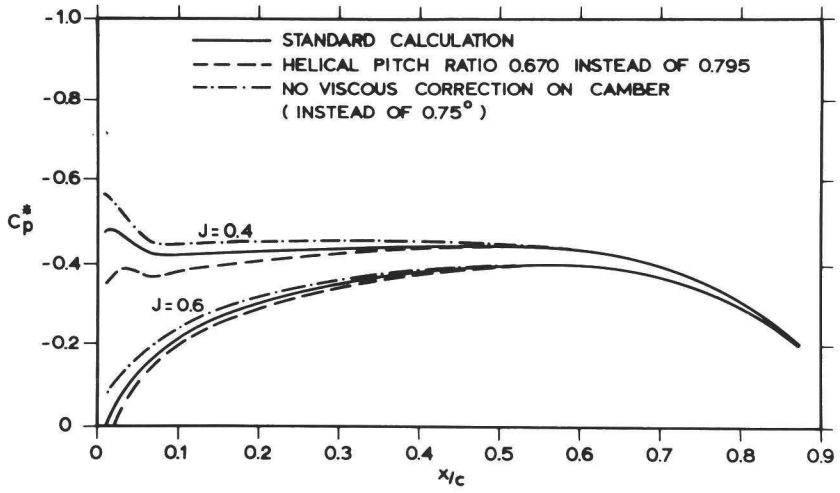

Fig. 2.5. Effect of variation of the helical pitch and of viscous corrections on the calculated pressure distribution . (Propeller B at r/R=0.6).

ratio corresponds to a change of the pitch angle of 3 degrees.

The sensitivity of the pressure distribution for the choice of the helical pitch is small relative to the accuracy of $C_p^2/4$. In the strongly non-linear pressure peaks at the leading edge the influence of the helical pitch is larger, as is shown in Fig. 2.6. These variations in the minimum pressure due to pitch variations indicate the accuracy which should be attributed to the calculated minimum pressures.

Similarly the effect of the helical pitch on the calculated open-water diagrams is shown in Fig. 2.7, indicating in which range the calculated results can be varied rather arbitrarily.

2.5. CORRECTIONS FOR VISCOUS EFFECTS ON THE LIFT

Viscosity not only causes frictional drag, it also influences the lift of a profile by changing the circulation. When no separation occurs far upstream of the trailing edge this effect remains small.

Calculation of the effect of viscosity requires calculation of the boundary layer for which the pressure distribution is needed. This therefore leads to an iteration. The numerical complexity, along with other approximations, do not warrant such an iteration to determine a small effect.

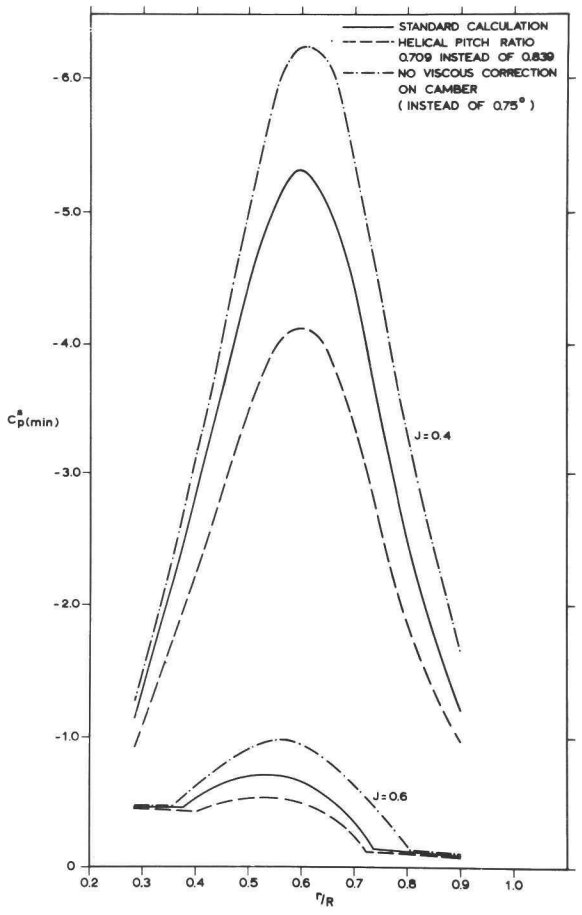

Fig. 2.6. Effect of variation of the helical pitch and of viscous corrections on the calculated minimum pressures.

Therefore an estimate of the effect of viscosity on the lift has to be made

Generally viscosity reduces the lift of a propeller section, which can be accounted for by a decrease of the effective angle of attack or, in the case of a propeller, by a decrease of the propeller pitch.

The standard correction applied in the program is a reduction of the propeller pitch by 0.75 degrees. This is a crude assumption, made by Van Gent (1977), with the aim to bring the calculated open-water diagrams in agreement with calculations. Especially in regions with a light loading, as

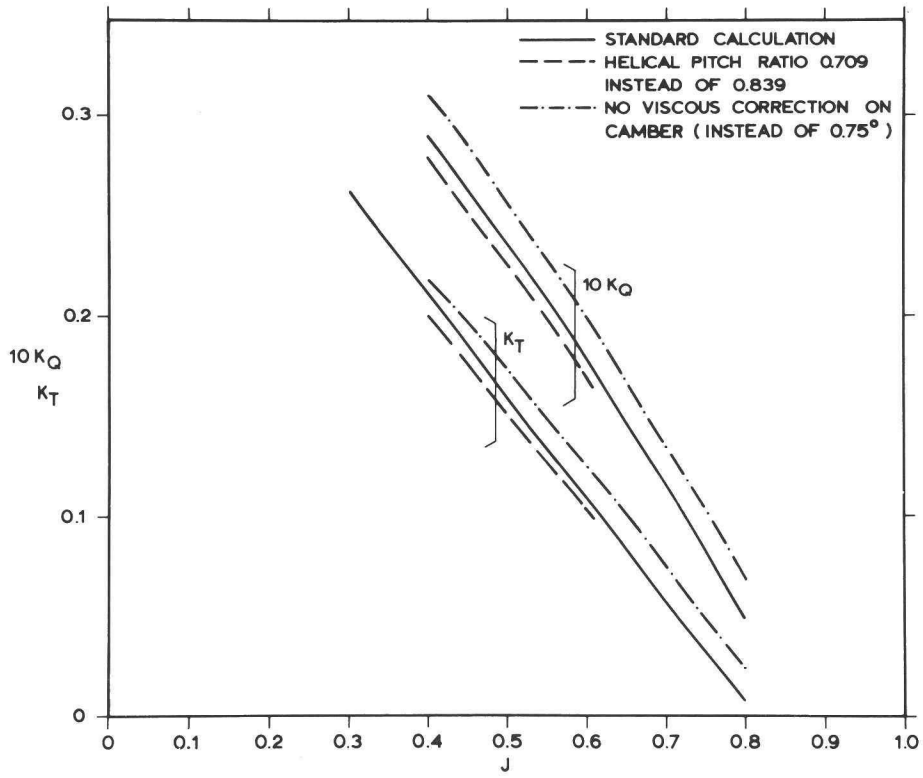

Fig. 2.7. Effect of variation of the helical pitch and of viscous corrections on the calculated open-water curves. (Propeller S).

occurs e.g. in the tip region of propellers B and S, this correction is too large or can even have the wrong direction.

The effect of the application of this viscous correction on the pressure distribution, on the minimum pressure and on the open-water curves is shown in Figs. 2.4 to 2.7. Although this viscous correction needs refinement its effects are comparable with those of helical pitch variations.

2.6. EFFECTS OF THICKNESS ON THE LIFT

In a non-planar case the three-dimensional thickness distribution induces a normal velocity component on the propeller inflow, generally reducing the

angle of attack. This effect is taken into account in a similar way as the viscous correction by reducing the propeller pitch by a certain angle. This angle now varies over the radius. As a standard procedure these corrections were taken from interpolation polynomials calculated by Van Oossanen (1974) and representing the corrections as calculated by Morgan et al (1968) with parameters: the number of blades, the blade area ratio, the induced advance ratio, the blade thickness and the radius. The induced advance ratio is approximated by the pitch ratio. Since it is the non-planar geometry of the propeller blades which generates this normal velocity component it can be expected that the pitch distribution is important. The calculations of Morgan et al were, however, carried out for constant pitch only, and it is necessary to check the error made by the use of the interpolation polynomials. The normal velocities, translated in angle of attack corrections, were therefore also calculated using the correct source distribution. A program, developed by Wels (1976) was used for these calculations. In Fig. 2.8 the corrections on the angle of attack are given for propeller S, calculated both ways. They are compared with the angle of attack variations, caused by variation of the helical pitch. As can be seen the error made by using the polynomials is smaller than the uncertainty caused by the choice of the pitch of the trailing vortices, so the use of the polynomials is accurate

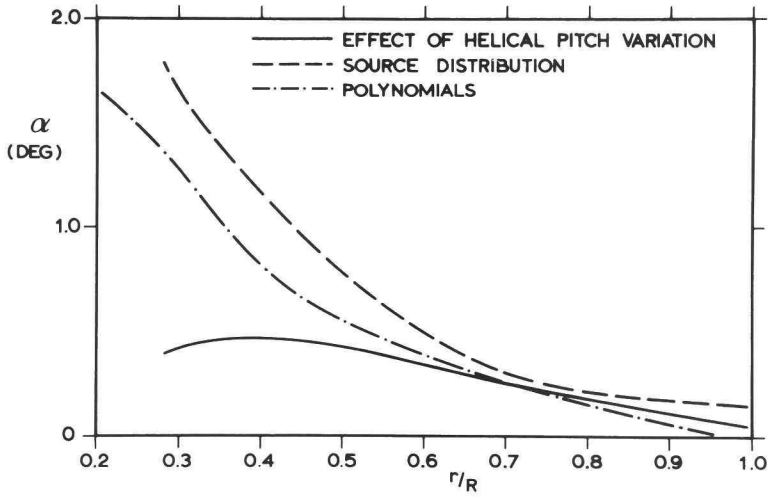

Fig. 2.8. Correction on angle of attack or pitch due to thickness. (Propeller S).

enough in this case. Fig. 2.8 also shows that the correction for viscosity of 0.75 degree is dominant and should be refined first.

2.7. DETERMINATION OF THE MAGNITUDE OF THE SECTIONAL INFLOW VELOCITY

The velocity components used to determine the magnitude of the sectional inflow velocity V_E are shown in Fig. 2.9.

The axial inflow velocity U and the circumferential velocity ωr are known. When the velocity u_w is known, the induced velocity V_i is calculated assuming that V_i is perpendicular to V_E, which is true in the two-dimensional linearized case, and assuming that the direction of V_E is the pitch angle β_p, which is allowed since the angle of attack is small.

The vorticity in the propeller wake is represented by the trailing vortices on a helical plane. Contraction modifies this rotation, and the effect is largest on the axial component of the rotation, causing an additional axial inflow velocity component u_w. The velocity u_w is calculated by using an actuator disk model of the same radial load distribution as the propeller. An iteration is necessary to carry out this calculation, but a maximum of three iterations is already sufficient to obtain the required accuracy of 1% in thrust and torque. (Van Gent, 1977).

The magnitude of the velocity u_w is given in Fig. 2.10 for propeller S. This velocity component is only significant in the hub region. There it is, however, important, because it keeps the angles of attack small, making it possible for the loading at the hub to go to zero while the linearization

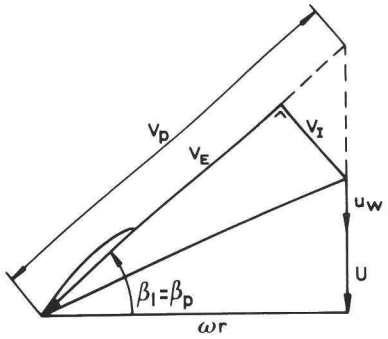

Fig. 2.9. Determination of the magnitude of the sectional inflow velocity V_E.

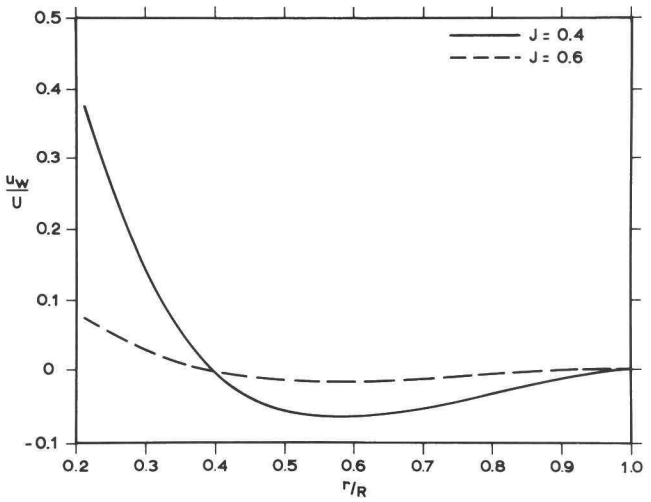

Fig. 2.10. Axial velocity component u_w (Propeller S).

remains valid.

No corrections for the roll-up of the vortex sheet were made in the present calculations.

With the resultant velocity V_E and as boundary condition the slope of the camberline corrected for thickness and viscous effects, the vortex or dipole distribution can be calculated.

2.8. THE CALCULATION OF THE LIFT DISTRIBUTION

The solution of the lifting surface problem is straightforward now, although it is a cumbersome numerical problem due to the highly singular character of the integral equation.

The problem is solved by fulfilling the boundary conditions in a discrete number of control points on the propeller blades. The choice of the number of control points is a trade-off between computer time and required accuracy. In the present calculations control points at four chordwise and ten spanwise positions were chosen.

The pressure distribution in spanwise direction is fairly regular and ten control points in that direction are sufficient for an accurate representation.

The positions of the control points were taken as:

$$\frac{r_k}{R} = (1+\frac{r_i}{R})-(1-\frac{r_i}{R})\cos\frac{k\pi}{N+1} \qquad (2.5)$$

N = number of spanwise control points.

This is more difficult in chordwise direction, where the leading edge singularity can lead to a sharp peak at the leading edge. For this lift distribution the interpolation polynomial

$$\Delta p = \sum_{p=0}^{P-1} C_p \, H_p(s) \qquad (2.6)$$

is taken, where the functions H_p are Tschebychoff polynomials in the chordwise direction s. The number of chordwise control points is P and the chordwise positions of the control points are taken according to Multhopp (1955) as:

$$\frac{s_k}{C} = \tfrac{1}{2}(1-\cos\frac{2\pi(k+1)}{2P+3}) \qquad k = 0(1)P-1 \qquad (2.7)$$

The behaviour of the pressure in eq. 2.6 has been discussed by Van Gent (1979). To illustrate the sensitivity of the calculated pressure distribution for the number of chordwise control points the pressure distribution at propeller S was calculated with six instead of four chordwise control points. The difference in C_p^* with the standard calculation of four control points was less than 0.01, except near the pressure peak at the leading edge. The calculated minimum pressures are compared in Fig. 2.11. Differences occur only in the highly non-linear pressure peak at the leading edge and their magnitude is comparable to those due to variations in the helical pitch.

The solution of the lifting surface problem is the propeller blade loading. To arrive at the pressure distribution on the blades the blade thickness must be taken into account.

2.9. THE CALCULATION OF THE PRESSURE DISTRIBUTION

The linearization makes it possible to separate the effects of lift and thickness, apart from a slight interaction as treated in section 2.6. The vortex or dipole distribution gives the propeller loading, and the source

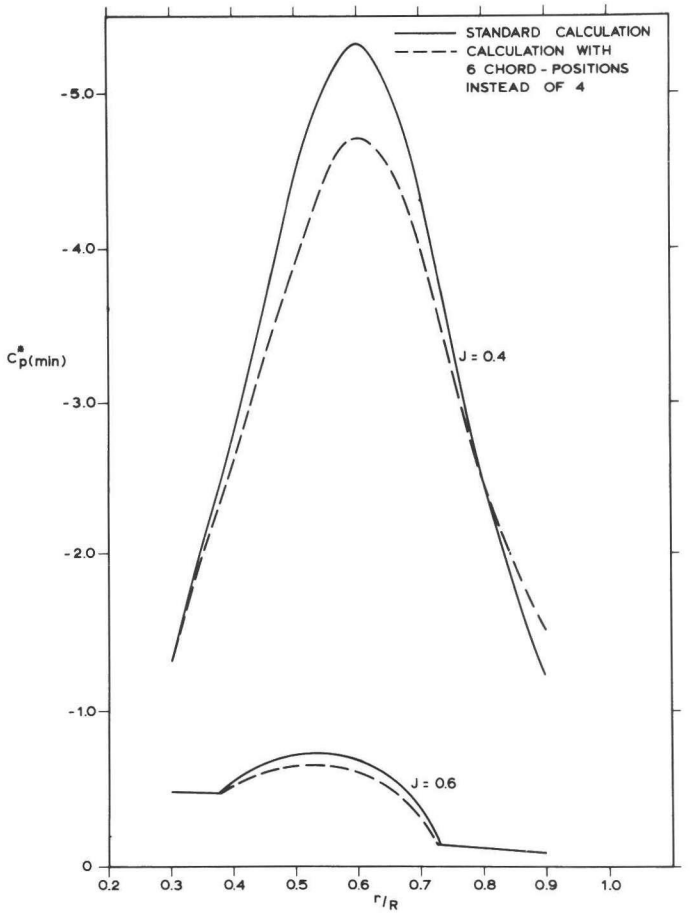

Fig. 2.11. Effect of the number of chordwise control points on the calculated minimum pressure coefficients of propeller S.

distribution gives the mean pressure between suction and pressure side. Both results are, however, infinite at the leading edge, which is the price to be paid for the linearization.

A method to eliminate this singularity is given by Lighthill (1951) and Van Dijke (1964), which yields:

$$\frac{u'}{V_E} = \left(\frac{x}{x+\frac{1}{2}\rho_\ell}\right)^{\frac{1}{2}} \left(\frac{u}{V_E} + \frac{\rho_\ell}{4x}\right) \qquad (2.8)$$

in which ρ_ℓ is the leading edge radius, u' is the corrected velocity at a distance x from the leading edge and u is the velocity at that position obtained from the linearized theory (see also Tsakones et al, 1979).

The velocity component due to the lift can easily be calculated from eq. 2.6, but for the calculation of the velocity component due to the thickness the detailed distribution of the sources near the leading edge is required. The latter solution was not available and therefore another approach is used.

In the present calculations the chordwise lift distribution, as given by eq. 2.6, is translated into an effective camber distribution and angle of attack by

$$f(s) = \frac{c}{2\pi r V_e^2} \sum_{p=1}^{P-1} \frac{1}{k} (C_{p-1}+C_p) \cos \frac{2\pi(P+1)}{2P+3} \qquad (2.9)$$

$$\alpha = \frac{1}{\pi r V_e^2} (C_o+C_1) + \frac{C_2+C_3}{3} + \frac{C_4+C_5}{5} + \ldots\ldots \qquad (2.10)$$

where the coefficients C_p are the coefficients of eq. 2.6 as calculated by the lifting surface program. This effective camberline f(s) is combined with the geometrical thickness distribution, which gives the two-dimensional effective profile. The pressure distribution on this effective profile is calculated at the angle of attack α from eq. 2.10 using Goldstein's third approximation. (see e.g. Robinson and Laurman, 1956).

This approach is non-linear and gives a finite pressure in the leading edge region. It accounts for the propeller thickness in a two-dimensional way and neglects the effect of the blade aspect ratio on the mean pressure. This is only allowed because the propeller blades are thin and a large error in the calculated mean pressure is still a relatively small error in the total pressure distribution, which is dominated by the lift.

To illustrate the error the linearized three-dimensional mean pressure on propeller S was calculated by using a source dustribution on the blades, as programmed by Wels (1976). Only five chordwise control points were used on four radii. These three-dimensional mean pressures were compared with two-dimensional calculations of the mean pressure and the difference at midchord is given in Fig. 2.12 as the two-dimensional error. It is compared in Fig. 2.12 with the error due to linearization $C_p^2/4$.

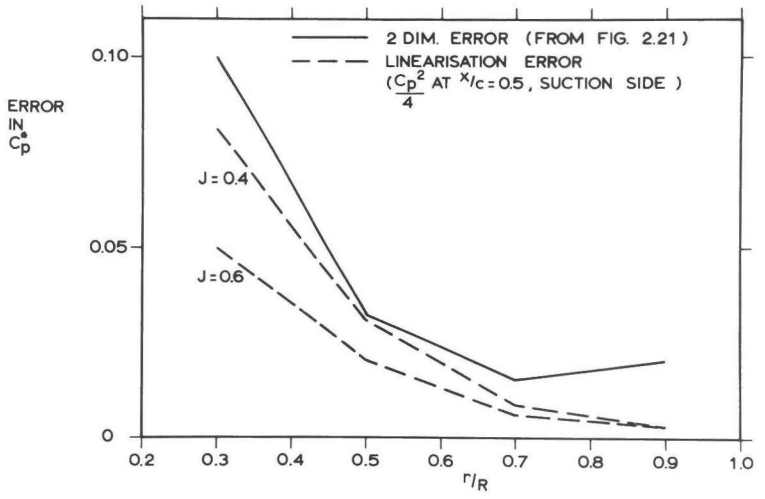

Fig. 2.12. Errors due to the two-dimensional calculation of the thickness effect. (Propeller S).

Although the error due to the two-dimensional approach of the thickness was larger than the linearization error, the order of magnitude is the same. Since the two-dimensional mean pressure is lower than the three-dimensional mean pressure, the pressures calculated on the suction side in the present calculations will tend to be too low in the midchord region.

The calculated lift coefficient of the effective profile will be slightly higher than followed from the lifting surface calculation. (some 15% near the hub, only a few per cent near the tip). Since the propeller loading, as calculated with the lifting surface theory, has to be maintained, the lift on the effective profile has been maintained using Pinkerton's (1934) method.

Finally, the thus calculated pressure coefficient C_p^* is related to V_E. Since this velocity is not easily found the incoming velocity $V=u^2+w^2r^2$ was taken as the reference velocity, taking:

$$C_p = (\frac{V_e}{V})^2 \, C_p^* \qquad (2.11)$$

These last two corrections were not applied in previous papers (Kuiper, 1978b, 1979b).

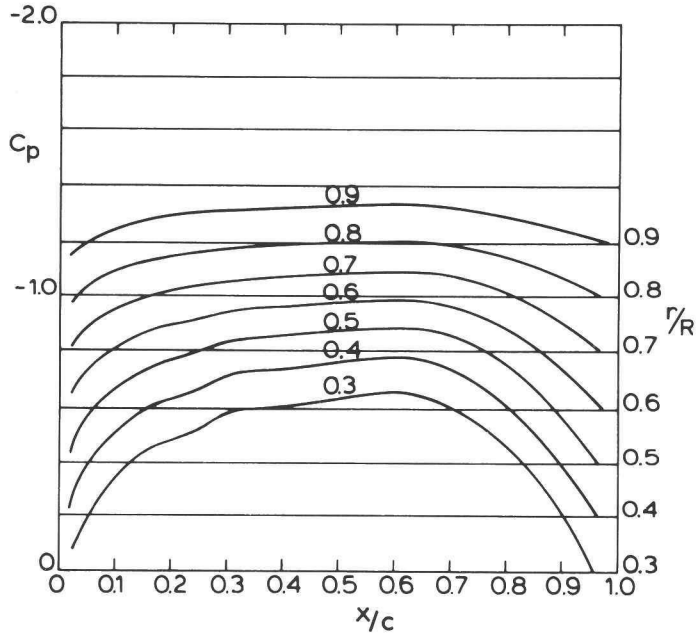

Fig. 2.13. Calculated pressure distribution on propeller B at J=0.6.

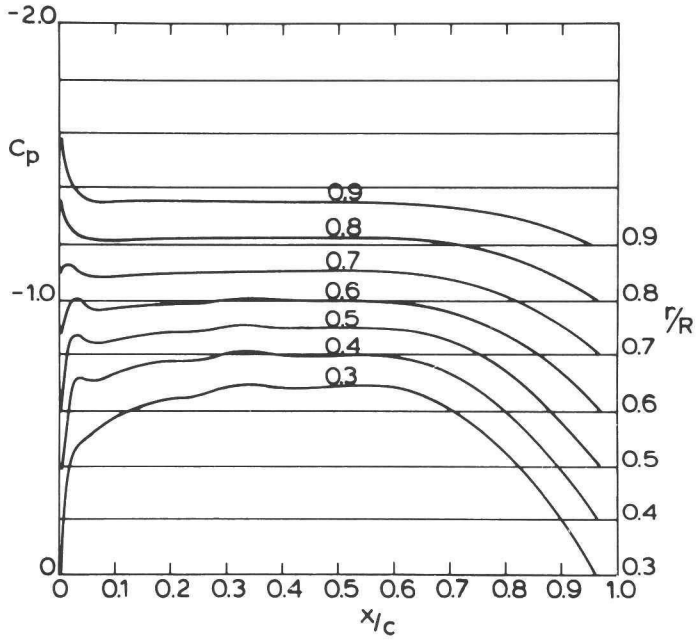

Fig. 2.14. Calculated pressure distribution on propeller B at J=0.4.

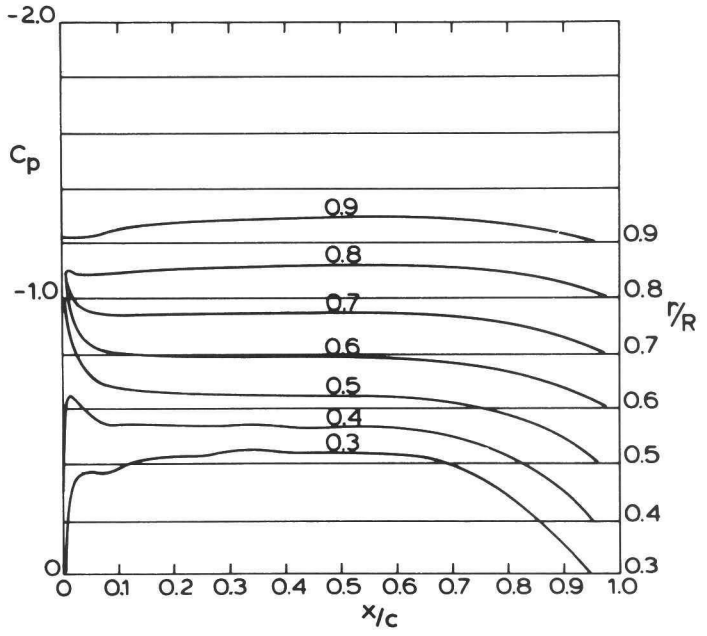

Fig. 2.15. Calculated pressure distribution on propeller S at J=0.6.

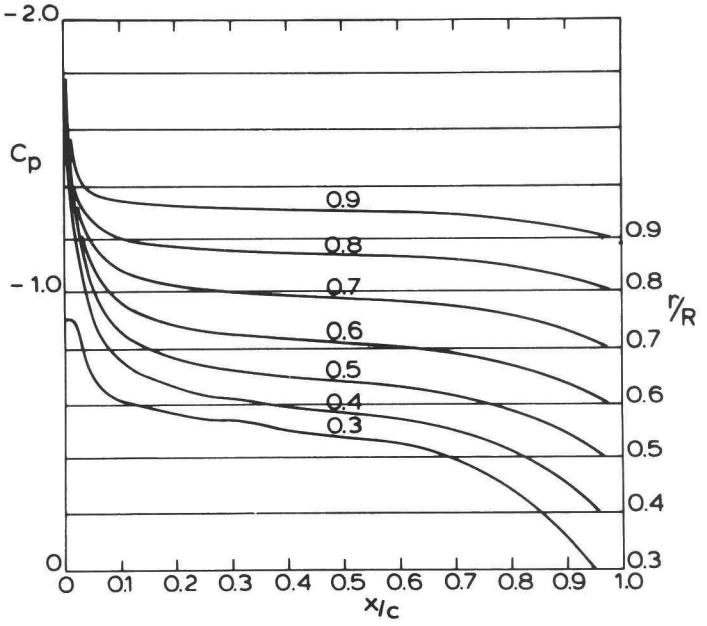

Fig. 2.16. Calculated pressure distribution on propeller S at J=0.4.

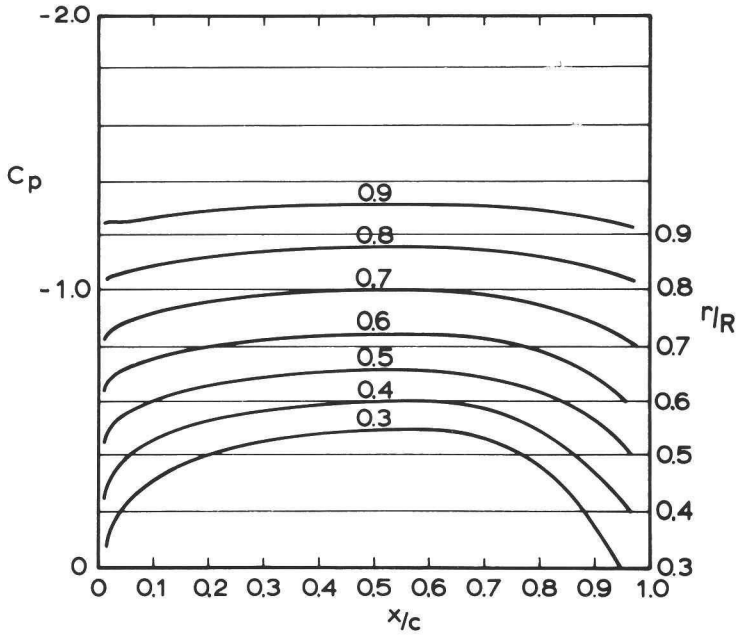

Fig. 2.17. Calculated pressure distribution on propeller V at J=0.5.

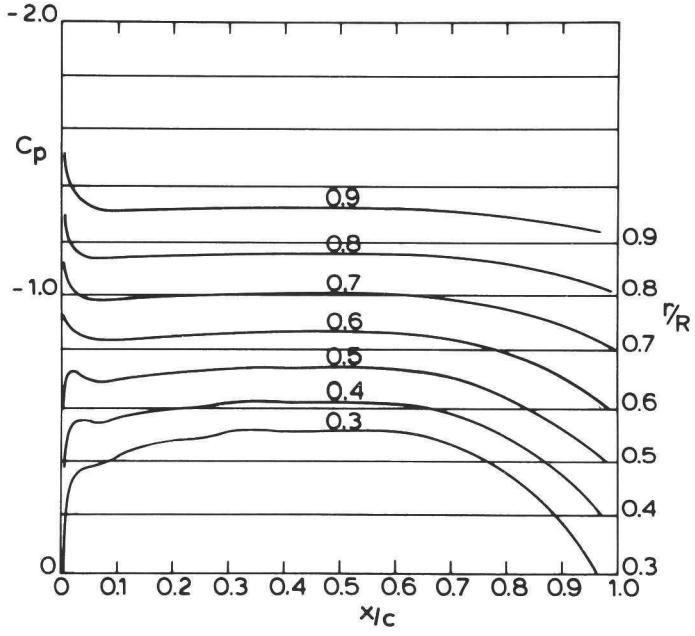

Fig. 2.18. Calculated pressure distribution on propeller V at J=0.4.

The calculated pressure distributions on propellers B, S and V in the investigated conditions are given in Figs. 2.13 to 2.18. These pressure distributions are used for the analysis of the boundary layer on the blades and of the cavitation properties of the propellers.

2.10. CALCULATION OF THE OPEN-WATER DIAGRAMS

The open-water diagrams or K_T-K_Q-J-curves form a means to check the calculations, since thrust and torque are relatively easy to measure. The coefficients K_T and K_Q are defined as:

$$K_T = \frac{T}{\rho n^2 D^4} \tag{2.12}$$

$$K_Q = \frac{Q}{\rho n^2 D^5} \tag{2.13}$$

For the calculation of these open-water curves the sectional drag is needed, and both thrust and torque are affected by the rather difficult calculation of the sectional drag.

Since this drag calculation does not directly affect the calculated pressure distribution we will only touch upon it, mainly to assess the sensitivity of the thrust coefficient for the calculated sectional drag. The calculation method of Van Gent (1979) is followed.

The forces, acting on a propeller section, are given in Fig. 2.19.

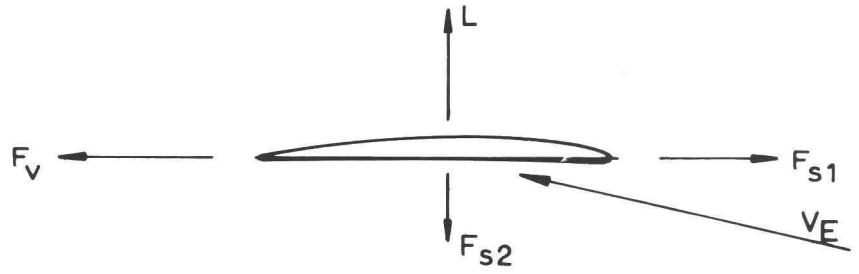

Fig. 2.19. Force components on a propeller section.

The lift force L can be calculated from the lift distribution Δp as given in eq. 2.6 and contains only the coefficient C_o:

$$L = c\, C_o \tag{2.14}$$

The suction force F_s at the leading edge, which in a two-dimensional flow makes the resulting non-viscous force perpendicular to the inflow velocity, is calculated from the leading edge singularity and can be expressed as:

$$F_s = \frac{C}{\frac{1}{2}\rho V_\ell^2 \pi} \sum_{p=0}^{p-1} C_p^2 \tag{2.15}$$

To account for viscous effects F_{s1} is taken as $\frac{1}{2}F_s$. For similar reasons the lift is decreased by half the suction force, so $F_{s2}=\frac{1}{2}F_s$. The viscous drag force F_v is calculated with a single friction coefficient of 0.0008 for all conditions.

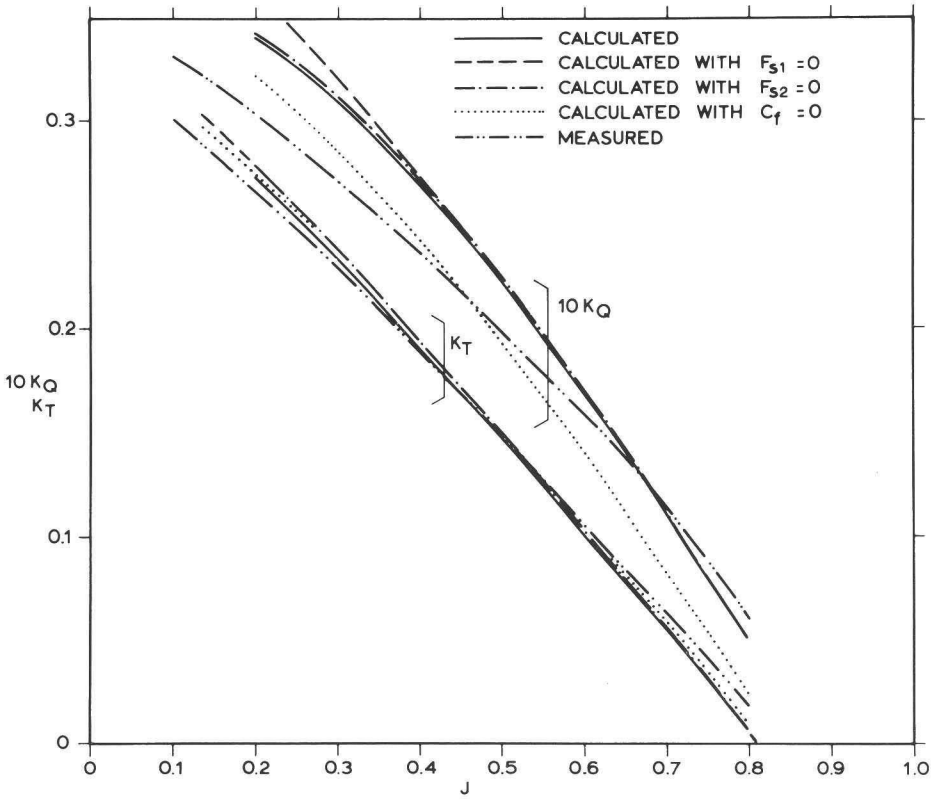

Fig. 2.20. Effect of various sectional forces on the open-water curves of propeller S.

To assess the sensitivity of the open-water curves for these rather crude approximations the open-water diagram of propeller S was calculated with $F_{s1}=0$, $F_{s2}=0$ and $C_f=0$ respectively. The results are shown in Fig. 2.20. Especially the thrust coefficient K_T is insensitive for those approximations and can therefore be used as a rough check of the calculations.

The measured open-water curve of propeller S is also given in Fig. 2.20 and the agreement of the measured and calculated thrust coefficients is good. In Figs. 2.21 and 2.22 the calculated open-water curves are compared with the measurements for propeller B and V and the thrust coefficients are again accurately calculated. The agreement of the calculated torque coefficients is bad, so the viscous effects on the propeller have to be calculated more accurately. This does, however, not affect the calculation of the pressure distribution.

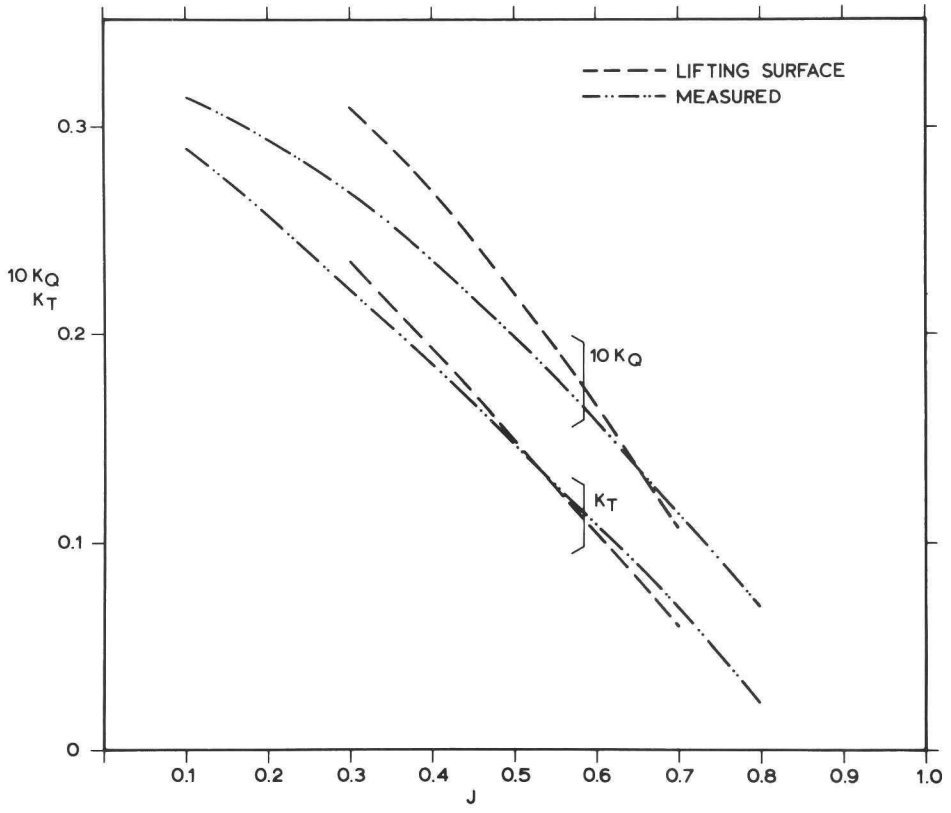

Fig. 2.21. Open-water curves of propeller B.

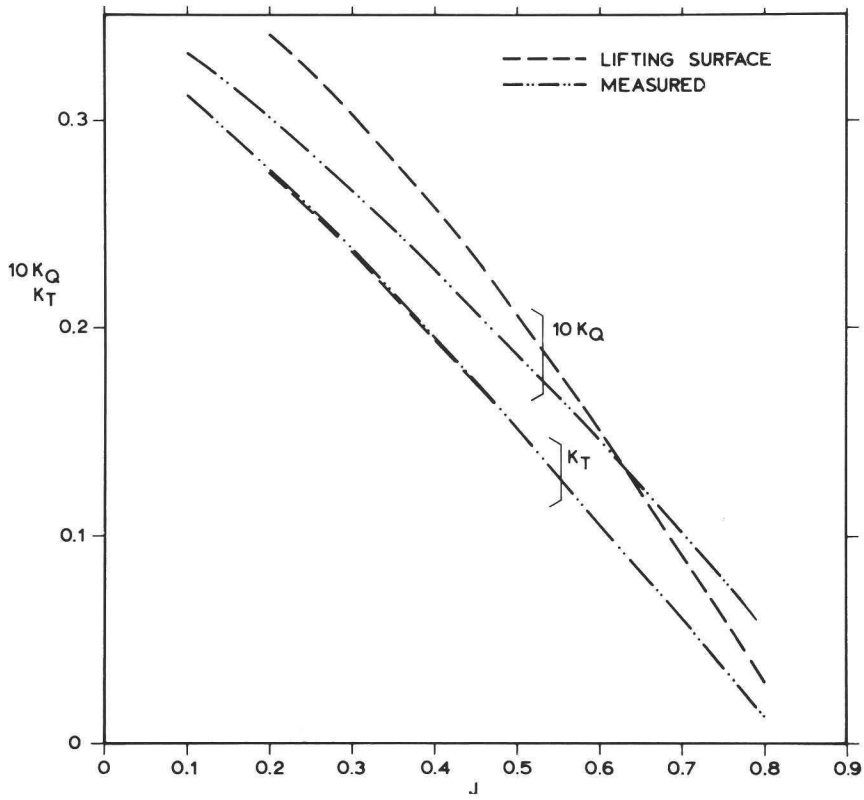

Fig. 2.22. Open-water curves of propeller V.

In order to obtain a good correlation between the calculated and measured thrust coefficients an empirical correction, applied in the standard program, had to be left out. This empirical correction was found to cause the discrepancies in the calculated thrust coefficients in an earlier study (Kuiper, 1979b). Since this empirical correction for the calculated pressure distribution is not used in this study, it is further discussed in Appendix 2.

2.11. COMPARISONS WITH DATA FROM LITERATURE

To get an impression of the merits of the chosen calculation method the measurements of Takei (1979) were compared with results of the present program. The open-water curves are compared in Fig. 2.23 and the pressure distributions at r/R=0.77 for three different advance ratios are given in

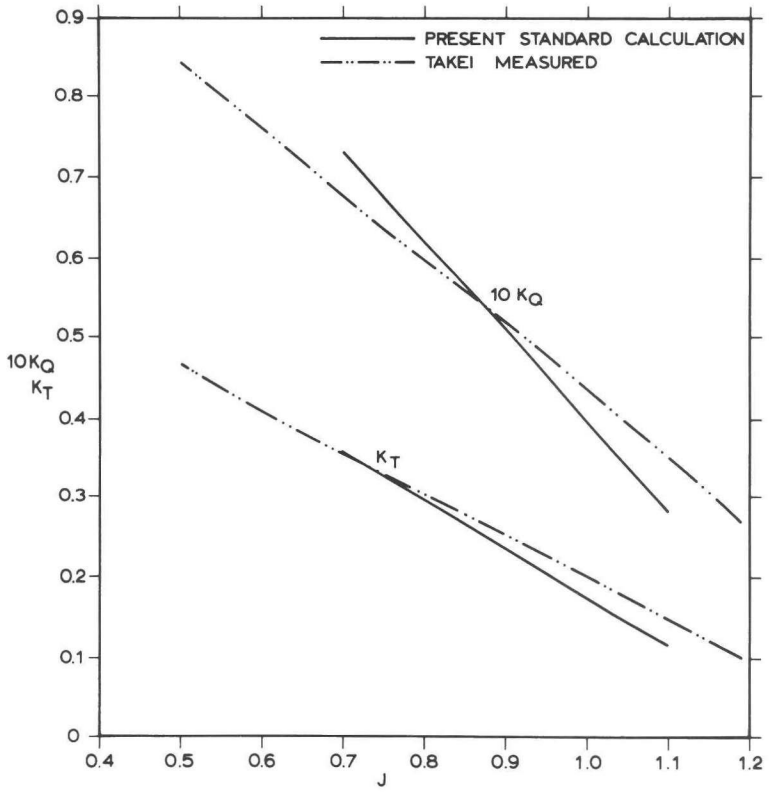

Fig. 2.23. Open-water curves of the Takei propeller.

Fig. 2.24. The agreement between the calculated and the measured pressure distributions is good, which gives some confidence in the calculation method.

A comparison between a large number of calculations was made by the propeller committee of the 15th I.T.T.C. (1979). The results of the present program for that propeller (N.S.R.D.C. Propeller 4118) are shown in Fig. 2.25, together with the band in which the majority of the calculated pressures were reported. At inner radii the present calculation method predicts a lower pressure at midchord (at least on the suction side), presumably due to the two-dimensional treatment of the thickness. The shape of the pressure distribution is similar for most calculations, although the minimum pressures at the leading edge can differ widely.

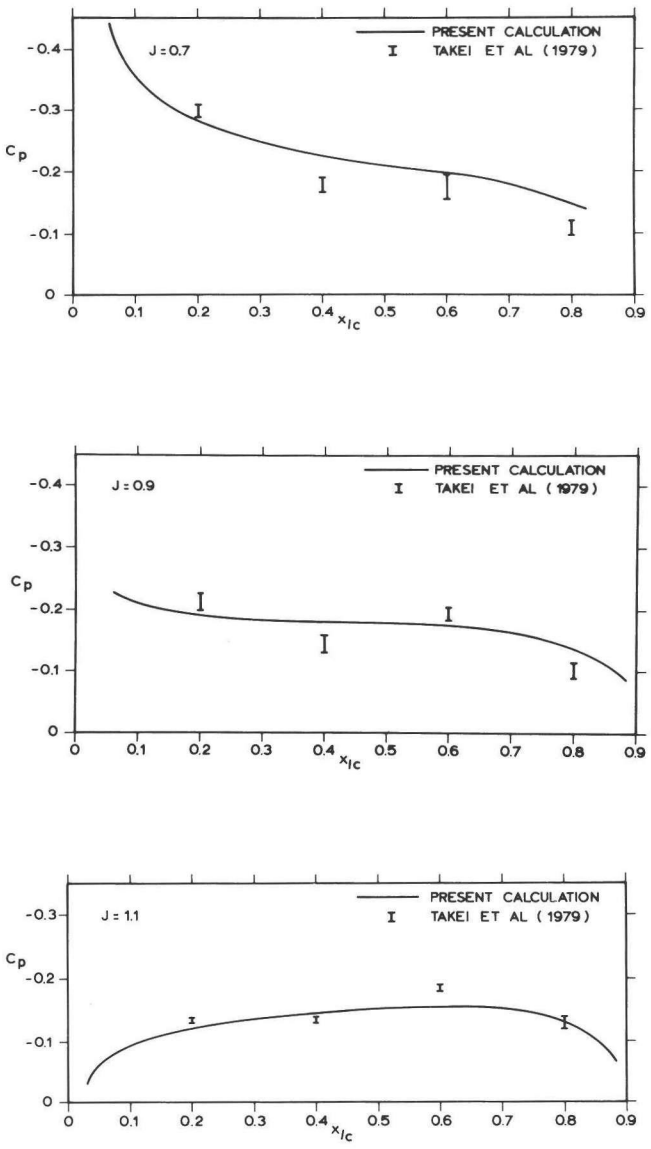

Fig. 2.24. Pressure distributions on the Takei propeller at r/R=0.77.

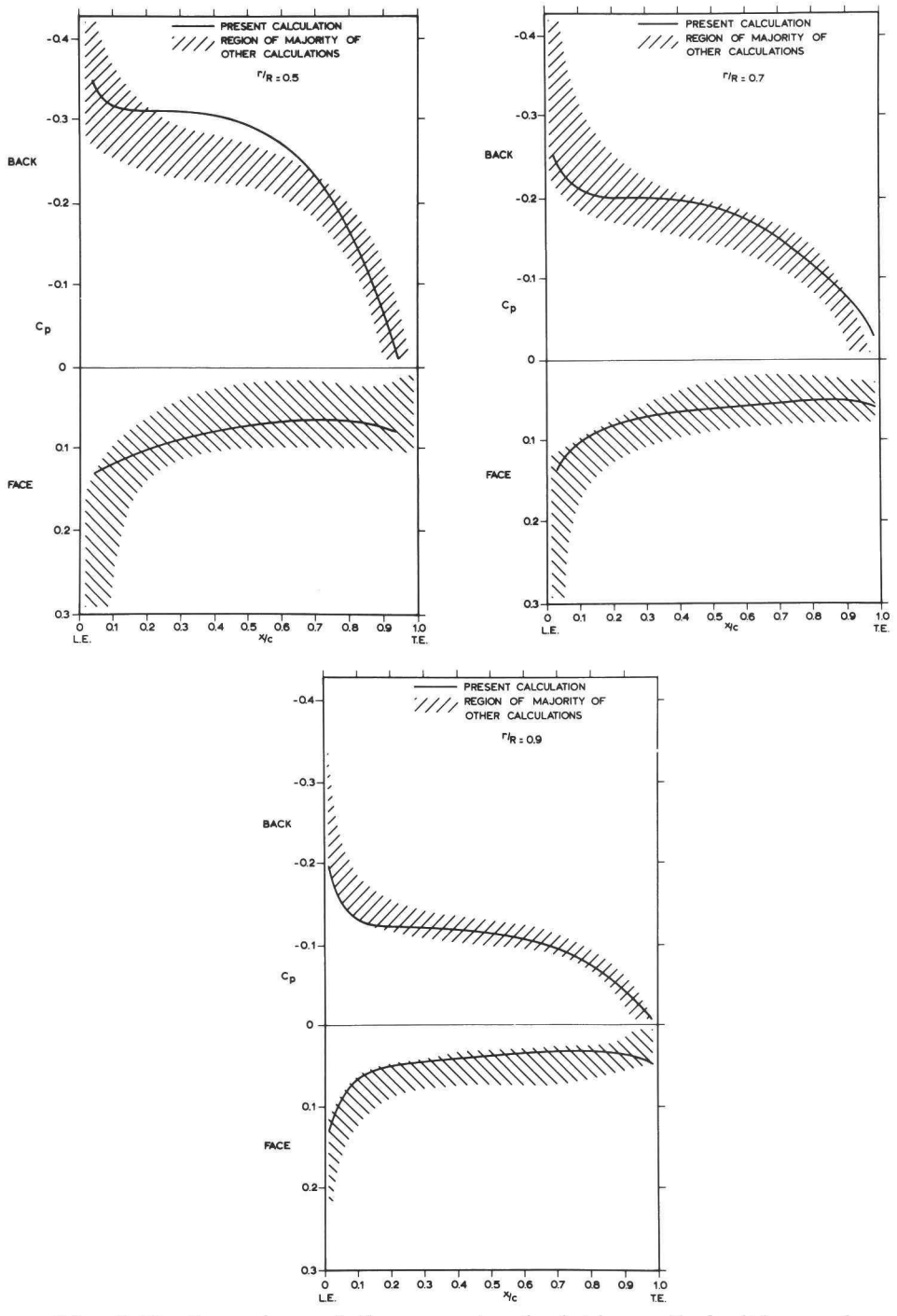

Fig. 2.25. Comparison of the present calculation method with a number of other methods for the same propeller.

3.The boundary layer on propeller blades

The character of the boundary layer on the suction side of propeller blades is investigated. Paint tests were developed to visualize the character of the boundary layer and possible side effects due to the paint are discussed. The general behaviour of the boundary layer is summarized from earlier investigations and the character of the boundary layer on propellers B, S and V is shown and discussed.

The similarity parameter for the propeller boundary layer is the propeller Reynolds number (eq. 1.5). When a propeller is tested behind a ship model the Froude number (eq. 2.7) has to be maintained, which implies that at the same advance ratio J (eq. 2.8) the Reynolds number on model size is smaller than that on the prototype by a factor $\lambda^{3/2}$, where λ is the scale ratio. Generally this means that the Reynolds number on model scale is one or two orders of magnitude smaller than on the prototype. Also in a cavitation tunnel, where the Froude number is less important, the Reynolds number of the prototype is, for technical reasons, almost never maintained on model scale.

This strong decrease of the Reynolds number affects the propeller boundary layer and causes regions where the boundary layer is laminar. When this occurs the propeller thrust and torque are dependent on the location of transition and this makes it difficult to extrapolate measured model data into full-scale values. Extrapolation methods such as the "equivalent profile method" (Lerbs, 1951) assume a fully turbulent boundary layer on the propeller blades, although some empirical corrections for laminar flow regions are sometimes made (Lindgren, 1967).

A common criterium for the absence of a strong Reynolds dependency is a minimum sectional Reynolds number of 2×10^5 at 0.7R. The sectional Reynolds number is defined as

$$Re(0.7) = \frac{V.c(0.7)}{\nu} \qquad (3.1)$$

with c(0.7) as the chord length and V as defined in eq. 2.9, both on r=0.7R. However, boundary layer visualuzations with paint by Meyne (1972), Sasajima (1975) and Tsuda and Konishi (1978) showed that regions with a laminar boundary layer flow could persist up to much higher sectional Reynolds numbers.

Until now the attention has been focussed on the relation between the boundary layer on the propeller blades and the propeller performance (thrust and torque). In this study the relation between the boundary layer and cavitation inception will be investigated. For that purpose the paint test technique is used. This technique is described and discussed next. Some systematic results of paint tests on propeller models are subsequently presented in this section and finally the character of the boundary layer on propellers B, S and V is visualized for correlation with cavitation observations in sections 6, 7 and 8.

3.1. PAINT TESTS ON PROPELLER MODELS

The character of the boundary layer can be judged from the local frictional stress, exerted on the blade by the fluid. When the boundary layer becomes turbulent this stress will increase strongly. Because the centrifugal force remains constant this results in a change of direction of the local friction force on the blade surface when transition occurs. This change of direction is visualized by paint streaks on the blade surface.

An example is shown in Plate 3.1. On blade 2 the paint streaks are thicker and directed more outward in the leading edge region than in the trailing edge region. The transition region is located where the thicker streaks change into thinner streaks in nearly circumferential direction.

On blade 1 the leading edge was roughened as will be described in section 4. The laminar region has disappeared and the flow is turbulent over the whole suction side at radii larger than 0.3R. At the leading edge, where the highest flow velocities occur, the paint was washed away.

The paint, used in the present tests, is white lead-oxide, mixed with linseed oil. This mixture is insoluble in water and makes fine streaks on metal and painted surfaces, provided these surfaces are not greasy. A red fluorescent dye ("Dayglo" daylight fluorescent pigment, Switzer Brothers, Inc., Cleveland, Ohio) is used to colour the paint. The very thin paint streaks, sometimes hardly visible to the eye, can be photographed with good contrast using ultra-violet illumination.

Ultra violet illumination was obtained by using a normal electronic flashlight (light value 45) covered with a bandpass filter (Oriel type G-774-3550, peak at 3550A). The resulting illumination is mainly ultra violet, but contains some blue light, which is advantageous, because the unpainted parts of the propeller blade become visible in a blue color. The flashlight was positioned at a distance of 50 cm from the blades. The pictures were taken with a 400 ASA colour negative film (Kodak CH 400) using a diaphragm of f5.6.

Before the test the paint was applied to the leading edge, as shown in Fig. 3.2. The proper viscosity of the paint was determined experimentally and depends on the propeller Reynolds number.

All paint patterns reported in this study were taken in the Depressurized Towing Tank under atmospheric conditions. The time required to arrive at the desired conditions after the paint started to run was about 10 seconds. The run-time of a paint test was about 60 seconds, the stopping time about 8 seconds.

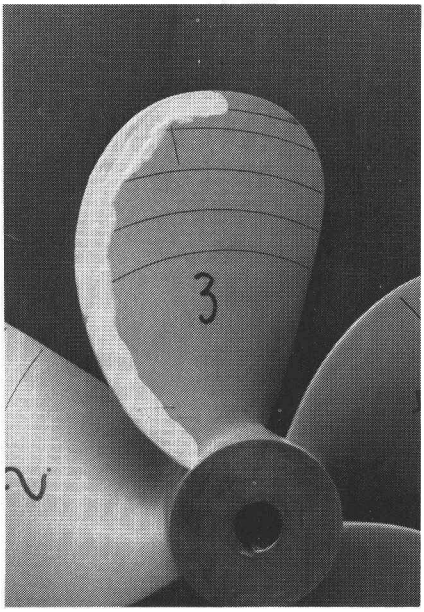

Fig. 3.2. Application of the paint.

3.2. POSSIBLE SIDE EFFECTS DUE TO THE PAINT LAYER.

The paint layer on the blade surface may change the boundary layer on the blades, while the direction of the paint streaks may differ from the direction of the frictional forces on top of the paint layer. An analysis of these effects is given by Squire (in Maltby, 1962). This analysis can be slightly modified for the case of a rotating propeller.

Consider a paint layer of thickness h with a boundary layer of thickness δ, as shown in Fig. 3.3. The paint moves very slowly over the propeller blade and the Reynolds number involved is low. (It takes about 60 seconds for the paint to flow over a chord of 0.1 m, so the characteristic velocity is 1.7×10^{-3} m/sec. With a kinematic viscosity of 10^{-4} this results in a Reynolds number of the order 1. The equations for creeping motion can be used for the paint velocity $\bar{v}_p(u_p, v_p)$

$$\frac{\partial \bar{v}_p}{\partial t} + \frac{1}{\rho_p} \text{grad } p_p = \nu_p \nabla^2 \bar{v}_p - \bar{\omega} x (\bar{\omega} x \bar{r})$$
$$\text{div } \bar{v}_p = 0 \qquad (3.1)$$

The centrifugal force is included, while the Coriolis forces can be neglected due to the low local velocities.

The connection between fluid and paint can be written as

$$\mu_p \frac{\partial \bar{v}_p}{\partial z} = \mu_f \frac{\partial \bar{v}_f}{\partial z} \qquad (3.2)$$

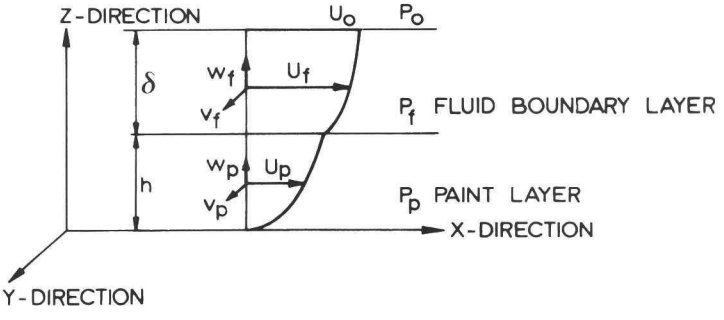

Fig. 3.3. Coordinate system in the paint layer and the fluid boundary layer.

In the fluid boundary layer the velocity $\bar{v}_f$ is O(1) and the derivatives in z-direction are therefore of $O(1/\delta)$. When the viscosity of the paint μ_p is large relative to that of the fluid μ_f ($\mu_f/\mu_p=\varepsilon$) it can be found from eq. 3.2 that $\frac{\partial \bar{v}_p}{\partial z} = O(\varepsilon/\delta)$. When h is of $O(\delta)$ this means that $\bar{v}_p=O(\varepsilon)$. As long as the viscosity of the paint remains high ($\varepsilon<<1$) the paint velocity $\bar{v}_p$ will be low and the effect of the paint on the boundary layer will be small.

When only the terms of the order ε/δ^2 are retained in eq. 3.1, as analysed by Squire, this leads to

$$\nu_p \frac{\partial^2 u_p}{\partial z^2} = \frac{1}{\rho_p} \frac{\partial p_o}{\partial x}$$

$$\nu_p \frac{\partial^2 v_p}{\partial z^2} = \frac{1}{\rho_p} \frac{\partial p_o}{\partial y} - \omega^2 r \qquad (3.3)$$

Integration gives

$$u_p = \frac{1}{\mu_p} \frac{\partial p_o}{\partial x} \left(\frac{z^2}{2} - hz\right) + \left(\frac{\partial u_p}{\partial z}\right)_{z=h} \cdot z$$

$$v_p = \frac{1}{\mu_p} \left(\frac{\partial p_o}{\partial y} - \rho\omega^2 r\right)\left(\frac{z^2}{2} - hz\right) + \left(\frac{\partial v_p}{\partial z}\right)_{z=h} \cdot z \qquad (3.4)$$

Written in fluid properties, using the boundary condition eq.(3.2), this yields

$$u_p = \frac{\varepsilon}{\mu_f} \frac{\partial p_o}{\partial x} \left(\frac{z^2}{2} - hz\right) + \varepsilon z \left(\frac{\partial u_f}{\partial z}\right)_{z=h}$$

$$v_p = \frac{\varepsilon}{\mu_f}\left(\frac{\partial p_o}{\partial y} - \rho_p \omega^2 r\right)\left(\frac{z^2}{2} - hz\right) + \varepsilon \left(\frac{\partial v_f}{\partial z}\right)_{z=h} \qquad (3.5)$$

The direction of the friction force of the paint on the wake can now be written as

$$tg\alpha_p = \left(\frac{\partial v_p}{\partial z}\right) / \left(\frac{\partial u_p}{\partial x}\right)_{z=0} \qquad (3.6)$$

or

$$tg\alpha_p = \frac{(\frac{\partial v_f}{\partial z})_{z=h} - \frac{h}{\mu_f}(\frac{\partial p_o}{\partial y} - \rho\omega^2 r)}{(\frac{\partial u_f}{\partial z})_{z=h} - \frac{h}{\mu_f}\frac{\partial p_o}{\partial x}} \qquad (3.7)$$

The angle of the friction force between fluid and paint is

$$tg\alpha_f = \left[\frac{\partial v_f}{\partial z} \Big/ \frac{\partial u_f}{\partial z}\right]_{z=h} \qquad (3.8)$$

which is also the angle of the friction force of the fluid without paint.

The difference between eqs. 3.7 and 3.8 is the variation of the direction of the paint velocity over the paint thickness. This variation can be significant, as the following example will illustrate.

Consider a rotating disk sector. The friction forces in radial and tangential direction are

$$\tau_r = C_{fr}\ \rho\omega^2 r^2\ \frac{\nu}{\omega r^2 \phi}$$

$$\tau_\theta = C_{f\theta}\ \rho\omega^2 r^2\ \frac{\nu}{\omega r^2 \phi} \qquad (3.9)$$

In a laminar boundary layer at 20^o from the leading edge (ϕ=0.35) the friction coefficients are calculated to be 0.22 and 0.39 respectively. Taking some values which are representative for the situation on a propeller model (ρ_f=1000 kg/m^3, ω=38 rad/sec or 6 rps, r=0.10, ρ_p=4000 kg/m^3, h=10^{-5} m) the results from eqs. 3.7 and 3.8 are: $\alpha_f=30^o$ and $\alpha_p=43^o$. So the angle of the paint velocity changes rapidly over the height of the paint layer, even if it is as thin as 10 μm. The angle of the paint streaks can therefore very well be larger than those of the fluid without paint.

An increase of ω at the same Reynolds number, thus at a smaller radius (ω=152 rad/sec, r=0.05) results in $\alpha_p=53^o$. So an increase of the rotation rate at a constant Reynolds number tends to increase the angle of the paint streaks.

Such a variation of the rotation rate at a constant Reynolds number was carried out on propeller B for three different diameters, as shown in Plate 3.4. The angle of the paint streaks in the laminar region is remarkably constant. Since the paint streaks are at least 10 μ_m thick this indicates that

the streak angle is close to α_f and independent of ω.

A special situation occurs at laminar separation. Then, from eq. 3.7,

$$\mu_f \frac{\partial u_f}{\partial z} - h\frac{\partial p_o}{\partial x} = 0 \qquad (3.10)$$

while the fluid flow separates when $\mu_f \frac{\partial u_f}{\partial z}=0$. The error $h\frac{\partial p_o}{\partial x}$ may be significant when the adverse pressure gradient is large, as occurs behind the low-pressure peak at the leading edge. In those regions the fluid velocities are high, keeping the paint thickness h and thus the error limited.

In a transition region which is close to separation the paint thickness increases and separation may be indicated too early, although the pressure gradient is only moderately adverse.

3.3. SOME SYSTEMATIC INVESTIGATIONS OF THE PROPELLER BOUNDARY LAYER

No systematic data on the character of the boundary layer on a propeller blade are available. Generally it is assumed that a transition region exists from the hub to the tip. An increase of Reynolds number moves the transition region to the leading edge. This assumption underlies the idea of a critical Reynolds number, which is the Reynolds number at which transition occurs close to the leading edge at all radii. In an earlier study (Kuiper, 1978b) this was investigated and some results will be summarized.

When a laminar region exists at the leading edge, as is e.g. the case in Plate 3.1 on the smooth blade, an increase in Reynolds number will indeed shift the transition region towards the leading edge. However, it requires very high Reynolds numbers to bring the transition region close to the leading edge, as is shown in Fig. 3.5 on two commercial propellers. The sectional Reynolds number at r=0.7R must be much higher than 10^6 to obtain such a condition. The critical Reynolds number will be much higher than 2×10^5 in this case, although the effect of laminar regions on thrust and torque will become very small long before all laminar regions have disappeared.

The same propellers at a heavier loading exhibited a turbulent boundary layer from the leading edge on, specifically near the blade tips. At a certain radius the paint streaks of the laminar flow region were cut off

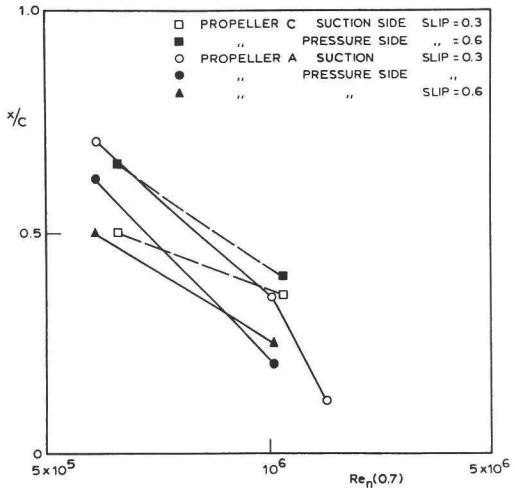

Fig. 3.5. Chordwise position of the transition region.

and a turbulent region started, as sketched in Fig. 3.6. This sudden change of the boundary layer is caused by a short laminar separation bubble at the leading edge in the turbulent region. The radius at which this occurs was called the "critical" propeller radius. (A better name is "separation" radius to avoid confusion with the critical bubble radius and this name will be used further). The occurrence of laminar separation is independent of the Reynolds number and the separation radius was indeed found to be independent of the Reynolds number, as is shown in Fig. 3.7. The separation radius is very sensitive for variations in loading, as is illustrated by the data of Sasajima (1975) in Fig. 3.7, who found that the separation radius was

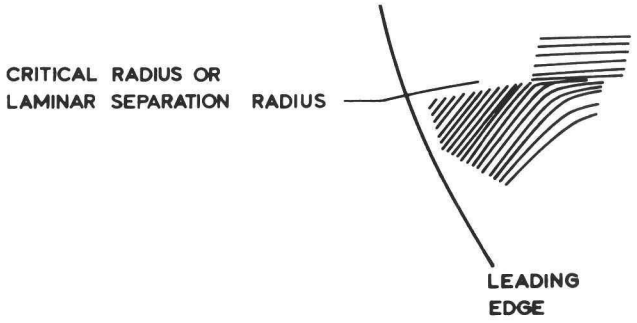

Fig. 3.6. Paint pattern at the separation radius.

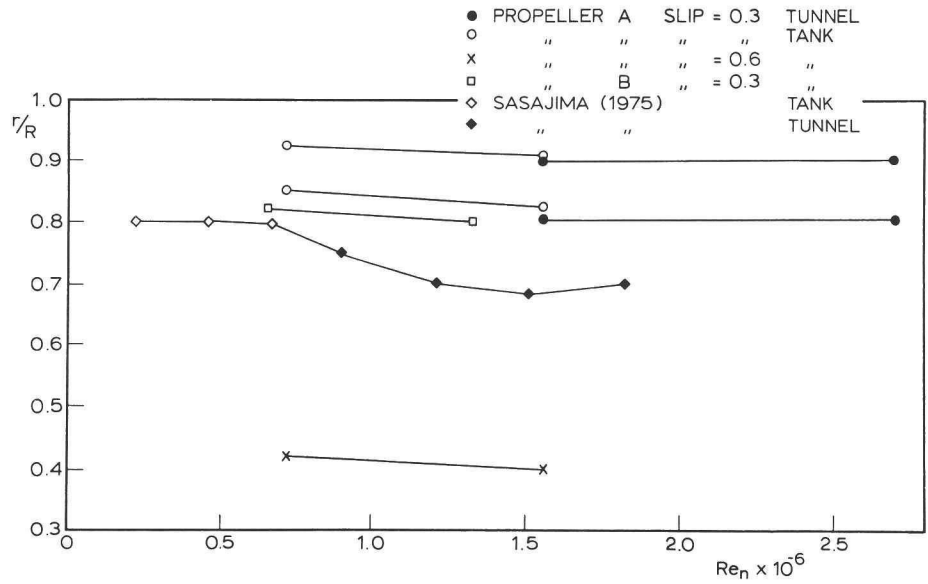

Fig. 3.7. Variation of the separation radius with Reynolds number.

constant in the towing tank but varied slightly in the cavitation tunnel, where the propeller loading can be influenced by wall effects.

The separation radius can also provide an indirect check of the calculated pressure distribution. The boundary layer thickness in the leading edge region was calculated with Thwaites' method (see e.g. Rosenhead, 1963). For this calculation the two-dimensional pressure distribution over the propeller sections was used, which was found to be allowed in the leading edge region of rotating foils by Dwyer and McCroskey (1971). The occurrence of laminar separation at each radius was predicted by using the modified values of Curle and Skan (see also Rosenhead, 1963) and the thus calculated separation radius was compared with observations of paint tests. The agreement was good, as is shown in Fig. 3.8. Since the calculated separation radius depends on the pressure distribution in the minimum pressure region this good correlation gives some confidence in the calculated minimum pressures in that region.

The character of the boundary layer on the suction side of a propeller blade can now be described as in Fig. 3.9. In the region of high loading AB, generally at the propeller tip, a short laminar separation bubble exists near the leading edge, making the boundary layer turbulent over the rest of the

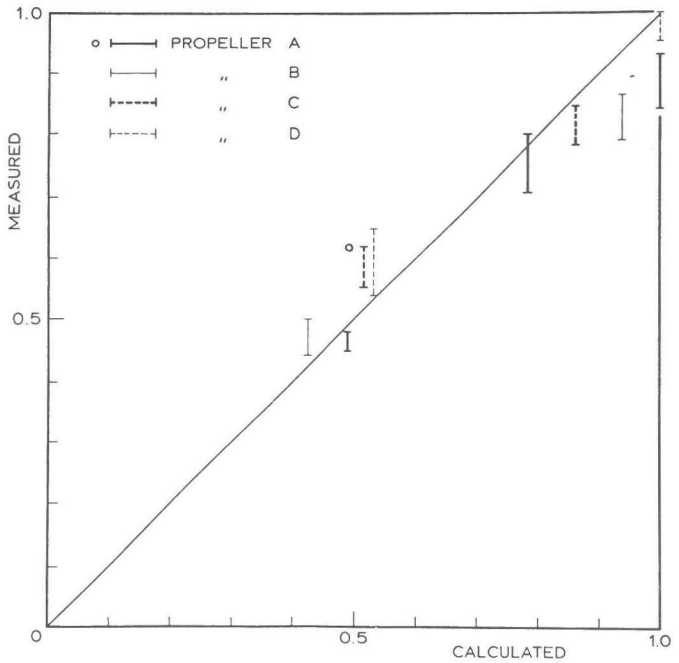

Fig. 3.8. Correlation between calculated and observed separation radius.

chord. The separation radius is found at BC and its radial position is strongly dependent on the propeller loading. The region CD is a transition region, its chordwise position depends on the Reynolds number but is generally located at some distance from the leading edge. The region DE is a region of laminar separation at midchord due to the very low sectional Reynolds number at those radii in combination with thick propeller sections.

The position of the points B, C and D can vary strongly with the shape of the propeller sections, the propeller loading and the propeller Reynolds number.

The boundary layer on the pressure side of a propeller blade is generally less complex. In normal operating conditions no laminar separation occurs on the pressure side and a significant laminar region exists near the leading edge. Transition often occurs more gradually than on the suction side due to a favourable pressure gradient. In such a case the paint streaks bend continuously from the laminar to the turbulent direction.

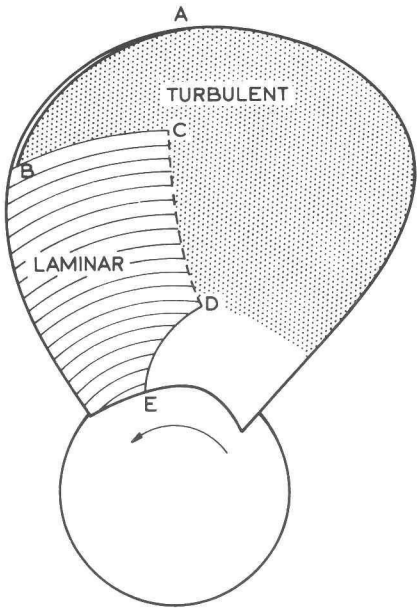

AB SHORT LAMINAR SEPARATION BUBBLE
BC CRITICAL RADIUS
CD TRANSITION REGION
DE LAMINAR SEPARATION

Fig. 3.9. Schematic representation of the boundary layer regimes on the suction side of a propeller.

3.4. THE BOUNDARY LAYER ON PROPELLERS B, S AND V.

The character of the boundary layer on propellers B, S and V was investigated in the Depressurized Towing Tank at atmospheric pressure. if not specifically mentioned the suction side is observed.

Calculations of the laminar boundary layer were made by using Thwaites' method, based on the two-dimensional chordwise pressure distribution at the propeller sections as mentioned before. Based on the same pressure distribution the stability of the laminar boundary layer was calculated by using the diagrams of Smith and Gamberoni (1956), from which the amplification factor of an initial disturbance of a certain unstable frequency can be calculated. Transition is generally assumed when the amplification factor exceeds e^9 at any frequency. The calculated maximum amplification factors at the location of transition on the propeller blades did not exceed e^2. So stability

calculations, if appropriate, should be made in three dimensions (Mack, 1977). Such calculations were not made during this investigation .

The Reynolds numbers, given in the pictures are the propeller Reynolds numbers. They can easily be converted into the sectional Reynolds number at r=0.7R, as given by eq. 3.1 by

$$Re(0.7) = 0.75\ Re_n \tag{3.11}$$

in which relation the influence of the advance velocity is neglected.

3.4.1. The boundary layer on propeller B.

The paint patterns on propeller B at J=0.6 and 0.4 are given in Plates 3.10 and 3.11 respectively. The calculated pressure distribution at J=0.6 is nearly shock free (Fig. 2.13). The calculations show a small low pressure peak near the leading edge at J=0.4 (Fig. 2.14), but no laminar separation is caused by this peak, as shown in Plate 3.11. The effect of the Reynolds number on the chordwise position of transition is moderate at J=0.6 and small at J=0.4. In any case it requires very high sectional Reynolds numbers to bring transition to the leading edge. A further increase of the propeller loading does not change the transition location, as is shown in Plate 3.12. The tip region, however, becomes turbulent due to laminar separation at the leading edge and the separation radius is at r=0.77R.

That the boundary layer can remain completely laminar, even at a sectional Reynolds number at 0.7R of 4.2×10^5, is shown in Plate 3.13.

3.4.2. The boundary layer on propeller S.

The paint pattern on propeller S at J=0.6 is shown in Plate 3.14. A low pressure peak was calculated at the leading edge (Fig. 2.15) but the calculations of the laminar boundary layer indicated no separation. This is confirmed by Plate 3.14.

The paint pattern of Plate 3.14 at the higher Reynolds number is remarkable. A number of turbulent streaks, originating near the leading edge, disturb the laminar region, although the transition region is only slightly moved towards the trailing edge by the increase in propeller Reynolds number.

In this case the increase of the Reynolds number and the subsequent decrease of the boundary layer thickness make the boundary layer more sensitive for surface irregularities. This blurred type of paint pattern is regularly obtained in a cavitation tunnel, partly because of the higher Reynolds number which may be obtained there, but also partly because of particles attaching themselves to the leading edge. When a fully turbulent boundary layer on a propeller blade is obtained by an increase of the Reynolds number it is generally by particles or surface irregularities.

The question may arise why such turbulent streaks did not occur on propeller B at J=0.4, which has a pressure distribution similar to that of propeller S at J=0.6. The explanation is that the thickness of the blades of propeller B is twice that of propeller S. The minimum pressure on propeller S therefore occurs much closer to the leading edge and the region with an adverse pressure gradient, which is sensitive for disturbances, begins when the boundary layer is thinner than on propeller B.

The paint patterns on propeller S at J=0.4 are given In Plate 3.15. There is a sharp low pressure peak at the leading edge (Fig. 2.16) which causes laminar separation at the leading edge. This separation bubble is clearly visible on Plate 3.15. An increase of the Reynolds number, which is not shown in Plate 3.15, decreases the chordwise length of the separation bubble. Two blades are shown in Plate 3.15 to illustrate the difference between the blades.

The way in which the separation bubble ends near the tip is very abrupt. On blade 2 the "long" separation bubble ends at r=0.73R. In the region $0.73<r/R<0.92$ some areas with laminar flow are present. At $r>0.92R$ the boundary layer is turbulent from the leading edge on, possibly a short separation bubble is present there. On blade 4 this region starts at r=0.87R, at the radius where the "long" separation bubble ends.

Gaster (1966) measured the length of separation bubbles and related them with the Reynolds number based on the local velocity u_s and the momentum thickness θ_s at the location of separation. Huang and Peterson (1976) approximated this relation by

$$\frac{\ell_s}{\theta_s} = \frac{350}{\log_{10} Re_{\theta s}} \cdot \frac{300}{Re_{\theta s}} \qquad \text{for} \quad Re_{\theta s} < 300 \tag{3.12}$$

where $Re_{\theta s} = \frac{u_s \theta_s}{\nu}$. In Fig. 3.16 the length ratio of the separation bubble as found from Plate 3.15 is plotted against $Re_{\theta s}$ as calculated. The trend is similar to that of eq. 3.12 but the observed length is smaller. It must be kept in mind, however, that the data supporting eq. 3.12 were in the range $150 < Re_{\theta s} < 450$.

When laminar separation occurs the boundary layer is very sensitive to the shape of the leading edge. Small differences between the blades can lead to large deviations of the separated region, as shown in Plate 3.17. In this

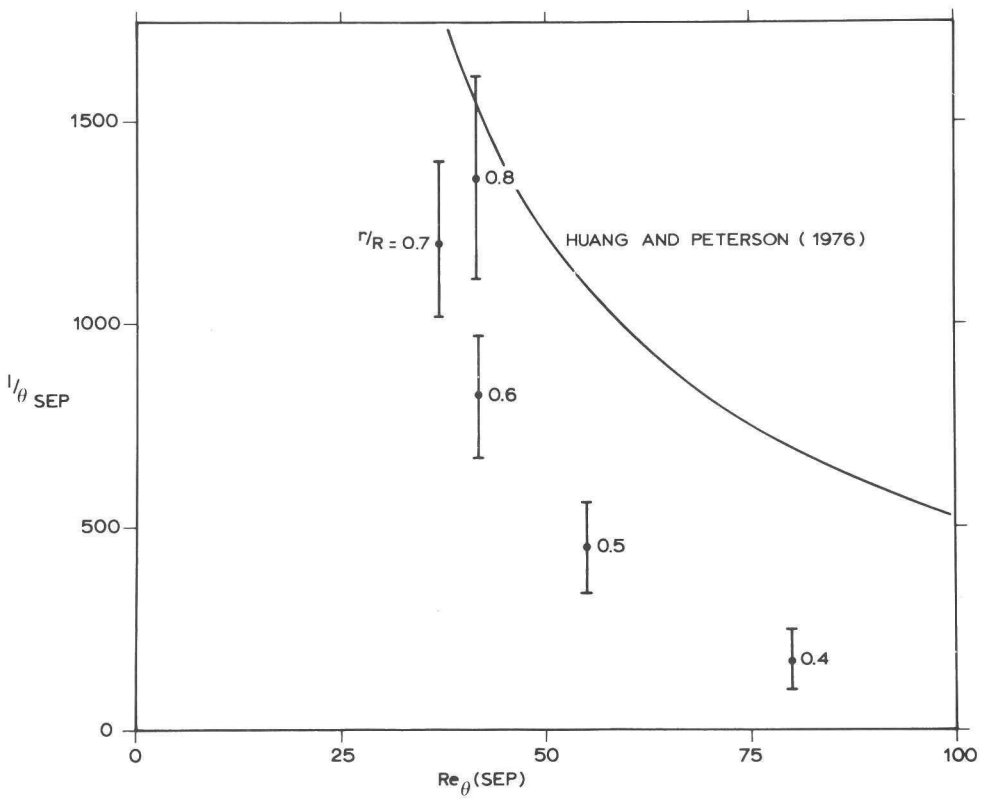

Fig. 3.16. The length ratio of the separation bubble vs the Reynolds number based on momentum thickness.

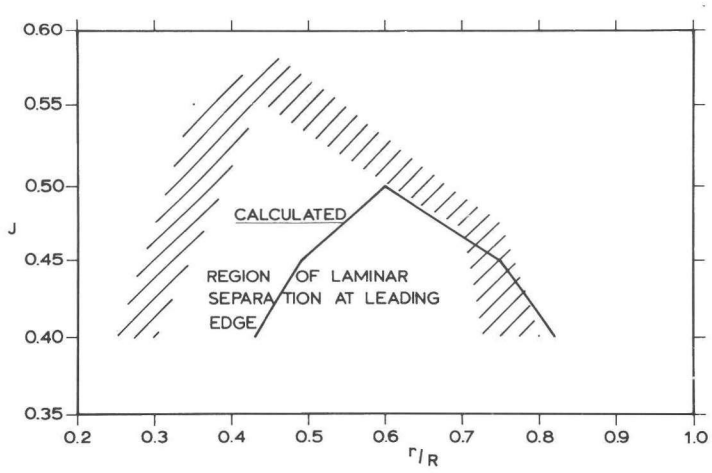

Fig. 3.19. Calculated and observed separation radii on propeller S.

condition the observed differences between the blades of propeller S are large. On blade 1 no separation is found, on blade 4 a separation bubble is present up to r=0.65R, with turbulent streaks up to r=0.8R. These variations can cause large differences in cavitation behaviour, as will be shown in section 7.

The increase of the separated region with increasing loading is shown in Plate 3.18. The observed separation radii are compared with the calculated radii in Fig. 3.19. The agreement is good near the tip, but at inner radii separation occurs earlier than calculated. Apart from discrepancies in leading edge shape this may be caused by the two-dimensional treatment of the thickness in the calculation method, which causes an underestimation of the leading edge pressure peak at thicker blade sections.

3.4.3. The boundary layer on propeller V.

The paint patterns on propeller V at J=0.5 were very similar to those on propeller B at J=0.6, as given in Plate 3.11. Therefore they are not shown here.

Very close to the tip a separated region couls sometimes be observed. This became more apparent at J=0.4, as shown in Plate 3.20. At the highest Reynolds number the increased sensitivity for surface irregularities is illustrated by the turbulent streak. The blades of propeller V are as thick

as those of propeller B and the turbulent streaks were also less frequent than on propeller S at the same Reynolds number.

The sensitivity of the chordwise location of transition to the Reynolds number is negligible, the sensitivity of the separation radius to manufacturing accuracy and loading is illustrated by the variation of this radius between both blades.

4. Roughness at the leading edge

The application of a very narrow region with artificial roughness at the leading edge is used to induce transition to turbulence in the boundary layer. The geometrical implications are discussed and the consequences on cavitation inception are investigated on a circular cylinder. Some measurements of the influence of leading edge roughness on thrust and torque are given.

4.1. THE APPLICATION OF ROUGHNESS AT THE LEADING EDGE

Boundary layers on propeller blades can be laminar over considerable regions, as was shown by paint tests. An increase in Reynolds number does not generally move the transition region to the leading edge. Whenever an increase in Reynolds number is effective in this respect, it is through the mechanism of surface irregularities. So it is only natural to try to stimulate this process by means of artificial roughness.

This is common practice in testing the hull resistance of ship models. A similar use of tripping devices was made on propeller models to eliminate the Reynolds dependency of the propeller thrust and torque. The use of tripping devices has not been generally applied to propeller models because of the sensitivity of the pressure distribution at the leading edge to the propeller geometry in that region and because artificial roughness may cause cavitation inception prematurely.

Still the removal of the laminar boundary layer region can be of prime importance, as will be shown later, and the drawbacks of tripping devices have to be compared with the drawbacks of laminar boundary layer flow.

Only very few investigations with tripping devices in cavitating conditions have been reported. Gates (1977), used a trip wire on a hemispherical headform upstream of the maximum pressure point and observed with the Schlieren technique that laminar boundary layer separation disappeared, as did the cavitation. Arndt (1976) tried trip wires located at 10% of the chord on

propeller blades, but he found that the cavitation pattern depended strongly on the position and the diameter of the wire. (see also Kuiper, 1978a). To avoid this, distributed roughness was applied at the leading edge of propeller blades.

To represent the condition on the prototype, the boundary layer should be made turbulent almost from the leading edge on. Application of roughness elements in the low-pressure region should be avoided because this may generate early cavitation inception. Consequently the roughness should be applied in the region with a favourable pressure gradient between the stagnation point and the leading edge.

Technically this is not feasible on thin propeller blades, where the minimum pressure occurs very close to the leading edge. On thicker blade sections, as occur near the hub, this is feasible, but the strongly favourable pressure gradient stabilizes the laminar boundary layer and it requires large disturbances to induce turbulence in this region (Feindt, 1956). The effect of the pressure gradient on the stability of the boundary layer is very pronounced (see e.g. Lin, 1955) and the pressure gradient is very strong near the leading edge, so the disturbances in that region must be large indeed, thereby affecting the section shape. From paint tests it was found that no turbulent boundary layer was generated by 60 μm carborundum when it was only applied in regions with a strong favourable pressure gradient. So the presence of roughness elements in the low-pressure region near the leading edge cannot be avoided.

The size of the roughness elements should be as small as possible to avoid a change in the leading edge contour of the propeller sections, which is a point of continual concern for any propeller manufacturer. However, on a flat plate a critical roughness height exists for distributed roughness. Below this height the roughness is ineffective. At the critical roughness height transition will abruptly jump from the location of the smooth condition to a position upstream on the roughness, in a way similar to three-dimensional single roughness elements (Klebanoff et al, 1955). Feindt (1956) found a minimum roughness Reynolds number for transition.

$$\frac{V.k}{\nu} > 120 \qquad (4.1)$$

where k is the roughness height and V is the outer flow velocity.

The leading edge of the propellers B, S and V was roughened with carborundum of a grain size of about 60 μm. The particles have a very irregular shape with sharp edges. The carborundum was glued to the surface of the propeller with very thin varnish over a width of approx. 1 mm from the leading edge on. Near the hub the carborundum was applied over a wider distance, approx. equal to the nose radius of the sections. An impression of such an application is given in Fig. 4.1. The effect of the carborundum was verified by paint tests.

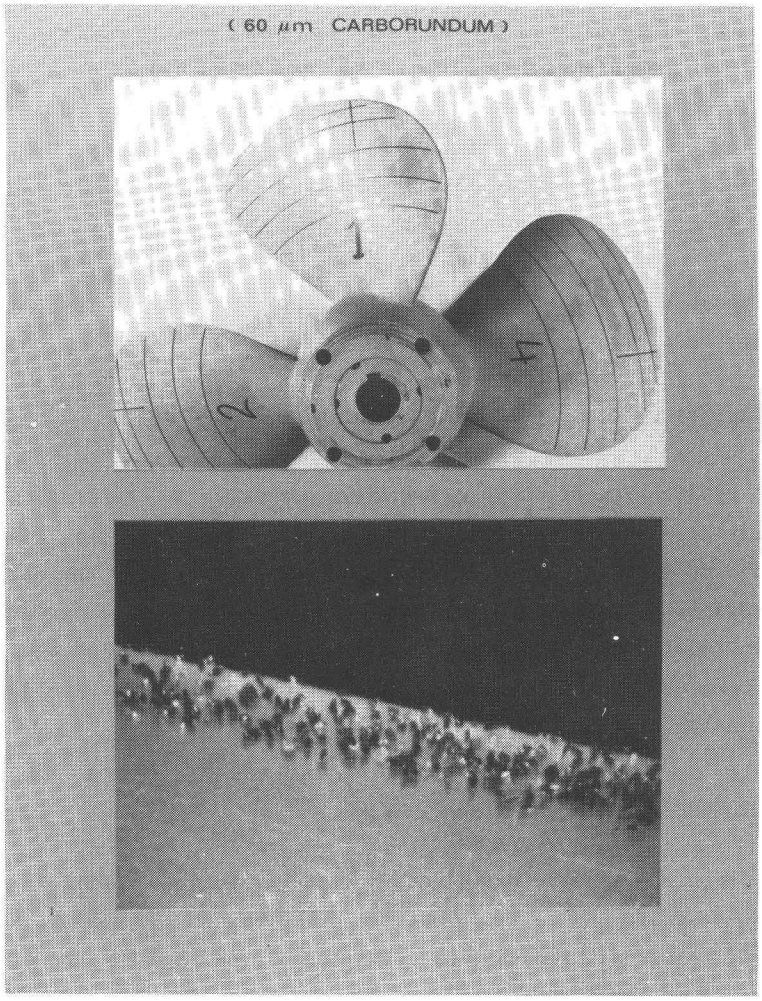

Fig. 4.1. Application of leading edge roughness.

Application of a smaller grain size of 30 μm was also tried but a number of problems occurred. Firstly, it was very difficult to obtain an even spreading of the grains since they tended to clog together. Secondly, even if applied as good as possible, the boundary layer was often not turbulent. The roughness Reynolds number at $Re_n = 10^6$ and r=0.5R is below 200 for 30 μm grain size. It is therefore plausible that the critical grain size is approached. Therefore only 60 μm carborundum was used in this investigation.

The question may arise if it is necessary for cavitation inception on the roughness elements that the boundary layer becomes turbulent. It could be imagined that inception takes place on the roughness elements while the boundary layer remains laminar. In cavitation tests, however, no effect of roughness on cavitation inception was found when the boundary layer was not tripped, so the effectiveness of the roughness on cavitation inception can be judged from its effect on the boundary layer.

An example of the effect of leading edge roughness on the paint pattern has already been given in Plate 3.1.

4.2. THE EFFECT OF ROUGHNESS ON THE LEADING EDGE GEOMETRY

The application of 60 μm carborundum particles to the leading edge will effectively displace the contour of the propeller sections by say 40 μm, which influences the pressure distribution and specifically the minimum pressure at the leading edge. This error in the geometry of the propeller sections has to be compared with other errors which are made on model scale, viz., the manufacturing errors and the errors in effective geometry due to deviations in the Reynolds number.

4.2.1. The manufacturing accuracy

The required manufacturing accuracy for prototype propellers is given by the ISO-standard and we will restrict ourselves to the very high accuracy propellers. (class S). The maximum deviation of the leading edge from the design is 0.5 mm. At a scale ratio of 25, which is taken as representative, this means a tolerance of $\pm$ 20 μm on model scale (ISO/DIN 484/1 - 1977). The tolerance for the thickness outside the leading edge is +2/-1 mm on the

prototype or +80/-40 μm on model scale.

The actual manufacturing accuracy of model propellers is often worse. To investigate this the difference between the blades of propellers B, S and V was investigated. The contour of the propeller sections was visualized by using a laser beam focussed into a slit at the position of the leading edge of the propeller blade. The reflection of the contour was observed and photographed through a microscope. The arrangement is sketched in Fig. 4.2. Photos , obtained in this way are given in Figs. 4.3 and 4.4 for a smooth and a roughened blade respectively. The accuracy which can be obtained from these observations is estimated to be $\pm$ 20 μm.

The maximum variations in the section contours at a certain radius is shown in Fig. 4.5. These contours were measured without roughness at the leading edge. The maximum deviation between the propeller blades of one propeller was about 100 μm.

The application of 60 μm roughness at the leading edge is therefore within the manufacturing accuracy of the propeller blades. It may influence the pressure distribution, and thereby the cavitation on the blades but this

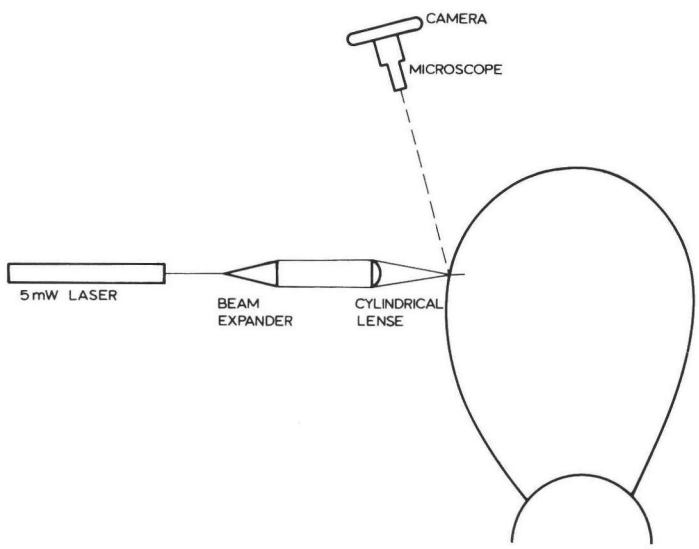

Fig. 4.2. Arrangement of leading edge contour observations.

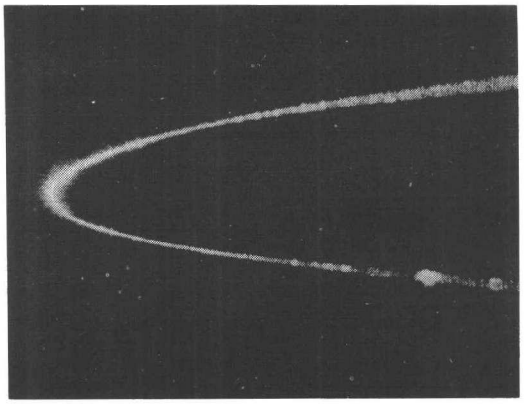

Fig. 4.3. Leading edge contour of a smooth blade (Propeller S at r=0.6R).

influence will be within the influence caused by the differences which may exist between the smooth blades.

4.2.2. Reynolds number effects on the geometry

The large difference in Reynolds number between model and full scale causes a difference in the relative displacement thickness of the boundary layer δ^*/c, which can be considered as an effective contour change. As a crude approximation of this effect the thickness of the boundary layer δ_s at

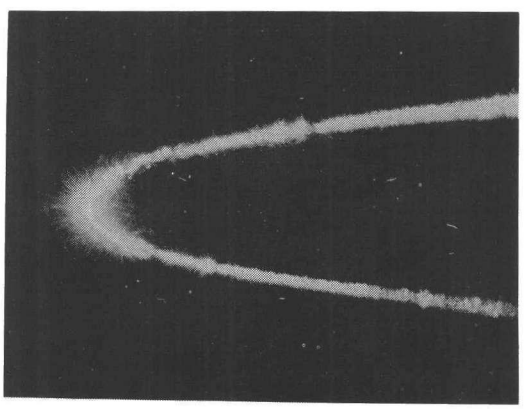

Fig. 4.4. Leading edge contour of a roughened blade (Propeller S at r=0.6R).

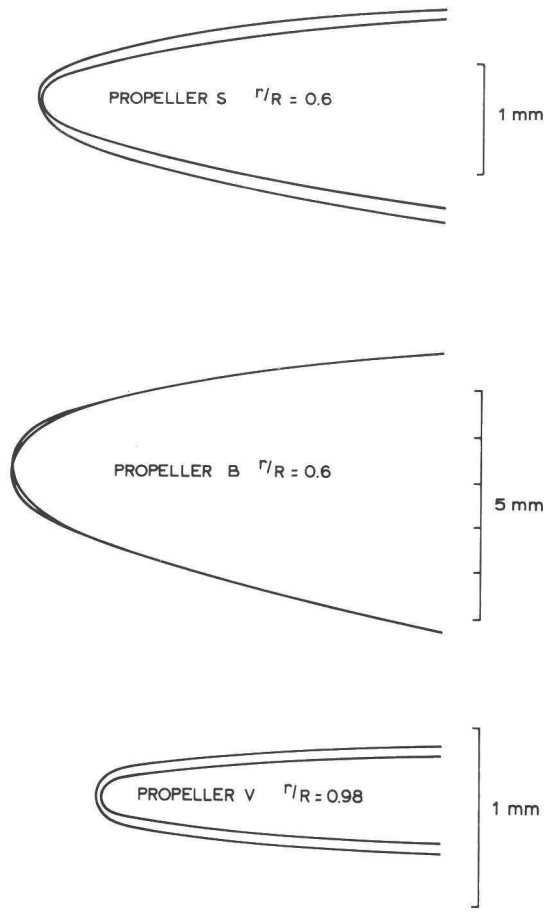

Fig. 4.5. Observed maximum variations of the leading edge contour.

the stagnation point can be considered

$$\frac{\delta_s}{c} = 2.4 \frac{\partial(u/V)}{\partial(s/c)} Re_c^{-\frac{1}{2}} \qquad (4.2)$$

in which V is the sectional inflow velocity, u the local velocity on the suction side and s the distance along the foil from the stagnation point. Re_c is the sectional Reynolds number $\frac{V.c}{\nu}$. (See e.g. Schlichting, 1968, p 88, 89). The derivative of the flow velocity near the stagnation point depends on the leading edge ratio and varied between 50 and 1000 on propeller B, S and V. Assuming $Re_c = 10^8$ and c=2 m on the prototype eq. 4.2 gives a boundary layer thickness of 15 to 68 μm, which corresponds to a displacement thickness on

full scale of some 5 to 23 μm. For proper geometric scaling the displacement thickness on the model should therefore be from 0.1 to 1 μm

However, the boundary layer thickness is only very weakly dependent on the scale ratio. When the Froude number is maintained the Reynolds number Re_c in eq. 4.2 varies with $\lambda^{3/2}$ and it follows that

$$\frac{\delta(\text{prototype})}{\delta(\text{model})} = C\lambda^{1/4} \tag{4.3}$$

and with λ=25 the displacement thickness reduces to 2 to 10 μm on model scale. The error in the stagnation point will therefore be from 2 to 9 μm.

The boundary layer thickness at the minimum pressure point will be a few times that at the stagnation point. So an estimate of the geometrical error due to boundary layer displacement is 10 to 20 μm.

There is another, indirect, effect of the Reynolds number on the minimum pressure at the leading edge through its effect on the lift. Although the lift varied only slightly with Reynolds number and will hardly affect the propeller performance, this effect is amplified in the non-linear region near the leading edge, as was already shown in Fig. 2.6, where the viscous effect was estimated by a 0.75 degree pitch reduction.

A third viscous effect which influences the minimum pressure is the occurrence of laminar separation on model scale. When a separation bubble occurs the minimum pressure is generally decreased (see e.g. Gault, 1955) causing another difference in the effective geometry between model and full scale.

In general these Reynolds effects on the minimum pressures are considered to be smaller than those due to manufacturing errors, but they constitute a theoretical limit to the accuracy of the minimum pressure on model scale. In practice the errors are determined by the manufacturing accuracy of the propellers and the application of 60 μm carborundum is within that accuracy. The effect of leading edge roughness on cavitation inception through a change of the minimum pressure is therefore expected to be insignificant.

However, even if the mean pressure is not significantly changed by the roughness elements, the inception pressure can very well be influenced, which will be considered next.

4.3. CAVITATION INCEPTION ON ROUGHNESS ELEMENTS

Cavitation inception on single roughness elements was systematically investigated by Holl (1960). He used two-dimensional roughness elements such as triangles and circular arcs in a turbulent boundary layer without pressure gradient. Benson (1966) did the same for three-dimensional elements (spheres, cones and cylindrical studs) and Bohn (1972) investigated slots. Those data were summarized in a power law for the inception index on a flat plate:

$$\sigma_{ir} = C.(\frac{k}{\delta})^a \ (\frac{U_\ell \delta}{\nu})^b \tag{4.4}$$

with U_ℓ the velocity at the roughness height k. The constants a, b and C were determined for each type of roughness element (Bohn, 1972).

When such an element is positioned on a body with a certain pressure distribution C_{ps} on the smooth body, Holl (1960) used a superposition relation to calculate the inception index on the roughness

$$\sigma_i = -C_{ps} + \sigma_{ir}(1-C_{ps}) \tag{4.5}$$

From eq. 4.5 it is clear that the deviation from the classical inception law $\sigma_i=-C_{ps}$ is largest when C_{ps} is largest, which is in the minimum pressure region.

Arndt and Ippen (1968) investigated the influence of distributed roughness on cavitation inception and related the inception pressure with the turbulent pressure fluctuations in the boundary layer, which in turn are a function of the friction velocity at the wall. The result of their measurements was the simple relation

$$\Delta\sigma = 16\ C_f \tag{4.6}$$

in which C_f is the local friction coefficient and the cavitation index at inception is found from

$$\sigma_i = -C_p(\min)+\Delta\sigma \tag{4.7}$$

The application of distributed roughness also leads to an increase of the inception index relative to the inception index on the smooth body. Generally the increase is less than that due to a single roughness, as given in eq. 4.4.

The role of nuclei is ignored both in eq. 4.3 and in eq. 4.6. Arndt and Ippen paid detailed attention to this and observed gas bubbles in the turbulent boundary layer. The bubbles were large enough (about 200 μm in diameter) to become unstable at a local pressure close to the vapor pressure. As already mentioned the introduction the mean pressure in the boundary layer was higher than the critical pressure calculated from the observed critical radius and the bubbles therefore experienced local low pressures which were much larger than would follow from the rms-values of the turbulent wall pressure fluctuations. Anyhow, it is clear that eqs. 4.4 and 4.6 are only valid when enough large nuclei are available.

The application of eqs. 4.4 and 4.6 is often difficult because detailed knowledge of the roughness shape and of the boundary layer is required. This knowledge is generally not available, especially not in the steep pressure gradients near the leading edge of a propeller.

4.4. THE EFFECT OF ROUGHNESS ON CAVITATION INCEPTION ON A CIRCULAR CYLINDER

The effect of 60 μm carborundum in the region of a low-pressure peak was investigated by using a circular cylinder perpendicular to the flow. The pressure distribution and the friction coefficient on such a cylinder were measured by Achenbach (1968). The effect of distributed surface roughness on the pressure distribution and the boundary layer development on a circular cylinder was investigated by Achenbach (1971) and Güven et al (1980).

A 0.10 m diameter cylinder was placed in a vertical position in the test section of the NSMB large cavitation tunnel. Three holes of 1 mm diameter were used to measure the pressure distribution on the cylinder, which was done by rotating the cylinder. The arrangement is given in Fig. 4.6.

Inception measurements were carried out for two velocities, viz., 5.7 and 9.6 m/sec. The Reynolds number based on the cylinder diameter is between 5.7×10^6 and 9.6×10^6, which is in the critical range (Achenbach, 1968). In this range a laminar separation bubble exists downstream of the minimum pressure point and turbulent separation occurs further downstream.

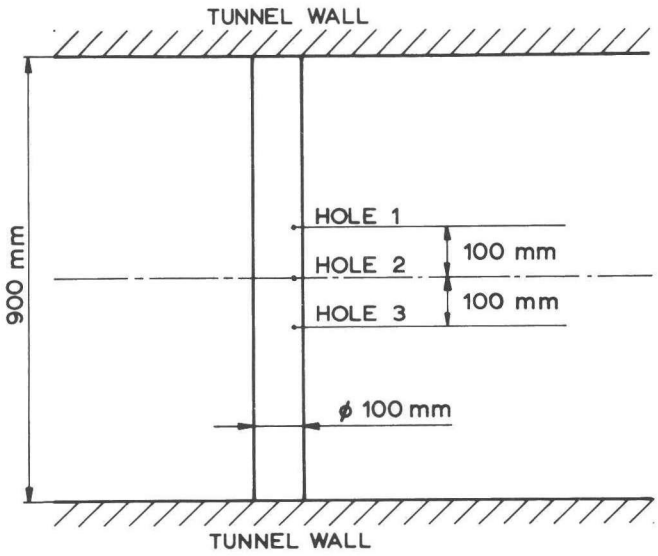

Fig. 4.6. Test arrangement of a circular cylinder in the cavitation tunnel.

4.4.1. Measurements on the smooth cylinder

The pressure distribution in the non-cavitating condition around the smooth cylinder is shown in Figs. 4.7 and 4.8 for both flow velocities. The difference between the pressure holes was rather large, but was very repeatable. Since these differences varied strongly with tunnel speed, it is believed that this was caused by the non uniformity of the inflow. The pressure in the region of pressure recovery was sometimes unstable, but no significant asymmetry in the pressure distribution was found. The minimum pressure occurs at 85^{o}, turbulent separation at 120^{o}.

Cavitation observations on the smooth cylinder are given in Plates 4.10 and 4.11, observed from a position as given in Fig. 4.9.

Cavitation inception does not occur simultaneously over the whole height of the cylinder. Although there is a very small variation in cavitation index over the height of the cylinder (<0.01) this is negligible. The main causes are the inflow variation and especially deviations from the cylindrical shape.

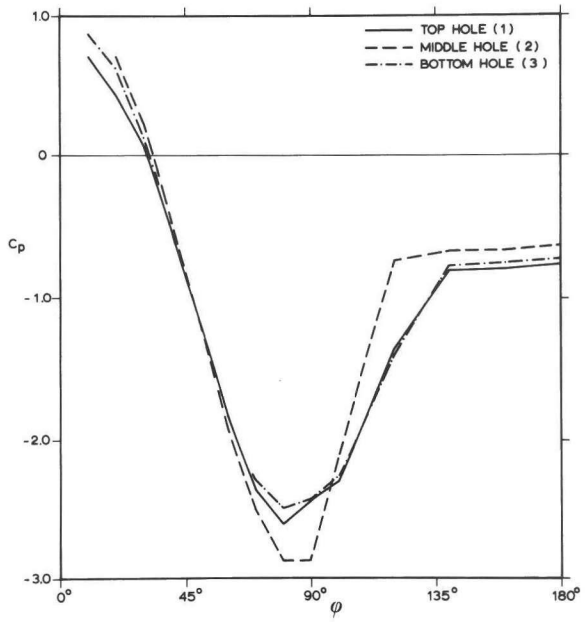

Fig. 4.7. Pressure distribution on the smooth cylinder at 5.7 m/sec.

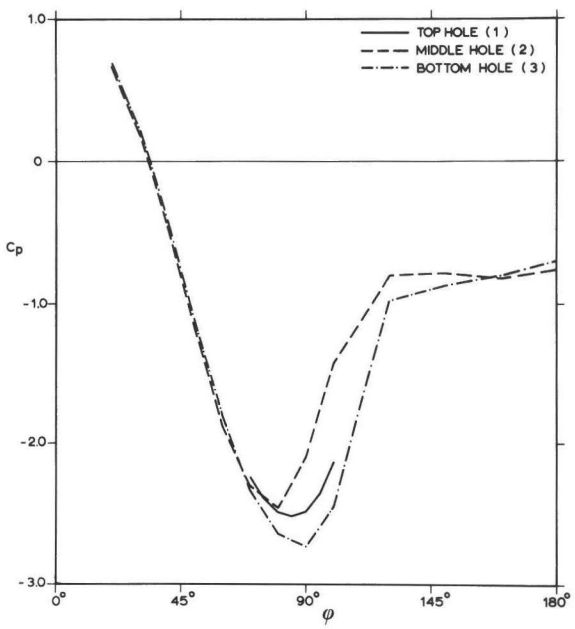

Fig. 4.8. Pressure distribution on the smooth cylinder at 9.6 m/sec.

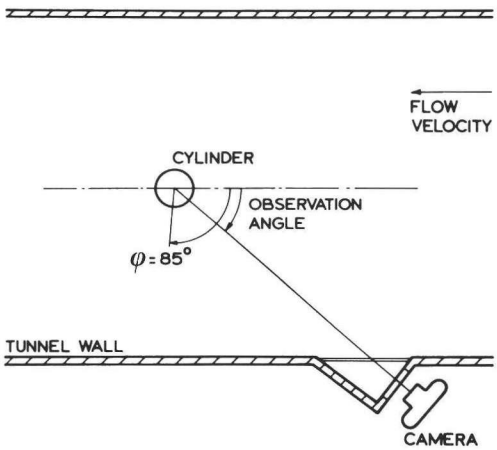

Fig. 4.9. Observation angle of the cylinder in the cavitation tunnel.

The type of cavitation is not bubble cavitation, although some cavitation bubbles were observed. The glassy appearance indicates that inception occurs at laminar separation, which is very well possible at this Reynolds number. Laminar separation occurs close to the minimum pressure in this case, so the inception index is close to the minimum pressure coefficient.

4.4.2. Measurements on the roughened cylinder.

The same cylinder was roughened by glueing 60 μm carborundum on the whole surface. Small regions around the pressure holes were left smooth to avoid edge-effects on the pressure measurements.

The pressure distribution around the roughened cylinder is given in Figs. 4.12 and 4.13. A drastic change has taken place, the increased local stress due to the roughness causes early turbulent separation and the minimum pressure is much higher than on the smooth cylinder. The resulting drag increase was already measured by Fage and Warsap (1929). The pressure distribution varies only slightly with the velocity and the cylinder is apparently in the trans-critical range (Achenbach, 1971) where the pressure distribution is only controlled by the roughness ratio k/D. Güven et al (1980) used the pressure recovery, expressed as the difference between the minimum pressure coefficient and the pressure coefficient in the wake, as a measure for the boundary layer at the minimum pressure point and he also found that above a

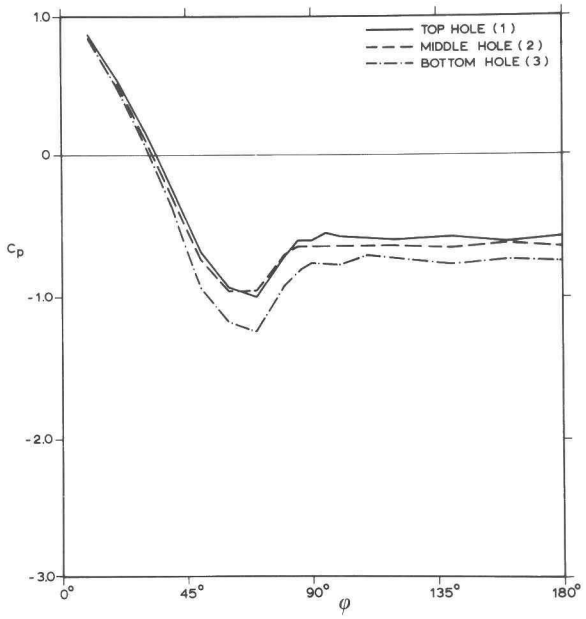

Fig. 4.12. Pressure distribution on the roughened cylinder at 5.7 m/sec.

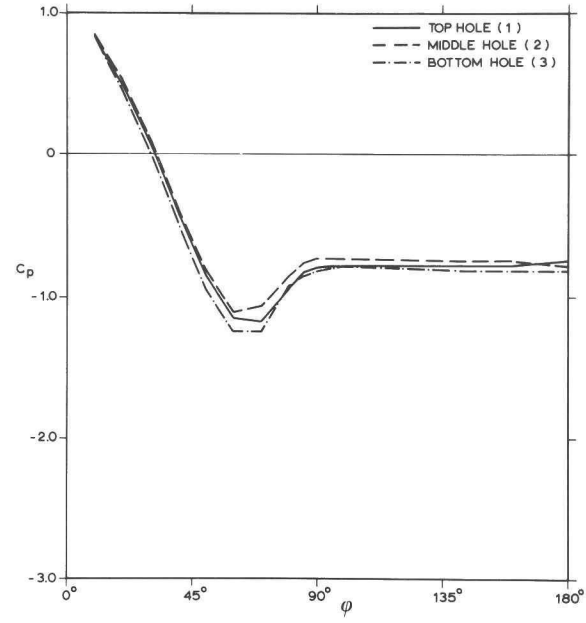

Fig. 4.13. Pressure distribution on the roughened cylinder at 5.7 m/sec.

certain Reynolds number the pressure recovery became constant and dependent on the roughness ratio only. The pressure recovery on the roughened cylinder is between 0.4 and 0.45 in Figs. 4.12 and 4.13 for $k/D=6x10^{-4}$ which is in agreement with the values of Güven et al, who found a value of about 0.5, although only for roughness ratios above $2x10^{-3}$.

Cavitation inception on the roughened cylinder occurs first in the wake, where local low pressures exist in the vortices. Only after extensive cavitation takes place in the wake inception occurs on the cylinder itself. This can affect the pressure distribution. An increase of the minimum pressure coefficient with 0.1 to 0.2 was measured in the cavitating condition, but cavitation on the pressure hole may have made this measurement unreliable.

At a velocity of 5.7 m/sec inception on the cylinder was very intermittent, as shown in Plate 4.14. The rather extensive cavitation at $\sigma=1.86$ occurred intermittently. At 10 m/sec a somewhat more stable cavitation was found at $\sigma=1.80$ (Plate 4.15) but its appearance with decreasing cavitation index was very abrupt. The location of the beginning of the cavity was close to the measured minimum pressure location.

The abrupt appearance of cavitation on the roughened cylinder indicates that inception is delayed, which is possible when there is a lack of nuclei. When this is the case the inception index is higher when enough nuclei are present.

The air content of the tunnel water was about 7 ppm by weight and the water at the location of the minimum pressure was not yet saturated. It is interesting to note this, since on the propeller models nuclei were generated by the roughness elements themselves, provided the fluid was locally supersaturated. This will be discussed in section 6.

4.4.3. Measurements on the cylinder with a single roughness line.

A line of 60 μm roughness particles was attached on the smooth cylinder. The line was about 5 particles wide and its total width was about 1 mm. The line was attached from tip to bottom at the position of the pressure holes, which interrupted the line.

Since circulation was generated by the roughness line the pressure distribution was only measured to find the position of minimum pressure, as is shown in Figs. 4.16 and 4.17. The minimum pressure was found at about 85^{o}, so

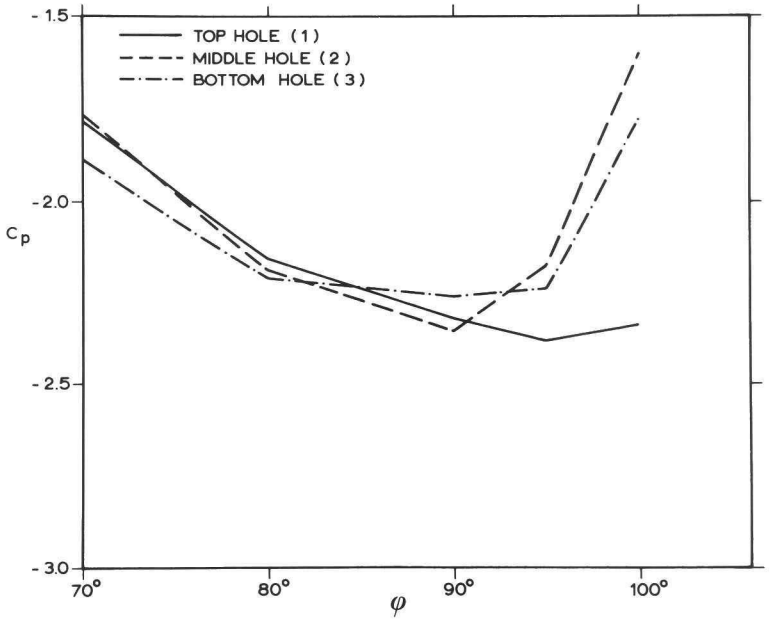

Fig. 4.16. Pressures on the roughness line at 5.7 m/sec.

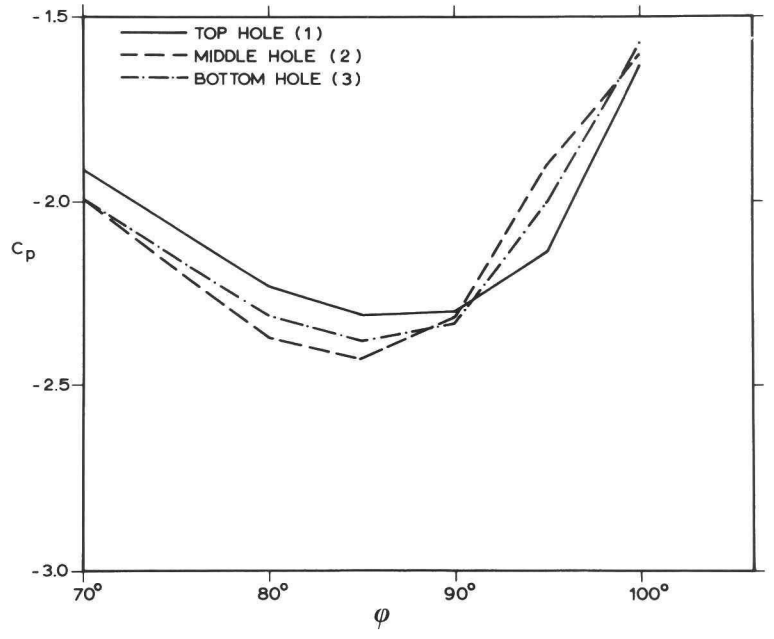

Fig. 4.17. Pressures on the roughness line at 9.6 m/sec.

the line was positioned there and inception measurements were made in this position. At 5.7 m/sec inception took place very suddenly and the cavitation pattern at inception is shown in Plate 4.18. At a tunnel velocity of 9.6 m/sec inception was gradual, as shown in Plate 4.19. The inception index in this condition is higher than at 5.7 m/sec.

4.4.4. Conclusions

The pressure coefficients at inception are compared with the inception index in Fig. 4.20. It is clear that both distributed roughness and the single roughness line cause early inception, that is $\sigma_i > -C_p(\min)$. The inception index on the smooth line is close to the minimum pressure coefficient with a tendency to be lower.

An exercise with available data from Bohn is possible by considering the roughness line as a two-dimensional circular element with a height to length ratio of 0.175. The constants in eq. 4.4 for this roughness element are

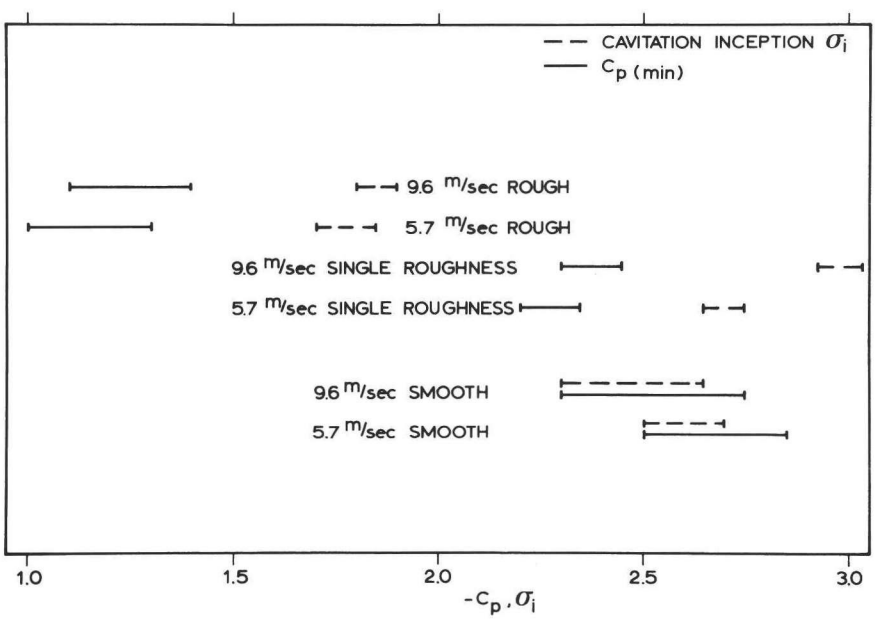

Fig. 4.20. Comparison of inception index with minimum pressure coefficient on the cylinder.

a = 0.344

b = 0.267

C = 0.041

The boundary layer thickness on a cylinder at 85^{o} was calculated by Schlichting (1968, p.160) and is given by

$$\frac{\delta}{D}\sqrt{2Re} = 2.8 \tag{4.8}$$

At a Reynolds number of $5.7x10^{5}$ the boundary layer thickness at 85^{o} is $2.6x10^{-4}$ and $k/\delta=0.23$. Again from the calculations of Schlichting the velocity in the boundary layer at 0.23δ is estimated to be 0.5 U, where U is the outer velocity at that location. U is found from

$$\frac{U}{V} = \sqrt{1-C_p} \tag{4.9}$$

and with $C_p=-2.4$ (from Fig. 4.16) we have $u_s=5.26$ m/sec and $\frac{u_s\delta}{\nu}=1361$ ($\nu=1.004x10^{-6}$). The result from eq. 4.4 is $\sigma_{ir}=0.17$ or from eq. 4.5 $\sigma_i=2.98$ which is close to the observed inception index.

A similar exercise can be made for the distributed roughness using the friction coefficient as measured by Achenbach (1971) in the minimum pressure region of roughened cylinders:

$$\tau_\omega = 0.0014\,\rho V^2 \tag{4.10}$$

where V is the tunnel velocity (The value 0.014 was for $Re=6.5x10^{5}$ with a roughness ratio $k_s/D=1.1x10^{-3}$. (k_s is the equivalent sand roughness height, which is not necessarily equal to the grain size).

The minimum pressure coefficient in these measurements was about -2 and the local friction coefficient in the minimum pressure region therefore is

$$C_f = \frac{\tau_\omega}{\frac{1}{2}\rho U^2} = 0.0093 \tag{4.11}$$

with U the outer velocity at the minimum pressure point, which is 1.73V (from eq. 4.9) at $C_p=-2$.

Application of this friction coefficient in eq. 4.6 leads to $\Delta\sigma=0.15$, which is much smaller than the measured difference of about 0.5. Even at the

highest friction coefficient measured by Achenbach ($k_s/d=4.5x10^{-3}$ and $Re=3x10^6$) the wall friction coefficient in eq. 4.10 was only 0.025. Combined with the low $-C_p(min)=1.1$ on the roughened cylinder (Figs. 4.12 and 4.13) the calculated $\Delta\sigma$ is still only 0.36. Apparently the strong pressure gradient changes the structure of the turbulent boundary layer and stimulates inception, making eq. 4.6 less applicable.

Distributed roughness may indeed increase the inception index. Extrapolation to the situation at the leading edge of a propeller is still difficult. The leading edge radius is generally small and the roughness ratio k_s/d on a thin blade (as on propeller S at 0.6R) can be as high as 0.2. Experiments with roughness at the leading edge are necessary to investigate the inception behaviour in such a condition. This will be done in section 7.

4.5. EFFECTS OF LEADING EDGE ROUGHNESS ON THE THRUST AND TORQUE OF PROPELLERS B, S AND V.

The application of roughness at the leading edge affects the propeller performance (thrust and torque) in two ways. Firstly by changing the boundary layer on the blades and secondly by their own resistance. As shown in section 3 the character of the boundary layer is rather complex and the effect of roughness at the leading edge will be accordingly complex.

The open-water diagrams of propellers B, S and V were measured in the smooth and in the roughened condition. The measurements were carried out with the propeller in front of the catamaran, as shown in Fig. 4.21. The disturbing effects of the catamaran were avoided in this way, while the conditions were similar as during the paint test to preserve the character of the boundary layer. The torque and thrust were measured with a new dynamometer, mounted inside of the propeller hub, instead of with the regular dynamometer which is mounted in the shaft. The frictional effects of the bearings are thus avoided.

The measured open-water curves are given in Figs. 4.20 to 4.22. Also measured was propeller A, of which the geometry and the open-water curves are given in Appendix 2.

The effect of the leading edge roughness of the thrust and torque coefficients are shown in Figs. 4.22 and 4.23. The accuracy of the measured thrust coefficient is estimated to be $\pm$ 0.002 and that of the torque coefficient $\pm$ 0.003. The possible errors in the difference is therefore twice these values, as indicated in Figs. 4.22 and 4.23.

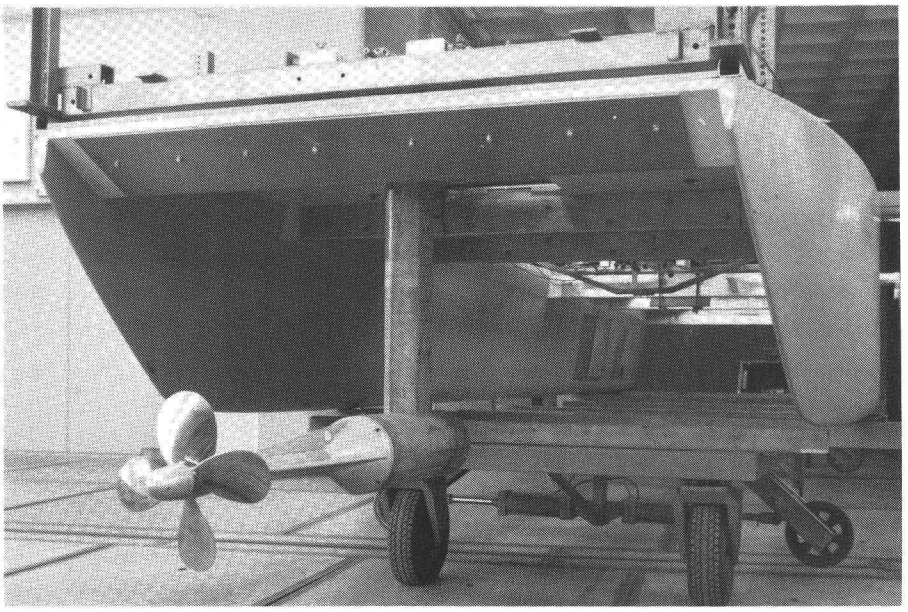

Fig. 4.21. Test arrangement for open-water measurements.

A method to correct the thrust and torque coefficient for variations in the boundary layer of the propeller is the method of Lindgren (1972) based on the drag variations of the propeller section at 0.75R. The effect of an increase of the sectional drag ΔC_D on the propeller section at 0.75R is given as

$$\Delta K_T = -0.28 \quad \Delta C_D \; P/D \; \left(\frac{c.Z}{D}\right)_{r=0.75R} \tag{4.12}$$

$$\Delta K_Q = +0.248 \; \Delta C_D \; \left(\frac{c.Z}{D}\right)_{r=0.75R} \tag{4.13}$$

Using ΔC_D=0.0066 as a representative value, which is the difference in drag coefficient between a fully laminar and a fully turbulent flat plate at Re=10^6, we arrive at

$$\Delta K_T = -0.0018$$
$$10\Delta K_Q = 0.022$$

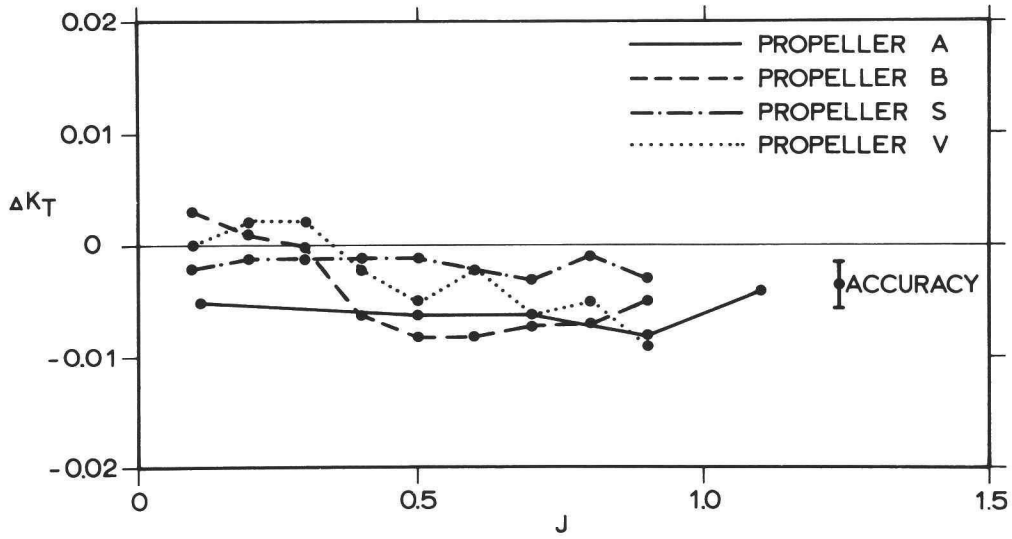

Fig. 4.22. Effect of leading edge roughness on the thrust coefficient.

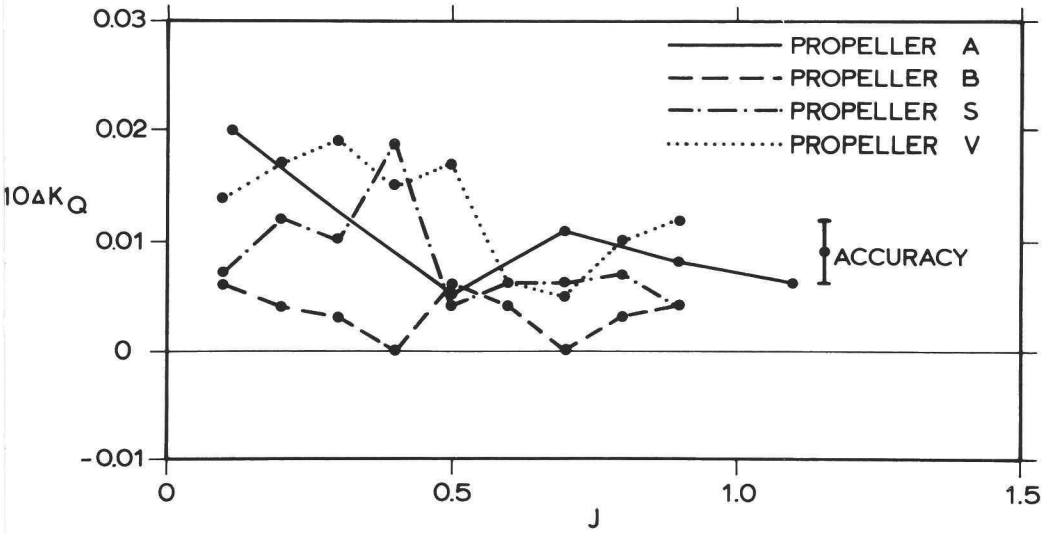

Fig. 4.23. Effect of leading edge roughness on the torque coefficient.

The measured increase of the torque coefficient is about half this value, which indicates that the own resistance of the leading edge roughness is negligible. The measured decrease of the thrust coefficient, however, is significantly

larger in some conditions, which indicates that the character of the boundary layer influences the lift of the sections. This effect was ignored in eqs. 4.12 and 4.13.

The influence of leading edge roughness on the performance of a model propeller needs further investigation, which is beyond the scope of this study.

5. Nuclei

In cavitation test facilities the nuclei content is often insufficient for cavitation. This is specifically the case in a Depressurized Towing Tank. Electrolysis proved to be an appropriate means to generate nuclei. The production of gas bubbles from a cathode wire is investigated in this section and the application of electrolysis in the Depressurized Towing Tank is described. Efforts to apply electrolysis in the NSMB Large Cavitation Tunnel are also mentioned.

5.1. THE PRESENCE OF NUCLEI

The modelling of nuclei as gas bubbles raises the question where these bubbles originate. In a stable fluid they cannot persist. Either they will be driven into solution by the surface tension (eq. 1.8) or they will rise to the surface. Gas bubbles with a diameter up to 100 μm rise like solid spheres because of the existence of surface active materials present in untreated water (see Levich, 1962) and the rise velocity V_b can be approximated by Stokes' law

$$V_b = \frac{1}{18} \frac{g\, d_b^2}{\nu} \qquad (5.1)$$

where d_b is the bubble radius. Eq. 5.1 holds good as long as the Reynolds number $V_b . d_b / \nu$ is smaller than one.

Free gas bubbles can be driven into solution by applying a high pressure in the tunnel before the test or by a resorber. Both methods stimulate diffusive resolution of the gas bubbles. Still it is very difficult to remove all the gas from the water. Several theories have been devised to explain the persistence of free gas, e.g. the presence of a monomolecular shell on small bubbles, which prevents diffusion (Fox and Herzfeld, 1954), the constant generation of nuclei by cosmic rays (Sette and Wanderling, 1967) or the presence of hydrophobic particles which contain free gas in crevices (Harvey et al, 1947).

Only the last hypothesis has been experimentally confirmed for cavitation inception since the use of filtered water did reduce the inception index in a cavitation tunnel (Keller, 1972).

It is very difficult to observe and count free gas bubbles because they are very small and sensitive to disturbances in the flow. Out of many possible methods to detect nuclei (see Morgan, 1972) only direct observation by holography (Peterson, 1972) and measurements by scattered light (Keller, 1974, 1979) were used in combination with cavitation measurements. The results of both methods have been compared, showing a good agreement in one case (Peterson et al, 1975) but large discrepancies in another (Billet and Gates, 1979). Oldenziel (1979) developed a measuring technique by counting the noise pulses of bubble collapses in a venturi. This technique has the potential to measure a bubble spectrum. It correctly discriminates nuclei which are active in cavitation inception but has the drawback that a water sample has to be extracted from the flow, with the possibility that the free gas content is changed.

In a cavitation tunnel free gas bubbles are generated by the impeller, by sharp corners in the circuit and by the cavitating device in the test section. In a depressurized towing tank these mechanisms are not present and the nuclei content will be very low, resulting in serious delays of cavitation inception. Therefore Noordzij (1976) applied electrolysis in the Depressurized Towing Tank to create additional nuclei. Similar problems were met by Albrecht and Bjorheden (1975) in their free surface tunnel. They generated free gas bubbles by small cavitating jets. Control of the nuclei content was obtained in a special cavitation tunnel by Schiebe (1969).

The application of electrolysis will be further investigated now and electrolysis will be used both in the Depressurized Towing Tank and in the Cavitation Tunnel to generate additional nuclei.

5.2. GENERATION OF NUCLEI BY ELECTROLYSIS

When electrolysis is applied, water is decomposed into its components hydrogen and oxygen as given by the reaction equations

$$4H_2O + 4e \rightarrow 2H_2\uparrow + 4OH^- \qquad \text{(cathode)}$$

$$4OH^- + 4e \rightarrow 2H_2O + O_2\uparrow \qquad \text{(anode)}$$

The total amount of gas, produced at both poles, depends on the current only and is 1.74×10^{-7} $m^3 A^{-1} sec^{-1}$. (at 1013 mbar and 0^oC). The amount of hydrogen is twice the amount of oxygen and the cathode is therefore often used for the production of gas bubbles. The method is therefore also called the "hydrogen bubble technique", a technique known as a method for flow visualization.

For flow visualization it is important that the bubbles are very small (e.g. below 10 μm in diameter) to avoid deviations of the bubble path from the streaklines (Schraub et al, 1965; Davis and Fox, 1967). When electrolysis is used for cavitation inception larger bubbles are necessary to bring the critical pressure near the vapor pressure. In principle only the largest bubbles are of importance, provided they are sufficient in number. To investigate the maximum bubble size and the parameters controlling the maximum bubble size some investigations on stainless steel cathode wires were carried out.

The parameters which must be taken into account are

d	wire diameter	(m)
V	flow velocity	($msec^{-1}$)
p	static pressure	($kgm^{-1}sec^{-2}$)
ρ	specific mass of the water	($kg\ m^{-3}$)
s	surface tension (water to air)	($kg\ sec^{-2}$)
ν	kinematic viscosity of the water	($m^2 sec^{-1}$)
G	gas production per unit length of the wire	($m^2 sec^{-1}$)
g	acceleration due to gravity	($m\ sec^{-2}$)

The gas density, gas diffusion and thermodynamic effects are considered to be unimportant and are therefore neglected. Chemical effects like corrosion of the wire and the acidness of the water may play a role in the static case when the bubbles rise due to buoyancy (Tory and Haywood, 1971) but these effects are also considered negligible when there is a fluid flow past the wire.

The gas volume produced by the cathode per unit length can be found from

$$G = \frac{I}{\ell} \frac{1013}{p_g} \frac{273+t}{273} \; 1.16 \times 10^{-7} \; (m^3 sec^{-1}) \qquad (5.2)$$

where: I = the current through the wire

ℓ = the length of the wire

p_g = the gas pressure

t = the temperature in ^oC

The gas pressure p_g can be found from the static equilibrium

$$p_g = p - p_v + \frac{2s}{R} \qquad (5.3)$$

where R is the bubble radius and p the static pressure at the wire.

The eight mentioned parameters can be written in dimensionless form as

$$\pi_1 = \frac{p}{\rho V^2} \qquad \text{pressure coefficient} \qquad (5.4)$$

$$\pi_2 = \frac{G}{Vd} \qquad \text{gas production parameter} \qquad (5.5)$$

$$\pi_3 = \frac{V.d}{\nu} \qquad \text{Reynolds number} \qquad (5.6)$$

$$\pi_4 = \frac{V}{\sqrt{gd}} \qquad \text{Froude number} \qquad (5.7)$$

$$\pi_5 = \frac{\rho V^2 d}{s} \qquad \text{Weber number} \qquad (5.8)$$

When the velocity V is zero the pressure coefficient becomes meaningless and the velocity V in all parameters has to be replaced by G/d. This situation, where the Froude number is dominating, has to be distinguished from the situation with velocity, where the shear forces remove the gas bubbles from the wire and where the Reynolds number is dominant. The rule of thumb that the bubble diameter is roughly equal to the wire diameter is only applicable in the static case, and even then only when the gas production is low, as is illustrated in Fig. 5.1. With increasing current the size of the bubbles

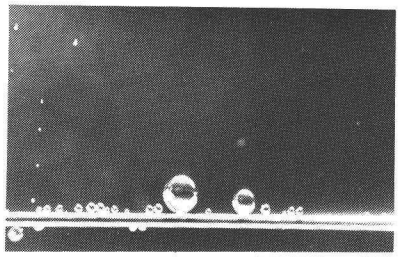

$I = 0.12$ A/m

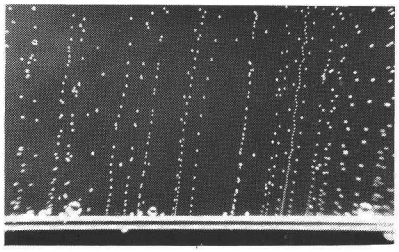

$I = 0.45$ A/m

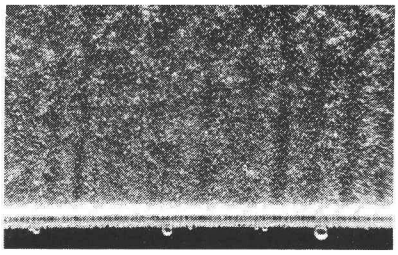

$I = 2.80$ A/m

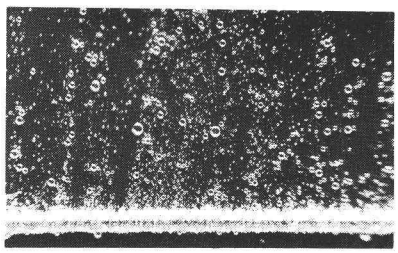

$I = 7.20$ A/m

Fig. 5.1. Hydrogen bubbles rising from a horizontal cathode wire at atmospheric pressure. (wire diameter 0.3 mm).

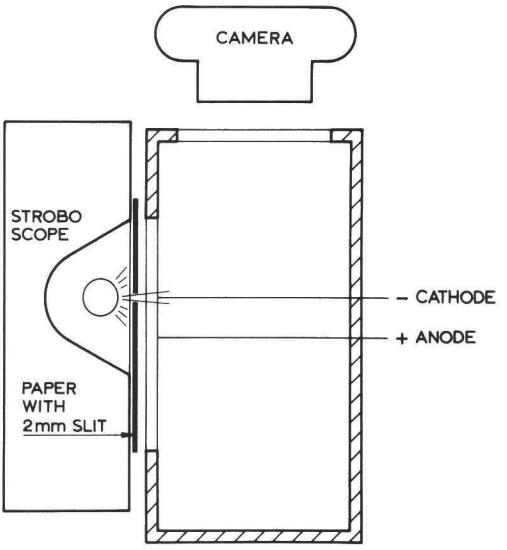

Fig. 5.2. Arrangement for observations of hydrogen bubbles.

decreases, until at a large gas production their maximum size increases again due to amalgamation.

When there is a significant velocity the situation is different. This was investigated more closely in the NSMB high speed cavitation tunnel, which has a test section of 5x10 cm. A description of this tunnel is given by Van der Meulen (1978), Two wires were mounted in the test section, as shown in Fig. 5.2. and photographs were taken of the bubbles coming from the cathode. Two wire diameters, 0.3 and 0.9 mm, were investigated.

A typical sequence of observations is shown in Plate 5.3, where the pressure parameter π_1 (eq. 5.4) was varied on a 0.9 mm diameter cathode. The Reynolds number, based on the wire diameter is 2700 and the flow is subcritical.

Periodically the bubbles concentrate in rows. For both wire diameters the Strouhal number d/λ (with d the wire diameter and λ the wave length, which is equal to two times the distance between the bubble rows) was always near 0.2. The bubble rows are therefore caused by the Kármán vortices.

The gas production parameter π_2 (eq. 5.5) was maintained by keeping the ratio I/p constant. This implies (eq. 5.2) that it is assumed that $p=p_g$ and that the influence of the surface tension and of the vapor pressure is negligible (eq. 5.3). However, there is a visual increase in the amount of gas produced at higher pressures in Plate 5.3. So the surface tension has a considerable effect. This gives an indication about the size of the bubbles produced, because it implies that the term 2s/R in eq. 5.3 is of the same order of magnitude as the static pressure p. From Plate 5.3 this means that at a pressure of 270 mbar the average bubble radius is less than 10 μm in diameter, which is not visible on the photographs. The increase in gas volume with increasing pressure is visible to a pressure of at least 1080 mbar, where larger bubbles of some 0.1 mm become visible. This means that also in that case the majority of the gas is still present in much smaller gas bubbles.

Variation of the gas production by an increase of the current is shown in Plate 5.4 and the effect is similar, though more pronounced, as in Plate 5.3. With a small gas production very small bubbles are produced. When the amount of gas is increased the bubbles apparently coalesce in the Kármán vortices and individual bubbles of 200 μm in diameter were observed in the case of 16 A/m in Plate 5.3. The current in this situation is, however, extremely high.

Variation of the Reynolds number (eq. 5.6) on the 0.9 mm cathode did not change the picture as given in Plate 5.3. At higher Reynolds numbers, thus at higher pressures, the gas volume again increased when I/p was kept constant, so the average bubble diameter remained extremely small.

A reduction of the wire diameter from 0.9 to 0.3 mm strongly reduced the visible gas production. In the conditions of Plate 5.3 the gas production was nearly invisible. Both the maximum and the average bubble size apparently depend on the wire diameter. Since the Reynolds number was shown to have little effect this means a strong Weber number effect (eq. 5.8).

From these observations it can be concluded that the average bubble size, produced by electrolysis, is very small. Only with sufficient gas production larger bubbles are formed, which are estimated to have a maximum size of 0.2 times the wire diameter.

5.3. THE APPLICATION OF ELECTROLYSIS IN THE DEPRESSURIZED TOWING TANK

Electrolysis was applied in the Depressurized Towing Tank using a wire grid as shown in Fig. 5.5. This grid was mounted at a distance of 1.6 meter in front of the propeller, as shown in Fig. 1.3. The wires were 0.3 mm in diameter and the current through each set of the wires was 0.2A in all conditions, so the strength of the current per unit length was always 0.4 A/m.

5.3.1. Bubble stream observations

The bubble stream from the electrolysis wires could be observed in the propeller position by using a light source nearly opposite to the camera. Examples of such observations are given in Fig. 5.6. The propeller has been replaced by a profile with a centimeter scale and the anode wire was at a larger distance from the cathode (7.5 cm) so only the bubble stream from the cathode wire is observed. The pressures given in Fig. 5.6 are the pressures at the wire.

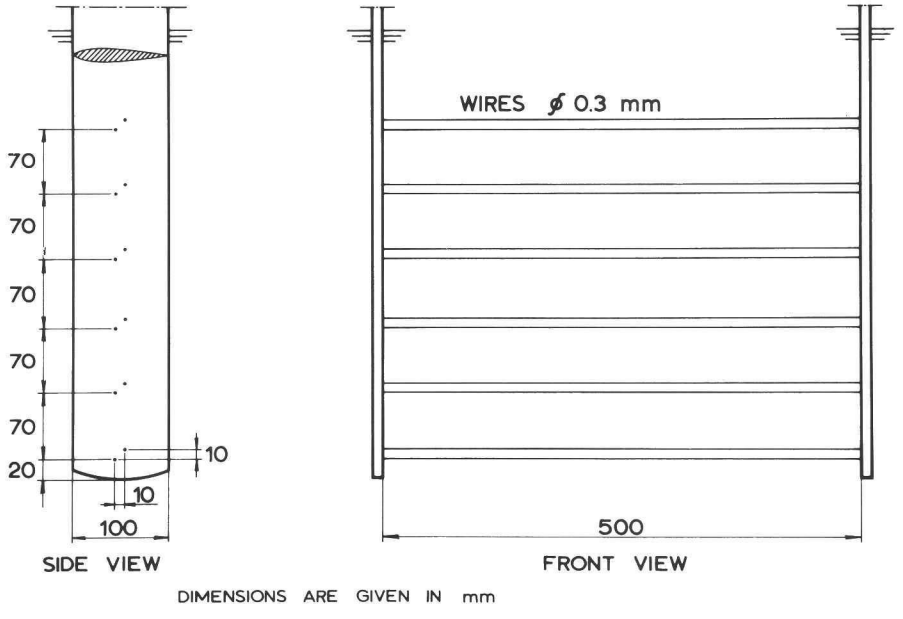

Fig. 5.5. Electrolysis grid used in the Depressurized Towing Tank.

a

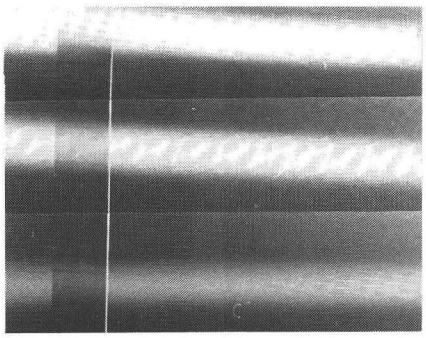

1 m/sec

2 m/sec

3 m/sec

Variation in velocity (80 mbar, 1.6 A/m)

b

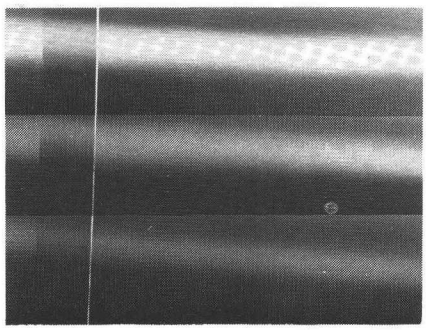

80 mbar

120 mbar

160 mbar

Variation in pressure (1 m/sec, 1A/m)

c

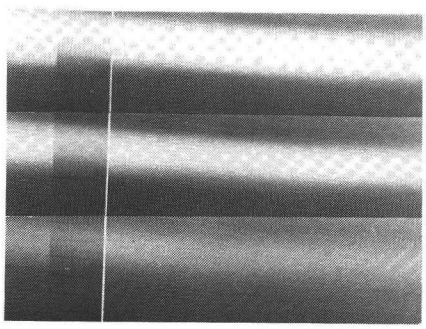

1.6 A/m

1.0 A/m

0.4 A/m

Variation in current (1 m/sec, 80 mbar)

Fig. 5.6. Observations of bubble streams in the Depressurized Towing Tank.

The bubbles reach the propeller position in sheets with a thickness of about 3 cm. An estimate of the width of the wake behind a cylinder is (e.g. Schlichting, 1968, p.692)

$$w = 1.14\ (x.C_D.d)^{\frac{1}{2}} \qquad (5.9)$$

with x the distance behind the wire, C_D the drag coefficient of the wire and d the wire diameter. In the range of Reynolds numbers used for the electrolysis wires (Re_D=300 to 1200) the drag coefficient is always nearly one and the wake at a distance of 1.6 m behind the 0.3 mm diameter wire is calculated from eq. 5.9 to be 25 mm. This is close to the observed thickness of the bubble stream, so it can be concluded from this estimate that the bubbles remain in the wake of the wire.

The highest free gas density in Fig. 5.6, at 1 m/sec, 80 mbar and 1.6 A/m corresponds with the free gas density of 16 A/m in Plate 5.4, which is very high. In this condition the largest bubbles will occur and these bubbles will rise to the surface at a velocity which is approximately given by Stokes' law (eq. 5.1). Variation of the velocity in Fig. 5.6 hardly affects the thickness of the bubble layer, and from this observation it can be inferred that the rise velocity is less than 0.5 cm/sec, which means that the maximum bubble size is below 100 μm in diameter. This is in accordance with the observation in Plate 5.4, that at a high gas production the largest bubbles were about 0.2 times the wire diameter, which is 60 μm in the case of Fig. 5.6.

5.3.2. Measurements with scattered laser light

Some efforts were made to measure the bubble spectrum behind an electrolysis grid by using the scattered laser light technique. These measurements were carried out by Keller (unpublished). The size range which could be measured in these tests was from 15 to 150 μm in diameter.

The measured spectrum without electrolysis is given in Fig. 5.7. The spectrum is expressed in the bubble number density, as defined by Gates (1977):

$$\text{number density} = \frac{\text{number of bubbles with diameters between } d_1 \text{ and } d_2}{(d_1 - d_2)} \qquad (5.10)$$

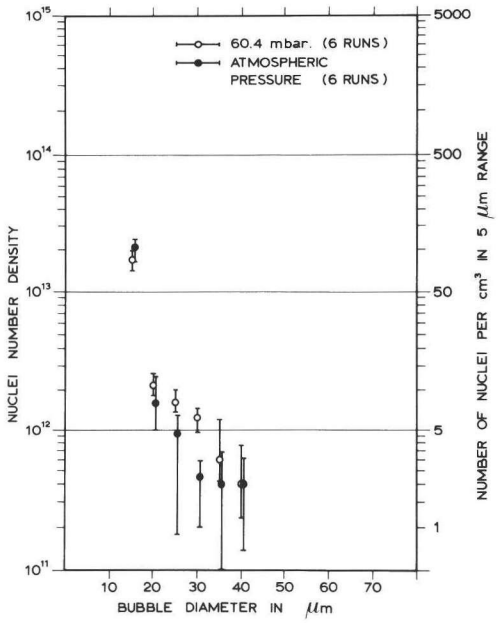

Fig. 5.7. Nuclei distributions in the Depressurized Towing Tank without electrolysis.

The measured bubble spectrum was not significantly affected by the tank pressure, as is shown in Fig. 5.7. This indicates that the laser light was scattered by solid particles. However, since the reflection properties of these particles are unknown the measured size distribution has little meaning. Anyhow no nuclei larger than 50 μm in diameter are present in the Depressurized Towing Tank.

Results of similar measurements behind the electrolysis grid are given in Fig. 5.8. The tank pressure was 60 mbar, while the measured position was 0.4 m below the water surface, so the pressure at the wire was 100 mbar, a situation close to the situation of Fig. 5.6c at 0.4 A/m.

From Fig. 5.8 the free gas ratio in the control volume can be calculated to be 1.96×10^{-6}, reduced to standard conditions (1013 mbar and $0^{o}C$). In this calculation the gas pressure in the bubbles was taken from eq. 5.3, so the surface tension was accounted for.

The total amount of gas, produced by both the cathode and anode per unit length is 6.96×10^{-7} m^3/sec reduced to standard conditions. At a flow

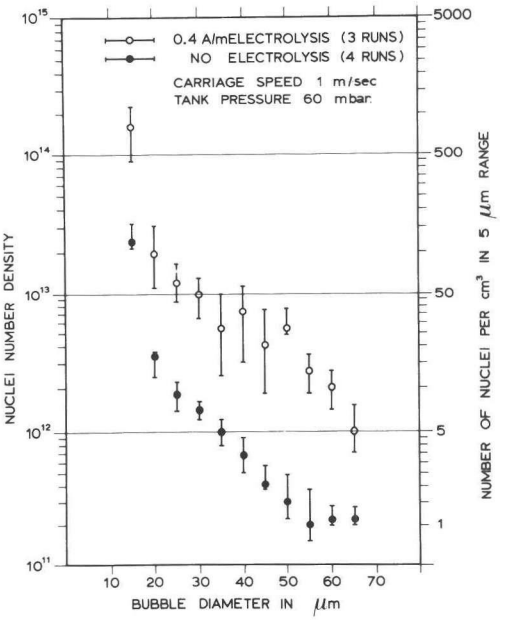

Fig. 5.8. A nuclei distribution in the Depressurized Towing Tank with electrolysis.

velocity of 1 m/sec and with a thickness of the bubble layer of 3 cm (from Fig. 5.6) this leads to a gas volume ratio in standard conditions of 2.3×10^{-6}, which is in good agreement with the value of 1.96×10^{-6} as calculated from the bubble spectrum.

The gas production in this case is comparable to the condition with 1.6 A/m in Plates 5.3 and 5.4. Still the maximum bubble size is about 70 μm. So also in cases with a low gas production the maximum bubble diameter seems to be about 0.2 times the wire diameter, which is larger than observed immediately behind the cathode wire. Possibly some amalgamation of small bubbles takes place during the time between bubble generation and measurement of the bubbles at the propeller location.

5.4. ELECTROLYSIS IN THE CAVITATION TUNNEL

Some measurements of the nuclei spectrum in the NSMB Large Cavitation Tunnel were reported by Arndt and Keller (1976). They measured nuclei with a diameter in the range of 10 to 150 μm. They found a strong dependency of the

total free gas volume on the rate of supersaturation in the test section. When the water in the test section was not saturated the free gas content was nearly independent of the total air content of the water. Typical numbers of bubbles in the range of 80-150 μm were found from 0.5/cm^3 at a low total air content of 7.5 ppm to 15/cm^3 at a high air content (12.5 ppm by weight) although the conditions were not completely given.

So at a low air content only a few bubbles with a diameter over 100 μm are present in the tunnel.

Application of electrolysis in a cavitation tunnel requires a higher current due to the higher tunnel velocity relative to that in a depressurized towing tank. Vibrations of the wires caused frequent breaking of the electrolysis wires, so a different arrangement was chosen.

A foil was mounted horizontally through the center of the test section, at a distance of 1.6 m in front of the propeller. On the upper side of the foil two 5 mm wide and 0,2 mm thick stainless steel strips were glued at 1 cm distance from each other. These strips were used as the electrodes.

In order to maintain a constant gas production at increasing velocities and pressures the current has to increase with V^3. Electrolysis in a cavitation tunnel therefore requires high currents. The maximum current which could be obtained in the described condition was 6 A/m. This was only effective at the minimum tunnel pressure at a low velocity.

Although the amount of gas, produced by electrolysis, is fairly small the combination of long exposure times together with a high current can produce dangerous amounts of gas. Electrolysis can therefore not be an appropriate means of bubble generation in a cavitation tunnel and other methods have to be investigated (see e.g. Albrecht and Bjorheden, 1975).

6. Experimental results with bubble cavitation

The influence of the boundary layer and of the nuclei content on bubble cavitation is investigated on propeller B. For this purpose electrolysis and roughness at the leading edge are applied and various Reynolds numbers are considered. The differences between the occurrence of bubble cavitation in the Depressurized Towing Tank and the Cavitation Tunnel are also investigated.

When the pressure gradient downstream of a low pressure region is moderate, the flow will remain attached to the surface when cavitation starts and bubble cavitation occurs. Bubble cavitation is considered to be highly erosive and model tests are often carried out to verify if no bubble cavitation occurs. It is therefore very important to simulate the inception of bubble cavitation properly on model scale.

Inception of bubble cavitation was investigated with propeller B. This propeller has thick blades with large cambers to avoid a low pressure peak at the leading edge.

In this section the experimental data are given. The implications of the observations are discussed in section 9.

6.1. PROPELLER B AT J=0.6 IN THE DEPRESSURIZED TOWING TANK

At an advance ratio of 0.6 the pressure distribution on the suction side of propeller B has no sharp peak at the leading edge. The minimum pressure occurs in the midchord region of the blade sections, as Fig. 2.13 shows. The calculated minimum pressure coefficients are plotted in Fig. 6.1.

The sectional minimum pressure coefficient has to be compared with the sectional cavitation index σ, as defined in eqs. 1.25 to 1.27. The propeller cavitation index σ_n (eq. 1.20) can be considered as a dimensionless expression for the pressure at the propeller shaft, so at one value of σ_n a radial distribution of σ can be calculated, as has been done in Fig. 6.1. The value

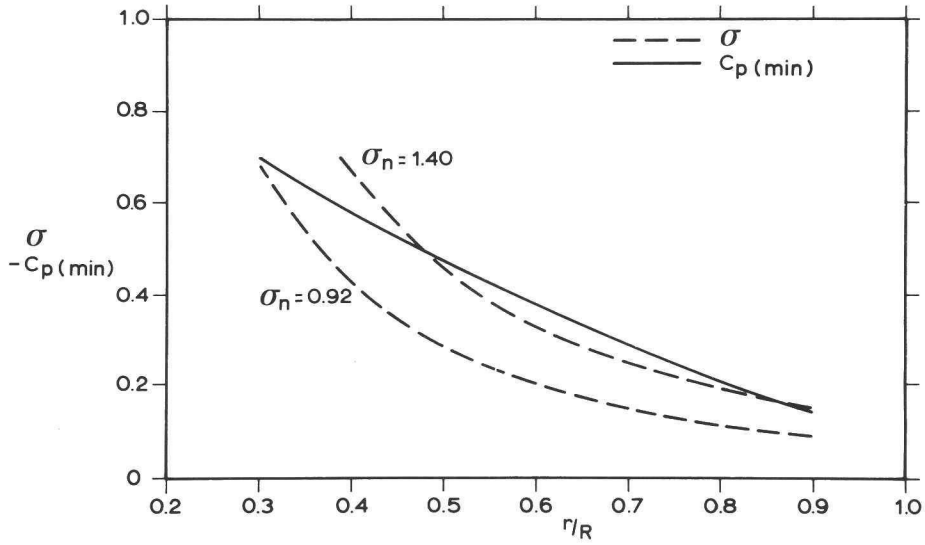

Fig. 6.1. Radial distribution of the calculated minimum pressure coefficients and of cavitation indices on propeller B at J=0.6.

of σ varies with the blade position, depending on the number of revolutions. The sectional cavitation index σ in Fig. 6.1 and similar Figures are always calculated for the blade in top position at a number of revolutions corresding to a Reynolds number $Re_n=1.1x10^6$.

The condition in which the observations were made, are given in dimensionless form by Re_n, J and σ_n. From these data the tank pressure, the number of revolutions and the advance velocity of the propeller can be found when the temperature is known, which was always about 10^oC in the Depressurized Towing Tank and 20^oC in the Cavitation Tunnel.

Observations were made with two blades smooth (blades 2 and 4) and with two blades roughened at the leading edge (blades 1 and 3). The observations in one condition were made during one run, electrolysis was applied in the second half of the run using a constant current of 0.4 A/m in all conditions. Twelve photographs of the whole propeller in different positions were taken during one run to verify if the cavitation was steady.

without electrolysis *with electrolysis*

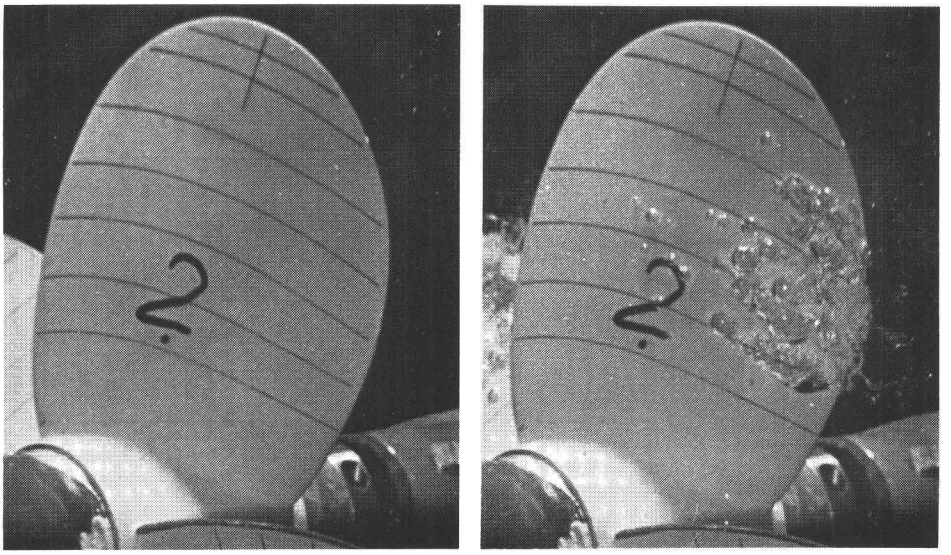

smooth

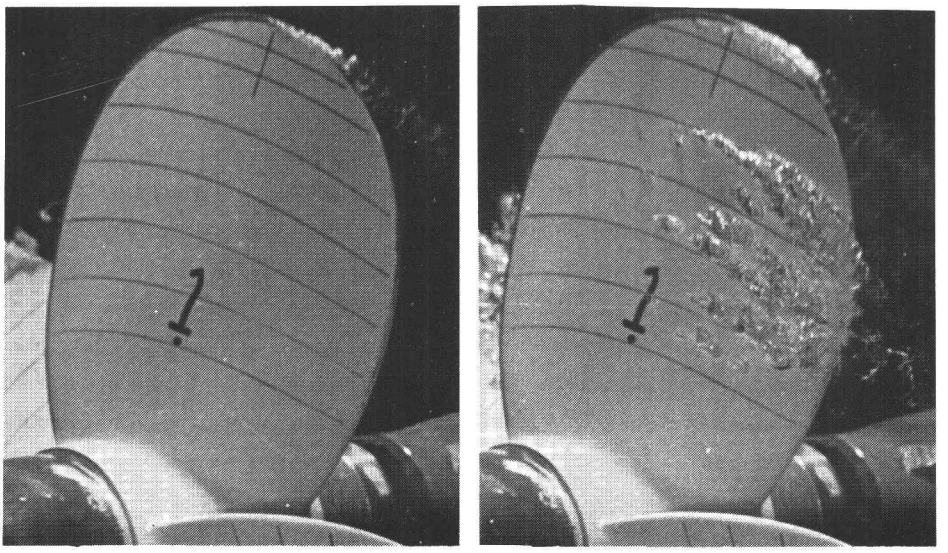

roughened at the leading edge

Fig. 6.2. Cavitation observations in the Depressurized Towing Tank on propeller B at J=0.6 (σ_n=0.92, Re_n=1.1x10^6).

Observations of the cavitation pattern on propeller B at σ_n=0.92 are shown in Fig. 6.2. At this low cavitation index the minimum pressure over the whole radius is lower than the vapor pressure, as Fig. 6.1 shows, because $-C_p(\min)$ is always larger than σ. Still no cavitation occurs on the smooth blade in Fig. 6.2. This may be explained by a lack of nuclei of adequate size and the maximum bubble size present in the tank water can be calculated from this observation as follows.

The minimum radius of nuclei needed for cavitation inception can be calculated. From eq. 1.3 it is found that for inception it is necessary that

$$p(\min) < p_v - \frac{4s}{3R_{crit}} \tag{6.1}$$

which can be rewritten as

$$R_{crit} > \frac{-8s}{3\rho V^2(\sigma + C_p(\min))} \tag{6.2}$$

This minimum critical radius is plotted in Fig. 6.3, using the difference between σ and $C_p(\min)$ from Fig. 6.1. The corresponding initial bubble radius

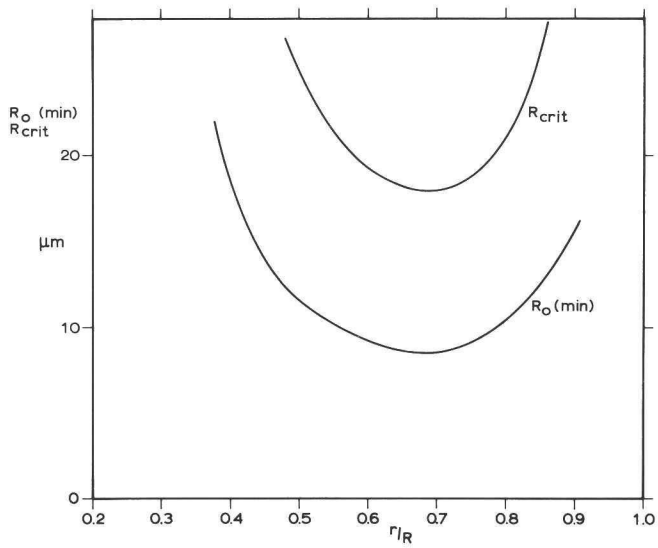

Fig. 6.3. Critical bubble radius and minimum bubble radius needed for cavitation inception in the condition of Fig. 6.2.

R_o in the incoming flow can be found from eq. 1.2 with

$$K = \frac{2}{3} s R_{crit}^2 \qquad (6.3)$$

The resulting values of R_o are also plotted in Fig. 6.3 and bubbles with a radius of less than 10 μm or a diameter of less than 20 μm are necessary for inception at r=0.7R. At other radii larger bubbles are needed, so the nuclei in the tank water were smaller than 20 μm in diameter.

Electrolysis has a drastic effect. Many bubbles occur between r=0.45R and r=0.85R. The radial extent is still somewhat less than would follow from Fig. 6.1. Apart from errors in the calculation method this could mean that the size of the electrolysis bubbles is limited. According to Fig. 6.3 a maximum bubble size of 30 μm in diameter would restrict cavitation to $0.45<r/R<0.9$. This bubble size is 10% of the wire diameter which is in the range found in section 5 for these conditions.

The roughened blade without electrolysis in Fig. 6.2 is also free from bubble cavitation. On the smooth blade the boundary layer was laminar until midchord, as Plate 3.8 shows. With roughness the boundary layer, in this case, was on the verge of being fully turbulent. The paint pattern was similar as in Plate 3.14 at the high Reynolds number. Still this change of the boundary layer had no influence on the cavitation. The boundary layer has apparently no effect on bubble cavitation, as could be expected.

However, this condition appeared to be rather critical. An increase of the Reynolds number, a slight decrease of the cavitation index and even some disturbance of the tank water (caused when the tank water was deaerated the night before) each did cause bubble cavitation on the roughened blade without electrolysis. This phenomenon will also be observed in other conditions later on. Roughness also creates a short tip vortex. This will be discussed in section 8.

Somewhat confusing are the observations in the same condition at a higher Reynolds number, as shown in Fig. 6.4. In this condition the electrolysis wires were cavitating, generating large amounts of bubbles, even without electrolysis. However, those bubbles did not create cavitation. The mechanism causing this is not clear and we will pay further attention to it in section 9.

without electrolysis *with electrolysis*

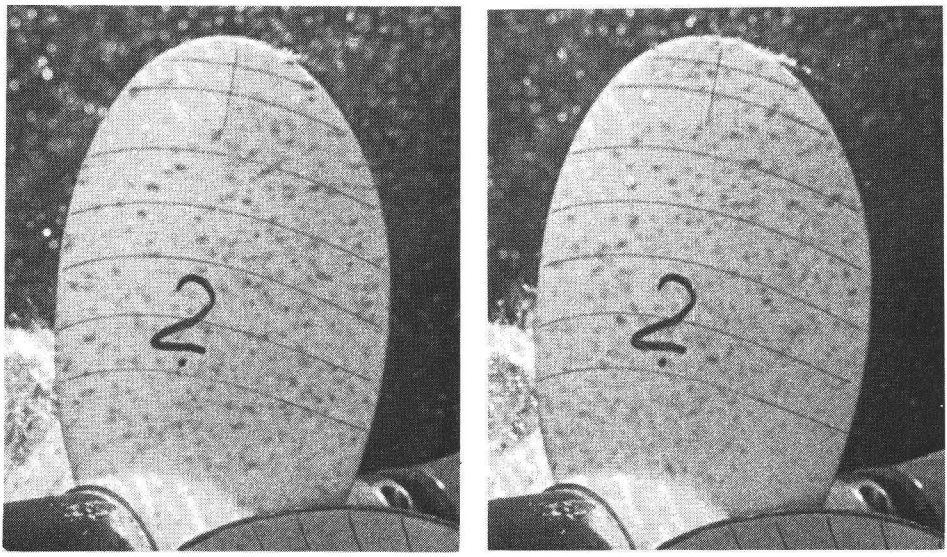

smooth

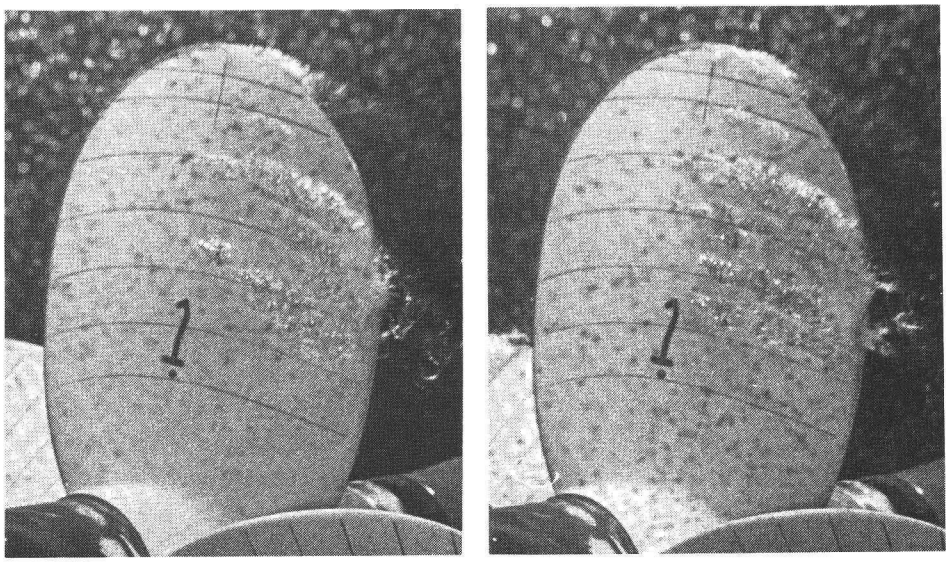

roughened at the leading edge

Fig. 6.4. Cavitation observations in the Depressurized Towing Tank on propeller B at J=0.6 (σ_n=0.92, Re_n=1.7x10^6).

On the roughened blade bubble cavitation does occur. The roughness apparently generates nuclei itself, as was also observed incidentally by Arndt and Ippen (1968). A minimum roughness height relative to the boundary layer thickness is apparently necessary for this since it did not happen in Fig. 6.2. The total air content in the tank was 15.2 ppm by weight and at the low tank pressure the water was therefore highly supersaturated, which is an essential condition for the generation of nuclei, as will be shown later on.

Electrolysis was ineffective on the smooth blade. This may be caused by the fact that the wires were cavitating, but since this was systematically found at higher tank pressures it is attributed to an inadequate maximum bubble size of the electrolysis bubbles. The gas production parameter π_1 (eq. 5.5) varies approximately with Re^{-3} whereas the critical bubble radius (eq. 6.2) varies with Re^{-2}. The maximum bubble size of the electrolysis bubbles is related with the gas production parameter and at a constant current the maximum bubble size can become too small with increasing Reynolds number.

When the maximum bubble size generated by electrolysis is in the range of the minimum bubble size needed for cavitation inception, the appearance of the bubble cavitation becomes strongly dependent on the electrolysis current, as is shown in Plate 6.5. The blade in Plate 6.5 is smooth and the condition is similar as in Fig. 6.2., but at a somewhat higher pressure.

The maximum size of the electrolysis bubbles at a current of 0.4 A/m is apparently about the minimum radius needed for inception, which can be calculated to be 10 μm at r=0.7R in a similar way as in Fig. 6.3. So at this pressure the maximum size of the electrolysis bubbles is about 20 μm in diameter.

An increase of the current, and thus of the gas production parameter, increases the maximum bubble size, until at 2.0 A/m a cavitation extent is reached similar as in Fig. 6.2, for which bubbles larger than 30 μm are required.

An increase of the gas production therefore increases the maximum bubble size, as was also found in Plate 5.4 for higher values of the gas production parameter.

It can also be seen from Plate 6.5 that an increase of the electrolysis

current increases the number of bubbles which become unstable. This increase in the number of bubble cavities reduces their maximum size. Large isolated cavitation bubbles are an indication for a lack of nuclei of adequate size.

6.2. PROPELLER B AT J=0.6 IN THE CAVITATION TUNNEL

Observations on propeller B were made in the Cavitation Tunnel at the same cavitation number as in Figs. 6.2 and 6.4. A higher Reynolds number was necessary because of the higher minimum pressure which can be reached in this facility. The observations are shown in Plate 6.6.

The total air content of the tunnel water was reduced to 6.5 ppm by weight. The test section was speckled with visible bubbles at this low tunnel pressure. Still only incidentally a large bubble cavity occurs on the smooth blade, as Plate 6.6 shows. The critical radius in this condition, needed for cavitation inception at r=0.7R, can be found from eq. 6.2 to be only about 8 μm. Measurements with the scattered laser technique indicated large amounts of nuclei of this size (Arndt and Keller, 1976). These were apparently solid particles, similar as in the Depressurized Towing Tank (Fig. 5.7) and surprisingly the Cavitation Tunnel contains only very small free gas bubbles in this condition.

Instead of bubble cavitation there are cavitating spots both on the smooth and on the roughened blades of Plate 6.6. This is a familiar type of cavitation. It is called spot cavitation because it originates on a fixed spot on the blade, as is e.g. the case on blade 4. The spot cavity on blade 1 has a less sharp point an reveals the origin of the spot: small bubbles, expanding and coalescing downstream. These bubbles originate from a surface imperfection and this imperfection can be located far upstream of the beginning of the spot. A decrease of the pressure in such a case moves the beginning of the spot towards the surface imperfections.

The roughness elements at the leading edge do, however not generate nuclei, contrary to what happened in Fig. 6.4. The Reynolds number in Plate 6.6 is higher than in Fig. 6.4 so the roughness height relative to the boundary layer thickness is larger. However, the water at the roughness elements at the leading edge was not saturated. (The water in the test section was nearly saturated, but the roughness elements are in a region with a higher

pressure). Apparently it requires both a minimum roughness height and locally supersaturated water for a roughness element to generate free gas bubbles.

Application of electrolysis in this condition in the Cavitation Tunnel causes some bubble cavitation. The large size of the bubble cavities, especially on blade 4 of Plate 6.6, indicates that the pressure on the blades is below the vapor pressure and that only few nuclei of adequate size are present. At this tunnel speed and pressure the maximum possible current of 6 A/m was necessary to observe any effect. At this current the maximum bubble size is calculated to be about 20 μm in diameter. At higher velocities or pressures electrolysis in the cavitation tunnel had no effect, similarly as in the Depressurized Towing Tank.

Arndt and Keller (1976) measured a rapid increase of the free gas content in the test section when the water in the test section was supersaturated. To obtain this the total air contents of the tunnel water was increased to 12.3 ppm. An abundant amount of gas bubbles was present in the test section in the same condition as in Plate 6.6, which impaired the visibility. In this section bubble cavitation appeared similar as in the Depressurized Towing Tank when electrolysis was applied, as is shown in Fig. 6.7. This Figure illustrates the profound effect the total air content in the tunnel can have on bubble cavitation.

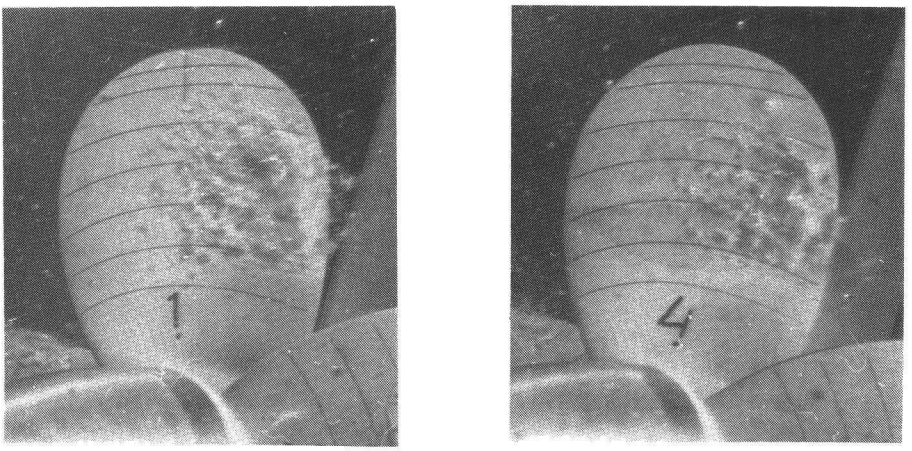

roughened *smooth*

Fig. 6.7. Cavitation observations in the Cavitation Tunnel with a high total air content. Propeller B at J=0.6 (σ_n=0.92, Re_n=2.11x10^6).

6.3. INCEPTION MEASUREMENTS ON PROPELLER B AT J=0.6.

The foregoing observations were made in a condition beyond the inception condition of the propeller. At inception only a few small cavities are formed, which do not interact with the pressure distribution. Such a condition can only be obtained when sufficient nuclei are present. Observations of cavitation inception were made in various conditions and the results are given in Tabel 6.1.

Facility	Total air content	Re_n	σ_i
CT	5.5 ppm by weight	2.11×10^6	1.1
CT	12.3 ppm by weight	2.11×10^6	1.3
DTT	Electrolysis 2 A/m	1.1×10^6	1.4

Table 6.1. Observed inception of bubble cavitation on propeller B at J=0.6.

The highest inception index was measured in the Depressurized Towing Tank with the maximum electrolysis current available. From Fig. 6.1 it can be seen that at this cavitation index the minimum pressure coefficient is close to the sectional cavitation index, so the observed inception index agrees with the calculations.

6.4. PROPELLER B AT J=0.4 IN THE DEPRESSURIZED TOWING TANK

At a heavier propeller loading the pressure distribution on the suction side of propeller B becomes very flat with a small low pressure peak at the leading edge, as Fig. 2.14 shows. This is a common type of pressure distribution, especially in naval applications, because it is the condition of maximum lift just before cavitation inception. Such a pressure distribution can cause special scale effects.

The calculated minimum pressure coefficients are given in Fig. 6.8, both for midchord and for the leading edge.

The small pressure peak at the leading edge does not cause laminar separation and the boundary layer remains laminar, as Plate 3.11 shows.

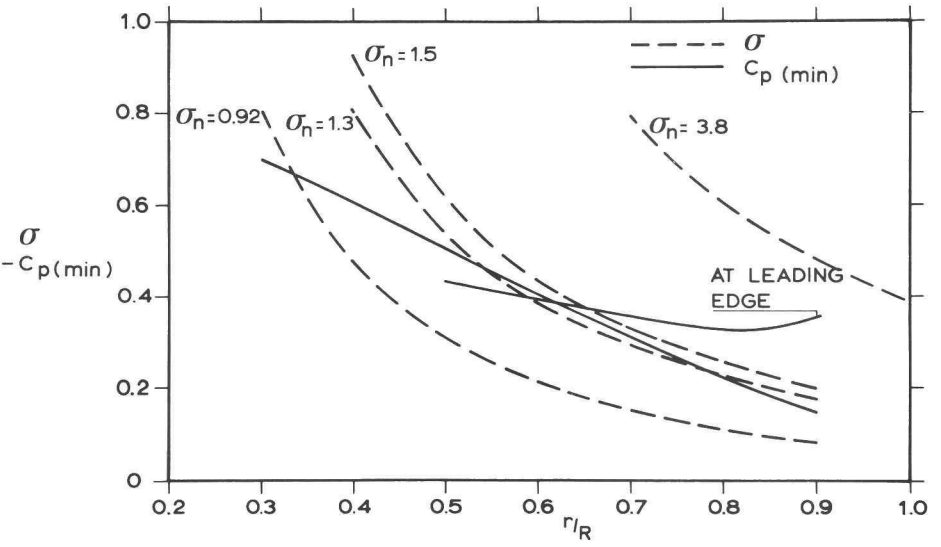

Fig. 6.8. Radial distribution of the calculated minimum pressure coefficients and of cavitation indices on propeller B at J=0.4.

Observations in the Depressurized Towing Tank are shown in Fig. 6.9. Although according to Fig. 6.8 the minimum pressure over the whole radius both at midchord and at the leading edge is far below the vapor pressure, no cavitation at all is found on the smooth blade without electrolysis. Only a few, large bubble cavities reveal that the pressure is indeed below the vapor pressure.

Electrolysis restores bubble cavitation in the midchord region. Two rows of bubble cavitation are present. This is caused by the layers in which the bubbles arrive in the propeller plane. Although enough nuclei are available no sheet cavity at the leading edge occurs. This is systematically found when the boundary layer in the region of the minimum pressure peak is laminar, as will be demonstrated in section 7.

On the roughened blade in Fig. 6.9 sheet cavitation occurs, although only from r=0.6R instead of from about r=0.5R as would follow from Fig. 6.8. At r<0.6R the roughness elements still generate bubbles and these bubbles create a fine screen of bubble cavitation downstream on the blade section. This screen has a finer structure than on the smooth blade with electrolysis,

without electrolysis *with electrolysis*

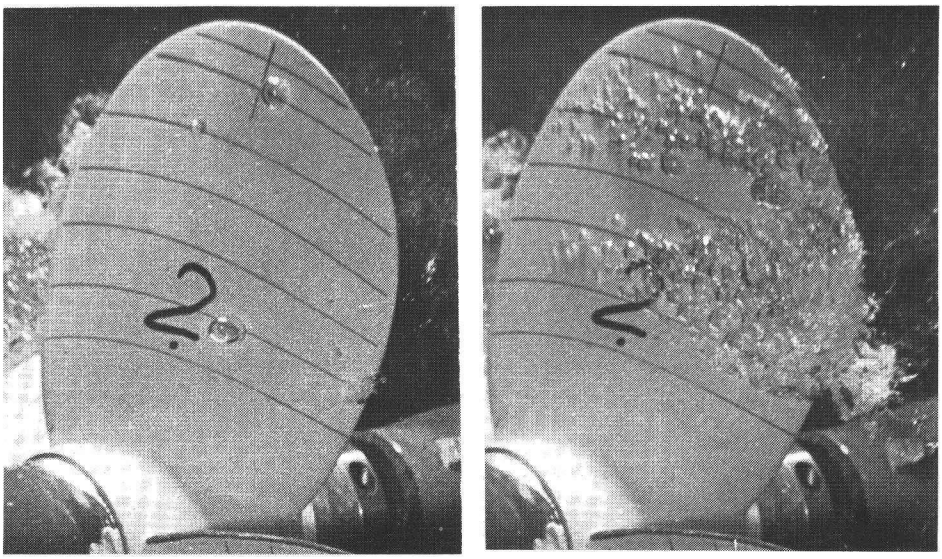

smooth

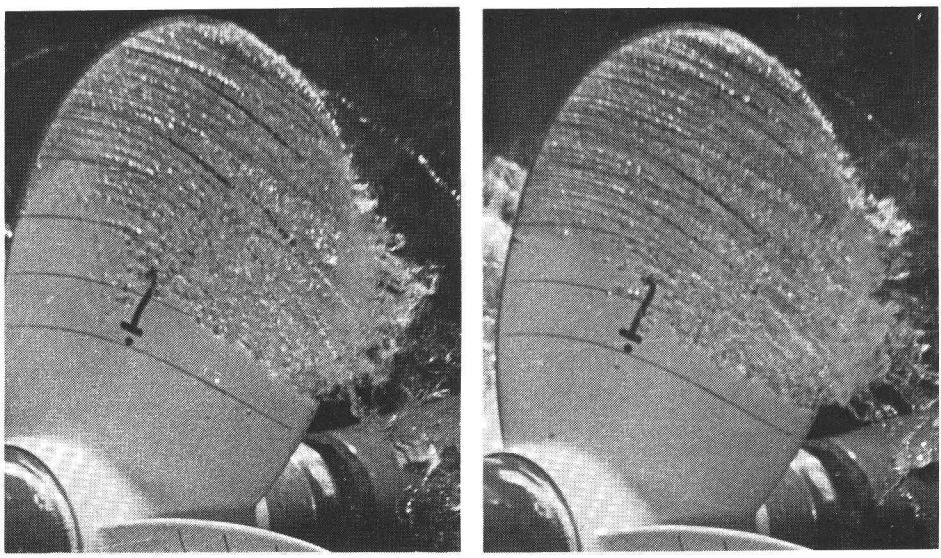

roughened at the leading edge

Fig. 6.9. Cavitation observations in the Depressurized Towing Tank on propeller B at J=0.4 (σ_n=0.92, Re_n=1.1x10^6).

which shows the influence of the nuclei size distribution and of the number of nuclei on bubble cavitation. Electrolysis has no additional effect on the roughened blade since enough nuclei are already available.

The difference between the smooth blade and the roughened blade without electrolysis is very large, which is typical for propellers with a flat pressure distribution at the suction side of the blades.

6.5. PROPELLER B AT J=0.4 IN THE CAVITATION TUNNEL

Observations of propeller B in the Cavitation Tunnel are shown in Plate 6.10. Although the Reynolds number is twice that of Fig. 6.9 the resemblance is striking, which illustrates that an increase in Reynolds number not necessarily decreases scale effects on cavitation inception.

The total air contents of the tunnel water was 5.2 ppm by weight and again it is found that at this velocity and pressure very few nuclei of adequate size are available in the test section. The large bubble cavity on the smooth blade illustrates the low pressure on the blade. Huge isolated bubble cavities are typical for tests in a cavitation tunnel with a very low nuclei content.

Electrolysis has only a very small effect because the maximum obtainable current was too low to create sufficient nuclei, but it indicates that an increase in nuclei increases the bubble cavitation.

Roughness at the leading edge has the same effect as in the Depressurized Towing Tank. Contrary to the condition at J=0.6 the roughness particles are now in a low pressure region where the water is supersaturated, so they can generate nuclei.

The only effect of the increased Reynolds number in the Cavitation Tunnel compared to that in the Depressurized Towing Tank (Fig. 6.9) is the occurrence of spots of cavitation on the smooth blade, apparently caused by surface irregularities on the leading edge which become effective at a higher Reynolds number. During some tests the number of streaks increased due to small particles which attached themselves to the leading edge. At the location of these spots paint tests show turbulent streaks through a laminar region, as is the case e.g. in Plate 3.20.

When the Reynolds number is further increased the number of spots on the smooth blade increases as well as is shown in Plate 6.12. In this Plate the cavitation index is higher than in Plate 6.10 and the relation between the spots at the leading edge and the bubble cavitation at midchord is clearly shown.

On the roughened blade a sheet cavity at the leading edge is present in Plate 6.12 and the chordwise extent of this sheet is much longer than the length of the isolated spots on the smooth blade, especially near the tip. This is also found on propeller S and will be discussed in section 7.

When the total air contents of the water in the Cavitation Tunnel was raised to 12.3 ppm by weight, similar as in Fig. 6.7, bubble cavitation appeared again, as Fig. 6.11 shows. The conditions in Fig. 6.11 are the same as in Plate 6.10. Even at this extremely high free air content no sheet cavitation occurs at the leading edge, and this phenomenon will be examined in section 7.

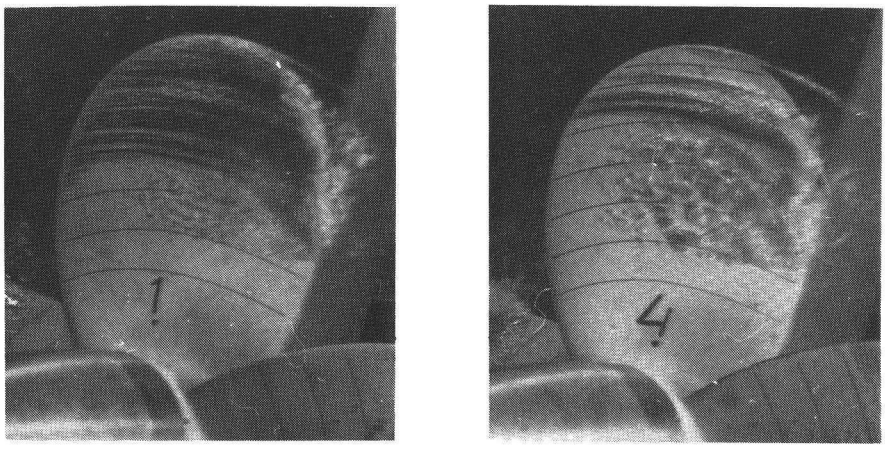

roughened *smooth*

Fig. 6.11. Cavitation observations in the Cavitation Tunnel with a high total air content. Propeller B at J=0.4 (σ_n=0.92, Re_n=2.11x10^6).

6.6. INCEPTION MEASUREMENTS ON PROPELLER B AT J=0.4

Inception of bubble cavitation on the smooth blade at the high total air contents of 12.3 ppm was measured in the Cavitation Tunnel. Inception of bubble cavitation on the smooth blade in the condition of Fig. 6.11 was called at σ_n=1.3. Fig. 6.8 shows that this agrees with the calculated minimum pressure coefficient.

The agreement between the calculated and the observed inception of bubble cavitation supports the calculated minimum pressure coefficient, which is important because the determination of the critical bubble radius in sections 6.1 and 6.2 depends on this pressure coefficient.

Inception of sheet cavitation near the tip was called on the roughened blade in the conditions of Fig. 6.11 at σ_n=3.8 and Fig. 6.8 shows that this is also in agreement with the calculated minimum pressure coefficient near the tip.

7. Experimental results with sheet cavitation

The influence of the boundary layer and the nuclei content on inception of sheet cavitation is investigated on propeller S, using the same means as on propeller B: electrolysis, roughness of the leading edge and variation of the Reynolds number in both the Depressurized Towing Tank and the Cavitation Tunnel.

When there is a strong pressure gradient behind a low pressure peak the flow will separate from the surface at cavitation inception and a sheet cavity occurs. This type of cavitation is common on ship propellers because their blades have a low chord-thickness ratio for efficiency reasons.

Inception of sheet cavitation was investigated with propeller S, which has thin blades and small cambers. The experimental data are given in this section, a discussion on the implications of the observations will be given in section 9.

7.1. PROPELLER S AT J=0.4 IN THE DEPRESSURIZED TOWING TANK

At an advance ratio of J=0.4 the pressure distribution on the suction side of propeller S has a very sharp peak at the leading edge, as was shown in Fig. 2.16. The calculated minimum pressure coefficient near the leading edge is given in Fig. 7.1 together with the radial distribution of the sectional cavitation index σ at different tank or tunnel pressures, which are expressed in the propeller cavitation index σ_n.

To illustrate the sharpness of the low pressure peak the calculated pressure coefficient at 1% of the chord is given in Fig. 7.1. The low pressure peak occurs over about 1% of the chord from leading edge only. The accuracy of the calculated minimum pressure is low because an arbitrary change of the helical pitch in the calculations changed the minimum pressure

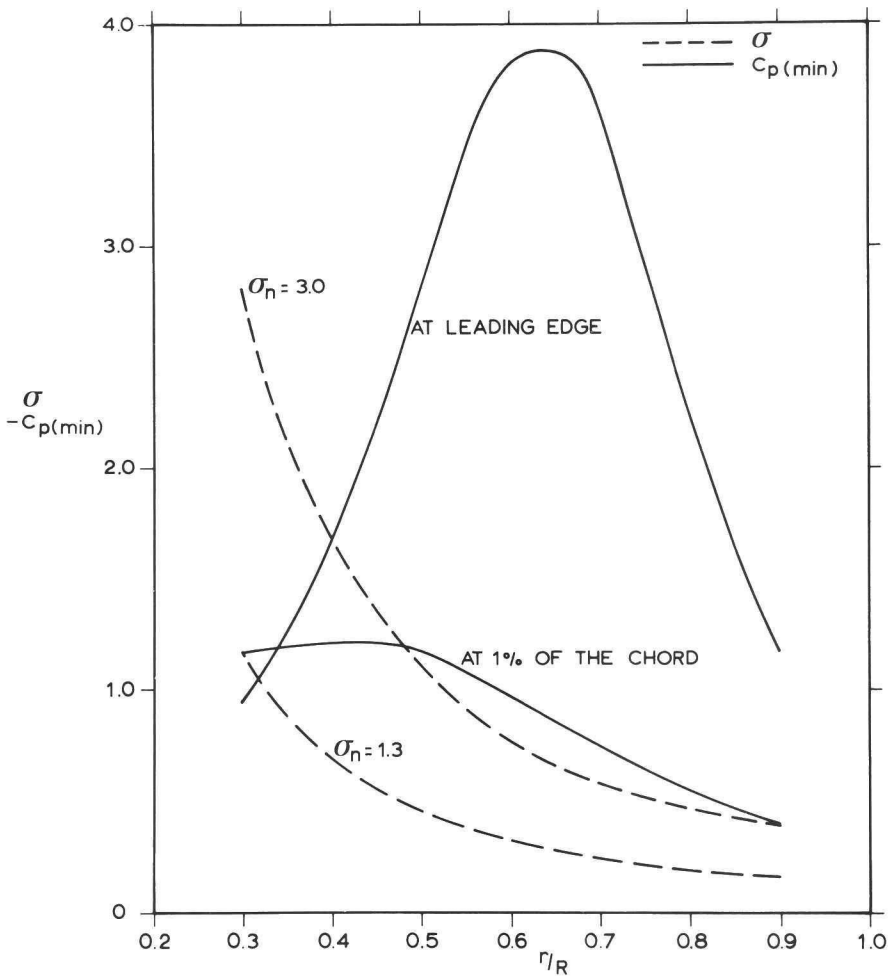

Fig. 7.1. Radial distribution of the calculated minimum pressure coefficients and cavitation indices on propeller S at J=0.6.

coefficient by as much as 25%, as was shown in Fig. 2.6.

The sharp pressure peak causes a laminar separation bubble from the hub to about 0.7R, as Plate 3.15 shows. The occurrence of this large separation bubble will also affect the pressure distribution and the minimum pressure coefficient. Between 0.7R and 0.9R a region of laminar flow with turbulent streaks occurs on blade 2 of Plate 3.15. At r>0.9R a very short separation bubble occurs.

without electrolysis *with electrolysis*

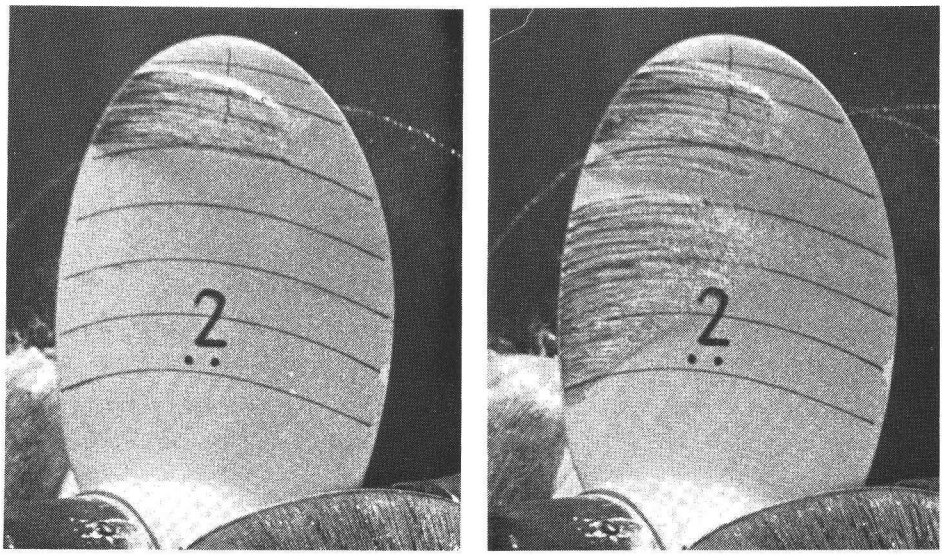

smooth

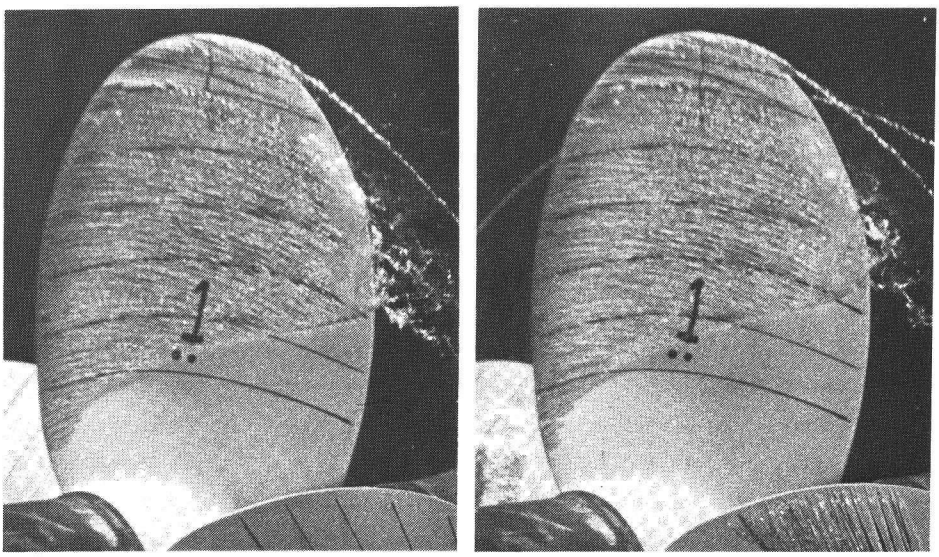

roughened at the leading edge

Fig. 7.2. Cavitation observations in the Depressurized Towing Tank on propeller S at J=0.4 (σ_n=1.3, Re_n=1.1x10^6).

Observations of the cavitating propeller S in the Depressurized Towing Tank are given in Fig. 7.2. Blades 1 and 3 are smooth, blades 2 and 4 are roughened at the leading edge with 60 μm carborundum. The observations were made in the same manner as those of propeller B (section 6.1).

The various boundary layer regions are reflected in the cavitation pattern of Fig. 7.2. In the tip region of the smooth blade a sheet is always present, but in the region of the pronounced separation bubble at inner radii the sheet on the smooth blade is absent without electrolysis. Although inception of sheet cavitation is generally found to be independent of the nuclei content this observation shows that a lack of nuclei can inhibit inception of sheet cavitation in a region with a laminar separation bubble. In additional photographs in the condition of Fig. 7.2 the sheet at inner radii was present, indicating that the nuclei contents of the water was about sufficient for cavitation inception. An increase of the Reynolds number, a decrease of the cavitation index and even a disturbance of the tank water (when the tank was deaerated the night before), each caused that the sheet at inner radii was present on the smooth blade without electrolysis. The difference between σ and $-C_p$ at 1% of the chord is already as much as 0.66 at r=0.6R, which implies a critical bubble radius of 5 μm. So only very small nuclei were present when cavitation inception was inhibited.

There is a distinct gap in the sheet cavity at about 0.75R. This gap is very persistent. Neither an increase of the Reynolds number nor a decrease of the cavitation index removed it. Electrolysis was also ineffective. The gap coincides with signs of laminar flow on blade 2, as shown in Plate 3.15, which indicates that laminar boundary layer flow inhibits cavitation inception.

Roughness at the leading edge removes the gap and a smooth sheet cavity occurs at the leading edge independent of electrolysis.

The chordwise extent of this sheet is larger than on the smooth blade. This is attributed to the presence of the gap in the sheet on the smooth blade rather than to the roughness at the leading edge because this difference decreased or disappeared both at higher and at lower pressures, when the influence of the gap is smaller, as will be shown below.

Observations at the same loading and Reynolds number, but at a lower cavitation index, are given in Fig. 7.3. This Figure shows that the gap in

without electrolysis *with electrolysis*

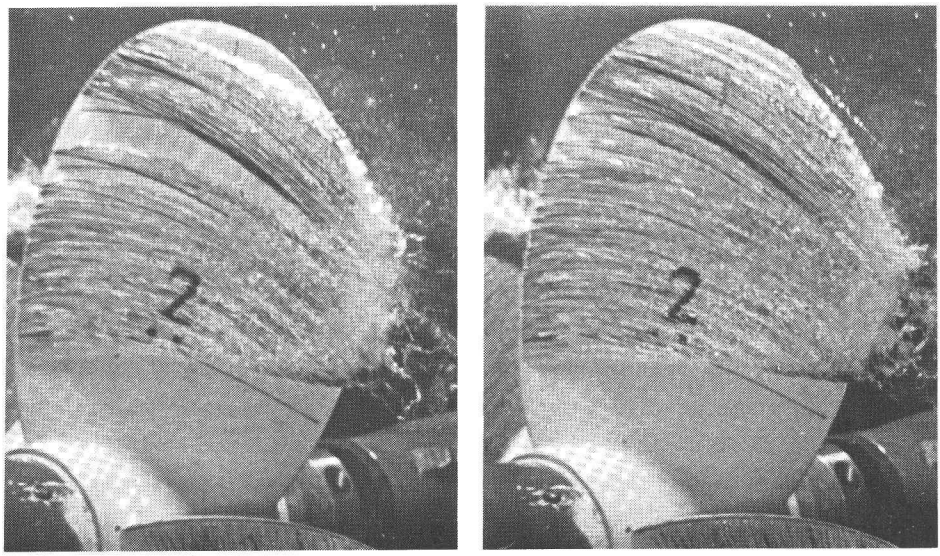

smooth

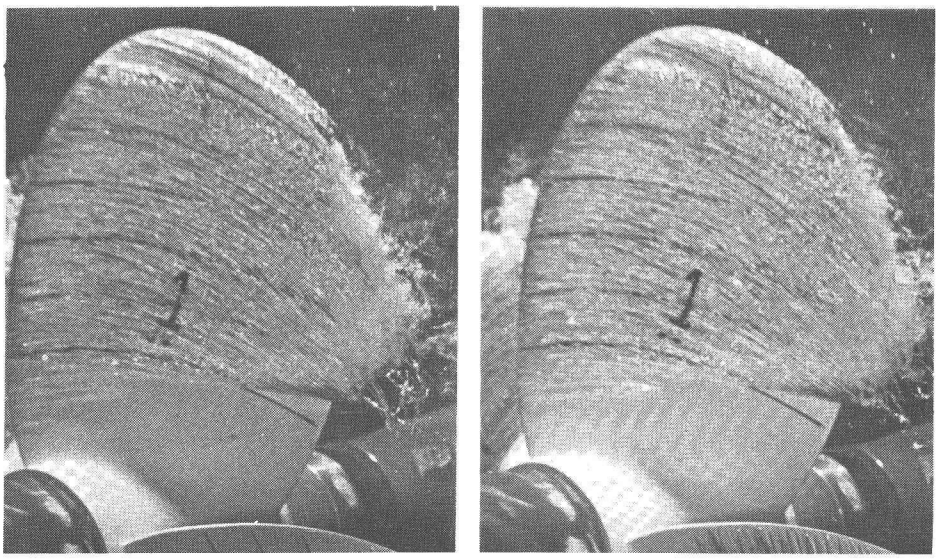

roughened at the leading edge

Fig. 7.3. Cavitation observations in the Depressurized Towing Tank on propeller S at J=0.4 (σ_n=0,92, Re_n=1.1x10^6).

the sheet of the smooth blade persists even in this extreme condition. It also shows that the difference between the cavity length of the smooth and the roughened blade has disappeared. Electrolysis does still not close the gap on the smooth blade, but causes inception of two spot cavities in the gap.

The sheet in Fig. 7.3 has a spot-like appearance at the leading edge, although the boundary layer in the non-cavitating condition exhibits a pronounced laminar separation bubble, which is generally related with a smooth glassy sheet. Apparently the cavity itself affects the pressure distribution and causes a strongly three-dimensional type of separation, similar as the patches of cavitation found by Arakeri (1973) on a headform.

The difference between the roughened and the smooth blade at higher pressures is shown in Fig. 7.4. At inner radii there is not much difference, although the sheet on the roughened blade extends slightly further inwards. The gap on the smooth blade between $0.72<r/R<0.83$ remains, although at $\sigma_n=2.0$ two spots are present in the gap. The sheet near the tip is reduced to a patch of cavitation. The cavity on the roughened blade reflects the calculated pressure distribution better.

The observations in Fig. 7.4 (made when the tank water was disturbed by deaerating the tank the night before) show that the sheet at inner radii remained up to $\sigma_n=2.2$.

7.2. PROPELLER S AT J=0.4 IN THE CAVITATION TUNNEL

The behaviour of propeller S at J=0.4 in the cavitation tunnel is similar to that in the Depressurized Towing Tank, as Plate 7.5 shows. The Reynolds number in the tunnel was higher because the lowest attainable pressure in the tunnel was higher. On Plate 7.5 some additional details can be distinguished.

Very characteristic is the shape and the structure of the sheet at $0.35<r/R<0.7$. There is a dark region with tangential streaks on its surface. At the end of this sheet a thin triangular region exists with a bubbly surface, while sometimes regular dark stripes in radial direction were visible, bearing resemblance with Tollmin-Schlichting waves. There is a smooth end of the sheet cavity when the length increases with increasing radius. When the length of the cavity is constant or decreases, a cloudy entrainment of

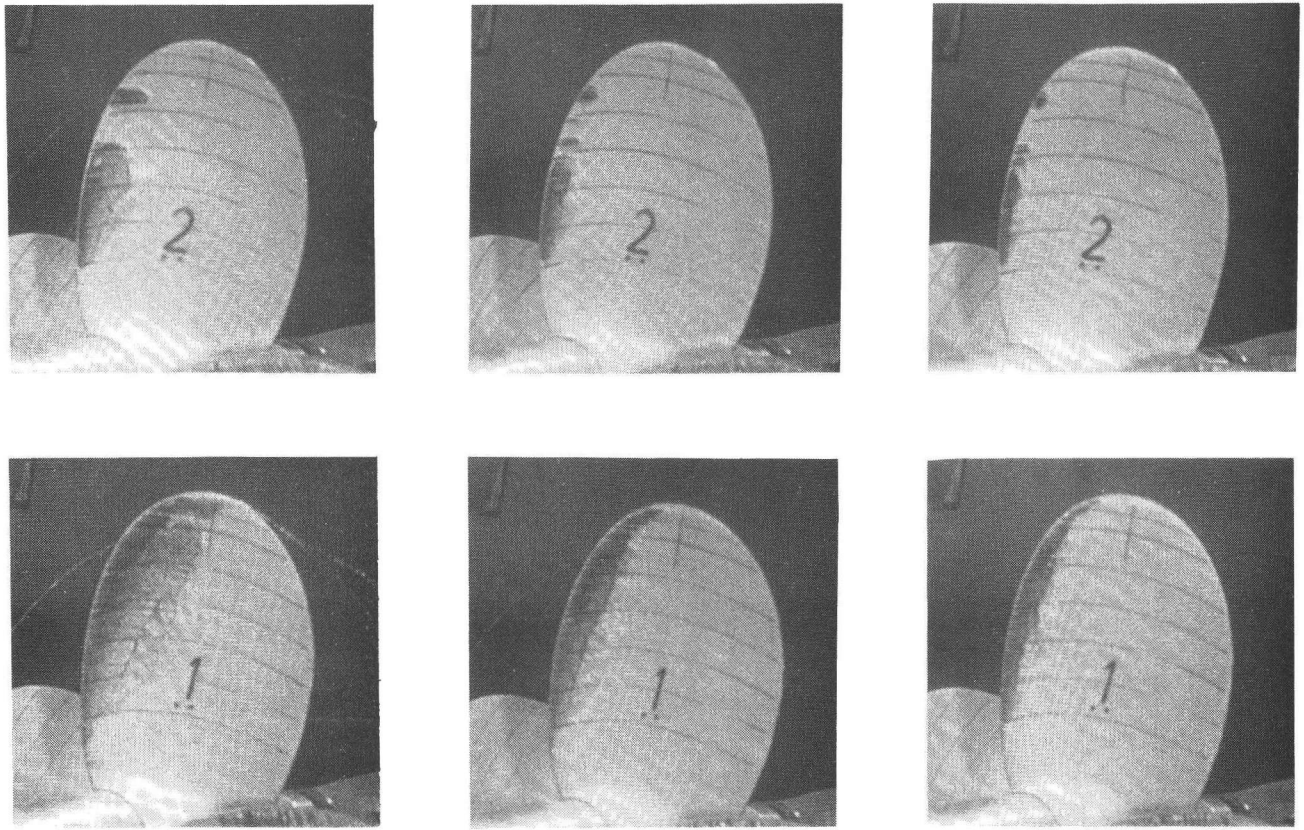

σ_n=1.7 σ_n=2.0 σ_n=2.2

Blade 1 roughened at the leading edge, Blade 2 smooth, Re_n=1.1x10^6.

Fig. 7.4. Differences between smooth and roughened blades with limited cavitation (Propeller S at J=0.4, Re_n=1.1x10^6).

vapor bubbles occurs, which is generally considered as erosive. The structure of the sheet is strongly three-dimensional and a sectional description of the sheet cavity will therefore be inadequate.

The leading edge of the sheet on the smooth blade is still finger-like, but the fingers are narrow and close together.

Two types of spot cavities appear in the gap on the smooth blade as shown in Plate 7.5. The wider spots are clearly caused by regions of laminar separation, which follows from the shape of the spots near the leading edge. The narrow spots are caused by surface imperfections.

Between 0.7R and the tip the cavity on the smooth blade of Plate 7.5 differs from that in Fig. 7.2. The gap is wider, with more spot cavities, and a sheet is located at the tip. This may be caused by a slightly different loading distribution due to tunnel wall effects and illustrates the sensitivity of regions near laminar separation for variations in loading. The roughened blade indicates a somewhat heavier loading in the Towing Tank than in the Cavitation Tunnel.

Application of roughness at the leading edge removes the gap, but does not change the characteristics of the sheet as described above. The cavity length on the roughened blade is again somewhat longer than on the smooth blade.

The cavitation pattern at a higher cavitation index (σ_n=2.2) is shown in Plate 7.6. This condition is comparable to that in Fig. 7.4, although tunnel wall effects might have caused a difference in propeller loading, while the Reynolds number is also higher. In Plate 7.6 the propeller loading seems to be somewhat higher than in Fig. 7.4: the sheet is somewhat longer and there are more patches of cavitation on the smooth blade at outer radii. Plate 7.6 shows again that the roughness at the leading edge does not affect the cavity at inner radii. The chordwise length of the patches of cavitation on the smooth blade is clearly less than of the sheet on the roughened blade. The cavity on the roughened blade correctly represents the calculated pressure distribution.

7.3. PROPELLER S AT J=0.6 IN THE DEPRESSURIZED TOWING TANK

In the foregoing observations it was systematically found that sheet cavitation was absent if the boundary layer in the low pressure region at the leading edge was laminar without separation. On propeller B at J=0.4 the sheet cavity could only be created by roughness at the leading edge (Plate 6.10, Fig. 6.9). On Propeller S at J=0.4 a gap in the sheet cavity occurred whenever there were regions of laminar flow without separation (Plate 7.5, Figs. 7.2 and 7.3).

This phenomenon was further investigated with propeller S at an advance ratio J=0.6. The calculated pressure distribution has a low pressure peak at the leading edge, as Fig. 2.15 shows. The peak is, however, not sharp enough to cause a laminar separation bubble at the leading edge, so the boundary layer remains attached and laminar up to the midchord region; although at higher Reynolds numbers the boundary layer becomes sensitive for surface irregularities (Plate 3.14).

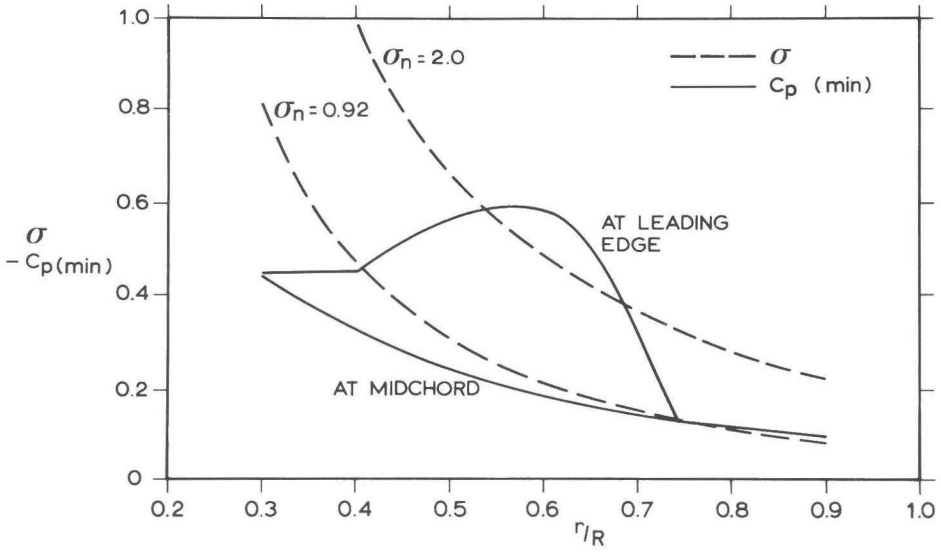

Fig. 7.7. Radial distribution of the calculated minimum pressure coefficients and cavitation indices on propeller S at J=0.6.

without electrolysis *with electrolysis*

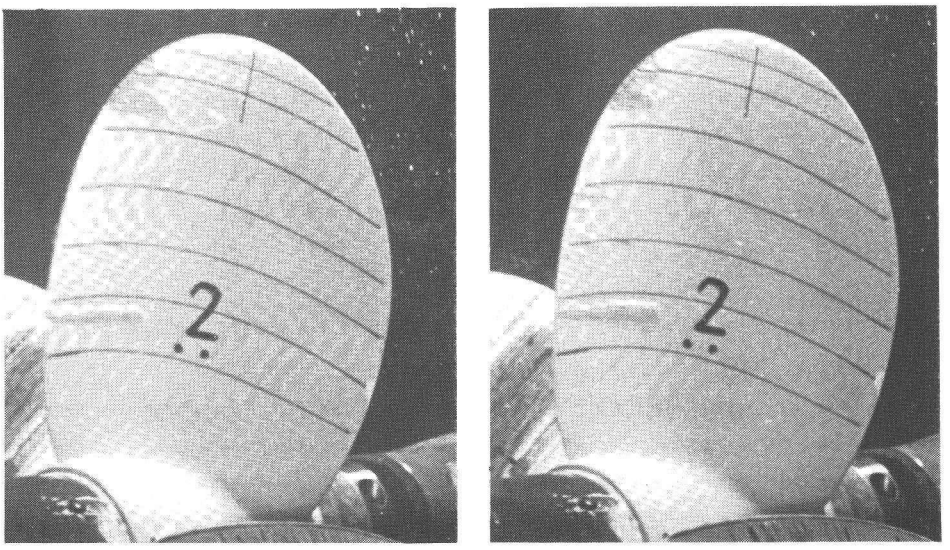

smooth

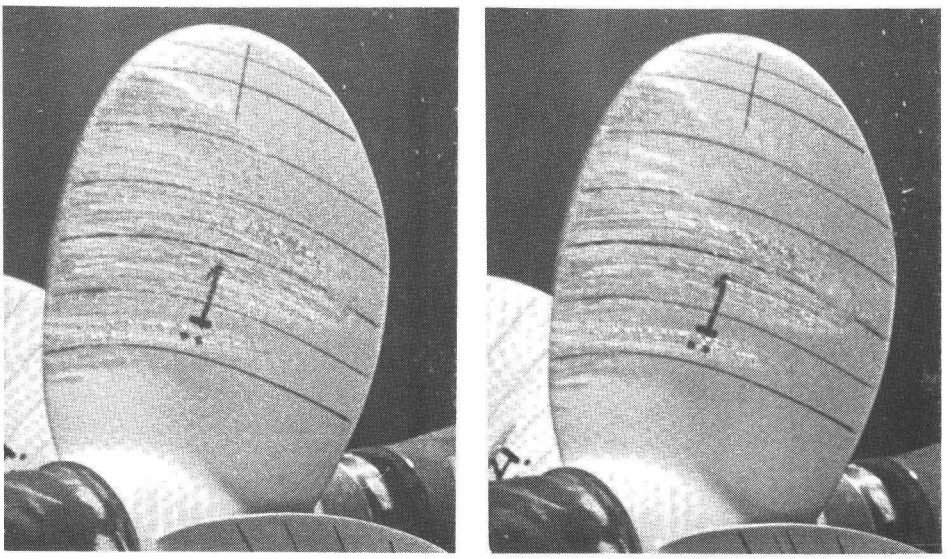

roughened at the leading edge

Fig. 7.8. Cavitation observations in the Depressurized Towing Tank on propeller S at J=0.6 (σ_n=0.92, Re_n=1.1x10^6).

The calculated minimum pressure coefficient at the leading edge is given in Fig. 7.7 together with the sectional cavitation index σ at various tank or tunnel pressures, which are expressed as σ_m.

Cavitation observations are shown in Fig. 7.8 at σ_n=0.92. Except for some isolated spots or patches no cavitation is present on the smooth blade without electrolysis, although the pressure at the leading edge is lower than the vapor pressure (Fig. 7.7) which is confirmed by the length of the spot cavities.

It is remarkable that electrolysis has no effect. Some bubbles can be observed near the leading edge, but no sheet cavity appears. Electrolysis did create bubbles in this condition, as observations on propeller B in exactly the same condition show (Fig. 6.2). From the observations in Fig. 6.2 as well as from the measurements in section 5 it was found that nuclei up to 30 μm in diameter were present in the flow when electrolysis was applied. The critical radius of the nuclei in the condition of Fig. 7.8 is 35 μm. These nuclei can be responsible for a difference of 0.09 (eq. 6.2) between the pressure coefficient C_p and the sectional cavitation index σ at r=0.6R in the condition of Fig.7.8. The calculated difference, however, is 0.35 and it is therefore not possible that a lack of nuclei in the flow causes this delay in inception. Some other mechanism must inhibit sheet cavitation inception when the boundary layer is laminar.

The picture on the roughened blade is drastically different. An extensive sheet cavity is present. The chordwise length of the sheet on the roughened blade is irregular. It seems that the roughness at some locations is not effective, causing gaps in the sheet cavity. Such a gap may influence the cavity length, as also happened at J=0.4.

Fig. 7.9 shows the cavitation pattern at the highest Reynolds number which could be obtained in the Depressurized Towing Tank. The cavitation index σ_n is at its lowest value of 0.67. The electrolysis wires are cavitating, as was also observed in Fig. 6.4, and a large amount of bubbles are present in the flow. Still no sheet cavitation occurs on the smooth blades without electrolysis. At midchord the pressure in this condition is also below the vapor pressure, and again the large bubbles do not create bubble cavitation, similar as on propeller B (Fig. 6.4).

When electrolysis is applied spot cavities appear, but only a fraction

without electrolysis *with electrolysis*

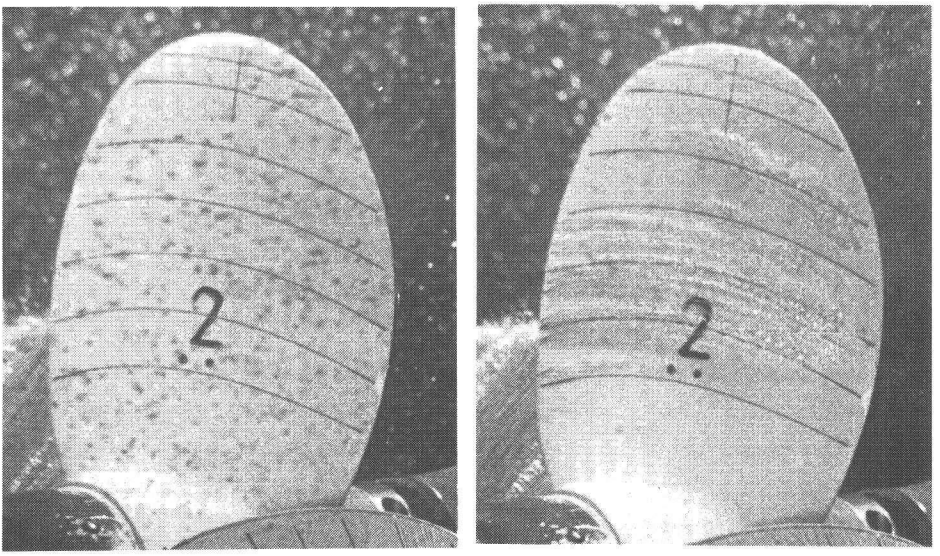

smooth

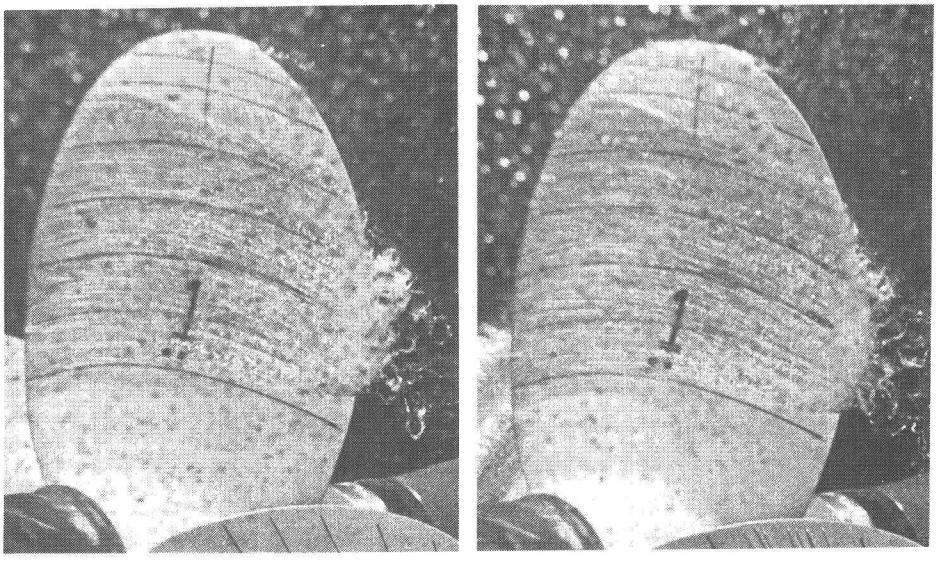

roughened at the leading edge

Fig. 7.9. Cavitation observations in the Depressurized Towing Tank on propeller S at J=0.6 (σ_n=0.67, Re_n=1.7x10^6).

of the sheet cavity on the roughened blade is present. At midchord near r=0.8R bubble cavitation occurs, similar as shown in Plate 6.12 on the smooth blade of propeller B. The sheet at the leading edge of propeller S is, however, still absent.

These observations show that it is nearly impossible to create sheet cavitation when the boundary layer is laminar near the leading edge. The streaks on the smooth blade with electrolysis in Fig. 7.9 can be related with turbulent streaks in the laminar boundary layer, as was observed in Plate 3.14 at the same Reynolds number. When these streaks are not present, there is no sheet cavitation, independent of the nuclei content, as shown in Fig. 7.8.

7.4. PROPELLER S AT J=0.6 IN THE CAVITATION TUNNEL

The cavitation pattern in the Cavitation Tunnel at J=0.6 is shown in Plate 7.10 at a cavitation index equal to that in Fig. 7.8. The Reynolds number was much higher, but only a few spots are present. Electrolysis did not have any effect, although in the same condition some bubble cavities were generated by electrolysis. Some large bubbles are visible in the flow, so the absence of the sheet cannot be explained by a lack of nuclei.

Roughness at the leading edge is again necessary to create the sheet at the leading edge. At this higher Reynolds number the roughness is more effective and the sheet is more regular than in Fig. 7.8. Plate 7.10 indicates that in the tunnel the propeller is lighter loaded than in the Depressurized Towing Tank, as was also found at J=0.4.

The spots on the smooth blade are much shorter than the sheet cavity on the roughened blade, similar as the spots in the gap at J=0.4.

7.5. INCEPTION OBSERVATIONS ON ROUGHENED PROPELLER BLADES

The foregoing observations were made in conditions of developed cavitation, where inception was only important because it could present the occurrence of developed cavitation. The experiments on the roughened cylinder showed that roughness caused an increase of the inception index and it is necessary to consider cavitation inception on the roughened blade more closely.

In the Depressurized Towing Tank cavitation observations were made near inception on the roughened blades of propeller S, both at J=0.4 en J=0.6. The length of the sheet cavity at a certain radius is plotted against the propeller cavitation index σ_n in Fig. 7.11. The radii which are considered are those radii at which cavitation was most persistent.

From Fig. 7.11 it appears that the cavity length is approaching a small but finite length when the cavitation index increases. This small cavity length persists up to high cavitation indices, but is often too small to measure accurately. An appropriate definition of inception on a blade with leading edge roughness is therefore the cavitation index at which the cavity length approaches an arbitrary small value. For propeller S at J=0.4 this is $2.0<\sigma_n<2.2$ and at J=0.6 this is $2.8<\sigma_n<3.0$.

The radial distribution of the sectional cavitation index for these propeller cavitation indices at inception are plotted in Figs. 7.1 and 7.7. The cavitation index $\sigma_n=2.2$ at J=0.6 agrees with the calculated minimum pressure coefficient, as Fig. 7.7 shows. The inception index $\sigma_n=3.0$ is close to the calculated pressure coefficient at 1% of the chord, as Fig. 7.1 shows. So this approach ignores the very short cavity length due to the sharp pressure peak at the leading edge.

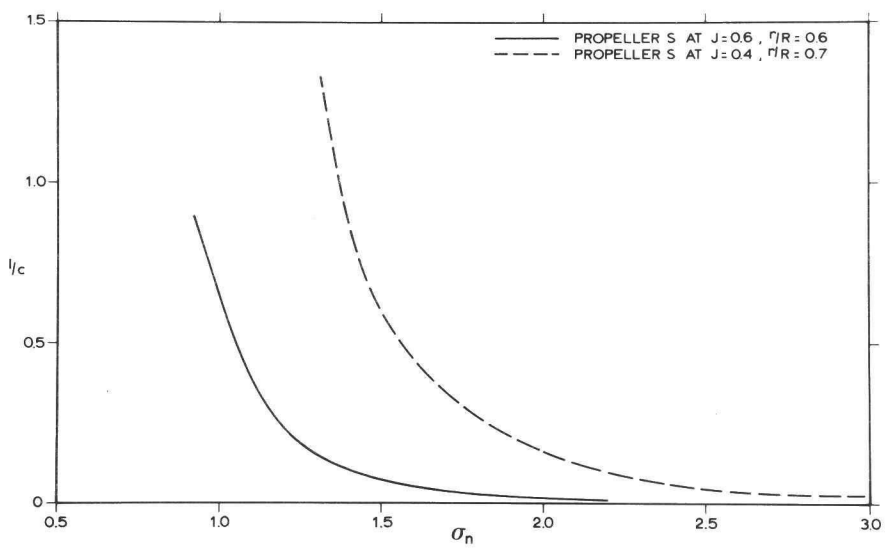

Fig. 7.11. Chordwise length ratio of the sheet cavity as a function of the propeller cavitation index.

In the cavitation tunnel more detailed inception observations are possible and inception was called on the roughened blade when the first tiny sign of cavitation was detected on the roughness elements. The results are given in the following Table.

Re_n	J	σ_i
1.7×10^6	0.6	3.4
2.1×10^6	0.6	3.0
1.4×10^6	0.4	6.8
1.8×10^6	0.4	7.3

Table 7.1. Visual inception measurements on a roughened blade of propeller S in the Cavitation Tunnel.

This table shows that cavitation was observed long before the sheet begins to grow in chordwise direction. From the calculated minimum pressure coefficients in Fig. 7.7 inception is found at σ_n=2.3. The observed inception index σ_n=3.0 to 3.4 therefore indicates an increase of the inception index by about 0.7 to 1.1 due to the roughness. A comparison with the smooth blade could not be made, of course, since on the smooth blade no inception occurred.

At the observed inception index σ_n=6.8 to 7.3 at J=0.4 the sectional cavitation index is still much lower than the calculated minimum pressure coefficient as shown in Fig. 7.1. The calculated minimum pressure is apparently too high. On the smooth blade cavitation became very intermittent at higher pressures and a consistent inception index could not be defined. Tiny spots remained visible until about σ_n=7.0 but these spots were also caused by surface imperfections, similar as on the roughened blade.

The inception measurements at J=0.6 show that there is indeed an increase of the inception index due to roughness at the leading edge. The resulting cavitation, however, remains very small.

8. Tip vortex cavitation

The character of a cavitating tip vortex is investigated on propeller V. The observed radius of the cavitating vortex core near inception hardly varies with the distance from the tip, although the vortex sheet rolls up and the strength of the tip vortex increases with the distance from the propeller tip. A description of the velocity field which accounts for both facts is given. Contrary to the inception index the radius of the cavitating core is independent of the nuclei content, the total gas content, the Reynolds number and even of roughness applied on the blade surface near the tip. This is used to determine cavitation inception on model scale. An empirical formula to predict inception on model scale is given in order to make a rough estimate of the inception index.

8.1. INCEPTION OF TIP VORTEX CAVITATION

Much attention has been paid to tip vortices generated by wings of airplanes because of the hazards these vortices create for following planes. In that case the situation far behind the wing tip, where the trailing vortex sheet is completely rolled up, is important. The rolled-up vortex sheet, with a maximum circulation equal to the maximum circulation on the generating wing, constitutes the initial condition for the calculation of decay and break-down of the trailing vortex. A review of this subject has been given by Widnall (1975). An extensive literature survey of methods to influence the tip vortex, with special interest in cavitation inception, has recently been given by Platzer and Souders (1979). Most data, however, concern the far field of the tip vortex. Cavitating tip vortices are generally attached to the propeller tip and the situation close to the tip is important. Therefore the roll-up of the vortex sheet has to be considered first.

Vortex roll-up occurs rapidly in the tip region, where the trailing vortex sheet is strongest. Numerical calculations give an indication of the

rapidity of roll-up. An example of such a calculation, from Moore (1974) is given in Fig. 8.1. The wing loading is elliptical with the maximum circulation Γ_o in the center of the wing at x=0. Moore considered discrete vortices and numerically calculated the path of these discrete trailing vortices. Fig. 8.1 shows that at already 5% of the semi-span behind the wing tip a discrete tip vortex exists. The detailed structure of the tip vortex could not be calculated by Moore since he had to collaps the tightly wound vortices in the tip vortex into a single vortex to maintain the stability of his calculation.

Moore verified that the strength of the tip vortex within 10% of the semi-span behind the tip can be approximated by Kaden's (1931) analytical result

$$\Gamma_{tip} = 0.1\ y^{1/3}\ \Gamma_o \qquad (8.1)$$

where y is the distance behind the tip, made dimensionless by the semi-span of the wing. From eq. 8.1 it follows that at y=0.1 already 46% of the total vorticity is present in the tip vortex. Moore calculated complete roll-up at y=10, but at y=1 already 80% of the circulation was concentrated in the tip vortex.

These results show that in the region immediately behind the propeller tip, the strength of the tip vortex is rapidly increasing with the distance from the tip. For the prediction of cavitation inception the pressure distribution on the tip vortex has to be known and therefore the velocity distribution in the tip vortex has to be considered now.

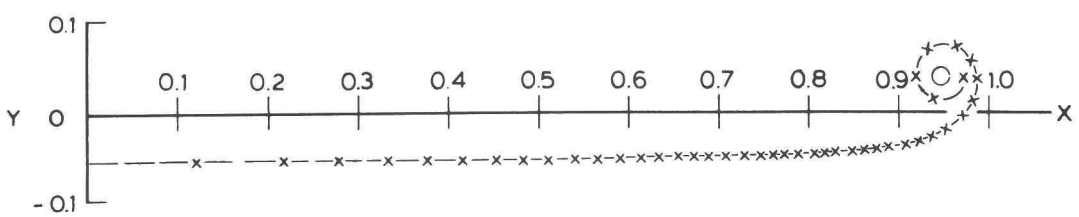

Fig. 8.1. Calculated shape of the trailing vortex sheet at a distance of 5% of the semi-span behind the wing (From Moore, 1974).

The simplest description of the tip vortex is a Rankine vortex, which has all vorticity concentrated and equally distributed in the vortex core with radius a_v, say. When roll-up is complete the strength of the tip vortex is equal to the maximum circulation Γ_o on the wing and the core radius a_v can be calculated e.g. by making use of conservation of energy during roll-up. (Spreiter and Sacks, 1951).

The vorticity distribution outside the vortex core of a Rankine vortex can be written as

$$v(r) = \frac{\Gamma_t}{2\pi r} \qquad r \geq a_v \tag{8.2}$$

and inside the core the velocity decreases linearly to zero

$$v(r) = \frac{\Gamma_t r}{2\pi a_v} \qquad r < a_v \tag{8.3}$$

The velocity has a sharp maximum at the radius a_v. The pressure distribution in the vortex can be found by integrating

$$\frac{\partial p}{\partial r} = \rho \frac{v^2(r)}{r} \tag{8.4}$$

This results in a minimum pressure in the center of the vortex core of

$$p_\infty - p_{min} = \frac{\rho \Gamma_t^3}{4\pi^2 a_v^2} \tag{8.5}$$

When the tip vortex is generated by roll-up of the trailing vortex sheet the velocity distribution can also be considered in an inviscid way, as sketched in Fig. 8.2. The vorticity spiral can be approximated by a circular distribution of vorticity with an outer radius a_t. When roll-up is complete the circulation of the vortex is equal to the maximum circulation Γ_o on the wing and the position of the vortex and the radial distribution of vorticity can be found by using Betz's hypothesis of conservation of impulse and of the moment of impulse during roll-up (Donaldson, 1971). Moore and Saffman (1973) related the velocity distribution in the trailing vortex with the loading distribution on the wing tip. The circulation near the tip of the wing can be approximated by

$$\Gamma(x) = \gamma \left(\frac{x}{D}\right)^{1-m} \tag{8.6}$$

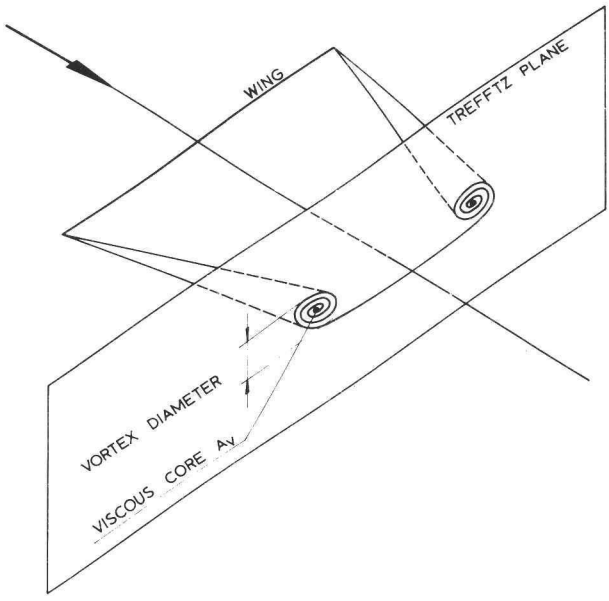

Fig. 8.2. Roll-up of the trailing vortex sheet.

where x is the distance from the wing tip and D is the wing span. When the vorticity between a point x/D on the wing near the tip rolls up into a vortex with radius x/ D the radial distribution of the velocity in the tip vortex is

$$v(r) = \frac{\Gamma(\lambda r/D)}{2\pi r} = \frac{\gamma \lambda^{1-m}}{2\pi (\frac{r}{D})^{m} D} \qquad r < a_t \tag{8.7}$$

The value $m=\frac{1}{2}$ represents an elliptical distribution of the circulation on the wing. Moore and Saffman now assume that λ is constant for all values of r and using the Betz condition of conservation of angular moment of vorticity they arrive at $\lambda=2-m$ for the completely rolled-up tip vortex. Rossow (1973) presents a similar approach for arbitrary span loadings.

This approach is inviscid and for m=0 the velocity in the center of the core becomes infinite according to eq. 8.7. A viscous core will therefore exist, with a radius a_v which is smaller than the radius of the vortex a_t.

Experiments with cavitation inception have been presented by McCormick (1962). Elliptical, rectangular and delta wings were investigated for several aspect ratio's and angles of attack. McCormick found the inception index of

the tip vortex to be independent of the aspect ratio. For the elliptical wing at a Reynolds number of 7×10^5 his data can be approximated by

$$\begin{aligned} &\text{elliptical wing} : \quad \sigma_i = 0.15\ \alpha^{1.29} \\ &\text{rectangular wing} : \quad \sigma_i = 0.10\ \alpha^{1.44} \end{aligned} \tag{8.8}$$

McCormicks results were remarkable since the strength of the rolled-up tip vortex is equal to the maximum circulation Γ_o on the wing, which varies with the aspect ratio. Also Γ_o is proportional with the angle of attack α, which means that when the vortex has the structure of a Rankine vortex the maximum pressure drop is proportional with α^2 (see eq. 8.5) instead of $\alpha^{1.29}$.

Chandrashekhara (1976) also measured the inception index of elliptical and rectangular foils, but he analysed the data as

$$\sigma_i = C_1\ \alpha^2 + C_2 \tag{8.9}$$

in which the constant C_2 was attributed to nuclei effects. Platzer and Souders (1980), however, also investigated an elliptical foil and found the cavitation index perfectly proportional with α^2.

McCormick found from his experiments that the inception index varied with the Reynolds number

$$\alpha_i = C\ Re^{0.35} \tag{8.10}$$

This relation was approximately also found by Billet and Holl (1979), who also found that the total air content influences the inception pressure.

In a semi-empirical analysis McCormick considered the tip vortex as a Rankine vortex with strength Γ_o and with a viscous core radius related to the boundary layer thickness at the tip. He assumed that

$$\delta = k.\frac{\ell}{Re_\ell^{0.35}} \tag{8.11}$$

with ℓ as the length as shown in Fig. 8.3 and Re_ℓ as the Reynolds number related to V_ℓ and ℓ. The cross-flow velocity V_A at the tip of an elliptical

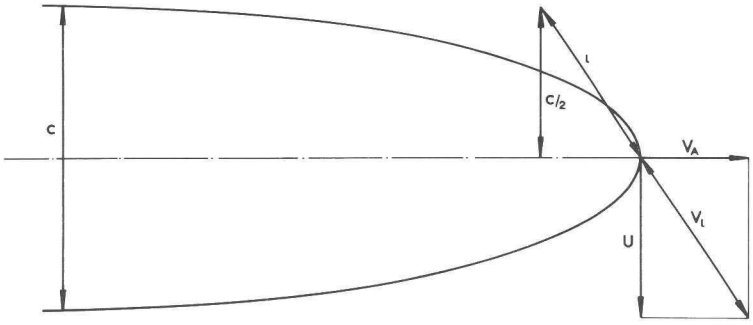

Fig. 8.3. Flow at the wing tip as assumed by McCormick (1962).

wing was by McCormick taken

$$\frac{V_a}{U} = K\left(\frac{\Gamma_o}{c.U}\right)^m \tag{8.12}$$

and the unknown values of k from eq. 8.11 and K and m from eq. 8.12 were, from the inception data as given in eq. 8.8, determined to be k=0.31, K=53.7, and m=0.8. A problem arises, however, from this result since for an elliptical wing the value Γ_o/cU is equal to half the lift coefficient, which is of the order one. This means that the cross-flow velocity V_A at the tip is an order of magnitude larger than the incoming flow velocity U, which is unlikely. This is probably caused by an overestimate of the vortex circulation Γ_o, as will be analysed later.

8.2. AN INVISCID ANALYSIS OF A CAVITATING TIP VORTEX

Cavitation inception is assumed to take place when the minimum pressure in the vortex is near the vapor pressure, provided enough nuclei of sufficient size are available. The minimum pressure occurs in the center of the vortex core, where viscosity is important. For its prediction it is, therefore, necessary to know the pressure distribution in the viscous core, however, this knowledge is not available.

In a cavitating vortex the viscous core is, at least partially, replaced by vapor and this vapor core can be treated as a solid core, rotating with an outer velocity equal to the fluid velocity. The pressure at this cavitating core radius a_c may be assumed to be the vapor pressure p_v, although it is possible that there is a considerable gas pressure in the core because the fluid is generally highly supersaturated at the vapor pressure. Using the

spiral vortex approach of Moore and Saffman (1974), three regions can be distinguished in the cavitating tip vortex:

1. The cavitating core radius a_c with a circulation Γ_c at $r=a_c$.

2. A rolled-up vorticity region, in which the radial velocity distribution is assumed to have the form

$$v(r) = \frac{C_1}{2\pi r^m} \qquad a_t > r > a_c \tag{8.13}$$

in which $C_1=\Gamma_c\, a_c^{m-1}$

3. An irrotational region outside the rolled-up vortex with radius a_t, inwhich the velocity distribution has the form

$$v(r) = \frac{C_2}{2\pi r} \qquad r > a_t \tag{8.14}$$

where $C_2=\Gamma_c(\frac{a_c}{a_t})^{m-1}$ to ensure continuity of the velocity at $r=a_t$.

The pressure at the cavitating core radius a_c can be calculated from eq. 8.4 with the velocity distributions from eqs. 8.13 and 8.14.

$$p_o-p(a_c) = \frac{\rho\Gamma_c^2}{8\pi^2 m a_c^2}\{1+(m-1)(\frac{a_c}{a_t})^{2m}\} \tag{8.15}$$

Near inception the cavitating core radius a_c is small and the ratio a_c/a_t is therefore assumed to be small. Eq. 8.15 can then be simplified to

$$\sigma = \frac{\Gamma_c^2}{4\pi^2 m\, a_c^2\, n^2 D^2} = \frac{(\Gamma_c/\pi nD^2)^2}{4m(\frac{a_c}{D})^2} \tag{8.16}$$

where $p(a_c)=p_v$.

The relation 8.16 between cavitation index, circulation at the cavitating core and cavitating core radius has two important consequences:

1. The circulation around the cavitating core contains only a small fraction of the total rolled-up vorticity.

2. The roll-up of vorticity, and thus the increase of the circulation Γ_t with increasing distance from the propeller tip, has no influence on the cavitating core radius a_c. This explains cavitation observations, where invariably the cavitating core radius is constant or decreasing with the distance from the tip, even at positions where the roll-up process has not yet been completed. When the vortex sheet is considered to be completely

rolled-up the strength of the circulation at the core is strongly over-estimated, which explains the improbable regression coefficients, obtained by McCormick in eq. 8.12.

Chandrashekhara (1976) also used a spiral vortex approach to derive the pressure at the viscous core radius a_v, but he also assumed the vortex to be completely rolled up and considers the ratio a_c/a_t as a constant, which leads to a modified Rankine vortex approach.

Eq. 8.16 provides a relation between the cavitation index, the radius of the cavitating core and the circulation around the cavitating core. The circulation Γ_c is a function of the propeller loading Γ_o, of the loading distribution m, of the core radius a_c and probably also of the shape of the propeller tip. For one propeller at one loading we therefore need the relation

$$\Gamma_c = \Gamma_c(a_c) \tag{8.17}$$

and this relation is unknown. Assuming that eq. 8.17 can be expressed as

$$\Gamma'_c = \frac{C}{a_c^{\frac{1}{p}-1}} \tag{8.18}$$

in which $\Gamma'_c=\Gamma_c/\pi nD^2$ and $a'_c=a_c/D$, we can write eq. 8.16 as

$$\sigma = \frac{C^2}{4m\ a'^{2p}_c} \tag{8.19}$$

In an earlier study (Kuiper, 1979a) a good correlation between measurements at propeller V at J=0.4 and eq. 8.19 with 2p=1 was found. This will now be investigated more extensively in various conditions.

8.3. OBSERVATIONS OF TIP VORTEX CAVITATION ON PROPELLER V

Observations of the tip vortex behind propeller V were made with two cameras. The first camera observed the tip vortex closely behind the blade, the second camera was focussed on the same vortex one revolution further downstream. An example of such observations is given in Fig. 8.4. These observations were made in the NSMB Large Cavitation Tunnel.

The conditions in which observations were made were varied systematically. A distinct tip vortex was present at the advance ratio's J=0.4 and J=0.5.

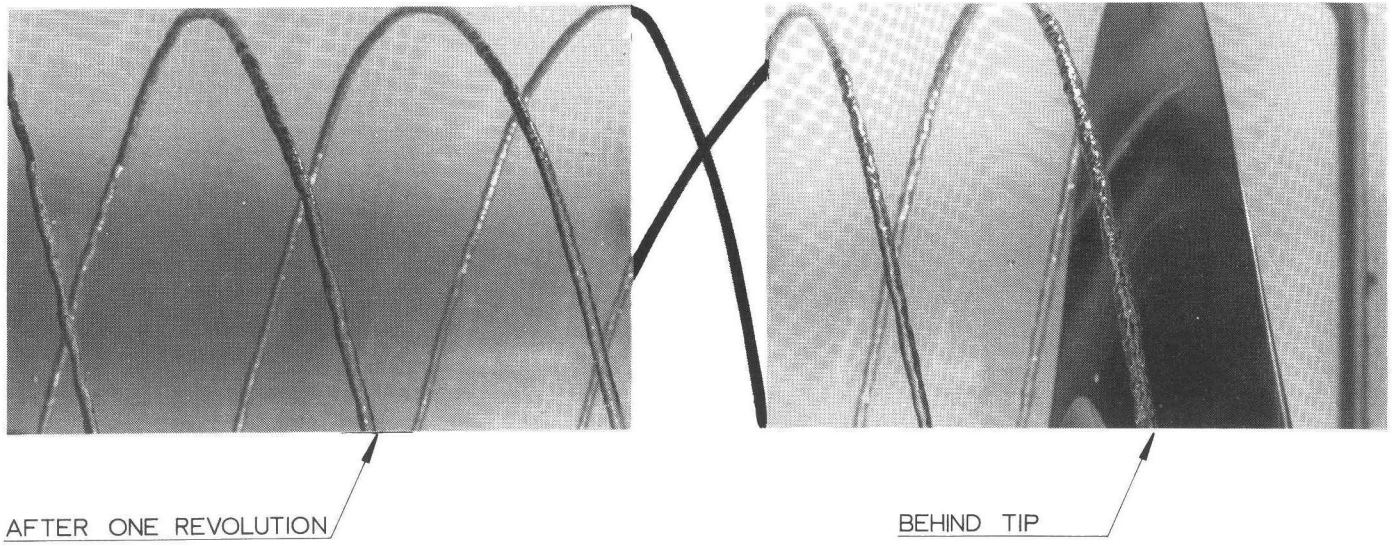

Fig. 8.4. Simultaneous observations of the tip vortex with two cameras.
(Propeller V at J=0.3, σ=3.0, Re=1.38x10^6)

Some observations were also made at J=0.3 but in this condition the tip vortex was connected with a sheet cavity at the suction side of the propeller blades and the maximum pressure in the tunnel was too low to make the cavitation disappear. At J=0.6 very little tip vortex cavitation was present, and it was always combined with pressure side cavitation on the blades.

The calculated radial distribution of the blade loading is given in Fig. 8.5. To illustrate the high loading of the blade tips of propeller V the radial load distribution of propeller S, which has a strongly unloaded tip, is also shown. The loading in the tip region, normalized with the maximum loading Γ_o, is given in Fig. 8.6, in which the well-known elliptical distribution is shown for reference. The maximum circulation Γ_o on propeller V can be found from

$$\frac{\Gamma_o}{\pi n D^2} = 0.65 \quad (0.82-J) \tag{8.20}$$

The effect of roughness was investigated by applying 60 μm carborundum on the blade surface between r=0.9R and the tip over the whole blade. To avoid disturbances of the tip vortex due to the roughness, the outer edge of the tip was kept free from roughness particles. The situation was just the opposite then when roughness was applied at the leading edge. Here the blade was roughened and the edge was kept clean. The roughness extended to less than 1 mm from the edge of the blades.

Two blades were kept smooth (blades 1 and 4), one blade was roughened at the suction side (blade 2) and one blade was roughened at the pressure side (blade 3). The two smooth blades were the blades which showed maximum differences in cavitation inception in the smooth condition to avoid confusion between effects of roughness and effects due to deviations in the blade geometry.

The tests were carried out at two propeller Reynolds numbers, $Re_n=1.38\times10^6$ and $Re_n=2.76\times10^6$. The required Reynolds number and advance ratio was obtained by controlling the flow velocity in the tunnel and the propeller revolutions. The thrust was measured as a check and it was found that the thrust coefficient varied with the Reynolds number due to tunnel wall effects.

The effective advance ratio, based on the measured thrust coefficient and the measured open-water diagram was therefore also calculated. Variation in the tunnel pressure affected the propeller thrust coefficient by less than 1% only.

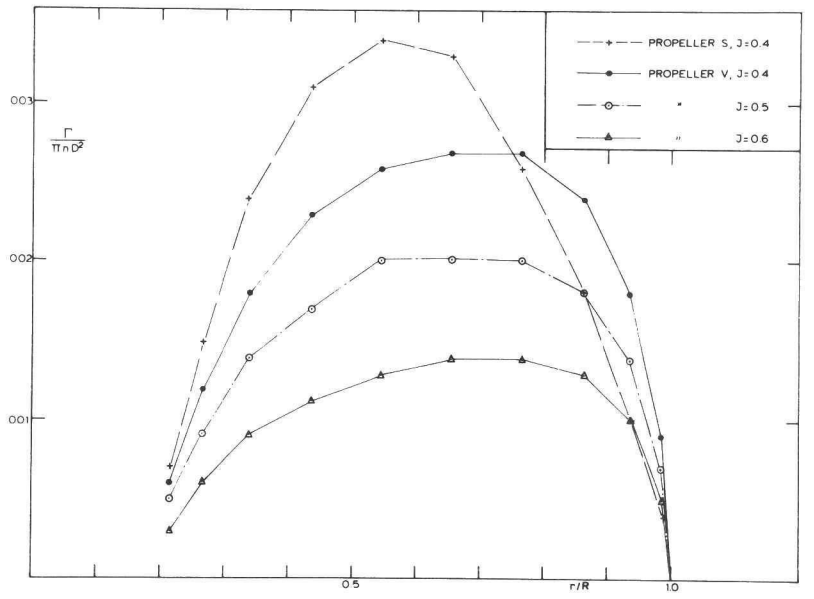

Fig. 8.5. Calculated radial distribution of the circulation.

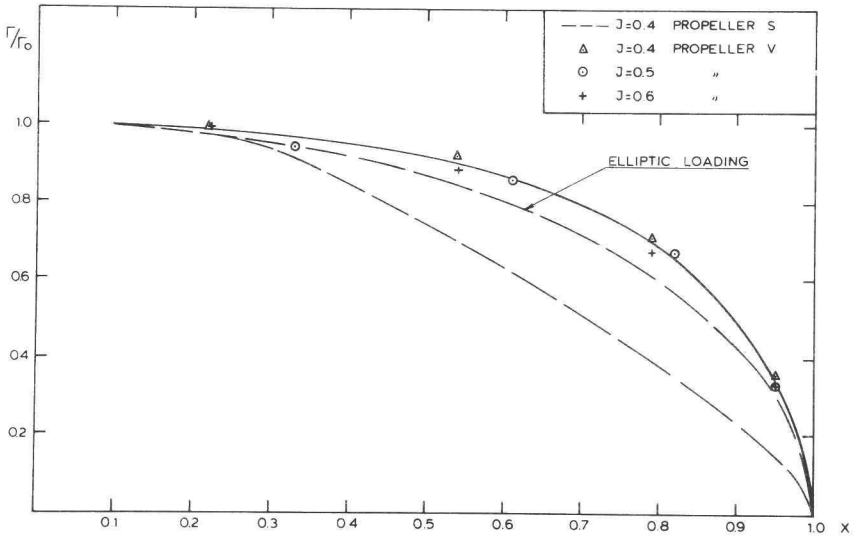

Fig. 8.6. Normalized circulation distribution at the propeller tip.

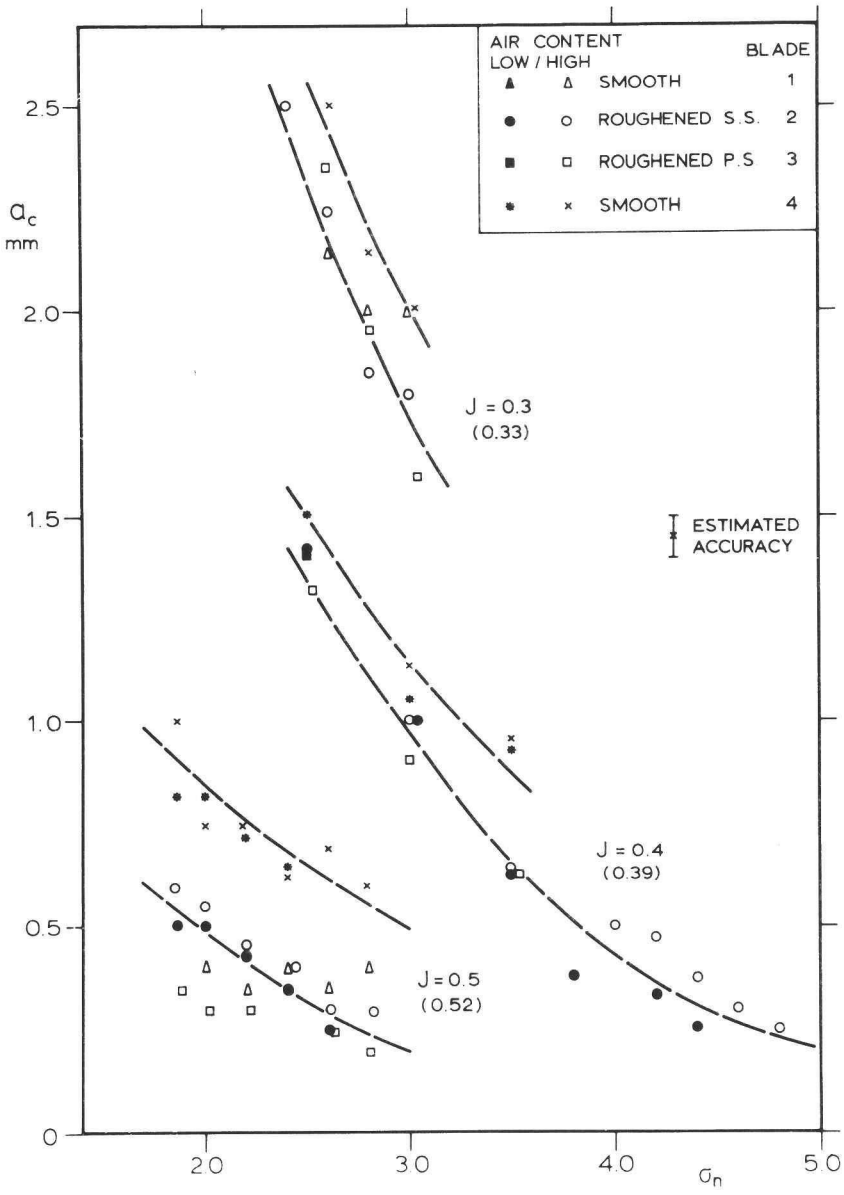

Fig. 8.7. Measured radii of the cavitating core of propeller V at $Re_n = 1.38 \times 10^6$.

The observations were made at two total air contents of the tunnel water, viz. 6.5 and 13 ppm.

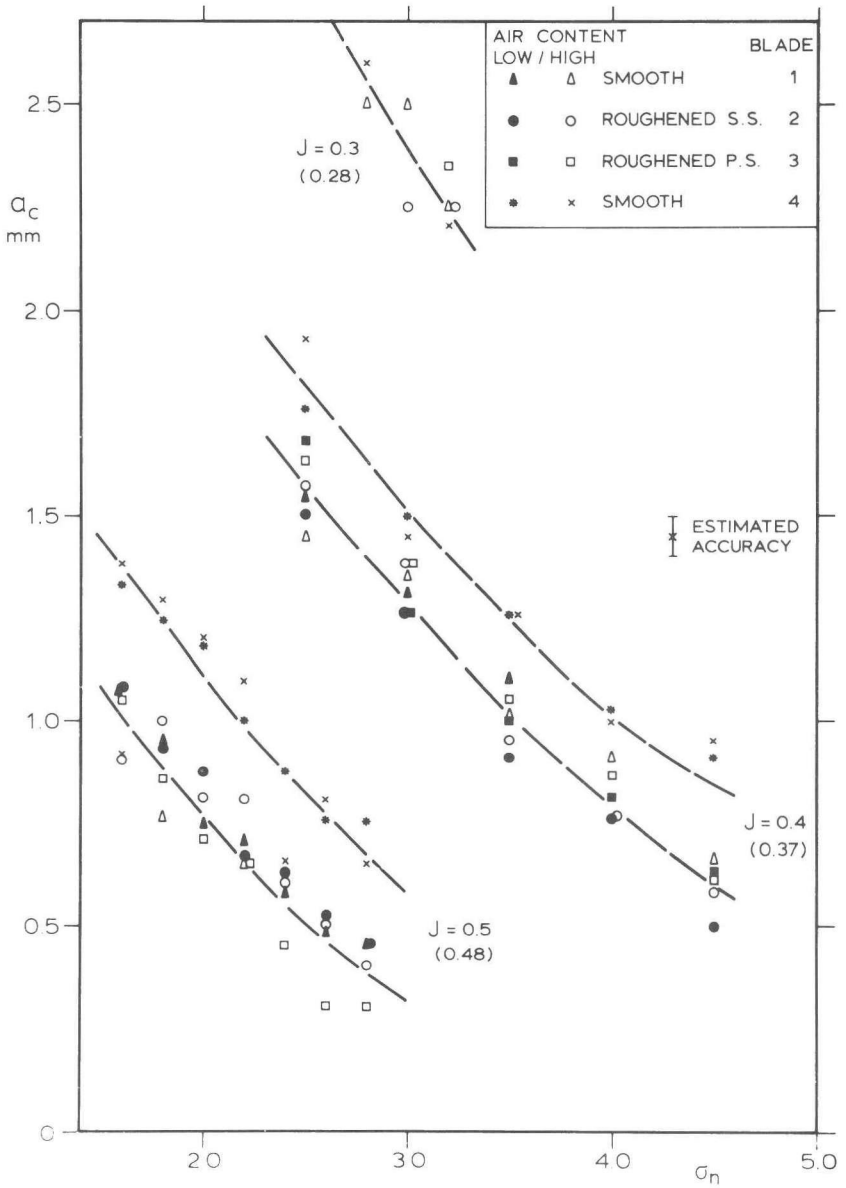

Fig. 8.8. Measured radii of the cavitating core of propeller V at $Re_n = 2.76 \times 10^6$.

Measurements of the cavitating core radius a_c were made from slides after projecting them ten times magnified. The measurements were made at about 45 degrees behind the tip and at one revolution further downstream, at about

405 degrees.

The results of the measurements at 45° behind the tip are shown in Figs. 8.7 and 8.8 for three advance ratios. The effective advance ratios based on thrust identity are given between brackets. In those Figures the data for one advance ratio nearly collaps on one line for all conditions, but the data of the smooth blade 4 differ from all other blades. This was caused by a slight deviation in the propeller tip of blade 4, as shown in Fig. 4.5, where the thinnest contour of propeller V is that of blade 4, while the pitch was slightly higher.

The radius of the core decreased over one revolution. This decrease has been plotted in Fig. 8.9 as a function of the radius at 45 degrees behind the tip.

Cavitation inception was also determined visually, where inception was called when the tip vortex was visible during about 50% of the time between the propeller tip and one revolution behind the tip. The results are given in Table 8.1. When cavitation inception could not be obtained because limitations of the tunnel pressure the upper or lower limit which could be reached is indicated in this Table.

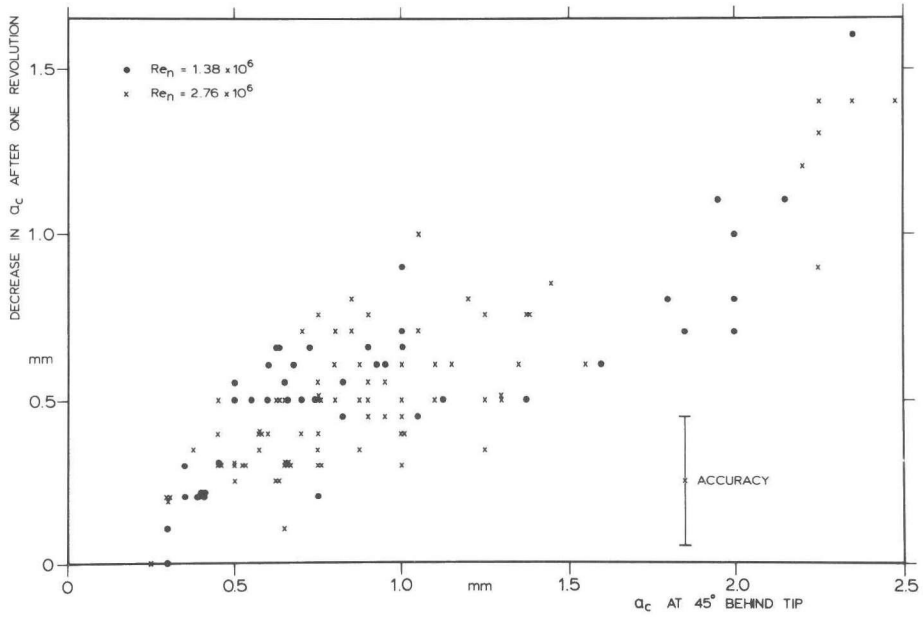

Fig. 8.9. Decrease of the radius of the cavitating core after one revolution.

J	J(eff)	Re_n	Blade 4 smooth	Blade 1 smooth	Blade 2 rough suction side	Blade 3 rough pressure side
0.3	0.33	1.38×10^6	>4.75	>4.75	>4.75	>4.75
0.3	0.28	2.76×10^6	7.66	6.19	7.50	6.28
0.4	0.39	1.38×10^6	>4.9 (4.41)	>4.9 (3.9)	>4.9 (4.41)	>4.9 (3.49)
0.4	0.37	2.76×10^6	6.86 (>4.75)	4.96 (4.5)	6.06 (>4.75)	4.29 (>4.75)
0.5	0.52	1.38×10^6	5.27 (2.45)	3.13 (1.99)	3.28 (3.13)	2.39 (1.69)
0.5	0.48	2.76×10^6	>4.75 (>4.73)	3.48 (2.89)	4.59 (4.36)	3.46 (2.87)
0.6	0.62	1.38×10^6	1.90	<1.90	<1.90	<1.90
0.6	0.59	2.76×10^6	2.74	1.95	2.0	1.59

Table 8.1. Inception indices of the blades of propeller V in various conditions.

(The data between brackets are for a low total air content, the others for a high total air content).

Various aspects of the foregoing observations and measurements will be discussed now.

8.3.1. Effects of roll-up of the vortex sheet.

The spiral structure of the trailing vortex sheet becomes visible at low cavitation indices, as Fig. 8.10 shows. There is a sheet cavity on the suction side of the blade in these conditions, which rolls up into a tip vortex. After one revolution the cavitating core has a cylindrical shape. At a somewhat lighter loading the spiral structure of the cavitating tip vortex becomes cylindrical with a periodically varying radius, as is illustrated in Fig. 8.11. An increase of the pressure or a decrease of the vortex strength finally causes a cylindrical cavitating core, as shown in Fig. 8.4.

These observations illustrate that roll-up of the vortex sheet indeed occurs up to some distance behind the blade tip and that in that region the radius of the cavitating core is not affected by the roll-up process.

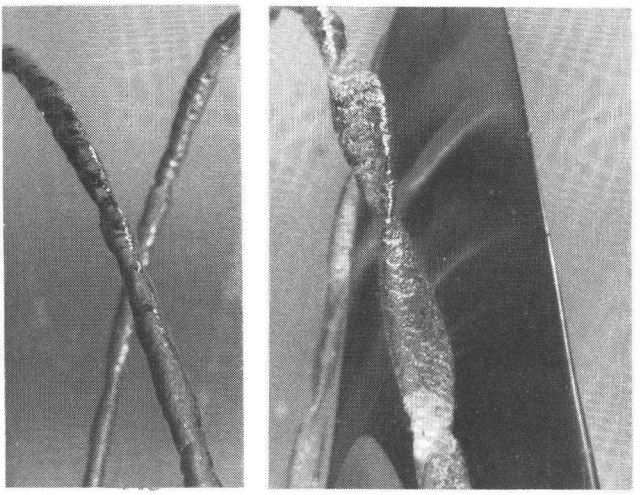

after one revolution *behind tip*

Fig. 8.10. Roll-up of the cavitating vortex sheet. (Propeller V blade 4 at J=0.3 , σ_n=2.0, Re_n=2.76x10^6).

8.3.2. Effects of the total air content.

When gas diffuses into the cavitating vortex core the pressure in the core, and subsequently the radius, will increase. Figs. 8.7 and 8.8 show that this is not the case since the total air contents of the water, which controls diffusion did not change the radius of the cavitating core.

At a high total gas contents of the tunnel water there are more nuclei present in the water, which may influence cavitation inception. From Table 8.1 it follows that an increase of the total air content in the tunnel always caused an increase in the inception index, as is shown in Fig. 8.12. Only on blade 2 with roughness at the suction side the effect was negligible at both Reynolds numbers, but only at J=0.5.

Tests in the Depressurized Towing Tank with propeller V confirmed the sensitivity of tip vortex inception to nuclei, as Fig. 8.13 illustrates. Without electrolysis no inception takes place, with electrolysis a cavitating core is present. In this case all blades were smooth.

The strong dependence of the inception index of the nuclei content is in contrast with the insensitivity of the radius of the cavitating core to this

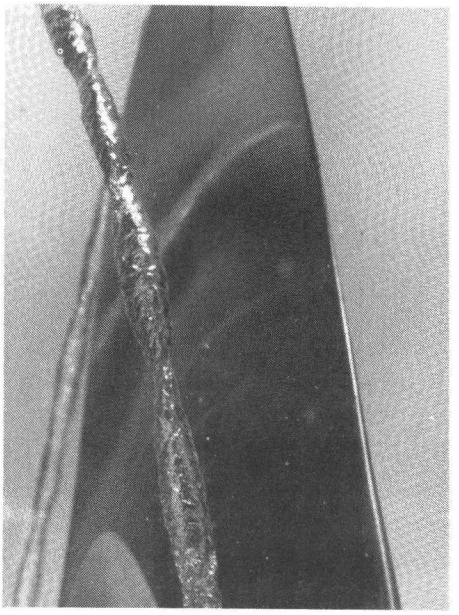

Fig. 8.11. Example of varying core radius (Propeller V blade 4 at $J = 0.7$, $\sigma_n=2.0$, $Re_n=1.38x10^6$)

parameter.

8.3.3. Viscous effects on cavitation inception.

At first sight there appears to be a significant influence of the Reynolds number on the radius of the cavitating core between Fig. 8.7 and Fig. 8.8. However, when the core radius at $\sigma_n=2.8$ is plotted on basis of the effective advance ratio the radii at both Reynolds numbers fall in line with each other, as Fig. 8.14 shows for the averages of blades 1, 2 and 3. So it may be concluded that the difference between Figs. 8.8 and 8.9 is caused by differences in effective advance ratio, resulting in differences in tip vortex strength. The Reynolds number does not influence the radius of the cavitating core. This agrees with earlier measurements at the same propeller V (Kuiper, 1979a) where no Reynolds number effects were found when the propeller thrust coefficient was kept constant, as will be discussed later (Fig. 8.22).

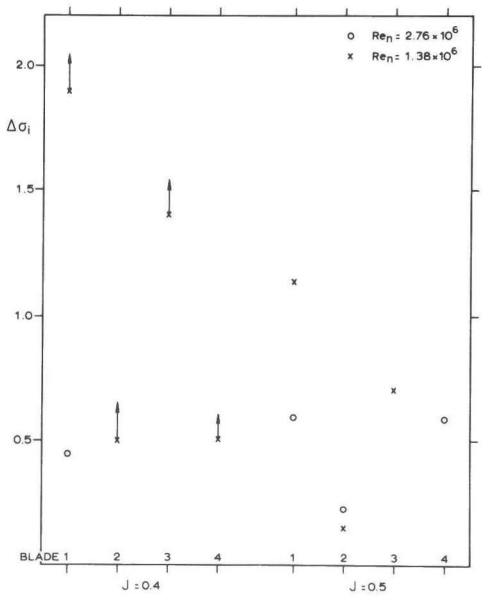

Fig. 8.12. Increase of the inception index due to an increase in total air content.

From the inception data of Tabel 8.1 the effect of the Reynolds number cannot be found directly because of the variation in effective advance ratio which occurs simulaneously with the variation in Reynolds number. The data from wings indicate that the inception index is proportional with $Re^{0.35}$ (McCormick, 1962; Billet and Holl, 1979). This would mean a 27% increase in σ_i when the propeller Reynolds number is doubled.

The Reynolds number effect on cavitation inception on the smooth blades has been plotted in Fig. 8.15 (from Table 8.1). Only at a low air content an increase of the inception index with increasing Reynolds number is found, which indicates that this apparent Reynolds effect is caused by a change in the nuclei content, as occurred in Fig. 1.1b.

It is particularly interesting to see if application of roughness affects the inception index. The results of Table 8.1 have been plotted in Figs. 8.16 and 8.17 for both roughened blades. Compared with the inception indices of the smooth blade 1 (Fig. 8.15) roughness at the suction side (Fig. 8.16) increases the cavitation index and roughness at the pressure side has no

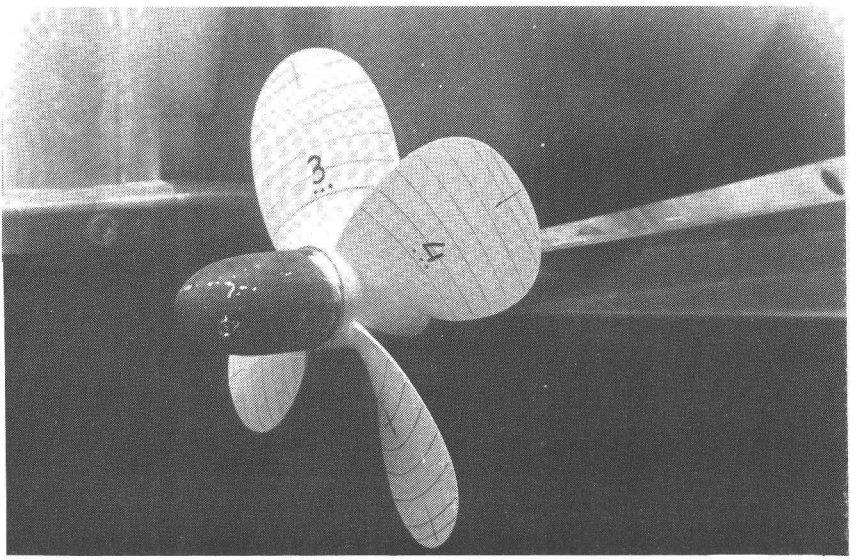

without electrolysis

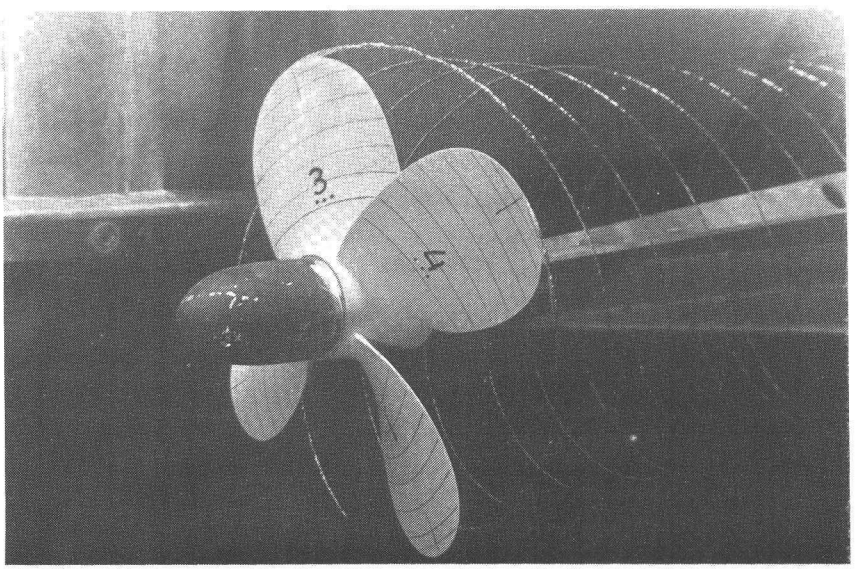

with electrolysis

Fig. 8.13. Influence of electrolysis in the Depressurized Towing Tank on tip vortex inception. (Propeller V at J=0.5, σ_n=1.32, Re_n=1.1x10

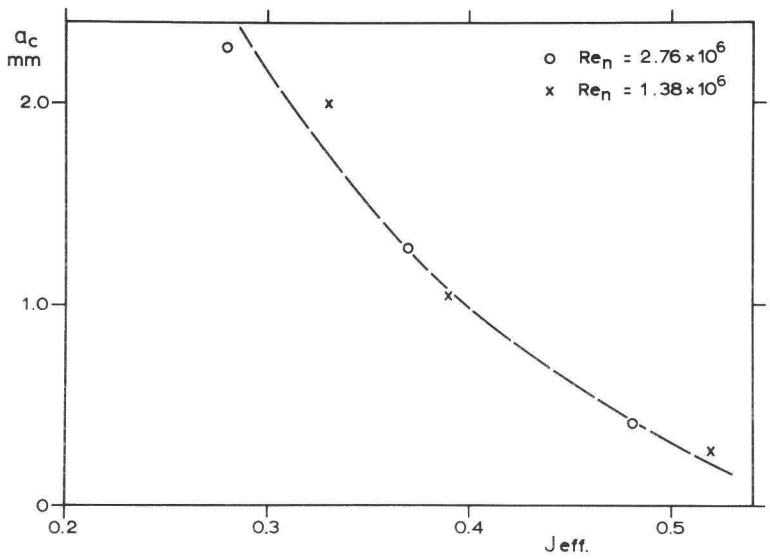

Fig. 8.14. The cavitating core radius behind blades 1, 2 and 3 of propeller V at σ_n=2.8.

effect. This is in contrast with McCormick's (1962) findings. He found that σ_i was reduced by roughness on the pressure side. Arndt (1976) found that application of roughness on the suction side of propeller A (see appendix 2) reduced the inception index. In that case the tip vortex was, however, positioned at the suction side, as Fig. A2.7 shows. Apparently it is important that the roughness is applied in the region where the tip vortex originates, as was also found by Platzer and Souders (1980). They found that roughness at both the pressure and the suction side reduced the inception index. From Fig. 6.2 of propeller B and from Fig. 7.2 of propeller S it is found that application of leading edge roughness increases the inception index, which may be because of the low nuclei content in that condition. In the cavitation tunnel roughness at the leading edge indeed suppressed tip vortex cavitation (Plate 7.6).

The foregoing shows that when the effect of roughness on tip vortex inception is investigated, it is very important to consider also the boundary layer near the tip, the nuclei content in the flow and the position of the tip vortex on the blade as well.

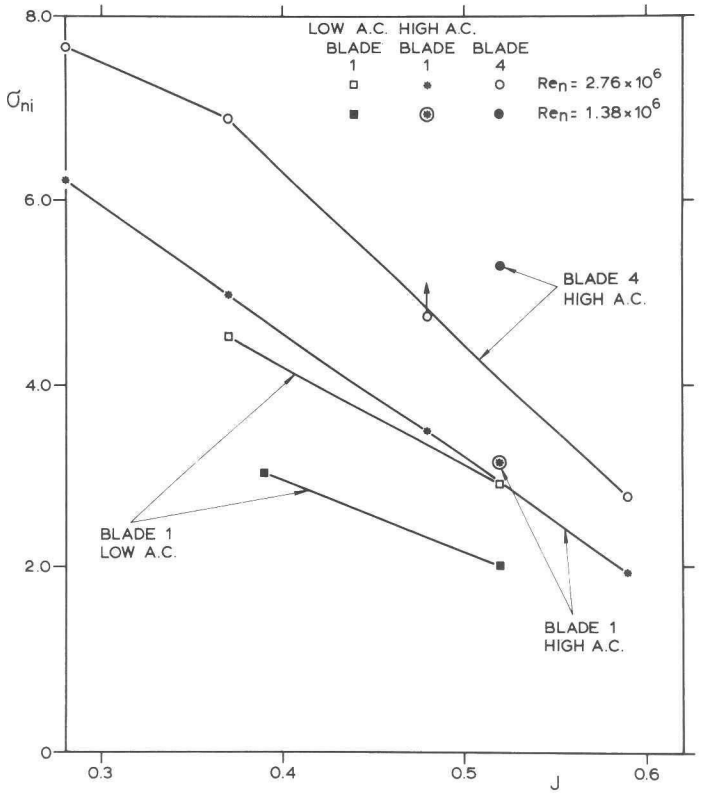

Fig. 8.15. Inception data on the smooth blades (blade 1 and 4) of propeller V.

It is remarkable that the increase of the inception index on the blade with roughness on the suction side is not reflected in the measured radii of the cavitating core (Figs. 8.7 and 8.8), which raises the question if an effect of roughness on tip vortex cavitation on model scale is relevant for the prototype. This has to be further investigated.

The boundary layer on the propeller blades also affects the appearance of the cavitating tip vortex, specifically the location of inception. As paint tests showed, the boundary layer on propeller V was laminar at the leading edge up to the tip, both on pressure and suction side. At an advance ratio J=0.4 laminar separation was about to start at the tip and a separation radius could be detected on the suction side, as Plate 3.10 shows. When the boundary layer was laminar at the tip detached cavitation inception occurred,

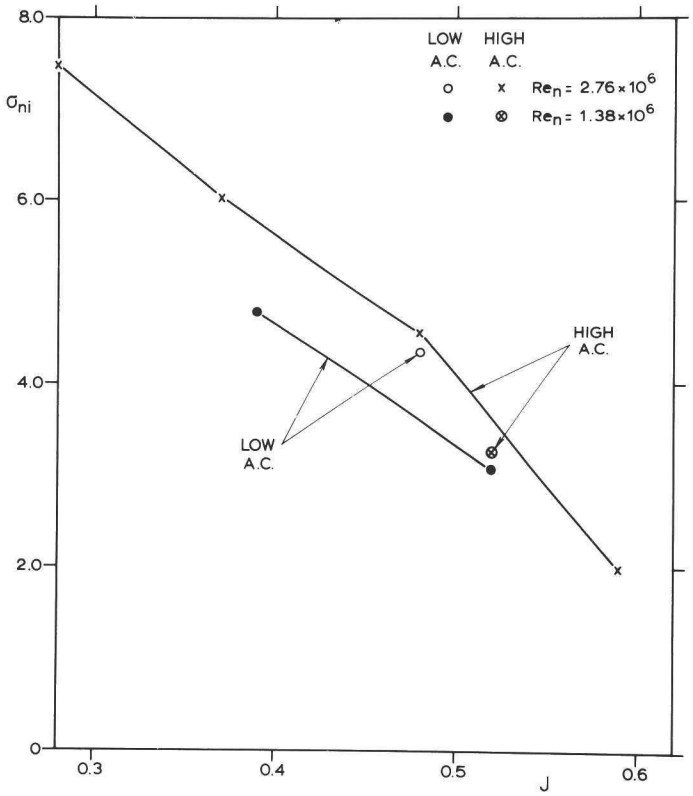

Fig. 8.16. Inception data on a blade of propeller V with roughness on the suction side (blade 2).

as is shown in Fig. 8.18 at J=0.4. In Fig. 8.19 propeller V is shown at J=0.5 in the Depressurized Towing Tank and detached inception takes place on all blades. Application of electrolysis did not change this appearance, and also in the cavitation tunnel a detached tip vortex was found at high total air content. Apparently the same mechanism which prevents cavitation inception of sheet cavitation in a laminar boundary layer also prevents inception of the tip vortex at the blade.

If laminar separation occurs in the boundary layer at the propeller tip the cavitating tip vortex is always attached to the tip and inception takes place at the propeller tip, as is shown in Fig. 8.20.

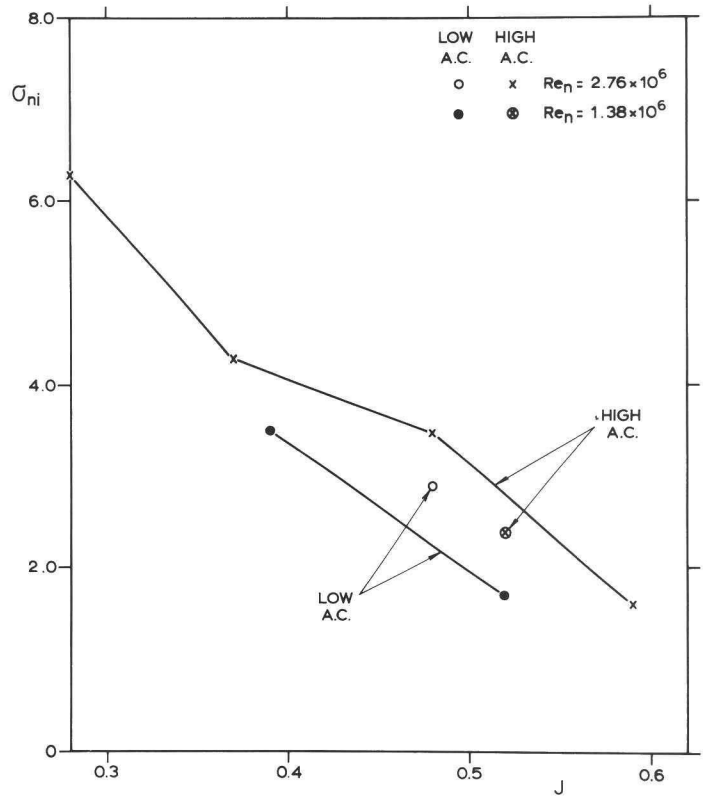

Fig. 8.17. Inception data on a blade of propeller V with roughness at the pressure side. (blade 3).

8.4. DETERMINATION OF CAVITATION INCEPTION OF A TIP VORTEX FROM THE RADIUS OF THE CAVITATING CORE

The visual determination of a tip vortex is difficult. At inception the cavitating core is not starting at an infinitely small radius, but it appears intermittently at a finite inception radius. Fig. 8.21 gives some examples of the appearance of a cavitating tip vortex near inception. These pictures are made with stroboscopic light and this frozen picture still gives much more detailed information than can be obtained by visual observation. To avoid this uncertain way of determination of the inception index it seems possible to use the measurements of the cavitating core radius for that purpose.

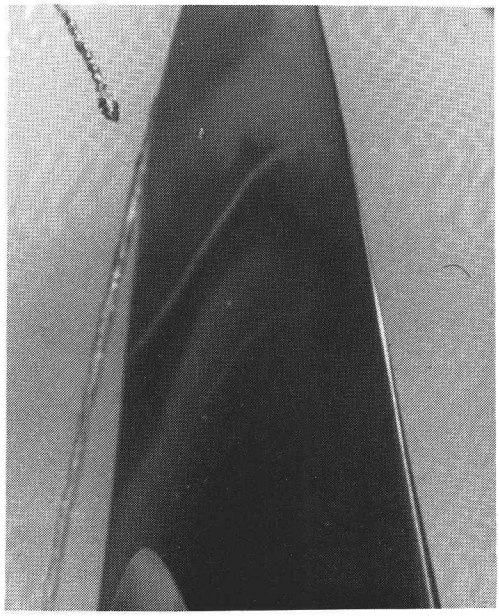

Fig. 8.18. Detached cavitation inception in the Cavitation Tunnel (Propeller V blade 1 at J=0.4, σ_n=2.5, Re_n=1.38x10^6).

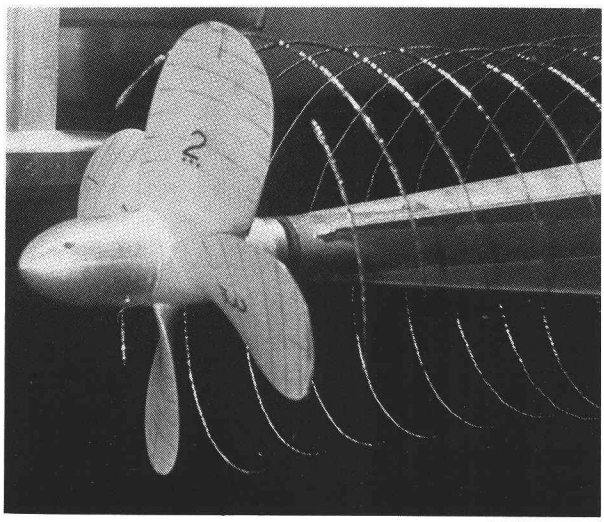

Fig. 8.19. Detached cavitation inception in the Depressurized Towing Tank (J=0.5, σ_n=1.0, Re_n=1.1x10^6).

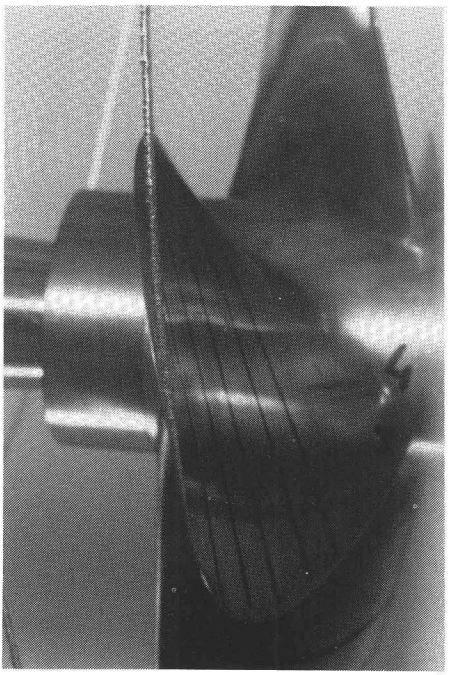

Fig. 8.20. Attached cavitation inception in the Cavitation Tunnel (Propeller V blade 4 at J=0.4, σ_n=3.90, Re_n=2.76x10^6).

In Figs. 8.7 and 8.8 an experimental relation between the cavitation index σ_n and the core radius a_c has been given. The minimum radius at inception was always about 0.25 mm, provided that inception was not delayed by a lack of nuclei. If cavitation inception is defined when the cavitating radius equals a minimum radius a_i of say 0.25 mm, we arrive at inception indices which are in the range of the inception indices from Table 8.1 as found from visual inception measurements. The advantage of this method to determine inception is that the sensitivity of the inception index to the Reynolds number and to the nuclei content is circumvented. However, a_c tends to go to the minimum radius a_i in an asymptotical way, which makes the determination of the inception index sensitive to the choice of the inception radius a_i and for the extrapolation to a_i.

In a similar way the advance ratio at which inception of the tip vortex occurs at a certain cavitation index can be obtained from Fig. 8.14, where the loading is varied at a constant cavitation index.

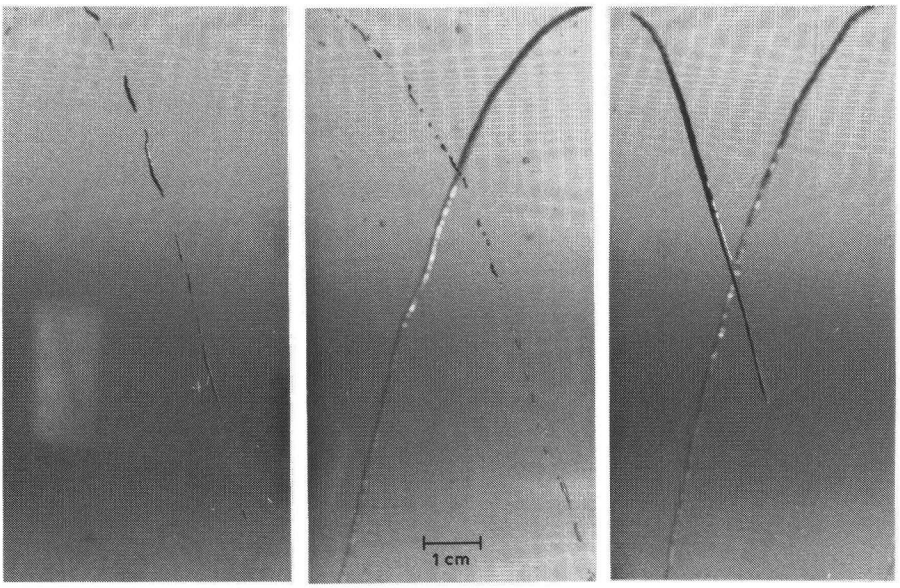

Fig. 8.21. Examples of tip vortices at cavitation inception.

A description of the relation between the cavitation index and the radius of the cavitating core in one propeller condition can help to determine σ_n, at a fixed inception radius a_i, from Figs. 8.7 and 8.8. A relation of the form

$$\sigma = \frac{C}{a'^{2p}_c} \tag{8.21}$$

as was derived in eq. 8.19 does not fit the measurements of Figs. 8.8 and 8.9. The correlation between measured values of a_c and σ and eq. 8.21 with 2p=1, as found earlier (Kuiper. 1979a) seems to be incidental since it could not be applied in other conditions. When eq. 8.21 is applied in the range of the smallest core radii a good correlation is found with 2p=0.5 instead of 1. This power also fits the earlier data as shown in Fig. 8.22. There also a curve for 2p=2 is shown, which power is found when the circulation Γ_c is independent of a_c and the vortex is considered as a Rankine vortex, as in eq. 8.5. For the determination of σ_i from a constant value of a_i, eq. 8.21 with a power 2p=0.5 can extrapolate the measurements close to inception.

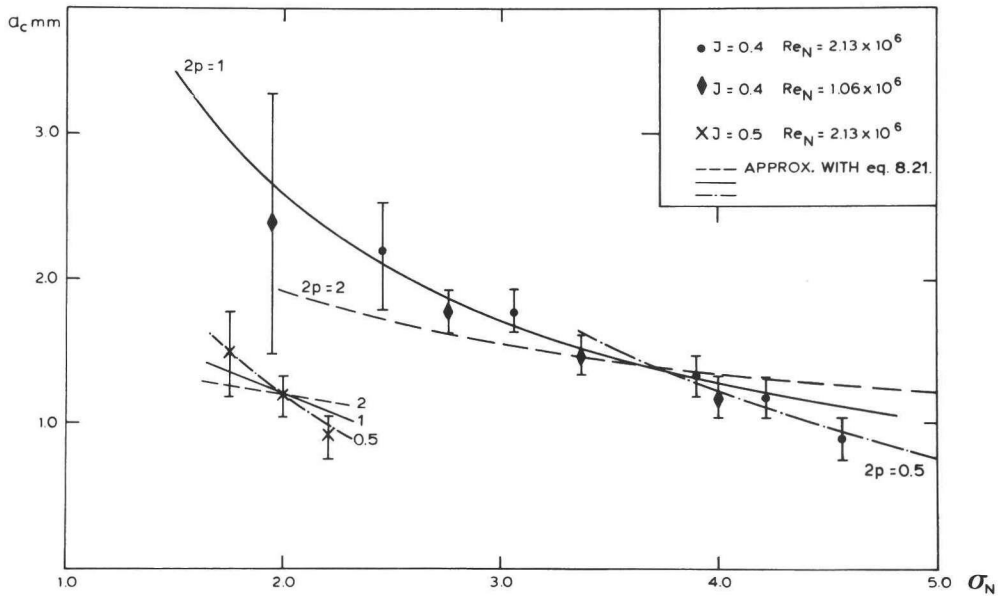

Fig. 8.22. Measured radii of the cavitating core of blade 4 of propeller V.

In this approach σ_i on model scale becomes independent of the Reynolds number, which contradicts some experimental results. From the inception observations on propeller V there are, however, indications that nuclei effects cause an apparent Reynolds dependency. When wings of different size are tested, as was done by McCormick and by Billet and Holl, wall effects on the different wings may cause differences in loading, resulting in an apparent Reynolds effect, similar as the difference between Figs. 8.7 and 8.8. So it is possible that the experimental variation of σ_i with $Re^{0.35}$ contains all those effects.

Inception on model scale is, however, only important to predict inception on the prototype and this can be done by the determination of an empirical value of the inception radius a_i on the prototype.

The present approach is inviscid and the cavitating core radius will, therefore, be proportional to the propeller diameter D. It follows from eq. 8.21 with 2p=0.5 that

$$\sigma_i = C_1 \left(\frac{\lambda}{a_c}\right)^{\frac{1}{2}} \tag{8.22}$$

where λ is the scale ratio. Noordzij found, for three propellers investigated behind a ship model in the Depressurized Towing Tank and also observed on full scale, that inception of tip vortex cavitation scaled approximately with $Re^{0.35}$, the same exponent as McCormick found on model scale. In a towing tank the Froude number has to be maintained and the Reynolds number scales with $\lambda^{3/2}$, which means that Noordzij scaled σ_i with $\lambda^{0.53}$. This is very close to eq. 8.22 and this indicates that with a power 2p=0.5 in eq. 8.21 the inception radius on the prototype can be taken equal to that on the model.

8.5. AN APPROXIMATE FORMULA FOR THE CAVITATION INDEX AT INCEPTION

A rough estimate of the inception index of the tip vortex is often needed in the design stage. Although visual determination of the inception index of a propeller tip vortex is difficult and inaccurate, this may provide the required estimate. Chandrashekhara (1976) determined the inception index for a series of propellers and analysed the inception index as

$$\sigma_i = C(P/D-J)^2 + \sigma_{res} \tag{8.23}$$

in which σ_{res} was attributed to nuclei effects. His results can also be analysed in terms of McCormick's analysis, as given in eq. 8.8 and 8.10, which in terms of a propeller yields

$$\sigma_i = C(P/D-J)^q \, Re_n^{0.35} \tag{8.24}$$

Data of Chandrashekhara, reduced to a propeller Reynolds number of 10^6 by using eq. 8.24, are plotted in Fig. 8.23. There is a systematic difference between the data of Chandrashekhara's propellers A and B and those of his propeller E. The results of our propeller V agree with those of propeller E. The shift is caused by the fact that the abcissa was taken as (P/D-J) at the tip, which is correct for propellers with a constant pitch over the radius. Propellers A and B of Chandrashekharam have, however, a strongly reduced tip loading. All data collaps on our curve if the pitch ratio at r=0.9R is taken as a reference. This was also done by Noordzij (1977).

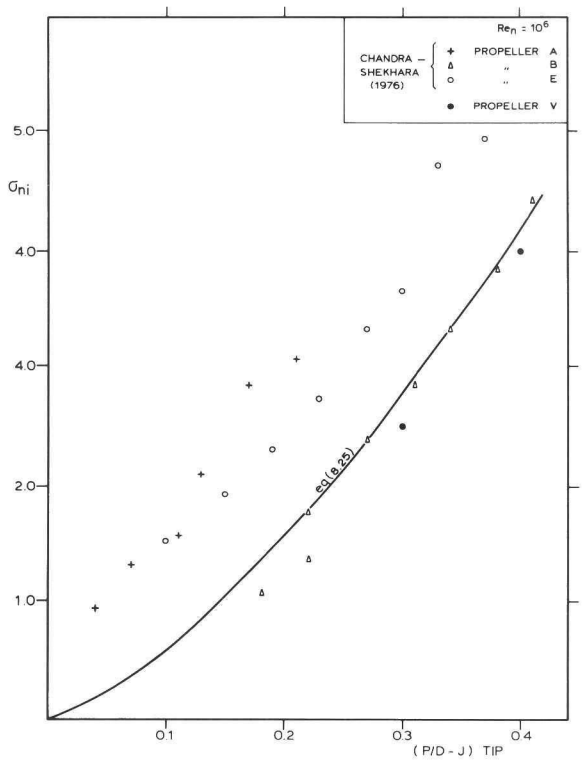

Fig. 8.23. Inception data of various propellers.

From Fig. 8.23 a rough approximation of the inception index of a tip vortex can be derived

$$\sigma_{ni} = 0.12\ (P/D-J)^{1.4}_{0.9R}\ Re_n^{0.35} \qquad (8.25)$$

The use of the power 0.35 for the Reynolds number has the same effect as the use of a constant inception radius at a constant Froude number in eq. 8.21 with 2p=0.5.

Eq. 8.25 can be used for an initial estimate of the inception index of a model propeller. That this equation also gives reasonable results for propellers with a strongly unloaded tip can be illustrated by the inception of the tip vortex on blade S at J=0.4, as shown in Plate 7.6. The tip vortex is near inception on the smooth blade and σ_n=2.2. Eq. 8.25 predicts σ_{ni}=2.06 in this condition.

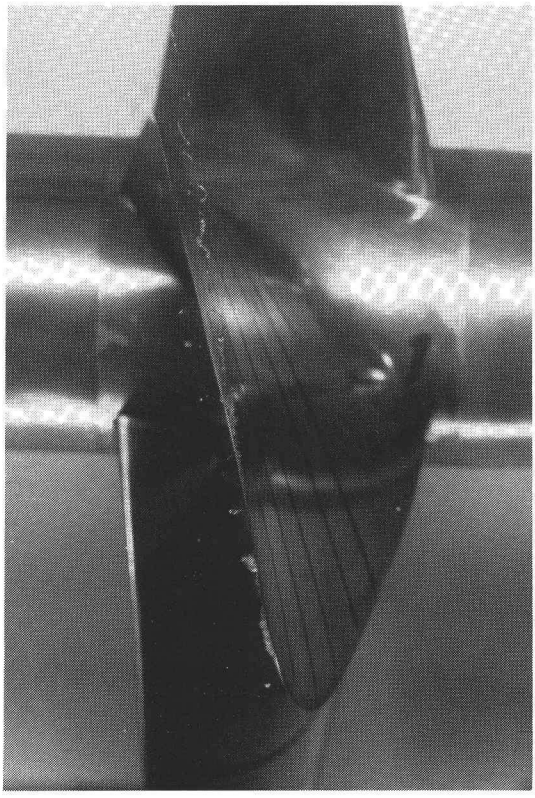

Fig. 8.24. Interaction between the tip vortex and pressure side cavitation. (Propeller V blade 1 at J;0.6, σ_n=1.46, Re_n=2.76x10^6).

Cavitation on the blade surface may strongly interact with the tip vortex, making the determination of a cavitating radius impossible. An example of such a case is shown in Fig. 8.24 where cavitation at the pressure side of the blade interferes with the tip vortex, which was perfectly straight at a somewhat higher loading. The applicability of the present inviscid approach to cavitation inception in complicated and unsteady situations has still to be investigated.

9.Discussion

Those aspects of cavitation which cause undesirable effects have to be properly simulated on model scale. This simulation is discussed for sheet and bubble cavitation. Based on the experimental results in sections 6 and 7 and on the paint tests in section 3 cavitation patterns can be interpreted and scale effects can be recognized. Measures to avoid scale effects such as the application of electrolysis and of roughness at the leading edge are examined and it is concluded that roughness at the leading edge reduces scale effects on cavitation inception in many cases. The implications of scale effects on cavitation inception are discussed and some examples are given.

The purpose of cavitation tests on model propellers is the prediction of possibly detrimental effects of cavitation on the prototype. The main effects are vibrations, noise and erosion. The risk of erosion is generally judged from the appearance of a cavity on the propeller. The presence of bubble cavitation and cloudy cavitation behind a sheet as shown in Plate 7.5, is considered to be erosive. Sheet cavitation on the pressure side is also avoided because of erosion danger. The location and the strength of erosion can be measured by using erosion sensitive coating on the propeller surface (Lindgren and Bjärne, 1974).

Vibratory hull forces, generated by the propeller and specifically by sheet cavitation on the propeller can be measured by using pressure pick-ups in the hull (Van der Kooij, 1979), while noise, radiated by cavitation on the propeller, can be measured by hydrophones at some distance from the propeller. When the cavitation is limited to part of the blade area the effect on the lift and drag of the propeller sections is small and therefore cavitation influences the propeller performance and the unsteady moments and forces on the propeller shaft only slightly (van der Kooij, to be published). But cavitation does change the blade spindle torque of controllable pitch propellers (Pronk, 1980).

The experimental results in section 6 to 8 show that a delay of cavitation inception can eliminate extensive cavitation. Cavitation inception is therefore not only important for the determination of the condition at which cavitation starts, but also for conditions with significant amounts of cavitation. When a propeller operates in a wake behind a ship cavitation may occur over a period during every revolution, which means that inception takes place at every revolution. Proper scaling of cavitation inception is very important in these conditions, e.g. because the rate of growth or collapse, and thus the effects of the cavitation are strongly influenced by the moment of inception.

Proper scaling of cavitation inception requires knowledge of the conditions on the prototype. This knowledge is very restricted, although much experience has been gained relating the cavitation behaviour on model scale with the detrimental effects on full size in a statistical way. This experience includes specific test conditions in specific test facilities. The prediction of the conditions on the prototype are therefore often better than a comparison between results in various facilities suggests. (e.g. I.T.T.C. 1969, 1978).

The statistical approach also includes differences between cavitation on model scale and on full scale. The cavitation pattern on the prototype was observed in a few cases only. Consequently it might be possible that scale effects in the wake field are offset by scale effects in cavitation inception. Also when the risk of erosion is judged visually the interpretation of cavitation patterns from full-scale experiences can account for scale effects on cavitation. Large errors are, however, possible, with unconventional designs.

The prediction of the effects of cavitation from model tests can only be improved if the prediction is based on physical instead of on statistical methods. Proper scaling of inception is only the beginning of such a prediction, but it is essential. From the experimental results presented in the previous sections the conditions, required for proper scaling of inception, can be described.

9.1. BUBBLE CAVITATION

Inception of bubble cavitation was defined as the condition in which a gas bubble in the fluid becomes unstable and expands rapidly. This instability occurs close to the vapor pressure if the critical bubble radius is sufficiently large.

The relation between the critical bubble radius and the difference between the vapor pressure and the inception pressure is given by eq. 6.2. Typical sectional velocities on propeller blades are 15 to 35 m/sec on full scale. If it is e.g. required that $|\sigma+C_p(\min)|<0.02$ the critical radius to be larger than 46 to 8 μm respectively. At atmospheric pressure this means that the minimum initial bubble diameter ranges from 5 to 20 μm. Nuclei of that size are present in sea water (e.g. Keller and Weitendorf, 1978) and on the prototype cavitation inception can indeed be expected if the minimum pressure is close to the vapor pressure.

9.1.1. The presence of nuclei

Cavitation observations in the Depressurized Towing Tank without electrolysis (section 6.1) have shown that nuclei beyond 20 μm in diameter are not present. It was even found that in the Cavitation Tunnel nuclei beyond 10 μm in diameter were absent when the total air content was low (section 6.2). This was not expected because visual inspection of the test sections in the condition of Plate 6.6 (which is at the lowest tunnel pressure of 200 mbar) revealed many speckles in the flow under stroboscopic illumination against a dark background. It must be concluded therefore that these speckles were either solid particles or that they were too small in number to cause frequent bubble cavitation. Judging the nuclei content in the test section of a cavitation tunnel by visual observation is apparently deceiving.

When the test section is supersaturated the amount of free gas rises rapidly, as was also found by Arndt and Keller (1976). In Fig. 6.7 the test section was 2.5 times supersaturated and bubble cavitation was present. However, in such a condition the test section is misty and the observations are impaired by the free gas in the test section. Bubbles of large diameter (about 5 mm) are also present in the flow, which may lead to "gaseous" cavitation, as will be considered later.

9.1.2. The effects of a lack of nuclei

When cavitation inception is delayed by a lack of nuclei a large cavity volume will appear at inception. When only a single nucleus expands a large bubble cavity is formed, as is shown e.g. in Plate 6.5 (at a current of 0.4 A/m) and in Plate 6.10 (on the smooth blade without electrolysis).

The rate of growth of an unstable gas bubble can be estimated from eq. 1.5 with p=p(min).

$$\dot{R}^2 = -\frac{1}{3}V^2 \ (\sigma + C_p(\min)) \tag{9.1}$$

The maximum radius R_{max} can be found from

$$R_{max} = R_{crit} + \dot{R}t \tag{9.2}$$

but since R_{crit} is always small relative to R_{max} the initial size can be neglected. So with $R_{max} = \dot{R}t$ and with $t = c/2V$ we have

$$\frac{R_{max}}{c} = C\left(-\frac{\sigma + C_p(\min)}{12}\right)^{\frac{1}{2}} \tag{9.3}$$

in which C is a constant of order the 1 and c is the chordlength of the propeller section.

In Plate 6.10 we have

$\sigma + C_p(\min) = -0.20$ (from Fig. 6.8)

$c = 0.12$ m

$R_{max} = 0.009$

from which it follows that the constant C is about 0.6.

The maximum cavity radius R_{max} is independent of the propeller revolutions. An increase in propeller revolutions will therefore not increase the bubble size. Large incidental bubble cavities indicate a difference between σ and $-C_p(\min)$ and thus a lack of nuclei. When the number of bubble cavities increases, as shown in Plate 6.5, the maximum size of the cavities decreases. Large amounts of bubble cavities occur only when large amounts of nuclei are present. It is, however, very difficult to supply such an amount of nuclei. When the smooth blade in Plate 6.12 had been perfectly smooth no bubble cavities at all would have been present. Even in Fig. 6.11 with a very high free gas content in the tunnel, the bubble cavities are still fairly large.

When the supply of nuclei is concentrated behind a roughness element a bubble stream occurs, leading to a spot cavity with a bubbly surface, as shown in Plate 6.6. The occurrence of such spots, starting away from the leading edge, are an indication that bubble cavitation is delayed by a lack of nuclei.

On commercial propellers bubble cavitation often occurs in the region near the hub, where the sectional Reynolds number is low. The initial bubble size, required for inception, is large while the sensitivity to surface irregularities is low. Bubble cavitation on model scale in those regions can therefore easily be overlooked. Artificial generation of nuclei can improve this and create bubble cavitation in regions where it generally is not found on model scale. Although this is an improvement of the simulation of bubble cavitation, the statistical rule that bubble cavitation is always highly erosive may need refinement in such a case, because the conditions in those regions can be such that the bubble cavities do not cause erosion.

9.1.3. The determination of inception

9.1.3.1. The effect of the Reynolds number.

If the cavitation index at inception is measured when only very small nuclei are present inception will be found at too low a cavitation index and this can be recognized, as mentioned above, by the size of the bubbles at inception. An increase of the number of revolutions, which implies an increase of the Reynolds number, often increases the inception index, suggesting that the inception of bubble cavitation depends on the character of the boundary layer. The increase in Reynolds number has, however, only an indirect effect: the sensitivity for surface irregularities and consequently the generation of nuclei increases.

9.1.3.2. The definition of inception.

The inception index should be determined in a condition with ample nuclei when the cavities reach a size which is just visible. When a fixed bubble size at inception is defined, however, the cavitation index becomes dependent on the model size. The precise definition of inception of bubble cavitation remains arbitrary. According to eq. 9.3 the maximum cavity size should be related with the chordlength of the propeller. The best way to determine inception of bubble cavitation is the acoustic way.

9.1.3.3. Gaseous cavitation.

Another risk of defining cavitation inception when very small cavities occur is gaseous cavitation. Gaseous cavitation occurs when gas bubbles in the flow grow to a visible size without being unstable when they arrive in a region where the pressure is close to the vapor pressure. The radius R_v of such a gas bubble can be found from static bubble equilibrium

$$R_v = \sqrt{\frac{K}{2s}} \tag{9.4}$$

with

$$K = R_o^3 \left(p_o - p_v + \frac{2s}{R_o}\right). \tag{9.5}$$

When inception is called at a certain bubble size the risk of gaseous cavitation increases with increasing pressure p_o, so with increasing propeller revolutions. Gaseous cavitation can be avoided when R_v from eq. 9.4 is small relative to the radius of the visual bubble cavities at inception, which requires a maximum initial bubble size.

The inception data from Table 6.1 can be analysed in more detail now, and we will consider the condition with the high air content in the tunnel and the inception condition in the Depressurized Towing Tank. The relevant data are

	CT	DTT	
Visually determined σ_{ni}	1.3	1.4	
Re_n	2.11×10^6	1.1×10^6	
V(0.7R)	14.21	9.3	m/sec
R_{crit} (from eq. 6.2)	50	110	μm
$p_o - p_v$	2.52×10^4	1.17×10^4	Pa
R_o(min)	20	40	μm
R_o(max)	180	240	μm

The maximum initial radius was determined from eqs. 9.4 and 9.5 with R_v = 1 mm. When cavitation inception is called when smaller bubbles are present R_o(max) becomes smaller.

In the Depressurized Towing Tank it requires bubbles of 480 μm in

diameter to cause gaseous cavitation. The electrolysis wires will not generate such large bubbles and gaseous cavitation can therefore be excluded. In the cavitation tunnel at the high air content it is very well possible that free gas bubbles of 360 μm in diameter were present in the flow and gaseous cavitation cannot be excluded.

9.1.3.4. Bubble screening

In the cavitation tunnel particles or bubbles were always visible, even at low air contents, but they did not cause bubble cavitation. Large bubbles were also observed in the Depressurized Towing Tank in Fig. 6.4, again without causing bubble cavitation. The mechanism behind this is not clear. Possibly some screening of bubbles takes place, as Johnson and Hsieh (1966) calculated. But screening occurs only at a sharp pressure peak and the pressure distribution in the condition of Fig. 6.4 on the suction side had no low pressure peak. Calculations of Kodama et al (1979) on a headform with only a moderately sharp pressure peak showed no effect of the bubble path on the inception pressure. Possibly the number density of the large bubbles is still too low, making the presence of bubble cavities so infrequent, that they are overlooked when photographs are taken. This has to be further investigated.

9.1.3.5. The use of propeller B as a standard cavitator

An interesting application of propeller B is its use as a standard cavitator.

Schiebe (1969) proposed a headform with an attached boundary layer for the measurement of the nuclei content in a tunnel. The combination of tunnel velocity and pressure, which can be investigated with such an axisymmetric body, is different, however, then when a propeller is tested. When e.g. the hemispherical body was investigated for the I.T.T.C. (Johnsson, 1969) most tunnels were operating at a much higher velocity and at a much lower pressure than normal. This drawback can be surmounted by using a propeller with attached flow only, like propeller B at J=0.6. When the blade surface of this propeller is polished it may act as a standard cavitator for bubble cavitation in realistic tunnel conditions.

9.1.4. Generation of nuclei by electrolysis

The main parameter controlling the maximum bubble size from a wire is the gas production parameter π_1 (eq. 5.5) at the cathode. This is illustrated in Plate 5.4. The gas production parameter at the cathode can be written as

$$\pi_1 = \frac{I/\ell}{(p_o - p_v)Vd} \frac{273+t}{273} \quad 1.16 \times 10^7 \qquad (9.6)$$

Here the effect of the surface tension on the gas pressure in the bubble has been neglected for reasons of simplicity, although it was shown in Plates 5.3 and 5.4 that this is not fully justified. The gas production parameter as defined in eq. 9.6 therefore only gives an indication of the real gas volume produced.

Fig. 6.2 shows a drastic effect of electrolysis. In this case the gas production parameter was 7.5×10^9 and the largest gas bubbles which were generated had a diameter of about 30 μm, which is about 0.1 times the wire diameter d. The gas production parameter $\pi_1 = 7.5 \times 10^{-9}$ is comparable to the situation in Plate 5.4 with a current of 4.5 A/m and there the largest bubbles were indeed of the order of 0.1 d. From Plate 6.5 it can be seen that an increase of the current increases the maximum diameter of the generated bubbles as well as their density. At a current of 0.4 A/m in Plate 6.5 the gas production parameter at the cathode is 2.6×10^{-9} and the minimum initial bubble diameter required for cavitation inception is about 20 μm or 0.07 d. From Plate 5.4 it can be seen that a bubble size of 0.2 d requires about 16 A/m or a gas production parameter of 3×10^{-8}.

These values give an idea of the maximum bubble size, generated behind an electrolysis wire and they show that electrolysis is only appropriate at low pressures and at low velocities. The majority of the gas is produced in very small bubbles and the largest bubbles are still only a fraction of the wire diameter. In a cavitation tunnel high currents are required to generate nuclei of adequate size, which is not attractive because this may lead to the collection of the explosive free gas in the tunnel. Therefore the method of artificial nuclei generation on the tunnel must be improved. In the Depressurized Towing Tank electrolysis is useful and to obtain consistent results the gas parameter as given in eq. 9.6 has to be maintained.

On the prototype only small nuclei are required for inception and those nuclei are present in large numbers behind a ship. Keller and Weitendorf (1978) measured 10 to 100 bubbles per m^3 in the range of 20-40 μm in diameter). To provide an equal number of expanding nuclei on model scale the number density of the nuclei above the minimum radius has to be scaled with λ^3, resulting in a very high number density on model scale.

Roughness at the leading edge provides a large number of nuclei (Plate 6.12 e.g.). It requires a high current to generate a similar number of expanding bubbles by electrolysis (Plate 6.5). It can therefore be expected that a fine screen of bubble cavitation as shown in Fig. 6.12 represents full-scale conditions.

The number of bubble cavities determines their maximum size. The effect of the number and of the size of bubble cavities on noise and erosion has not yet been investigated.

9.1.5. Generation of nuclei by roughness elements

The conditions in which bubbles are generated on roughness elements are not quite clear as yet. When the roughness does not cause a turbulent boundary layer it is also ineffective in generating nuclei. On the other hand it is possible that no nuclei are generated when the roughness elements are creating a turbulent boundary layer. This is shown in Plates 6.2 and 6.6. In Plate 6.6 the roughness elements have an adequate size relative to the boundary layer but the water at the roughness elements was not saturated. In Plate 6.2 the water was saturated but the height of the roughness was too low.

When roughness elements create turbulent streaks in the boundary layer in a flow with a low nuclei content, electrolysis causes spot cavities at such locations, as shown in Fig. 7.9.

9.2. SHEET CAVITATION

9.2.1. The effects of laminar boundary layer flow

The most striking result of the tests with sheet cavitation is the persistent lack of cavitation when the boundary layer is laminar in the low pressure region, irrespective of the nuclei content.

This result, in combination with the results of boundary layer observations, explains some scale effects often observed on propeller models, e.g. the fact that a sheet cavity on the prototype extends further inward than on the model (Bindel, 1969). On propeller S the tip was unloaded to avoid tip vortex cavitation, which caused a laminar separation bubble at inner radii. Commercial propellers have a heavier loaded tip and a critical radius or separation radius occurs, as sketched in Fig. 3.9. This separation radius limits sheet cavitation on model scale.

When the separation radius is large, the sheet cavity on model scale can be considerably suppressed, as is illustrated in Fig. 9.1., taken from Kuiper (1978a). In such a case application of roughness at the leading edge can strongly reduce scale effects.

Laminar regions frequently occur on model scale and can explain the experiences obtained with scale effects on propeller performance as already formulated in 1939 at the third I.T.T.C. conference. There it was concluded that scale effects on performance were largest at a small slip ratio on propellers with profiles with a rounded nose (ogival sections at that time) and if the blade sections at the root were thick (quoted by Yokoo, 1975).

The reason why cavitation is inhibited by a laminar boundary layer flow is not clear. A possible explanation might be that screening of nuclei occurs, as Johnsøn and Hsieh (1966) and Peterson (1972) calculated. Large bubbles are pushed away from the blade surface by the pressure gradient near the nose. Because the pressure peak is very sharp they do not arrive in the minimum pressure region on the blade. An extreme example of large bubbles which do not cause inception is shown in Fig. 7.9. However, such a phenomenon was also observed on propeller B in this condition where bubble screening is not plausible, so other effects may be involved in this case. Bubble screening should therefore be further investigated.

9.2.2. The effect of a laminar separation bubble

In a condition where the boundary layer is on the verge of laminar separation (Plate 3.17) the extent of sheet cavitation is extremely sensitive to the accuracy of the leading edge geometry. This is not primarily caused by the fact that the minimum pressure is very sensitive to the blade shape, but by the fact that laminar separation is sensitive to the blade shape, which in turn controls inception. This is a scale effect and application of roughness

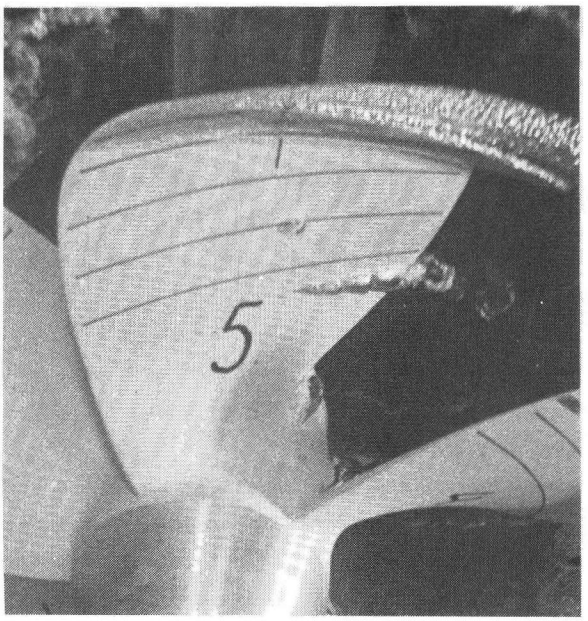

Fig. 9.1. Example of suppression of sheet cavitation by laminar boundary layer flow.

at the leading edge can reduce the scale effects and also reduce the differences between the blades.

The region where laminar separation occurs is also very sensitive to the propeller loading and, in the unsteady case, to the velocity distribution in the wake. Because sheet cavitation occurs only when laminar separation takes place the induced pressure fluctuations become also very sensitive to the wake distribution. This is partly caused by scale effects on cavitation inception but might erroneously be attributed to the wake distribution. Wake scale effects are overestimated in such a case.

Regions of laminar boundary layer flow may also influence the hull pressure fluctuations by changing the growth and collaps of sheet cavities. The sheet cavity, shown in Fig. 9.2, is collapsing while the propeller blade leaves the wake peak behind a model. The pressure distribution apparently causes laminar regions in the boundary layer and in those regions gaps occur in the sheet cavity on model scale. Application of roughness at the leading edge can prevent these gaps and decrease the scale effects on the measured pressure fluctuations on the hull.

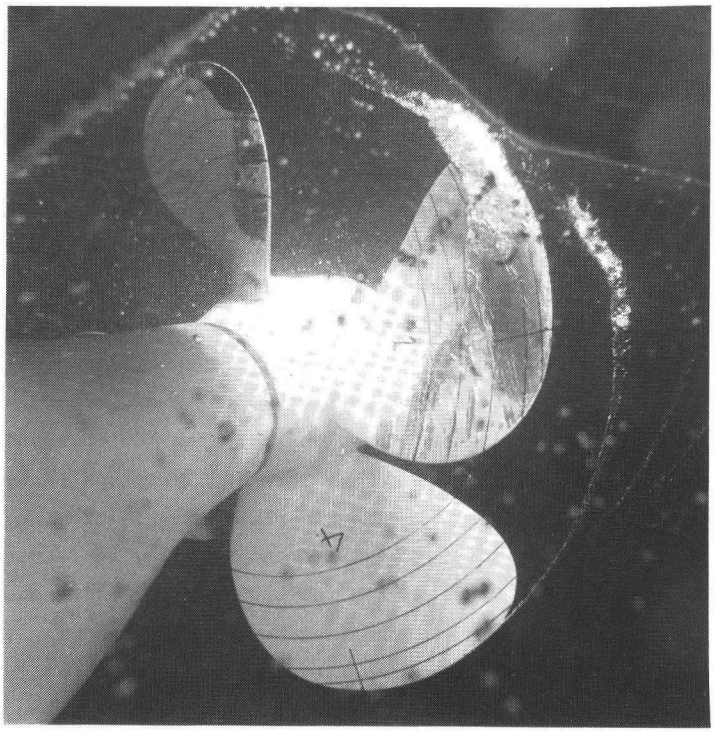

Fig. 9.2. Irregular disappearance of sheet cavitation due to laminar boundary layer flow.

9.2.3. Cavitation inception on roughness elements

The penalty for the application of roughness at the leading edge is early inception on the roughness elements. This effect, however, is very small, as shown in Fig. 7.11. The roughness elements create regions of low pressures in the boundary layer, with a length scale equal to the roughness height or less. Nuclei which arrive in this low pressure region may become unstable while the mean pressure is still higher than the vapor pressure. However, bubble growth will be arrested by the mean pressure and the cavitation which occurs on the roughness elements will remain small.

The precise inception pressure of sheet cavitation can no longer be visually determined when the blade is roughened at the leading edge, but generally this pressure is of no practical importance. For the risk of erosion or pressure fluctuations the pressure at which the sheet has a certain minimum length and starts to grow with decreasing pressure, as described in Fig. 7.11, is more important.

9.2.4. The effects of a lack of nuclei.

In the Depressurized Towing Tank the nuclei content is so low that inception in the region of a laminar separation bubble is sometimes inhibited, as Fig. 7.2 shows. This occurs especially on the blade where the separation bubble is longest, as on blade 2 of propeller S in Plate 3.15. Apparently the pressure at reattachment is important. When more small nuclei were present in the flow, as is the case in the Cavitation Tunnel, the sheet cavity appears at much higher pressures and the inception pressure is independent of the nuclei content, as is also found on headforms. (Arakeri and Acosta, 1979). The nuclei size, needed for inception in a region of a laminar separation bubble in the boundary layer is very small, which indicates that low pressures occur on a microscopic scale in the reattachment region. Very small nuclei, arriving in these low-pressure regions, will grow in size and develope into bubble cavities when the mean pressure at reattachment is below the vapor pressure, as Holl and Carroll (1979) showed with the bubble ring, which occurred in the reattachment region on a hemispherical headform.

When the pressure peak is sharp the mean pressure at reattachment will be close to the pressure at separation and the minimum pressure, so inception will take place when $\sigma=-C_p(\min)$. On full scale, where the Reynolds number is high, transition will occur before laminar separation can take place and the mean pressure at transition, which is also close to the minimum pressure, will determine inception. Although the mechanism is different the scale effects on inception of sheet cavitation will be small if a laminar separation bubble occurs on model scale. In this case the Reynolds number and the nuclei content have no influence.

The measurement of pressure fluctuations on the model hull can therefore best be carried out at the correct Froude number to maintain the correct pressure distribution in height over the propeller disk. An increase in Reynolds number will not improve the simulation of sheet cavitation. Roughness at the leading edge can always be applied; when a laminar separation bubble occurs on the smooth blade it has no effect, when attached laminar flow occurs it reduces scale effects on sheet cavitation.

Noordzij (1976) found a strong influence of electrolysis on the occurrence of sheet cavitation. It was verified that this occurred in a region with a separation bubble. This is a phenomenon, typical for facilities with

a very low free air content like the Depressurized Towing Tank, where a lack of nuclei can inhibit inception of sheet cavitation.

An example of such a phenomenon is given in Fig. 9.3 on a commercial propeller. All blades are smooth and extensive sheet cavitation occurs, except on one blade. The difference between the blades is within manufacturing tolerances, but paint tests show that the laminar separation bubble on blade 4 is, in chordwise direction, somewhat longer than on the other blades. In a situation with only very few nuclei this can mean the difference between extensive sheet cavitation or no cavitation at all, as occurs in Fig. 9.3.

In an unsteady condition where the propeller blade moves through the wake peak at every revolution this phenomenon occurs more frequently. When the pressure fluctuations on the hull are measured the result is a pressure signal which is not periodic with the blade frequency. When periodicity with

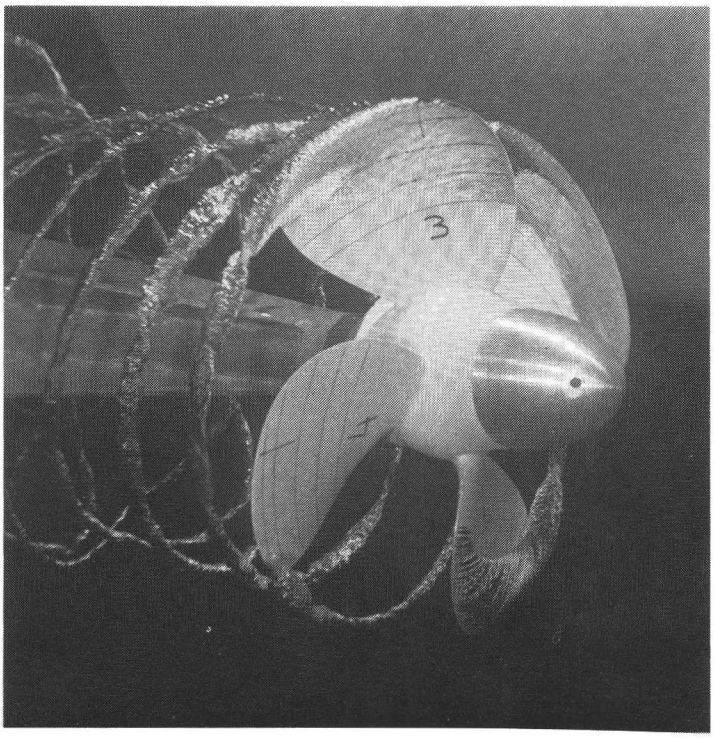

Fig. 9.3. Example of the effect of a lack of nuclei when a laminar separation bubble is present at the leading edge.

the blade frequency is still assumed, e.g. when periodic sampling and averaging is applied, an erroneous harmonic contents of the hull pressure fluctuations is obtained.

Application of roughness at the leading edge in a condition with low nuclei content will generate sheet cavitation in all conditions. The roughness elements, which are located in the minimum pressure region, create microscopic low-pressure regions which cause the gas to come out of solution, similar as with bubble cavitation. This was found in all conditions because the roughness elements are located in a position with a very thin boundary layer and near the minimum pressure where the water is nearly always supersaturated. Instead of electrolysis, application of roughness at the leading edge can therefore be a method to prevent scale effects on sheet cavitation. This can be used when the nuclei content is low and electrolysis should be avoided.

10. Conclusions

This investigation has made it clear that the cavitation pattern on a model propeller has to be interpreted in terms of the propeller boundary layer and of the nuclei contents of the water. The tendency to carry out cavitation observations at the highest possible Reynolds number to avoid scale effects on cavitation inception is not justified in general. The main effect of a high propeller Reynolds number is that surface irregularities become more pronounced, which is favourable for cavitation inception. Application of roughness at the leading edge in a controlled manner is more effective.

Roughness at the leading edge can also generate nuclei and can make an additional supply of nuclei, e.g. by electrolysis, unnecessary.

The most important results of this study can be summarized as follows:

1. The calculation method, used to determine the pressure distribution on the blades, gives results which correctly predict the cavitation behaviour of the investigated propellers, provided that inception takes place near the vapor pressure. The two-dimensional treatment of thick blade sections near the hub needs further refinement.

2. The boundary layer on the suction side of a propeller exhibits laminar regions in many conditions. An increase of the Reynolds number does not generally move the transition region to the leading edge, but may cause a local turbulent boundary layer due to surface irregularities. Laminar separation at the leading edge is extremely important on model scale and the separation radius determines the radial extent of sheet cavitation.

3. Application of roughness at the leading edge can be applied without an unacceptable influence on the minimum pressure at the leading edge. Roughness affects the propeller performance, which has to be investigated more closely, specifically the effect of roughness on the lift of the propeller sections.

4. The average size of nuclei from a wire is very small. Larger bubbles with a diameter in the order of 0.1 times the wire diameter are only generated if sufficient gas is produced. These larger bubbles are then formed by coalescence in the Kármán vortices behind the wire.

   The gas production parameter at the cathode for the generation of bubbles of that size should be at least 10^{-8}.

5. Visual determination of the free gas contents of a test section is deceiving. A low number density of large bubbles gives the impression that sufficient nuclei are present. In cases of bubble cavitation a lack of nuclei can be recognized by large single bubble cavities. Spot cavities also reveal that a lack of nuclei inhibits bubble cavitation.

6. For a proper scaling of bubble cavitation the number density of the nuclei should be high. A method to accomplish this is the application of roughness at the leading edge.

7. A laminar boundary layer at the leading edge of a propeller blade inhibits cavitation inception independent of the nuclei content. Roughness at the leading edge can restore inception in that case.

8. A lack of nuclei can suppress sheet cavitation inception in the region of a laminar separation bubble in the boundary layer, but only very small nuclei are needed.

9. Roughness at the leading edge can cause cavitation inception if the mean pressure is higher than the vapor pressure. In a sharp pressure peak the cavity is, however, very small.

10. The circulation around the cavitating tip vortex is only a fraction of the total vortex strength of the tip vortex. The total vortex strength increases with distance to the propeller tip due to roll-up of the vortex sheet. The circulation around the cavitating core is nearly constant.

11. The radius of the cavitating core of a tip vortex is independent of Reynolds number and nuclei content. This can be used for the determination of cavitation inception, both on the model and on the full-scale propeller.

12. An attached tip vortex occurs when the boundary layer separates near the tip. Detached tip vortex cavitation occurs if the boundary layer is laminar near the tip.

APPENDIX 1 : THE GEOMETRY OF PROPELLER B, S AND V

RADIUS	CHORD	PITCH RATIO	MAX. CAMBER	MAX. THICKNESS
r/R	C/D	P/D	$f\ max/C$	$t\ max/C$
.200	.2426471	.7441176	.0218939	.1978788
.250	.2617647	.8020221	.0251404	.1820225
.300	.2779412	.8312500	.0274762	.1686508
.400	.3036765	.8593750	.0314165	.1446731
.500	.3235294	.8639706	.0317614	.1210227
.600	.3367647	.8459559	.0288210	.0977074
.700	.3347059	.7950368	.0228896	.0757576
.800	.3235294	.7066176	.0157386	.0568182
.850	.3025735	.6575368	.0119684	.0486027
.900	.2669118	.6093750	.0079201	.0413223
.950	.2036765	.5577206	.0041516	.0361011
.975	.1496324	.5299632	.0024570	.0368550

Table A1.1. Geometry of propeller B.

r/R	0.3		0.4		0.5		0.6		0.7		0.8		0.9		0.95	
s/c x100	BACK	FACE	BACK	FACE	BACK	FACE	BACK	FACE	BACK	FACE	BACK	FACE	BACK	FACE	BACK	FACE
0.0	.06647	.04623	.04961	.03223	.03602	.02148	.02596	.01411	.01986	.01012	.01670	.00864	.01632	.00916	.01755	.01024
2.5	.08597	.03619	.06705	.02091	.05115	.01254	.03847	.00722	.02917	.00527	.02247	.00544	.01984	.00718	.01996	.00864
5.0	.09847	.02486	.07844	.01531	.06120	.00837	.04687	.00415	.03572	.00295	.02769	.00364	.02279	.00570	.02211	.00727
7.5	.10835	.01987	.08759	.01169	.06932	.00561	.05369	.00237	.04116	.00152	.03170	.00238	.02532	.00455	.02402	.00608
10.0	.11683	.01601	.09548	.00898	.07637	.00400	.05964	.00117	.04585	.00061	.03511	.00156	.02758	.00360	.02575	.00503
15.0	.13093	.01030	.10868	.00520	.08823	.00166	.06969	-.00023	.05370	-.00038	.04081	.00059	.03130	.00226	.02862	.00342
20.0	.14194	.00657	.11905	.00296	.09765	.00050	.07771	-.00075	.06004	-.00076	.04543	.00005	.03421	.00141	.03083	.00228
25.0	.15070	.00396	.12742	.00154	.10522	-.00008	.08417	-.00087	.06511	-.00080	.04914	-.00020	.03655	.00081	.03259	.00144
30.0	.15776	.00194	.13415	.00047	.11134	-.00048	.08939	-.00090	.06918	-.00075	.05204	-.00026	.03836	.00042	.03395	.00082
40.0	.16630	.00011	.14236	-.00020	.11887	-.00039	.09584	-.00044	.07429	-.00037	.05577	-.00021	.04067	.00001	.03564	.00012
50.0	.16865	.00000	.14467	0.00000	.12102	0.00000	.09771	0.00000	.07576	0.00000	.05682	0.00000	.04132	.00000	.03610	.00000
60.0	.16471	.00170	.14100	.00116	.11773	.00075	.09492	.00048	.07357	.00035	.05521	.00035	.04028	.00041	.03527	.00050
70.0	.15282	.00688	.12991	.00471	.10780	.00306	.08653	.00196	.06702	.00141	.05045	.00133	.03715	.00164	.03283	.00195
75.0	.14373	.01093	.12144	.00752	.10022	.00492	.08013	.00317	.06201	.00231	.04675	.00220	.03474	.00262	.03093	.00309
80.0	.13235	.01615	.11087	.01118	.09077	.00738	.07216	.00480	.05570	.00358	.04213	.00335	.03178	.00384	.02872	.00440
85.0	.11873	.02250	.09822	.01567	.07948	.01042	.06263	.00683	.04814	.00519	.03667	.00472	.02836	.00520	.02622	.00562
90.0	.10306	.02978	.08367	.02080	.06648	.01388	.05167	.00914	.03959	.00687	.03052	.00615	.02459	.00659	.02347	.00732
95.0	.08562	.03771	.06744	.02634	.05198	.01759	.03943	.01158	.03010	.00858	.02376	.00757	.02048	.00801	.02048	.00890
97.5	.07626	.04189	.05873	.02924	.04419	.01951	.03285	.01283	.02505	.00939	.02023	.00818	.01832	.00870	.01892	.00968
100.0	.06647	.04623	.04961	.03223	.03602	.02148	.02596	.01411	.01986	.01012	.01670	.00864	.01632	.00916	.01755	.01024

Table A1.2. Blade section geometry of propeller B.

RADIUS	CHORD	PITCH RATIO	MAX. CAMBER	MAX. THICKNESS
r/R	c/D	P/D	f max./c	t max./c
.200	.2426471	.7867647	.0180303	.1643939
.250	.2617647	.8308824	.0168539	.1428371
.300	.2779412	.8676309	.0160714	.1234788
.400	.3036765	.9154412	.0155569	.0889831
.500	.3235294	.9284926	.0151705	.0613636
.600	.3367647	.9047794	.0147380	.0429039
.700	.3397059	.8393382	.0133658	.0332251
.800	.3235294	.7340074	.0103409	.0286364
.850	.3025735	.6784926	.0083232	.0278250
.900	.2669118	.6235294	.0059917	.0282369
.950	.2036765	.5659926	.0037906	.0309567
.975	.1496324	.5349265	.0023342	.0361179

Table A1.3. Geometry of propeller S.

r/R	0.3		0.4		0.5		0.6		0.7		0.8		0.9		0.95	
s/c x100	BACK	FACE	BACK	FACE	BACK	FACE	BACK	FACE	BACK	FACE	BACK	FACE	BACK	FACE	BACK	FACE
0.0	.05308	.03826	.03426	.02361	.01920	.01182	.00928	.00415	.00541	.00108	.00611	.00185	.01064	.00561	.01476	.00862
2.5	.06692	.02755	.04463	.01627	.02678	.00720	.01498	.00132	.00981	-.00071	.00948	.00049	.01309	.00433	.01685	.00726
5.0	.07567	.02178	.05130	.01248	.03179	.00500	.01887	.00016	.01299	-.00142	.01207	-.00018	.01515	.00338	.01872	.00609
7.5	.08252	.01774	.05659	.00992	.03582	.00362	.02205	-.00045	.01567	-.00175	.01429	-.00060	.01693	.00265	.02039	.00509
10.0	.08836	.01454	.06113	.00794	.03932	.00262	.02484	-.00080	.01799	-.00187	.01620	-.00080	.01851	.00206	.02190	.00420
15.0	.09802	.00971	.06869	.00505	.04520	.00130	.02957	-.00111	.02193	-.00180	.01942	-.00092	.02113	.00124	.02440	.00284
20.0	.10551	.00640	.07460	.00318	.04985	.00059	.03336	-.00107	.02514	-.00154	.02205	-.00086	.02319	.00073	.02634	.00189
25.0	.11144	.00400	.07931	.00189	.05359	.00019	.03643	-.00090	.02773	-.00119	.02418	-.00072	.02485	.00040	.02788	.00118
30.0	.11621	.00212	.08311	.00089	.05660	-.00010	.03891	-.00073	.02981	-.00086	.02585	-.00052	.02613	.00019	.02907	.00067
40.0	.12193	.00026	.08771	.00003	.06031	-.00016	.04200	-.00028	.03245	-.00029	.02801	-.00020	.02777	-.00001	.03055	.00010
50.0	.12348	.00000	.08898	.00000	.06136	0.00000	.04290	0.00000	.03323	0.00000	.02864	0.00000	.02824	0.00000	.03096	.00000
60.0	.12077	.00142	.08687	.00087	.05973	.00042	.04160	.00013	.03214	.00002	.02774	.00007	.02750	.00005	.03023	.00042
70.0	.11259	.00574	.08050	.00350	.05481	.00170	.03766	.00053	.02886	.00008	.02506	.00027	.02531	.00101	.02810	.00164
75.0	.10633	.00911	.07563	.00557	.05105	.00273	.03466	.00088	.02637	.00017	.02298	.00048	.02361	.00163	.02645	.00261
80.0	.09849	.01342	.06954	.00824	.04636	.00408	.03092	.00137	.02324	.00036	.02040	.00079	.02154	.00239	.02451	.00371
85.0	.08909	.01864	.06225	.01149	.04076	.00574	.02647	.00199	.01950	.00063	.01735	.00115	.01913	.00324	.02233	.00491
90.0	.07828	.02463	.05386	.01521	.03431	.00763	.02134	.00270	.01525	.00087	.01391	.00149	.01648	.00409	.01993	.00618
95.0	.06626	.03119	.04452	.01926	.02712	.00967	.01560	.00343	.01053	.00104	.01010	.00178	.01358	.00495	.01732	.00750
97.5	.05981	.03466	.03951	.02140	.02325	.01073	.01251	.00379	.00801	.00109	.00811	.00186	.01206	.00536	.01596	.00816
100.0	.05308	.03826	.03426	.02361	.01920	.01182	.00928	.00415	.00541	.00108	.00611	.00185	.01064	.00561	.01476	.00862

Table A1.4. Blade section geometry of propeller S.

RADIUS	CHORD	PITCH RATIO	MAX. CAMBER	MAX. THICKNESS
r/R	c/D	P/D	f max/c	t max/c
.200	.2426471	.7393382	.0246212	.1643939
.250	.2617647	.7391544	.0243680	.1432584
.300	.2779412	.7391544	.0238095	.1250000
.400	.3036765	.7389706	.0225182	.0949153
.500	.3235294	.7386029	.0211364	.0696591
.600	.3367647	.7382353	.0201419	.0486900
.700	.3397059	.7389706	.0195887	.0318182
.800	.3235294	.7409926	.0203409	.0193750
.850	.3025735	.7431985	.0211422	.0150668
.900	.2669118	.7459559	.0220386	.0119835
.950	.2036765	.7503676	.0232852	.0110108
.975	.1496324	.7527574	.0233415	.0124079

Table A1.5. Geometry of propeller V.

s/c x100 \ r/R	0.3		0.4		0.5		0.6		0.7		0.8		0.9		0.95	
	BACK	FACE	BACK	FACE	BACK	FACE	BACK	FACE	BACK	FACE	BACK	FACE	BACK	FACE	BACK	FACE
0.0	.04620	.03118	.03063	.01925	.01787	.00952	.00712	.00128	-.00162	-.00574	-.00898	-.01233	-.01426	-.01784	-.01548	-.02008
2.5	.06095	.02108	.04226	.01201	.02686	.00485	.01393	-.00160	.00326	-.00680	-.00544	-.01190	-.01143	-.01637	-.01276	-.01826
5.0	.07050	.01593	.04943	.00851	.03291	.00251	.01865	-.00259	.00693	-.00685	-.00249	-.01109	-.00885	-.01487	-.01022	-.01650
7.5	.07809	.01251	.05608	.00629	.03783	.00129	.02256	-.00298	.01009	-.00658	.00016	-.01018	-.00647	-.01340	-.00783	-.01480
10.0	.08463	.00989	.06142	.00468	.04212	.00048	.02601	-.00310	.01288	-.00613	.00253	-.00920	-.00425	-.01197	-.00560	-.01319
15.0	.09554	.00613	.07037	.00248	.04938	-.00044	.03189	-.00294	.01767	-.00505	.00668	-.00724	-.00033	-.00929	-.00161	-.01020
20.0	.10410	.00376	.07744	.00126	.05518	-.00074	.03664	-.00245	.02163	-.00391	.01017	-.00544	.00300	-.00684	.00179	-.00754
25.0	.11043	.00216	.08312	.00054	.05985	-.00076	.04049	-.00187	.02485	-.00283	.01306	-.00386	.00579	-.00482	.00464	-.00567
30.0	.11644	.00094	.08770	.00001	.06363	-.00073	.04362	-.00137	.02746	-.00191	.01538	-.00251	.00804	-.00311	.00695	-.00339
40.0	.12313	-.00004	.09332	-.00021	.06840	-.00034	.04753	-.00045	.03080	-.00055	.01842	-.00068	.01102	-.00080	.01001	-.00087
50.0	.12500	0.00000	.09492	0.00000	.06966	0.00000	.04869	0.00000	.03182	0.00000	.01938	0.00000	.01198	0.00000	.01101	0.00000
60.0	.12196	.00114	.09243	.00069	.06785	.00032	.04707	.00001	.03050	-.00025	.01824	-.00049	.01092	-.00070	.00993	-.00078
70.0	.11278	.00460	.08492	.00279	.06159	.00131	.04219	.00006	.02655	-.00100	.01485	-.00199	.00774	-.00281	.00670	-.00314
75.0	.10576	.00733	.07919	.00446	.05697	.00212	.03848	.00014	.02355	-.00153	.01227	-.00307	.00534	-.00438	.00427	-.00490
80.0	.09849	.01086	.07205	.00665	.05122	.00322	.03387	.00032	.01981	-.00209	.00909	-.00436	.00240	-.00629	.00132	-.00707
85.0	.08650	.01517	.06350	.00935	.04434	.00460	.02837	.00059	.01533	-.00271	.00532	-.00588	-.00105	-.00856	-.00215	-.00966
90.0	.07442	.02010	.05366	.01243	.03643	.00617	.02203	.00088	.01025	-.00350	.00102	-.00769	-.00499	-.01124	-.00611	-.01268
95.0	.06047	.02546	.04269	.01574	.02760	.00782	.01494	.00112	.00457	-.00449	-.00378	-.00980	-.00942	-.01430	-.01058	-.01613
97.5	.05375	.02827	.03680	.01747	.02285	.00866	.01113	.00121	.00153	-.00507	-.00634	-.01100	-.01180	-.01599	-.01299	-.01803
100.0	.04620	.03118	.03063	.01925	.01787	.00952	.00712	.00128	-.00162	-.00574	-.00898	-.01233	-.01426	-.01784	-.01548	-.02008

Table A1.6. Blade section geometry of propeller V.

Appendix 2: AN EMPIRICAL CORRECTION FOR THE CALCULATED LIFT DISTRIBUTION.

It was found by Van Gent (1977) that when the lift distribution was calculated by the lifting surface program the calculated thrust was systematically smaller than the measured thrust, especially at higher propeller loadings. He therefore concluded that an additional velocity component was necessary for the sectional inflow velocity. He found that the proper slope of the thrust coefficient was obtained when the sectional inflow velocity was taken as:

$$V_p = \frac{\omega r}{\cos\beta_p} \qquad \text{(A2.1)}$$

This velocity is shown in Fig. 2.9 and it implies that the lift is increased with a factor V_p/V_E.

The empirical correction factor V_p/V_E yielded good results in the case of four commercial propellers (Kuiper, 1978b). One of these propellers, propeller A, is shown in Fig. A2.1 and the calculated and measured open-water curves are given in Fig. A2.2. The empirical correction is implemented in the standard program and gives a good agreement with the measurements.

Such an agreement was not found for propellers B, S and V (Kuiper, 1979b), where the calculation without the empirical correction yields better results

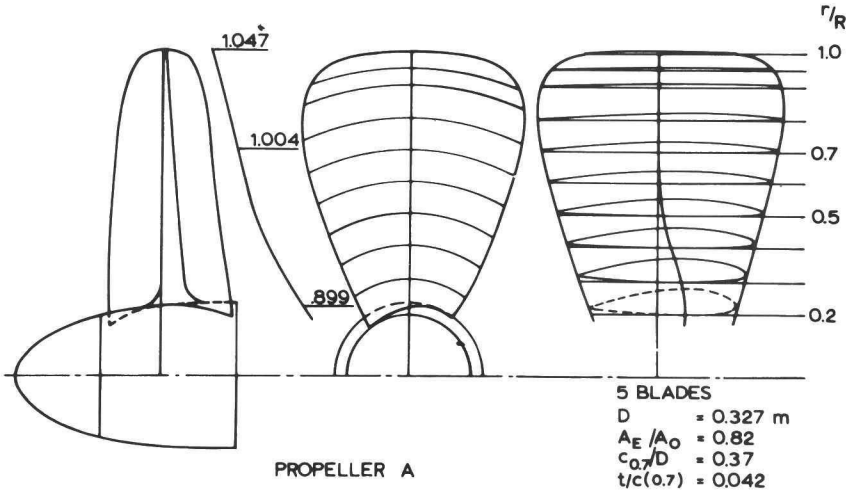

Fig. A2.1. Geometry of propeller A.

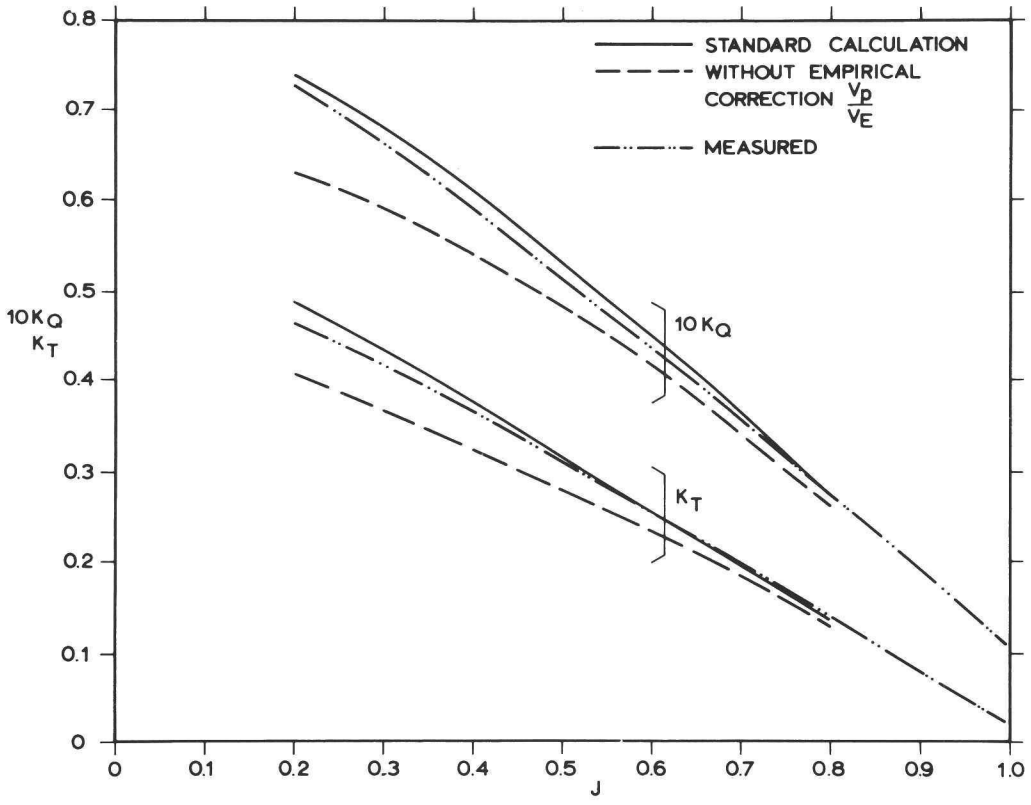

Fig. A2.2. Effect of the empirical correction V_p/V_E on the calculated open-water curves of propeller A.

for the thrust coefficient, as is shown for propeller S in Fig. A2.3.

The empirical correction V_p/V_e increases the propeller loading in the hub region, as shown for propeller S in Fig. A2.4. The loading of propeller A is concentrated near the tip, whereas the tip loading of propeller S is strongly reduced, as is shown by the radial pitch distribution in Fig. A2.5. It is therefore hypothesized that the correction, necessary to obtain the measured thrust coefficients by the calculations, is caused by the tip vortex, which increases the lift at the propeller tip.

Based on this assumption the correction V_p/V_e was replaced by a lift increase:

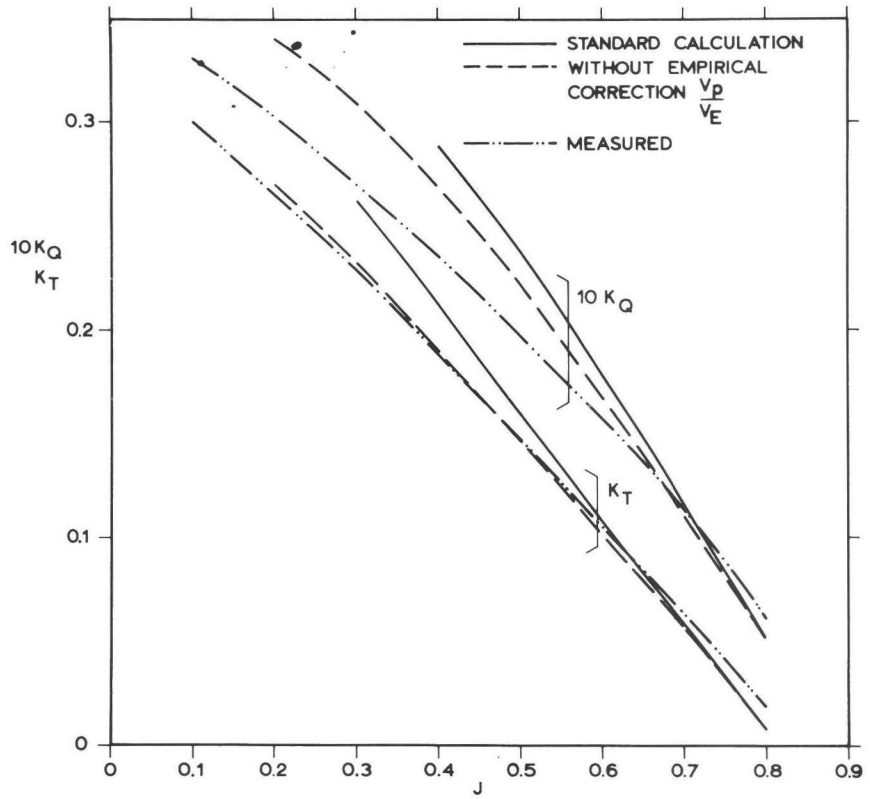

Fig. A2.3. Effect of the empirical correction V_p/V_E on the calculated open-water curves of propeller S.

$$\Delta L = \frac{k \frac{d\Gamma}{dr}}{(1+ \Delta x - r/R)^2} \qquad \text{(A2.2)}$$

where Γ is the radial distribution of the circulation, as calculated with the lifting surface theory and $d\Gamma/dr$ therefore represents the strength of the tip vortex. The constant k is an empirical factor, Δx represents a small distance between the tip vortex and the blade and avoids that the correction becomes singular at the tip.

With $\Delta x=0.1$ the measured thrust coefficient of propeller S could be calculated correctly at all advance ratio's, if the constant k was suitable chosen. The radial distribution of this lift increase is shown in Fig. A2.4 and is strongly concentrated in the tip region.

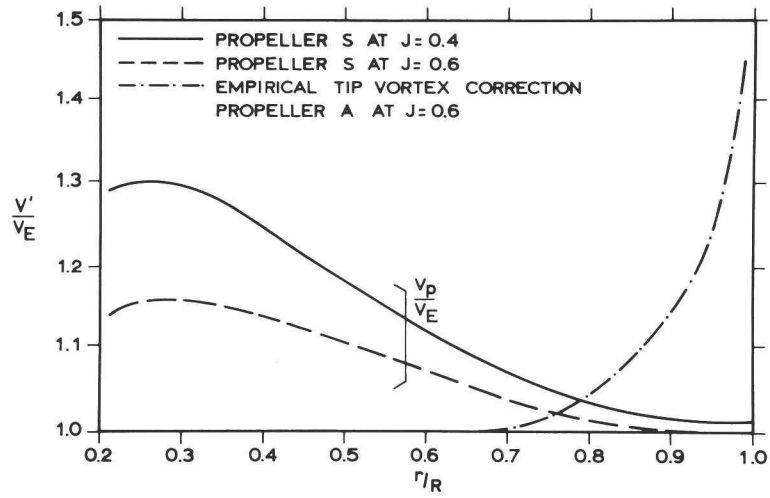

Fig. A2.4. Magnitude of the empirical correction V_p/V_E of propeller S.

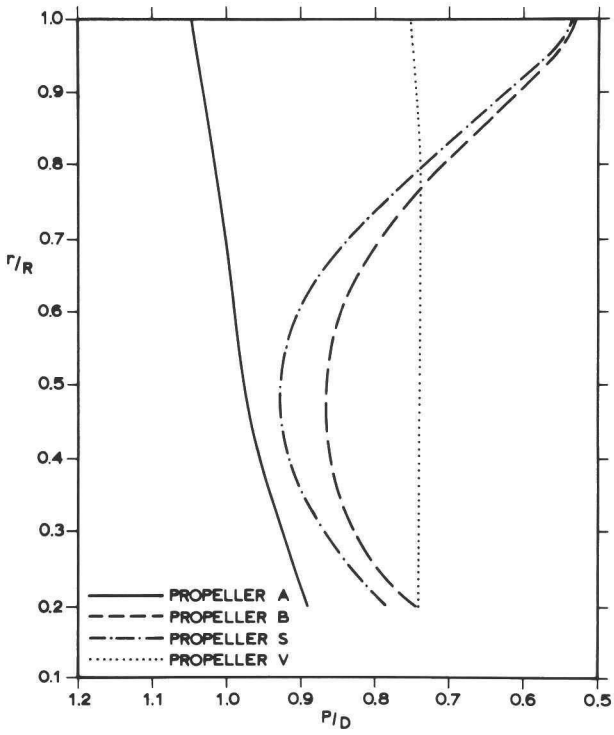

Fig. A2.5. Radial pitch distributions.

The application of eq. (A2.2) to propellers B, S and V with the same constant k resulted again in too high calculated thrust coefficients at low advance ratio's. This is specifically intriguing in the case of propeller V, which has a radial load distribution similar to that of propeller A, as can be seen from Fig. A2.5. Although a strong tip vortex is present at the blade tips of propeller V, no correction for the lift was necessary to obtain a good correlation of the thrust coefficient, as shown in Fig. A2.6. The cause of this might be the position of the tip vortex relative to the blade, as shown in Fig. A2.7. Propeller A, which requires a lift correction in the calculations, has a tip vortex originating at the leading edge and positioned on the suction side of the blade. Propeller V has a tip vortex which is not close to the blade over a significant distance.

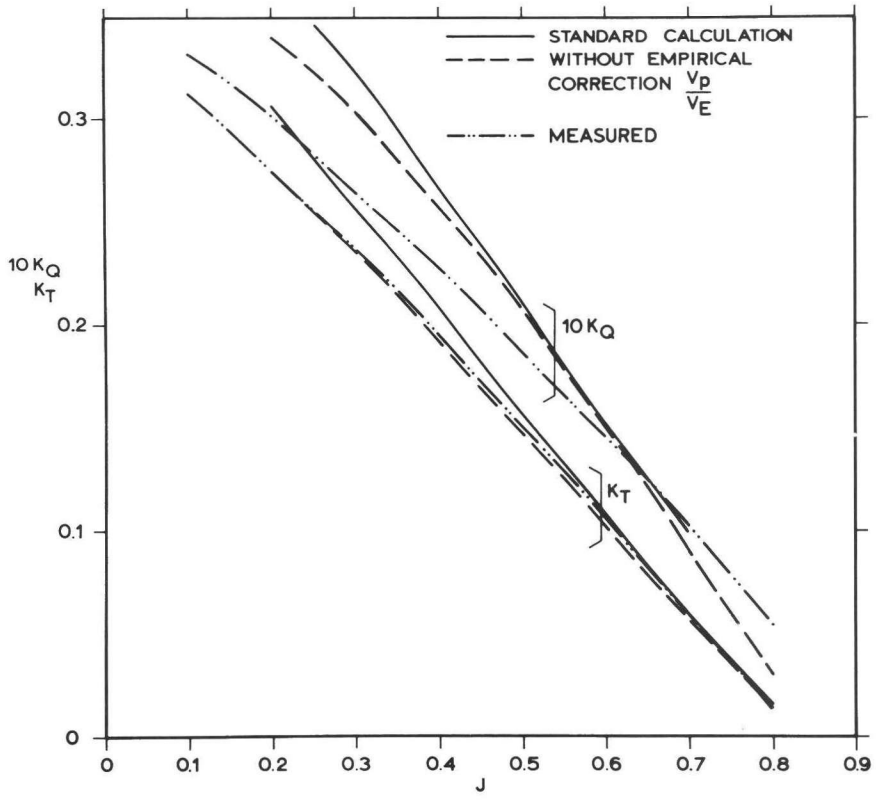

Fig. A2.6. Effect of the empirical correction V_p/V_E on the open-water curves of propeller V.

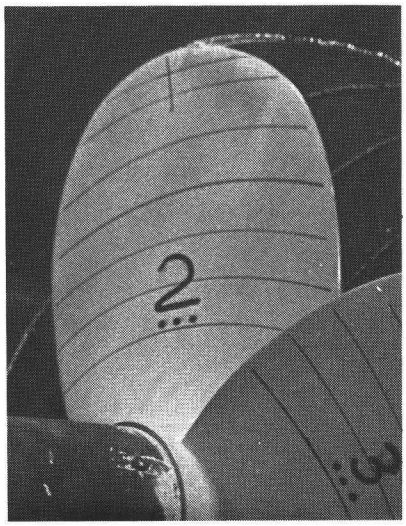

Propeller V

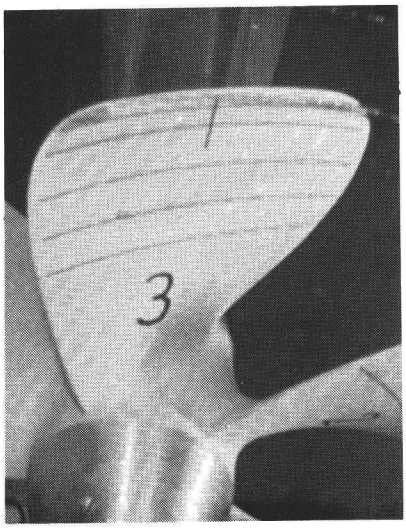

Propeller A

Fig. A2.7. Comparison of the positions of the tip vortices on propellers A and V.

On commercial propellers the position of the tip vortex is mostly like on propeller A, starting somewhere at the leading edge. On navy propellers, with a reduced tip loading, the position is typically like on propeller V. This may explain the general experience in the application of the standard program, that for navy applications the calculated thrust coefficients were too high, whereas it yielded good results for commercial propellers.

It is outside the scope of this study to investigate this phenomenon more closely. The correlation between the calculated and the measured thrust coefficient without any empirical correction justifies that such a correction is not used in the calculations of the pressure distribution, as carried out in Figs. 2.13 to 2.18. Application of the empirical correction V_p/V_E had an effect on the pressure distribution comparable in magnitude to the effect caused by variation of the helical pitch of the singular plane, as shown in Figs. 2.4 to 2.6.

REFERENCES

E. Achenbach, 1971, "Influence of Surface Roughness on the Cross-Flow around a Circular Cylinder", Journal of Fluid Mech., Vol. 46, pp 321-335.

E. Achenbach, 1968, "Distribution of Local Pressure and Skin Friction around a Circular Cylinder in Cross-Flow up to $Re=5x10^6$", Journal of Fluid Mech., Vol. 34, pp 625-639.

K. Albrecht, O. Bjorheden, 1975, "Cavitation Testing of Propellers in a Free Surface Tunnel utilizing Micro Air Bubble Control", Journal of Fluids Eng., p 523.

V.H. Arakeri, 1975, "A Note on the Transition Observations on an Axisymmetric Body and Some Related Fluctuating Wall Pressure Measurements", Trans. A.S.M.E., Journal of Fluids Eng.

V.H. Arakeri, 1973, "Viscous Effects in Inception and Development of Cavitation on Axisymmetric Bodies", Cal. Inst. of Technology, Pasadena, Rep. No. Eng. 183-1.

V.H. Arakeri, A.J. Acosta, 1973, "Viscous Effects in the Inception of Cavitation on Axisymmetric Bodies", Trans. A.S.M.E., Journal of Fluids Eng., pp 519-528.

R.E.A. Arndt, 1976, "Cavitation on Model Propellers with Boundary Layer Trips", Conference on Polyphase Flow, New Orleans.

R.E.A. Arndt, A.P. Keller, 1976, "Free Gas Content Effects on Cavitation Inception and Noise in a Free Shear Flow", Proc. I.A.H.R. Symposium, Paris, pp 3-16.

R.E.A. Arndt, A.T. Ippen, 1968, "Rough Surface Effects on Cavitation Inception", Trans. A.S.M.E., Journal of Basic Eng., pp 249-261.

B.W. Benson, 1966, "Cavitation Inception on Three-Dimensional Roughness Elements", David Taylor Model Basin, Rep. No. 2104.

M.L. Billet, E.M. Gates, 1979, "A Comparison of Two Optical Techniques for Measuring Cavitation Nuclei", A.S.M.E. Int. Symp. on Cavitation Inception, New York.

M.C. Billet, J.W. Holl, 1979, "Scale Effects on Various Types of Limited Cavitation", A.S.M.E. Int. Symp. on Cavitation Inception, New York.

S.G. Bindel, 1969, "Comparison between Model and Ship Cavitation", Twelfth I.T.T.C., Cavitation Committee, App. III, pp 365-370.

F.G. Blake Jr., 1949, "The Tensile Strength of Liquids", Harvard Acoustics Res. Lab. TM 12.

J.C. Bohn, 1972, "The Influence of Surface Irregularities on Cavitation: A Collation and Analysis of New and Existing Data with Application to Design Problems", Penn.State Univ., Ordnance Res.Lab., TM 72-223.

L.J. Briggs, 1950, "Limiting Negative Pressure of Water", Journal of Applied Physics, Vol. 21, pp 721-722.

M.V. Casey, 1974, "The Inception of Attached Cavitation from Laminar Separation Bubbles on Hydrofoils", Inst. of Mech. Engineers, Conference on Cavitation, Edinburgh, Scotland.

N. Chandrashekhara, 1976, "Analysis of the Tip Vortex Cavitation Inception at Hydrofoils and Propellers", Schiffstechnik, Heft 112.

J.W. Daily, V.E. Johnson Jr., 1956, "Turbulence and Boundary Layer Effects on Cavitation Inception from Gas Nuclei", Trans. A.S.M.E., Vol. 78, pp 1695-1706.

W. Davis, R.W. Fox, 1967, "An Evaluation of the Hydrogen Bubble Technique for Qualitative Determination of Fluid Velocities within Clear Tubes", Trans. A.S.M.E., Journal of Basic Eng., pp 771-781.

M. Dohrendorf, K. Kienappel, R. Voss, 1978, "Experimentelle und Theoretische Bestimmung der Druckverteilung an einem Propeller im Simulierten Schiffsnachstrom", Schiffstechnik, Vol. 25.

C. duP. Donaldson, 1971, "A Brief Review of the Aircraft Trailing Vortex Problem", Aeron. Res. Associates of Princeton, Princeton N.J., Rep. No. 155.

H.A. Dwyer, W.J. McCroskey, 1971, "Crossflow and Unsteady Boundary Layer Effects on Rotating Blades", A.I.A.A. Journal, Vol. 9, pp 1498.

M. van Dyke, 1964, "Perturbation Methods in Fluid Mechanics", Applied Mathematics and Mechanics, Vol. 8, Academic Press, New York-London.

P.S. Epstein, M.S. Plesset, 1950, "On the Stability of Gas Bubbles in Liquid-Gas Solutions", Journal of Chemical Physics , Vol. 18, pp 1505-1509.

A. Fage, J.H. Warsap, 1929, "The Effects of Turbulence and Surface Roughness on the Drag of a Circular Cylinder", Aeron. Res. Committee, Rep. and Mem. No. 1283.

E.G. Feindt, 1956, "Untersuchungen über die Abhängigkeit des Umschlages Laminar Turbulent von der Oberflächenrauhigkeit und der Druckverteilung", Jahrbuch der Schiffbautechnischen Gesellschaft, Band 50, pp 180-205.

H.G. Flynn, 1964, "Physics of Acoustic Cavitation", W.P. Mason, ed. Vol. I, Part B, Academic Press, New York-London.

F.E. Fox, K.F. Herzfeld, 1954, "Gas Bubbles with Organic Skin as Cavitation Nuclei", Journal of the Acoust. Soc. of Am., Vol. 26, pp 984-989.

M. Gaster, 1966, "The Structure and Behaviour of Laminar Separation Bubbles", Agard Conference on Separated Flows, Proc. No. 4, pp 814-854.

E.M. Gates, 1977, "The Influence of Freestream Turbulence, Freestream Nuclei Populations and a Drag-Reducing Polymer on Cavitation Inception on Two Axisymmetric Bodies", Cal. Inst. of Technology, Rep.No. Eng. 183-2.

D.E. Gault, 1955, "An Experimental Investigation of Regions of Separated Laminar Flow", N.A.C.A. Technical Note 3505.

W. van Gent, 1975, "Unsteady Lifting Surface Theory for Ship Screws", Journal of Ship Research, Vol. 19.

W. van Gent, 1977, "On the Use of Lifting Surface Theory for Moderately and Heavily Loaded Ship Propellers", Netherlands Ship Model Basin, Publ. No. 536.

W. van Gent, 1979, "Derivation of Propeller Blade Section Properties from Lifting Surface Theory", Fourth Lips Propeller Symposium, Drunen, The Netherlands.

O. Güven, C. Farell, V.C. Patel, 1980, "Surface-Roughness Effects on the Mean Flow past Circular Cylinders", Journal of Fluid Mech., Vol. 98, pp 673-701.

E.N. Harvey, W.D. McElroy, A.H. Whiteley, 1947, "On Cavity Formation in Water", Journal of Applied Physics, Vol. 18, pp 162-172.

J.L. Hess, A.M.O. Smith, 1972, "Calculation of Potential Flow about Arbitrary Three-Dimensional Lifting Bodies", Douglas Aircraft Company, Rep. No. MDC-J 5679-01.

O.W. Hoïby, 1970, "Three-Dimensional Effects in Propeller Theory", Norwegian Ship Model Experiment Tank, Publ. No. 105.

J.W. Holl, 1960, "An Effect of Air Content on the Occurrence of Cavitation", Trans. A.S.M.E., Journal of Basic Eng., Vol. 82, pp 941-946.

J.W. Holl, J.A. Carroll, 1979, "Observations of the Various Types of Limited Cavitation on Axisymmetric Bodies", A.S.M.E. Int. Symp. on Cavitation Inception, New York.

J.W. Holl, A.L. Kornhauser, 1970, "Thermodynamic Effects on Desinent Cavitation on Hemispherical Nosed Bodies in Water at Temperatures from 80 Deg. F to 260 Deg. F", Trans. A.S.M.E., Journal of Basic Eng., p 44.

J.W. Holl, G.F. Wislicenus, 1961, "Scale Effects on Cavitation", Trans A.S.M.E., Journal of Basic Eng., pp 385-398.

J.H. Hoyt, J.J. Taylor, 1979, "A Photographic Study of Inception and Cavitation in Jet Flow", A.S.M.E. Int. Symp. on Cavitation Inception, New York.

D.Y. Hsieh, M.S. Plesset, 1960, "The Theory of Rectified Diffusion of Mass into Gas Bubbles", Cal. Inst. of Technology, Rep. No. 85-15.

T.T. Huang, 1979, "Cavitation Inception Observations on Six Axisymmetric Headforms", A.S.M.E. Int. Symp. on Cavitation Inception, New York, 1979.

T.T. Huang, D.E. Hannan, 1975, "Pressure Fluctuations in the Region of Flow Transition", D.W. Taylor N.S.R.D.C. Report No. 4728.

T.T. Huang, F.B. Peterson, 1976, "Viscous Effects on Model-Full Scale Cavitation Scaling", Journal of Ship Research, Vol. 20, p 215.

C.A. Johnsson, 1969, "Cavitation Inception on Headforms" (Further Tests), Proc. of the Twelfth I.T.T.C., Rome, pp 381-392.

V.E. Johnson, T. Hsieh, 1966, "The Influence of Trajectories of Gas Nuclei on Cavitation Inception", Sixth Symp. on Naval Hydrodynamics, Washington D.C., pp 163-178.

H. Kaden, 1931, "Aufwicklung einer Unstabilen Unstetigkeitsflache", Ing. Arch., Vol. 2, pp 140-168.

H. Kato, 1977, "An Experimental Study on the Pressure Fluctuations on a Propeller Blade in a Wake", Proc. of the Symposium on Hydrodynamics of Ship and Offshore Propulsion Systems, Oslo.

A.P. Keller, 1972, "The Influence of the Cavitation Nucleus Spectrum on Cavitation Inception Investigated with a Scattered Light Counting Method", Trans. A.S.M.E., Journal of Basic Eng., p 917.

A.P. Keller, 1974, "Investigations concerning Scale Effects of the Inception of Cavitation", Inst. of Mech. Eng., Conference on Cavitation, Edinburgh, Scotland, pp 109-118.

A.P. Keller, 1979, "Cavitation Inception Measurements and Flow Visualisation on Axisymmetric Bodies at two Different Free Stream Turbulence Levels and Test Procedures", A.S.M.E. Int. Symp. on Cavitation Inception, New York, 1979.

A.P. Keller, E.A. Weitendorf, 1978, "A Determination of the Free Air Content and Velocity in Front of the "Sidney Express" Propeller in connection with Pressure Fluctuation Measurements", Twelfth Symp. on Naval Hydrodynamics, Washington D.C., pp 300-318.

R.W. Kermeen, J.T. McGraw, B.R. Parkin, 1955, "Mechanism of Cavitation Inception and the Related Scale-Effects Problems", Trans. A.S.M.E., Vol. 77, pp 533-541.

P.S. Klebanoff, G.B. Schubauer, K.D. Tidstrom, 1955, "Measurements of the Effect of Two-Dimensional and Three-Dimensional Roughness Elements on Boundary Layer Transition", Journal of Aeron. Sciences, p 803.

R.T. Knapp, A. Hollander, 1948, "Laboratory Investigations of the Mechanism of Cavitation", Trans. A.S.M.E., Vol. 70, pp 419-435.

Y. Kodama, S. Tamiya, N. Take, H. Kato, 1979, "Observations of the Various Types of Limited Cavitation on Axisymmetric Bodies", A.S.M.E. Int. Symposium on Cavitation Inception, New York, pp 75-86.

J. van der Kooij, 1979, "Experimental Determination of Propeller-Induced Hydrodynamic Hull Forces in the N.S.M.B. Depressurized Towing Tank", R.I.N.A. Symp. on Propeller Induced Vibration, London, pp 73-86.

G. Kuiper, 1974, "Cavitation Testing of Marine Propellers in the N.S.M.B. Depressurized Towing Tank", Inst. of Mech. Eng., Conference on Cavitation,Edinburgh, Scotland.

G. Kuiper, 1978a, "Cavitation Scale Effects - A Case Study", Int. Shipb. Progress, Vol. 25, pp 81-90.

G. Kuiper, 1978b, "Scale Effects on Propeller Cavitation Inception", Twelfth Int. Symp. on Naval Hydrodynamics, Washington D.C., pp 400-426.

G. Kuiper, 1979a, "Modelling of Tip Vortex Cavitation on Ship Propellers", Fourth Lips Propeller Symposium, Drunen, The Netherlands.

G. Kuiper, 1979b, "Some Experiments with Distinguished Types of Cavitation on Ship Propellers", A.S.M.E. Int. Symposium on Cavitation Inception, New York.

H.W. Lerbs, 1951, "On the Effect of Scale and Roughness on Free Running Propellers", Journal of the Am. Soc. of Naval Eng., Vol. 63, p 58.

V.G. Levich, 1962, "Physico-Chemical Hydrodynamics", Prentice Hall, Inc., Englewood Cliffs, N.J., U.S.A.

M.J. Lighthill, 1951, "A New Approach to Thin Aerofoil Theory", The Aeron. Quarterly, Vol. III, pp 193-210.

H. Lindgren, "Ship Model Correlation Method Based on Theoretical Considerations", Proc. Twelfth I.T.T.C., Performance Committee, App. II, p 181.

H. Lindgren, E. Bjärne, 1974, "Studies of Propeller Cavitation Erosion", Inst. of Mech. Eng., Conference on Cavitation, Edinburgh, Scotland.

L.M. Mack, 1977, "Transition Prediction and Linear Stability Theory", AGARD Conference Proceedings No. 224, Lyngby, Denmark, pp 1.1 - 1.22.

R.L. Maltby (ed), 1962, "Flow Visualization in Wind Tunnels Using Indicators", AGARDograph 70.

M.A. Mavludoff, 1965, "Measurement of Pressure on the Blade Surface of Non-Cavitating Propeller Model", Proc. of the Twelfth I.T.T.C., Tokyo, pp 290-292.

B.W. McCormick Jr., 1962, "On Cavitation Produced by a Vortex Trailing from a Lifting Surface", Trans. A.S.M.E., Journal of Basic Eng., pp 369-379.

J.H.J. van der Meulen, 1976, "A Holographic Study of Cavitation on Axisymmetric Bodies and the Influence of Polymer Additives", Netherlands Ship Model Basin, Publ. No. 509.

J.H.J. van der Meulen, 1978, "A Holographic Study of the Influence of Boundary Layer and Surface Characteristics on Incipient and Developed Cavitation on Axisymmetric Bodies", Twelfth Symposium on Naval Hydrodynamics, Washington D.C., pp 433-451.

K. Meyne, 1972, "Untersuchung der Propeller Grenzschichtströmung und der Einfluss der Reibung auf die Propeller-Kenngrössen", Jahrbuch der Schiffbautechnischen Gesellschaft, Band 66, pp 317-402.

D.W. Moore, 1974, "A Numerical Study of the Roll-up of a Finite Vortex Sheet", Journal of Fluid Mech., Vol. 63, p 225.

D.W. Moore, P.G. Saffman, 1973, "Axial Flow in Laminar Trailing Vortices", Proc. Royal Soc., London, A333, pp 491-508.

Wm.B. Morgan, 1972, "Air Content and Nuclei Measurements", Thirteenth I.T.T.C., Berlin-Hamburg, Report of The Cavitation Committee, App.I, pp 639-656.

Wm.B. Morgan, V. Silovic, S.B. Denny, 1968, "Propeller Lifting Surface Corrections", Trans. S.N.A.M.E., Vol. 76.

H. Multhopp, 1955, "Methods for Calculating the Lift Distribution of Wings", Aeron. Research Counsil, R&M No. 288.

E.A. Neppiras, B.E. Noltink, 1951, "Cavitation Produced by Ultrasonics", Proc. Phys. Soc., London, pp 1032-1038.

L. Noordzij, 1976, "Some Experiments on Cavitation Inception with Propellers in the N.S.M.B. Depressurized Towing Tank", Int. Shipb. Progress, Vol. 23.

L. Noordzij, 1977, "A Note on the Scaling of Tip Vortex Cavitation Inception", Int. Shipb. Progress, Vol. 24.

D.M. Oldenziel, 1979, "Bubble Cavitation in relation to Liquid Quality", Delft Hydraulics Lab., The Netherlands, Publ. No. 211.

R. Oshima, 1961, "Theory of Scale Effects on Cavitation Inception on Axially Symmetric Bodies", Trans. A.S.M.E., Journal of Basic Eng., Vol. 83, pp 379-384.

P. van Oossanen, 1974, "Calculation of Performance and Cavitation Characteristics of Propellers Including Effects of Non-Uniform Flow", Netherlands Ship Model Basin, Publ. No. 457.

B.R. Parkin, 1952, "Scale Effects in Cavitating Flow", Ph.D. Dissertation, Cal. Inst. of Techn, Pasadena.

B.R. Parkin, J.W. Holl, 1954, "Incipient-Cavitation Scaling Experiments for Hemispherical and 1.5 Caliber Ogive-Nosed Bodies", Rep. N.Ord 7958-264, Ordnance Res. Lab., The Penn.State Univ.

B. Persson, 1973, "On Bounds for the Threshold Pressure Initiating Bubble Growth", Journal of Fluids Eng., Vol. 95, pp 98-102.

F.B. Peterson, 1972, "Hydrodynamic Cavitation and Some Considerations of the Influence of Free Gas Content", 9th Symposium on Naval Hydrodynamics, Paris, pp 1131-1180.

F.B. Peterson, F. Daniel, A. Keller, Y. Lecoffre, 1975, "Determination of Bubble and Particulate Spectra and Number Density in a Water Tunnel with Three Optical Techniques, Proc. Fourteenth I.T.T.C., pp 27-52.

R.M. Pinkerton, 1934, "Calculated and measured Pressure Distributions over the Midspan Section of the NACA-4412 Airfoil", NACA Rep. No. 569.

G.P. Platzer, W.G. Souders, 1979, "Tip Vortex Cavitation Delay with Application to Marine Lifting Surfaces. A Literature Survey", David W. Taylor N.S.R.D.C., Bethesda, Md, R&D. Rep. No. DTNSRDC-79/051.

G.P. Platzer, W.G. Souders, 1980, "Tip Vortex Cavitation Characteristics and Delay on a Three-Dimensional Hydrofoil", 19th American Towing Tank Conference, Ann Arbor, Mich.

M.S. Plesset, A. Prosperetti, 1977, Annual Review of Fluid Mechanics, Vol. 9, pp 145-185.

M.S. Plesset, 1949, "The Dynamics of Cavitation Bubbles", Trans. A.S.M.E., Journal of Applied Mech., pp 277-288.

M.S. Plesset, D.Y. Hsieh, 1960, "Theory of Gas Bubble Dynamics on Oscillating Pressure Fields", Physics of Fluids, Vol. 3, pp 882-892.

C. Pronk, 1980, "Blade Spindle Torque and Off-Design Behaviour of Controllable-Pitch Propellers", Thesis Delft University of Technology.

A. Robinson, J.A. Laurmann, 1956, "Wing Theory", Cambridge University Press, p 130.

A.H. Roodbergen, 1976, "Berekening van het Stromingsveld om een Vrijvarende Scheepsschroef met behulp van de Panelenmethode", Technical University Twente.

L. Rosenhead (ed), 1963, "Laminar Boundary Layers", Oxford at the Clarendon Press.

V.J. Rossow, 1973, "On the Inviscid Rolled-up Structure of Lift Generated Vortices", Journal of Aircraft, Vol. 11, pp 647-650.

T. Sasajima, 1975, "A Study on the Propeller Surface Flow in Open and Behind Condition", Proc. Fourteenth I.T.T.C., Vol. 3, p 711.

F.R. Schiebe, 1969, "The Influence of Gas Nuclei Size Distribution on Transient Cavitation near Inception", Univ. of Minnesota, St. Anthony Falls Hydr. Lab., Proj.Rep. 107.

H. Schlichting, 1968, "Boundary Layer Theory", McGraw-Hill, Sixth ed.

F.A. Schraub, S.J. Kline, J. Henry, P.W. Runstadler, A. Littell, 1965, "Use of Hydrogen Bubbles for the Quantitative Determination of Time Dependent Velocity Fields in Low Speed Water Flows", Trans A.S.M.E., Journal of Basic Eng., p 429.

D. Sette, F. Wanderlingh, 1967, "Thermodynamic Theory of Bubble Nucleation Induced in Liquids by High Energy Particles", Journal of the Acoust. Soc. of Am., Vol. 41, pp 1074-1075.

A.M.O. Smith, N. Gamberoni, 1956, "Transition, Pressure Gradient and Stability Theory", Douglas Aircraft Co., Rep. No. ES 26388.

J.R. Spreiter, A.H. Sacks, 1951, "The Rolling Up of the Trailing Vortex Sheet and its Effect on the Downwash behind Wings", Journal of Aeron. Sci. Vol. 18, pp 21-33.

M. Takahashi, M. Oku, 1977, "The Cavitation Characteristics of MAU-Type Propellers", Journal of the Soc. of Naval Arch. of Japan, Vol. 141.

Y. Takei, K. Kodama, Y Kurobe, 1979, "Measurements of Pressures on a Blade of a Propeller Model", Ship Research Institute, Tokyo.

A.C. Tory, K.H. Haywood, 1971, "The Hydrogen Bubble Technique of Flow Visualisation: Factors Affecting Bubble Size and Buoyancy", A.S.M.E. Fluids Eng. Conference, Pittsburg, Pa.

S. Tsakonas, W.R. Jacobs, M.R. Ali, "Propeller Blade Pressure Distribution Due to Loading and Thickness Effects", Journal of Ship Research, Vol. 23, pp 89-107.

T.Tsuda, S. Konishi, 1978, "Effects of Reynolds Number on Propeller Characteristics", Note to the I.T.T.C. Propeller Committee.

F. van de Walle, 1962, "On the Growth of Nuclei and the Related Scaling Factors in Cavitation Inception", Proc. Fourth Symp. on Naval Hydrodynamics, pp 357-404.

H.C. Wels, 1977, "Study of Thickness Effects on the Pressure Distribution at Propeller Blades Using Linearized Singularity Distributions", Delft Technological University, Dept. of Naval Architecture.

S.E. Widnall, 1975, "The Structure and Dynamics of Vortex Filaments", Annual Review of Fluid Mechanics, Vol. 7, pp 141-166.

L. van Wijngaarden, 1967, "On the Growth of Small Cavitation Bubbles by Convective Diffusion", Int. Journal of Heat and Mass Transfer, Vol. 10, pp 127-134.

T. Yamazaki, 1978, "On Some Tank Test Results with a Large Model Propeller - 0.95 m in Diameter", Journal of the Soc. of Naval Arch. of Japan, Vol. 144.

K. Yokoo, 1975, "Review of Scale Effect on Propellers", Proc. Fourteenth I.T.T.C., Propeller Committee, pp 448-457.

NOMENCLATURE

		Dimension
a_c	radius of the cavitating vortex core	m
a_t	radius of the trailing vortex	m
a_v	radius of the viscous core of a vortex	m
C	- gas concentration in a fluid	$kg\ m^{-3}$
	- constant or coefficient	-
C_D	drag coefficient	-
C_f	friction coefficient	-
C_p^*	pressure coefficient $\frac{p-p_o}{\frac{1}{2}\rho V_e^2}$	-
C_p	pressure coefficient $\frac{p-p_o}{\frac{1}{2}\rho V^2}$	-
C_{ps}	pressure coefficient on a smooth surface	-
c	chord of a propeller section or wing	m
D	- diffusion coefficient	$m^2 sec^{-1}$
	- propeller diameter	m
d	wire diameter	m
d_b	bubble diameter	m
F_s	leading edge force due to singularity	N
F_{s1}	viscous drag correction on a propeller section	N
F_{s2}	viscous lift correction on a propeller section	N
Fr	Froude number $\frac{U}{\sqrt{gD}}$	-
G	gas production per unit length	$m^2 sec^{-1}$
g	acceleration due to gravity	$m\ sec^{-2}$
H_p	Tschebycheff polynomials for chordwise lift distribution	-
h	- shaft immersion of propeller	m
	- thickness of paint layer	m
J	advance ratio $\frac{U}{nD}$	-

K	constant representing the amount of gas in a bubble	Nm
K_T	propeller thrust coefficient $\frac{T}{\rho n^2 D^4}$	-
K_Q	propeller torque coefficient $\frac{Q}{\rho n^2 D^5}$	-
k	- roughness height	m
	- coefficient (in eq. 8.10)	-
k_s	equivalent sand roughness height	m
L	lift of propeller section	N
ℓ	length of electrolysis wire	m
ℓ_s	length of a laminar separation bubble	m
m	- exponent	-
	- mass of gas in a bubble	kg
N	number of spanwise control points in lifting surface calculation	-
n	number of propeller revolutions	sec^{-1}
P	number of chordwise control points in lifting surface calculation	-
p	- pressure	Nm^{-2}
	- exponent	-
p_a	pressure amplitude ratio	-
p_i	pressure at inception	Nm^{-2}
p_p	pressure in paint layer	Nm^{-2}
p_t	pressure in test section or in tank at shaft height	Nm^{-2}
p_v	vapor pressure	Nm^{-2}
p_o	- pressure at infinity	Nm^{-2}
	- initial pressure	Nm^{-2}
Q	propeller torque	Nm
R	- bubble radius	m
	- outer radius of propeller	m

R_{crit}	critical bubble radius	m
R_i	bubble radius at inception	m
R_{max}	maximum bubble or cavity radius	m
R_v	bubble radius at vapor pressure	m
R_o	initial bubble radius in undisturbed flow	m
Re	sectional Reynolds number $\frac{V.c}{\nu}$	-
Re_n	propeller Reynolds number $\frac{nD^2}{\nu}$	-
$Re_{\theta s}$	Reynolds number at separation $\frac{u_s \theta_s}{\nu}$	-
r	variable radius on a propeller or in a vortex	m
r_i	radius of propeller hub	m
s	- surface tension	Nm^{-1}
	- chordwise coordinate of a profile or propeller section	m
t	- time	sec
	- thickness of a propeller section	m
	- temperature	deg.
T	propeller thrust	N
U	- axial velocity of propeller	m sec^{-1}
	- tunnel flow velocity	m sec^{-1}
U_b	bubble velocity	m sec^{-1}
U_ℓ	fluid velocity at the roughness height in undisturbed flow	m sec^{-1}
u	perturbation velocity on a propeller section in chordwise direction	m sec^{-1}
u_f	fluid velocity in a propeller boundary layer in chordwise direction	m sec^{-1}
u_p	paint velocity on propeller surface in chordwise direction	m sec^{-1}
u_s	local outer flow velocity at separation	m sec^{-1}

u'	corrected perturbation velocity near the leading edge of a propeller section	m sec^{-1}
V	- flow velocity	m sec^{-1}
	- undisturbed inflow velocity of a propeller section	m sec^{-1}
V_a	spanwise velocity component near wing tip	m sec^{-1}
V_e	effective inflow velocity of a propeller section	m sec^{-1}
v	- perturbation velocity on a propeller section normal to the chord	m sec^{-1}
	- tangential velocity in a vortex	m sec^{-1}
v_f	fluid velocity in propeller boundary layer in radial direction	m sec^{-1}
v_p	paint velocity on propeller surface in radial direction	m sec^{-1}
We	Weber number $\frac{\rho U^2 R_{crit}}{s}$	-
w	- perturbation velocity on a propeller section in radial direction	m sec^{-1}
	- width of the wake behind a wire	m
x	- chordwise distance from the leading edge of a propeller section	m
	- distance from wing- or propeller tip	m
Z	number of propeller blades	-
α	angle of attack	rad
α_p	angle of paint streaks with tangential direction	rad
γ	circulation near the propeller tip	$m^2 sec^{-1}$
Γ	circulation	$m^2 sec^{-1}$
Γ_c	circulation around the cavitating core of a vortex	$m^2 sec^{-1}$
Γ_o	maximum circulation around a wing or propeller blade	$m^2 sec^{-1}$
δ	boundary layer thickness	m
δ_s	boundary layer thickness at the stagnation point	m

δ^*	displacement thickness of a boundary layer	m
θ	tangential direction (index)	-
θ_s	momentum thickness of a boundary layer at separation	m
λ	- scale ratio	-
	- contraction factor in vortex roll-up	-
μ	dynamic viscosity	$kg\ m^{-1} sec^{-1}$
ν	kinematic viscosity of fluid	$m^2 sec^{-1}$
ν_p	kinematic viscosity of paint	$m^2 sec^{-1}$
ρ	specific mass of fluid	$kg\ m^{-3}$
ρ_p	specific mass of paint	$kg\ m^{-3}$
ρ_ℓ	leading edge radius of a propeller section	m
ρ_g	specific mass of gas	$kg\ m^{-3}$
σ	sectional cavitation index $\frac{p_o - p_v}{\frac{1}{2}\rho v^2}$	-
σ_n	propeller cavitation index $\frac{p_o - p_v}{\frac{1}{2}\rho n^2 D^2}$	-
σ_i	cavitation index at inception	-
σ_{ir}	cavitation index at inception on a roughness element in constant pressure	-
τ	frictional stress	Nm^{-2}
ω	rotation rate of propeller	$rad\ sec^{-1}$
ω_o	resonance frequency of a gas bubble	sec^{-1}

SUMMARY

In model propeller testing it is assumed that cavitation starts when the minimum pressure on the blades is at the vapor pressure. Scaling of cavitation by maintaining Thoma's cavitation index is based on this assumption. However, to start cavitation (cavitation inception), nuclei are required to break the strong bond between the water molecules. The nuclei contents of the water can, therefore, be a factor in cavitation inception. Also the character of the boundary layer on the propeller blades may influence cavitation inception. The purpose of this investigation is to determine the inception conditions on model propellers and to devise test techniques to improve the prediction of cavitation on the prototype.

Three propeller models were designed and made to serve this purpose. Each propeller model exhibited a specific type of cavitation, viz. bubble, sheet and tip-vortex cavitation. The experiments were carried out in the Depressurized Towing Tank and in the large Cavitation Tunnel of the Netherlands Ship Model Basin in order to compare cavitation inception in both facilities. The experiments were carried out in uniform axial inflow.

A strongly simplified model of a nucleus is a spherical gas bubble in static equilibrium. This approach is described in section 1 and arguments are given why dynamic effects and gas diffusion can be ignored in cavitation inception on propeller models.

In section 2 the calculation of the pressure distribution on propellers in an undisturbed flow is described. The sensitivity of the calculation results to various assumptions made in the calculation method, is investigated.

The boundary layer on the blades of propeller models was investigated by paint tests. In section 2 regions with various types of boundary layer flow are given. Laminar flow and laminar separation are shown to be very important on model scale and very high Reynolds numbers are required to avoid these phenomena. Therefore the leading edge of the propeller blades was roughened with 60 μm carborundum to make the boundary layer turbulent. This technique is described in section 4. The influence of the roughness on the blade geometry is within the manufacturing accuracy of the propeller blades. Roughness may, however, cause early inception of cavitation, as is shown by tests with a cylinder in cross-flow.

The nuclei contents of the water was varied by electrolysis. The size of bubbles generated by wires is investigated in section 5.

The cavitation patterns on the propellers with bubble and sheet cavitation are shown in sections 6 and 7 respectively. These patterns are related with the calculated pressure distribution, with the character of the boundary layer as observed with paint tests and with the nuclei content of the water both with and without electrolysis. From the calculated pressure distribution cavitation inception can be predicted, provided that inception takes place at the vapor pressure. For the occurrence of bubble cavitation on model propellers additional nuclei must be generated in the tank as well as in the cavitation tunnel. Sheet cavitation is inhibited if the boundary layer is laminar. An increase of the Reynolds number does not improve this, although surface irregularities become effective at high Reynolds numbers. Application of roughness has a similar effect and may also produce nuclei. This technique may reduce scale effects on cavitation inception.

Tip-vortex cavitation is described in section 8. For the analysis of a cavitating tip vortex an inviscid description is used and a method to determine cavitation inception by measuring the radius of the cavitating core has been developed.

The results of this investigation may explain some of the scale effects which regularly occur in model testing, as discussed in section 9. This investigation also gives guidance to the application of electrolysis and to the use of roughened leading edges of model propeller blades.

The most important conclusions are summarized in section 10.

SAMENVATTING

Bij het beproeven van scheepsschroeven op modelschaal wordt aangenomen dat cavitatie ontstaat wanneer de laagste druk op een schroefblad gelijk is aan de dampdruk. Het verschalen van cavitatie door het constant houden van het cavitatiegetal van Thoma is op deze veronderstelling gebaseerd.

Voor het ontstaan van cavitatie (cavitatie inceptie) zijn echter kernen nodig die de sterke binding tussen de watermoleculen kunnen verbreken. Het kernengehalte van een vloeistof kan daarom mede bepalend zijn voor het ontstaan van cavitatie. Ook de grenslaag op het schroefblad kan het ontstaan van cavitatie beïnvloeden. Het doel van dit onderzoek is het bepalen van de condities waarin cavitatie op schroefmodellen ontstaat en het ontwikkelen van technieken die voorspelling van cavitatie op ware grootte verbeteren.

Daartoe werden drie schroefmodellen ontworpen en gemaakt, die elk slechts één bepaald type cavitatie vertoonden, namelijk bellen-, vlies- en tipwervel-cavitatie. De experimenten werden uitgevoerd zowel in de Vacuumtank als in de Cavitatietunnel van het Nederlands Scheepsbouwkundig Proefstation, zodat het ontstaan van cavitatie in beide faciliteiten kon worden vergeleken. Alle experimenten werden uitgevoerd in ongestoorde axiale aanstroming.

Een sterk vereenvoudigde voorstelling van een kern is een bolvormig gasbolletje dat in statisch evenwicht is met de omgeving. Deze benadering wordt in Hoofdstuk 1 beschreven. Ook wordt daarin aangegeven waarom dynamische verschijnselen en gas diffusie kunnen worden verwaarloosd bij het ontstaan van cavitatie op schaalmodellen.

In Hoofdstuk 2 wordt de berekening van de drukverdeling op schroeven in ongestoorde aanstroming beschreven. De afhankelijkheid van de berekenings-resultaten van allerlei veronderstellingen, die in de berekeningsmethode zijn gemaakt, wordt nagegaan.

De grenslaag op de bladen van schroefmodellen werd onderzocht met behulp van verfproeven. In Hoofdstuk 3 worden gebieden met verschillende typen grenslaagstroming aangegeven. Laminaire grenslaagstroming en laminaire loslating blijken op modelschaal erg belangrijk en er zijn zeer hoge Reynolds getallen nodig om deze verschijnselen te voorkomen. Daarom werd de voorkant van de schroefbladen kunstmatig ruw gemaakt met carborundumkorrels van ca. 60 µm, zodat de grenslaag turbulent werd. Deze techniek wordt beschreven in Hoofdstuk 4. De invloed van de aangebrachte ruwheid op de geometrie van de

schroefbladen is kleiner dan de fabricage-nauwkeurigheid van de schroefbladen. Ruwheid kan echter wel cavitatie inceptie vervroegen, zoals wordt aangetoond door proeven met een cylinder in dwarsstroming.

Het kernengehalte van de vloeistof is gevarieerd door toepassing van electrolyse. De grootte van de bellen die op dunne draden worden gevormd wordt onderzocht in Hoofdstuk 5.

Cavitatiebeelden op de schroeven met bellen- en vliescavitatie worden getoond in de Hoofdstukken 6 en 7 respectievelijk. Deze beelden worden in verband gebracht met de berekende drukverdeling, met het grenslaaggedrag op de bladen zoals dat met verfproeven is bepaald, en met het kernengehalte van de vloeistof, zowel met als zonder electrolyse. De berekende drukverdeling blijkt cavitatie inceptie goed te voorspellen mits maatregelen zijn getroffen om inceptie te laten plaatsvinden bij de dampdruk. Voor het verkrijgen van bellencavitatie op modelschroeven moeten daartoe kunstmatig kernen worden geproduceerd, ook in een cavitatietunnel. Vliescavitatie wordt volledig onderdrukt wanneer de grenslaag laminair is. Verhoging van het Reynoldsgetal verandert daaraan weinig, maar maakt dat de oppervlakteruwheid van de schroefbladen merkbaar wordt. Toepassing van ruwheid aan de voorkant van de bladen heeft een vergelijkbaar resultaat. Ook kan deze ruwheid kernen produceren. Aangetoond wordt dat schaaleffecten op cavitatie-inceptie daardoor worden verkleind.

Tipwervelcavitatie wordt onderzocht in Hoofdstuk 8. Bij de analyse van de caviterende tipwervel wordt een wrijvingsloze beschrijving van de caviterende tipwervel gebruikt en een methode voor het bepalen van cavitatie-inceptie door meting van de diameter van de caviterende wervelkern wordt beschreven.

De resultaten van dit onderzoek kunnen een aantal problemen verklaren die vaak voorkomen wanneer modelschroeven worden beproefd. Dit wordt beschreven in Hoofdstuk 9. Uit het onderzoek kunnen ook richtlijnen worden gevonden voor het toepassen van electrolyse en van ruwheid op schroefbladen.

De belangrijkste conclusies zijn samengevat in Hoofdstuk 10.

LEVENSBESCHRIJVING

De schrijver van dit proefschrift werd geboren te Rotterdam op 28 oktober 1943. Na in 1961 het diploma H.B.S.-B aan de 1e Christelijke H.B.S. te Rotterdam te hebben behaald, volgde hij de studie aan de Technische Hogeschool te Delft in de afdeling Scheepsbouwkunde, waar hij in 1968 afstudeerde. Inmiddels was hij reeds in dienst van het Nederlands Scheepsbouwkundig Proefstation getreden, waar hij onderzoek deed aan draagvlaktheorie voor scheepsschroeven. In 1970 werd hij hoofd van de Computerafdeling, in 1972 werd hij belast met de ontwikkeling en de leiding van de Vacuumtank te Ede. In 1976 werd een studiejaar doorgebracht op het Naval Ship Research and Development Center te Bethesda, Md, USA, als aanzet voor verder onderzoek naar het ontstaan van cavitatie. Dit proefschrift is een resultaat van dit onderzoek.

DANKWOORD

Ik ben de Directie van het Scheepsbouwkundig Proefstation dankbaar voor de gelegenheid die mij is geboden voor het schrijven van dit proefschrift en voor de aanmoediging daartoe, onder andere door mij in staat te stellen een jaar in de Verenigde Staten te studeren.

Bij de uitvoering van dit onderzoek zijn velen binnen het NSP betrokken geweest. De goede contacten met collega's in de researchgroep van het NSP waren erg belangrijk. Bijzonder veel dank ben ik verschuldigd aan Ir. J. van der Kooij, die door zijn critisch commentaar veel heeft bijgedragen tot dit onderzoek.

Voorts wil ik graag mijn dank betuigen aan de heer B. Millecam voor zijn aandeel in het fotografische werk, aan de heer W.C. Nieuwboer voor zijn vele taalkundige aanwijzingen, aan de heer J. Hootsen voor het vervaardigen van de meeste tekeningen en aan Mevr. G.P.M. Swint-Jongsma voor het persklaar maken van het manuscript.

PLATES

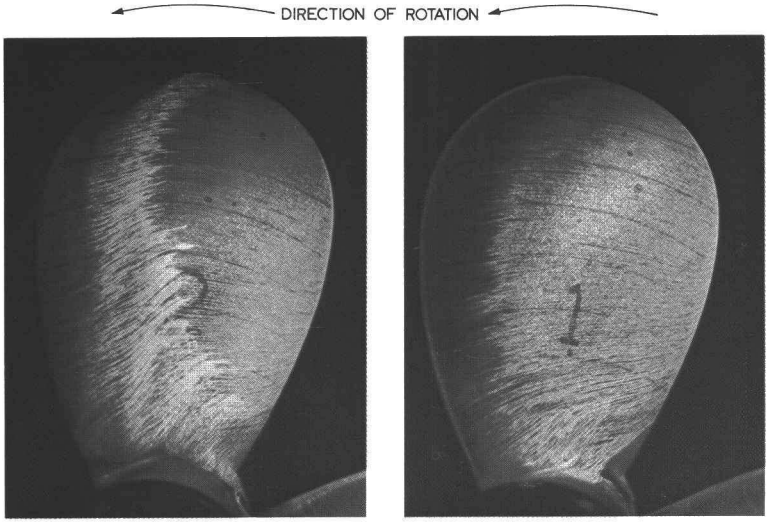

PLATE 3.1. EXAMPLE OF PAINT TEST WITH AND WITHOUT ROUGHNESS AT THE LEADING EDGE. PROPELLER B AT J=0,4, Re_{r_i}=1.7x10^6.

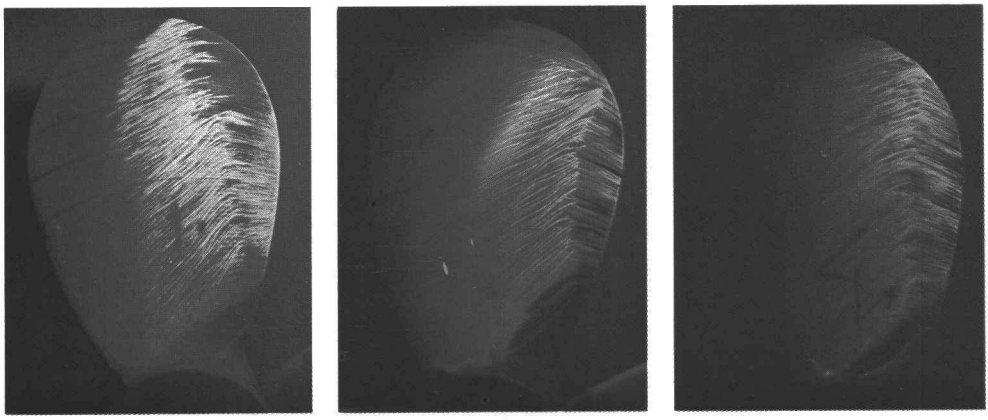

PLATE 3.4. PAINT PATTERNS ON THREE PROPELLERS WITH DIFFERENT SIZE (J=0.6, Re_{r_i}=1.1x10^6).

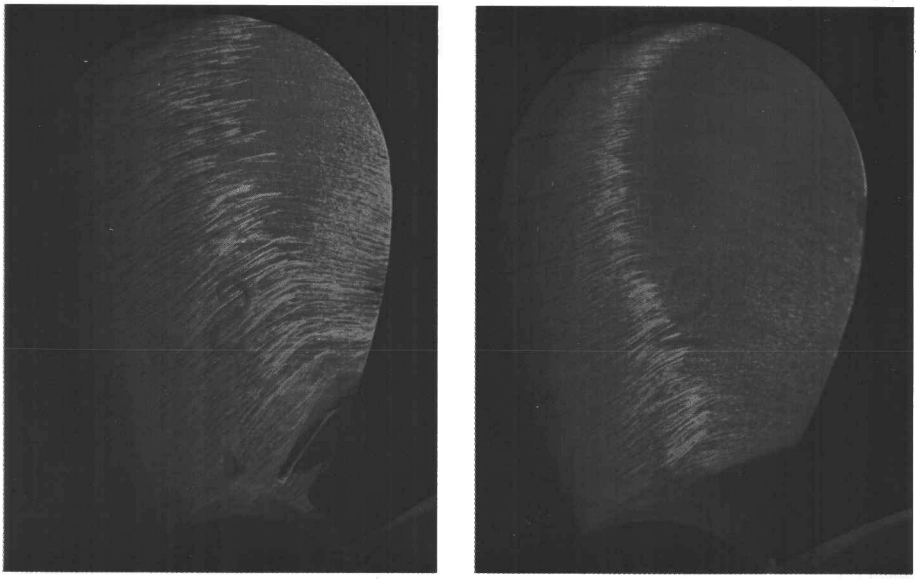

$Re_n = 1.1 \times 10^6$ $Re_n = 1.7 \times 10^6$

PLATE 3.10. PAINT PATTERN ON PROPELLER B AT J=0.6.

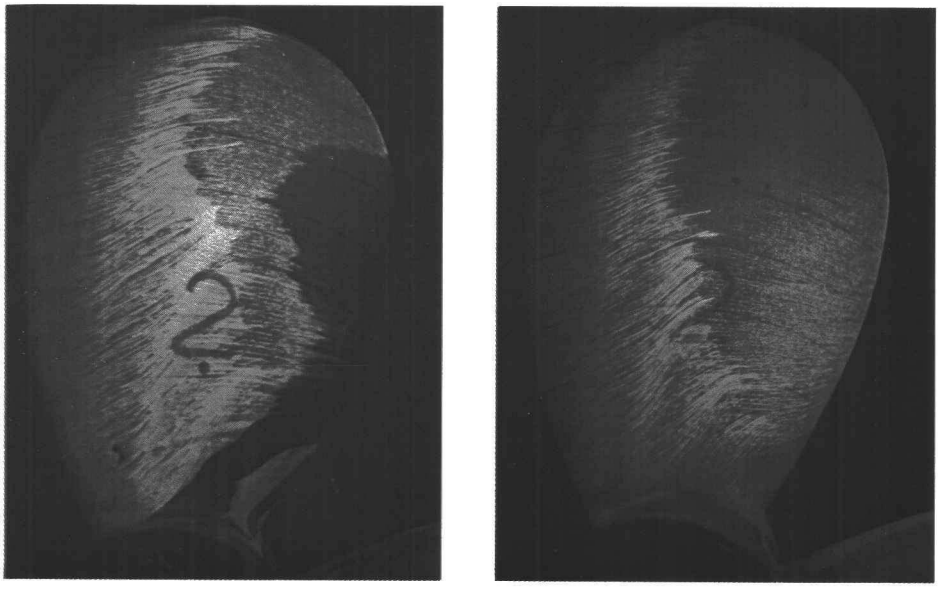

$Re_n = 1.1 \times 10^6$ $Re_n = 1.7 \times 10^6$

PLATE 3.11. PAINT PATTERN ON PROPELLER B AT J=0.4.

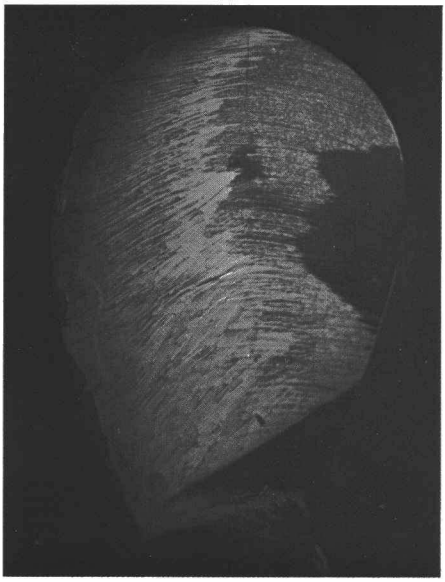

$Re_n = 1.1 \times 10^6$

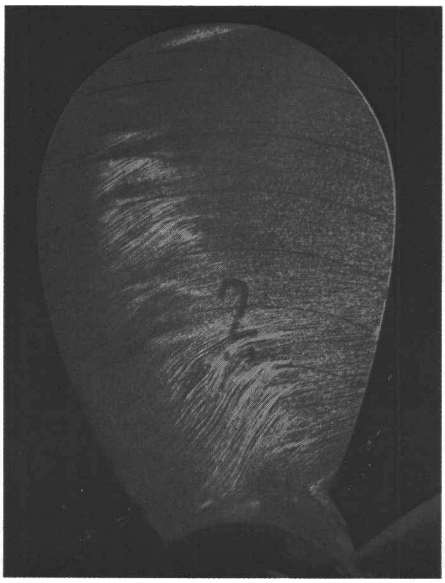

$Re_n = 1.7 \times 10^6$

PLATE 3.14. PAINT PATTERN ON PROPELLER S AT J=0.6.

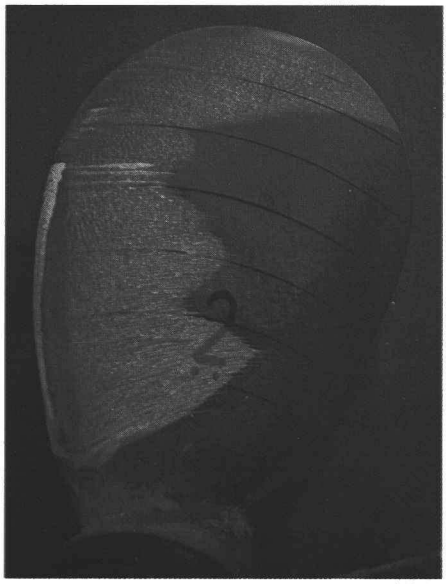

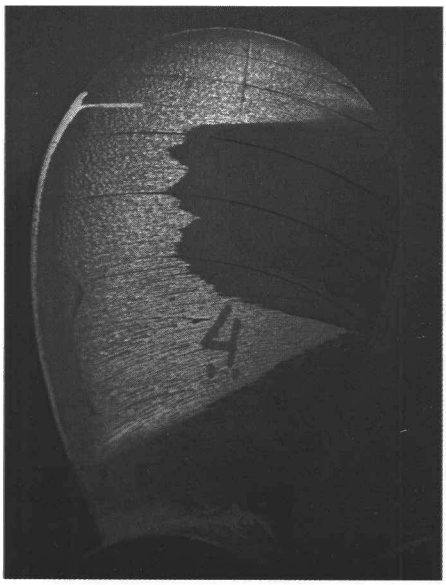

PLATE 3.15. PAINT PATTERN ON PROPELLER S AT J=0.4. $Re_n = 1.1 \times 10^6$.

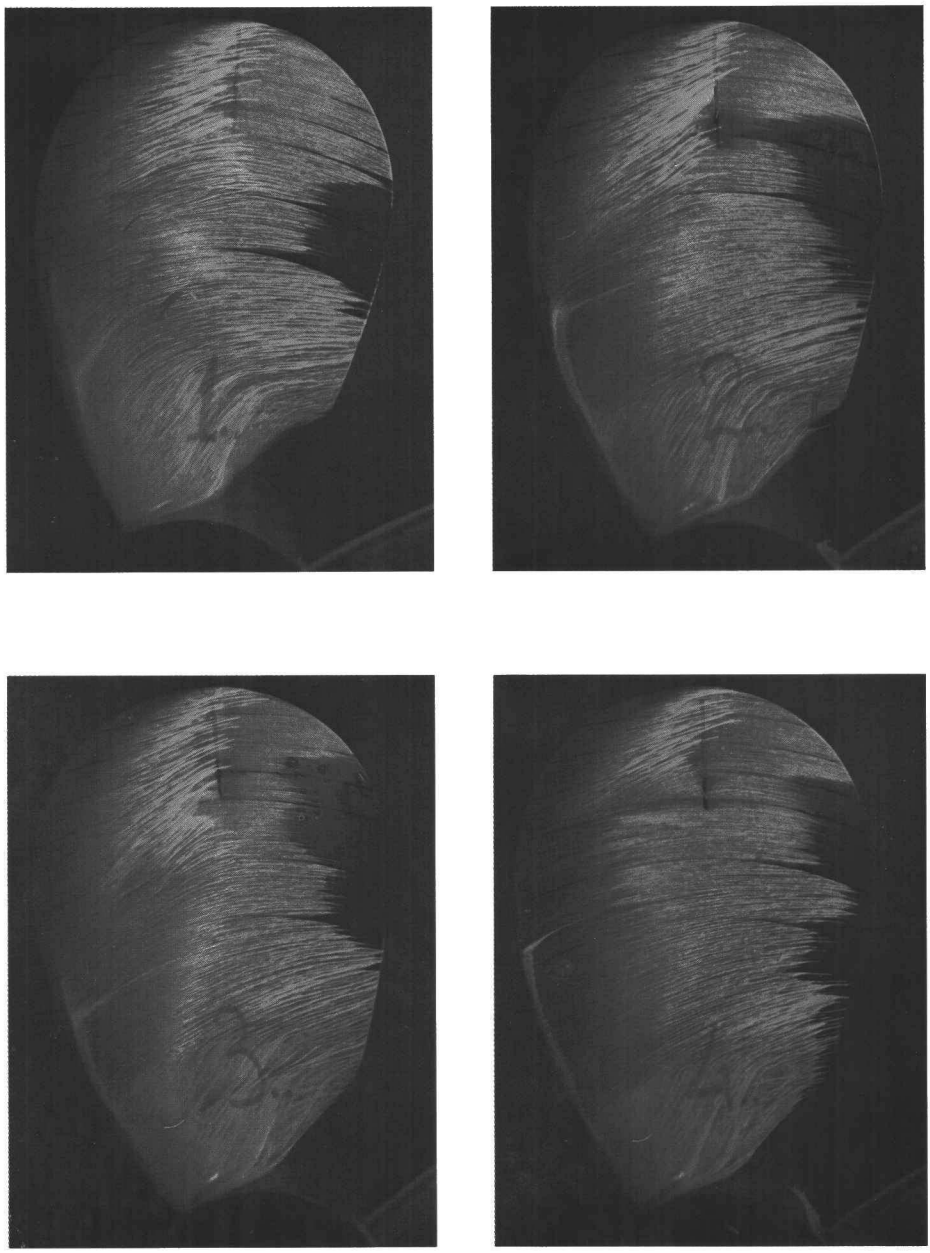

PLATE 3.17. DIFFERENCES BETWEEN THE BLADES WHEN LAMINAR SEPARATION OCCURS. IV
(PROPELLER S AT J=0.55, Re_n=1.1x10^6).

J = 0.60

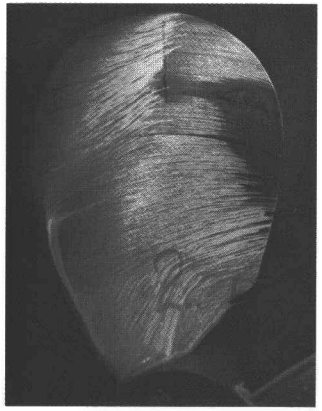

J = 0.55

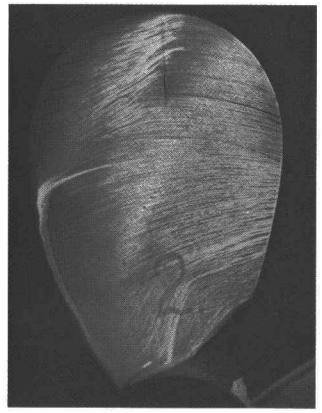

J = 0.50

J = 0.45

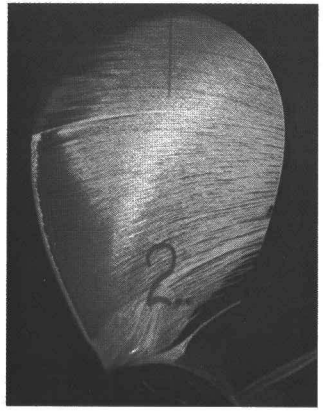

J = 0.40

PLATE 3.18. THE PAINT PATTERN ON PROPELLER S AT VARIOUS LOADINGS. V
(Re_n=1.1x10^6).

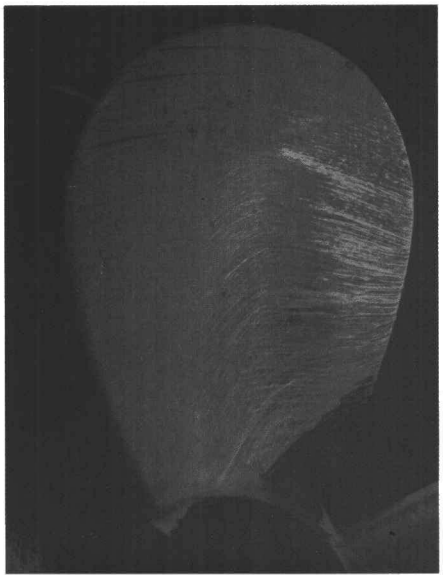

$Re_n = 1.1 \times 10^6$

PLATE 3.13. PAINT PATTERN ON PROPELLER B AT J=0.85.*

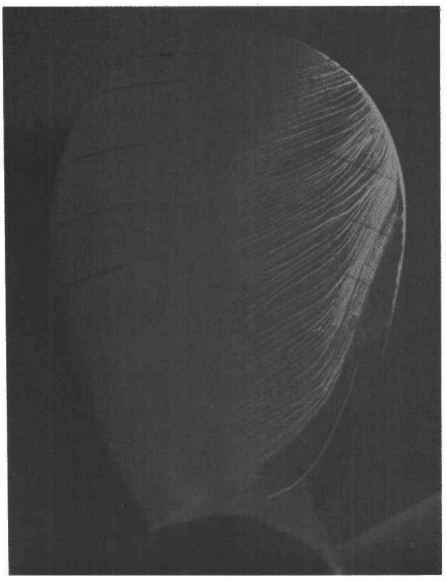

$Re_n = 0.56 \times 10^6$

PLATE 3.12. PAINT PATTERN ON PROPELLER B AT J=0.28.*

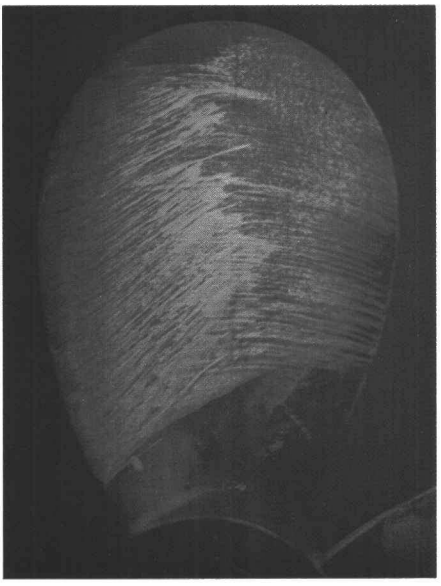

$Re_n = 1.1 \times 10^6$

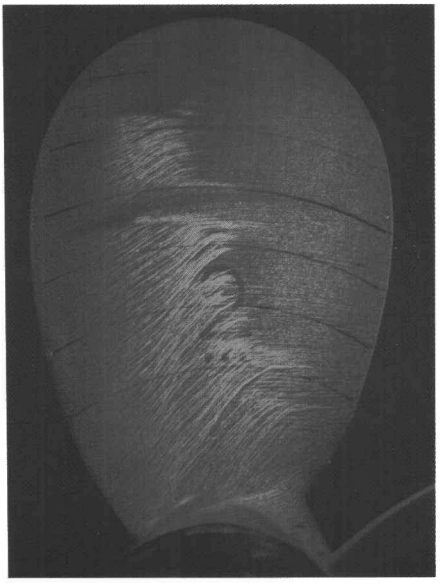

$Re_n = 1.7 \times 10^6$

PLATE 3.20. PAINT PATTERN OF PROPELLER V AT J=0.4.

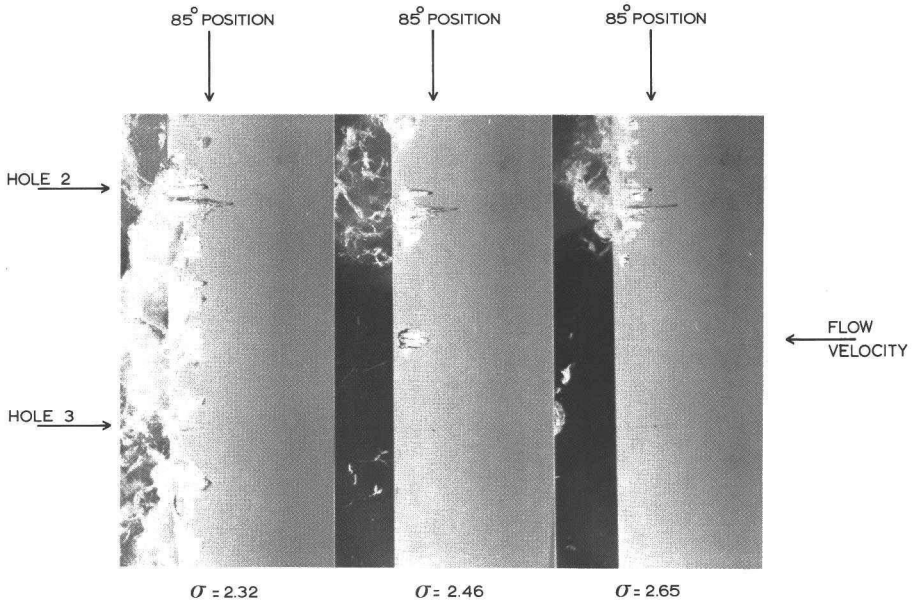

PLATE 4.10. CAVITATION OBSERVATIONS ON THE SMOOTH CYLINDER AT 5.7 m/sec.

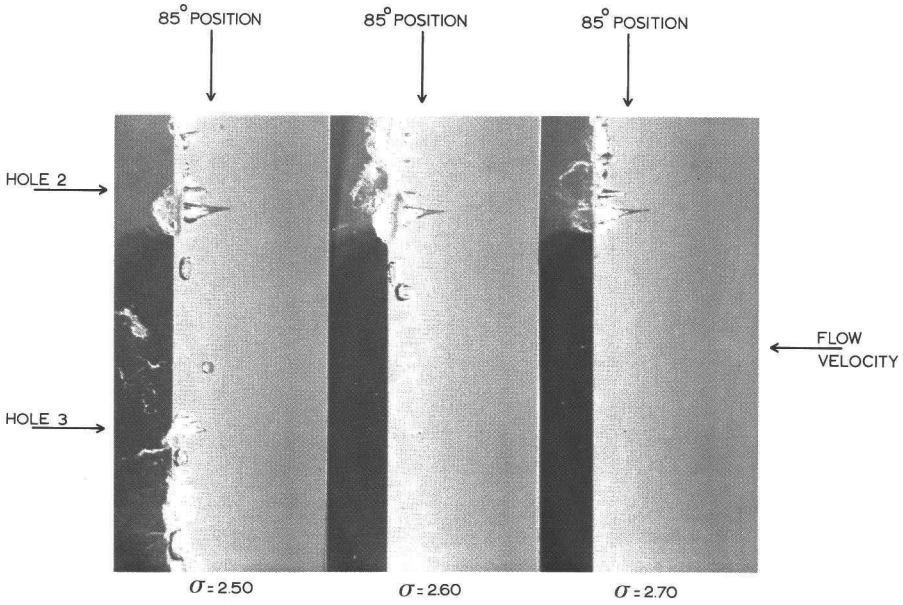

PLATE 4.11. CAVITATION OBSERVATIONS ON THE SMOOTH CYLINDER AT 9.6 m/sec.

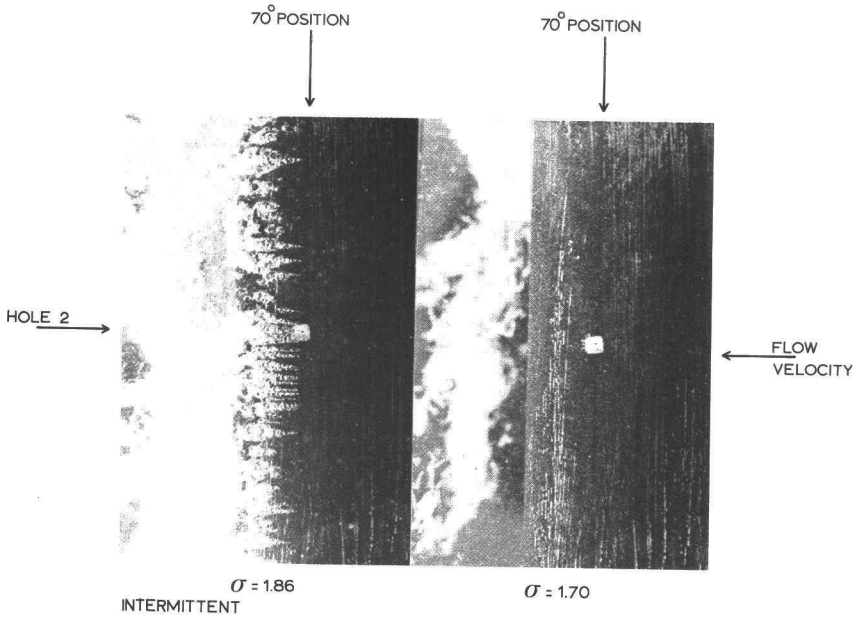

PLATE 4.14. CAVITATION OBSERVATIONS ON THE ROUGHENED CYLINDER AT 5.7 m/sec.

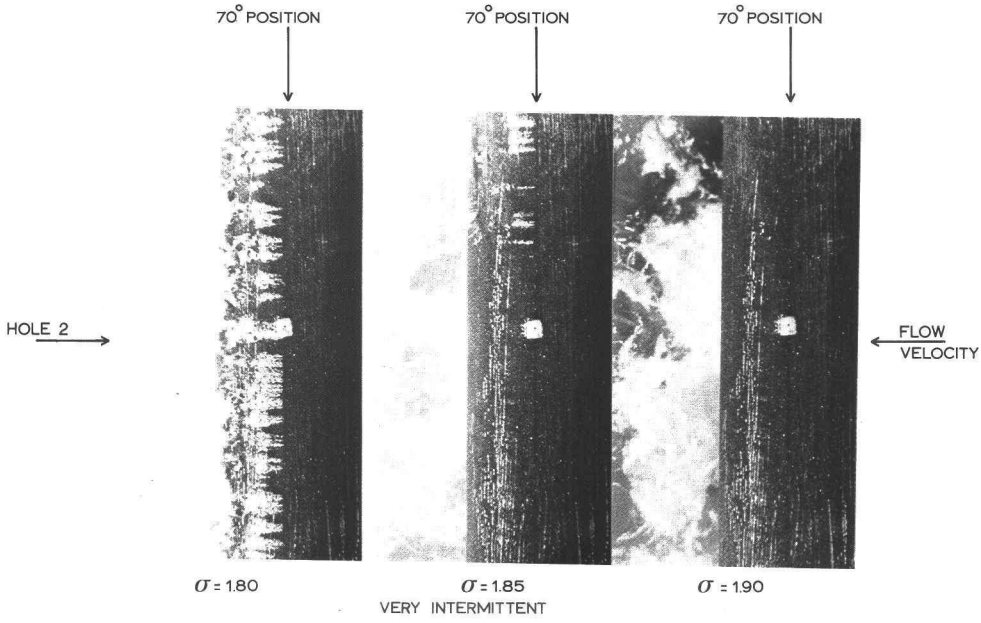

PLATE 4.15. CAVITATION OBSERVATIONS ON THE ROUGHENED CYLINDER AT 9.6 m/sec.

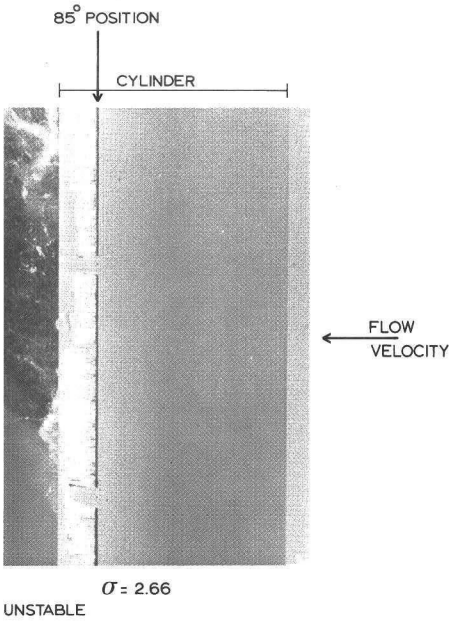

PLATE 4.18. CAVITATION OBSERVATIONS ON THE ROUGHNESS LINE AT 5.7 m/sec.

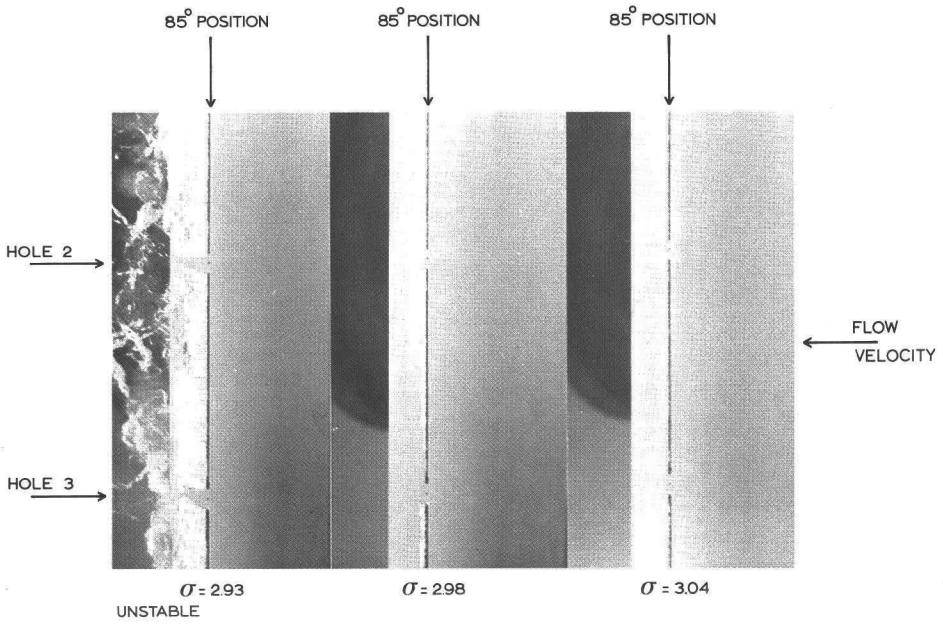

PLATE 4.19. CAVITATION OBSERVATIONS ON THE ROUGHNESS LINE AT 9.6 m/sec.

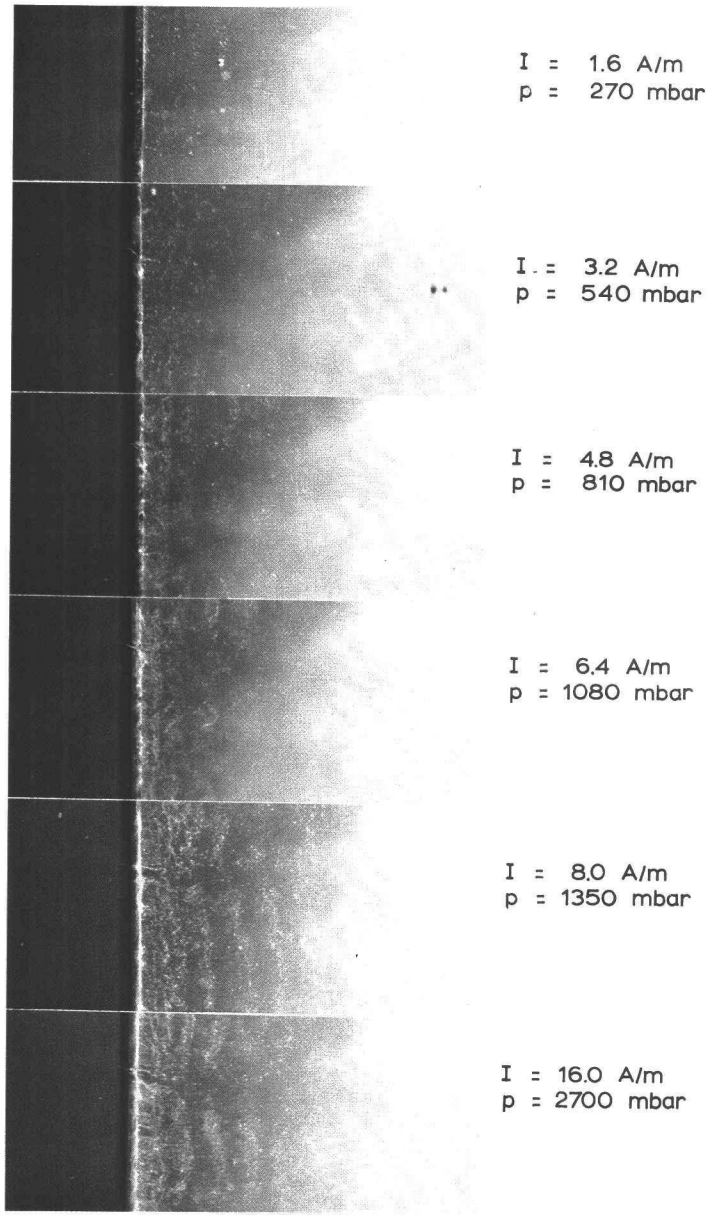

PLATE 5.3. THE EFFECT OF THE PRESSURE PARAMETER ON ELECTROLYSIS. (V=3 m/sec, WIRE DIAMETER 0.9 mm).

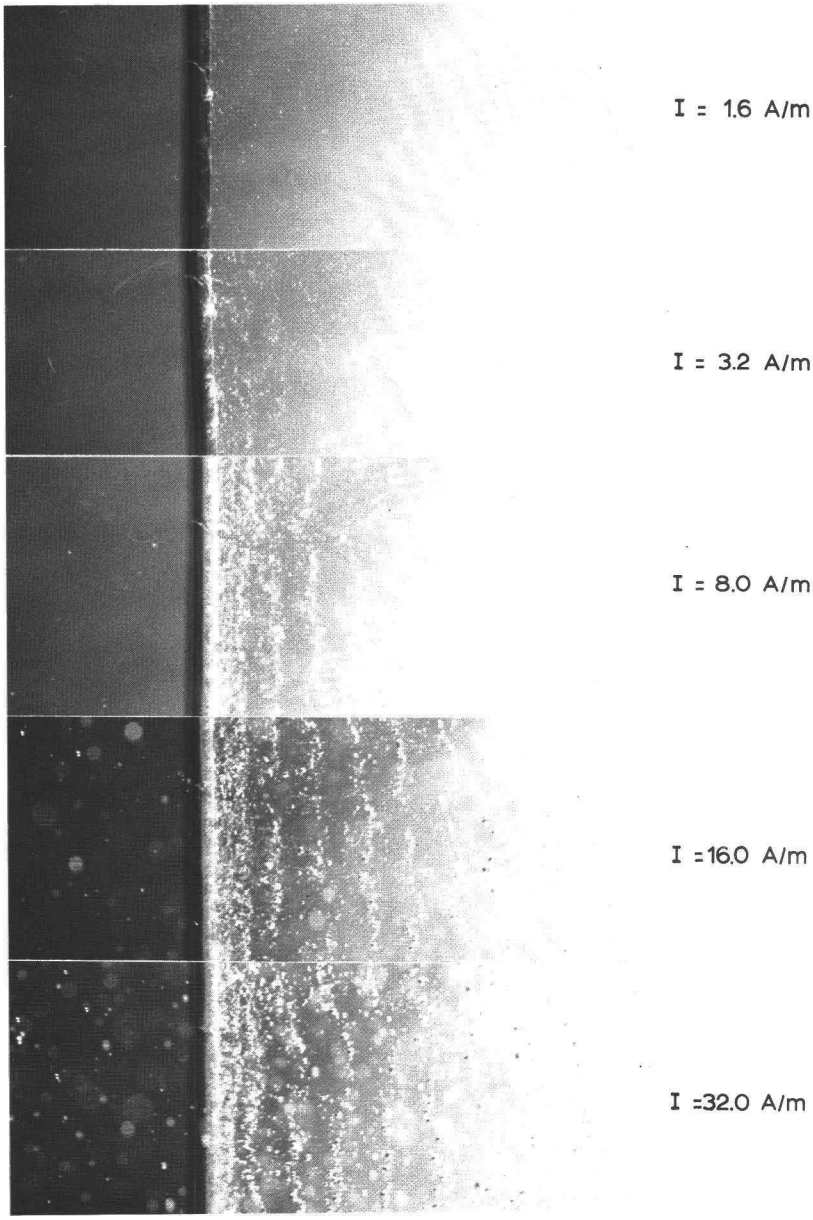

PLATE 5.4. THE EFFECT OF GAS PRODUCTION ON ELECTROLYSIS.
(V=3 m/sec, p=270 mbar, WIRE DIAMETER 0.9 mm).

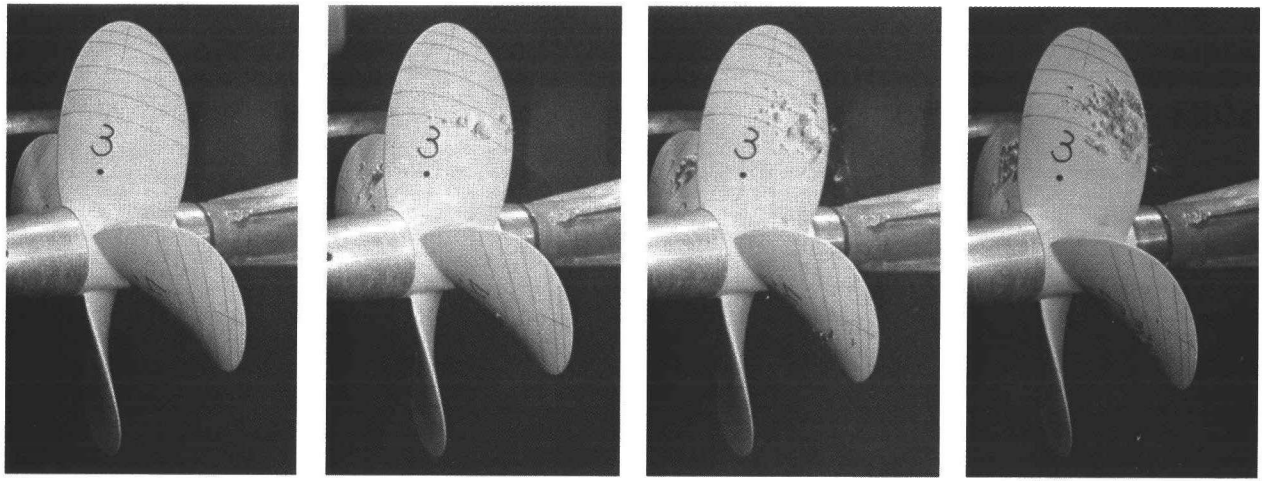

PLATE 6.5. VARIATION OF ELECTROLYSIS CURRENT ON PROPELLER B AT J=0.6. (Re_n=1.1x10^6, σ_n=1.0).

WITHOUT ELECTROLYSIS

WITH ELECTROLYSIS

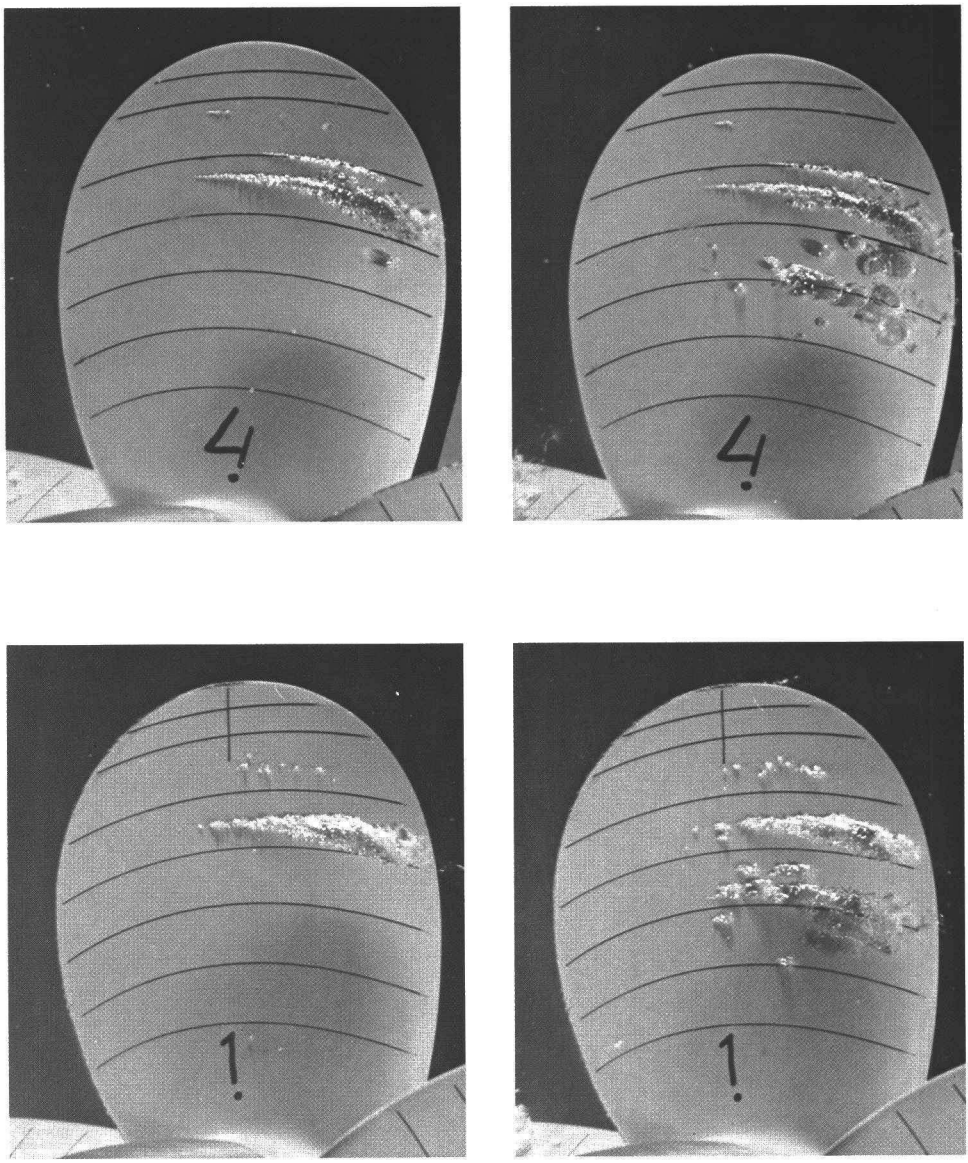

BLADE : 4 SMOOTH
BLADE : 1 ROUGHENED AT THE LEADING EDGE

PLATE 6.6. CAVITATION OBSERVATIONS IN THE CAVITATION TUNNEL. PROPELLER B AT J=0.6. (σ_n=0.92, Re_n=2.11x10^6).

WITHOUT ELECTROLYSIS

WITH ELECTROLYSIS

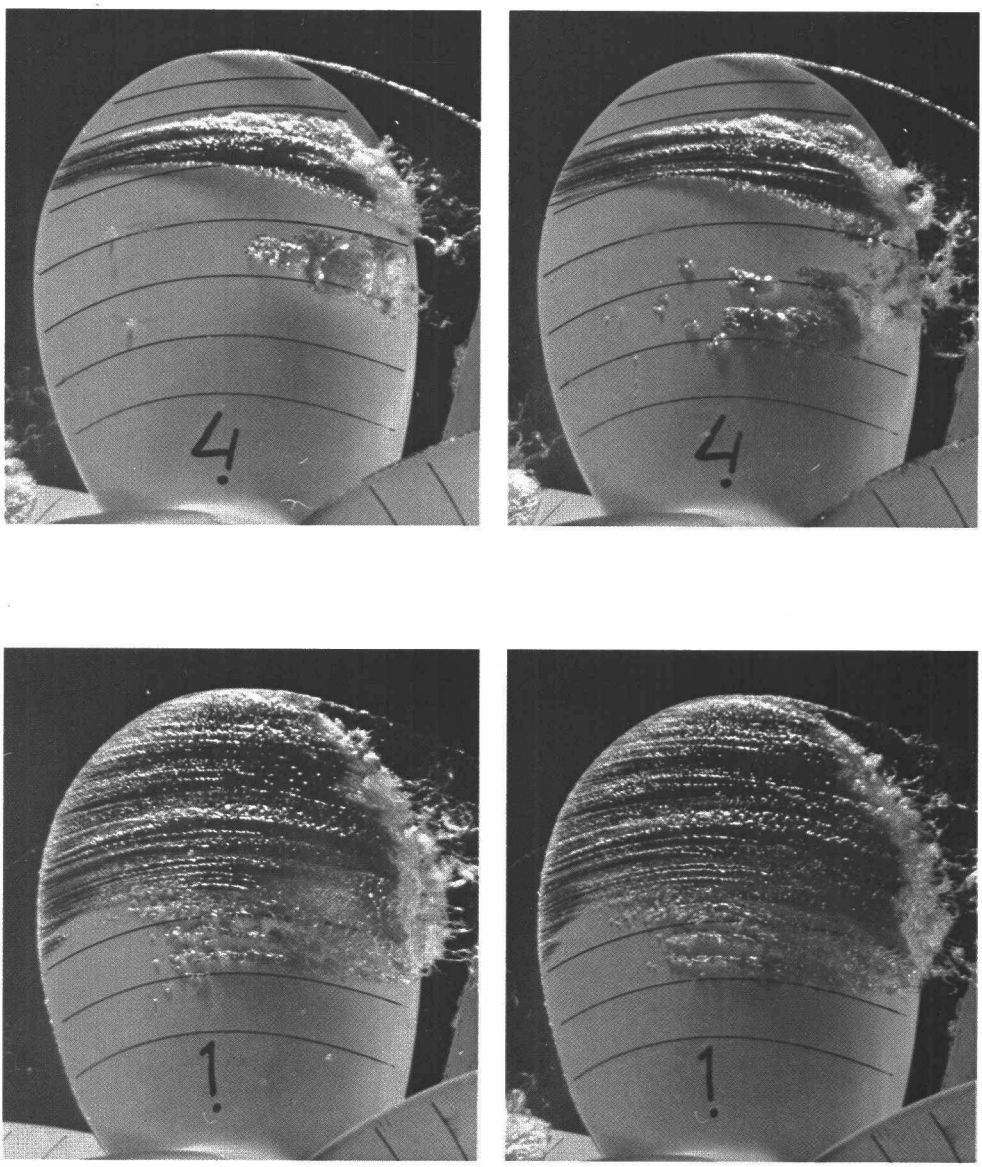

BLADE : 4 SMOOTH
BLADE : 1 ROUGHENED AT THE LEADING EDGE

PLATE 6.10. CAVITATION OBSERVATIONS IN THE CAVITATION TUNNEL. PROPELLER B AT J=0.4. (σ_n*=0.92,* Re_n*=2.11x10*^{6}).

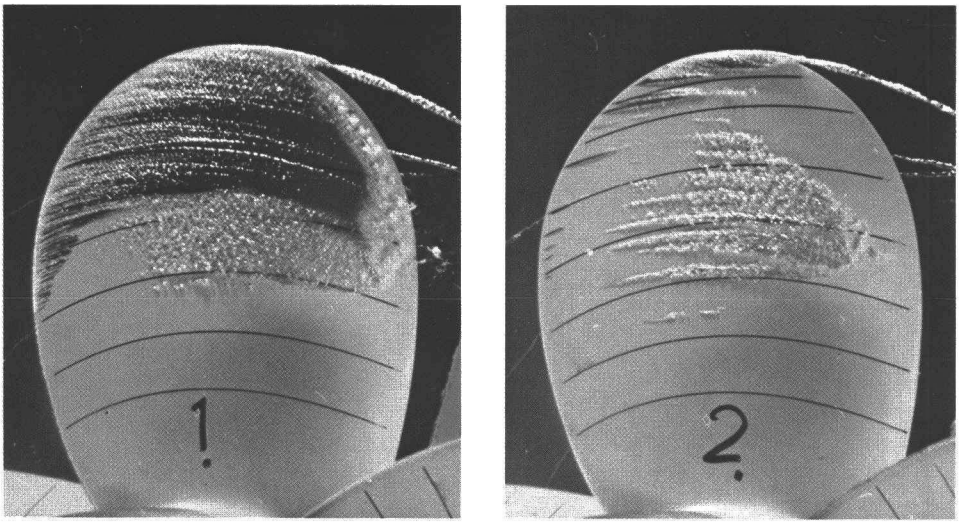

ROUGH SMOOTH

PLATE 6.12. CAVITATION OBSERVATIONS IN THE CAVITATION TUNNEL AT HIGH REYNOLDS NUMBER. (Re_n=2.88x10^6, σ_n=1.15 , J=0.4).

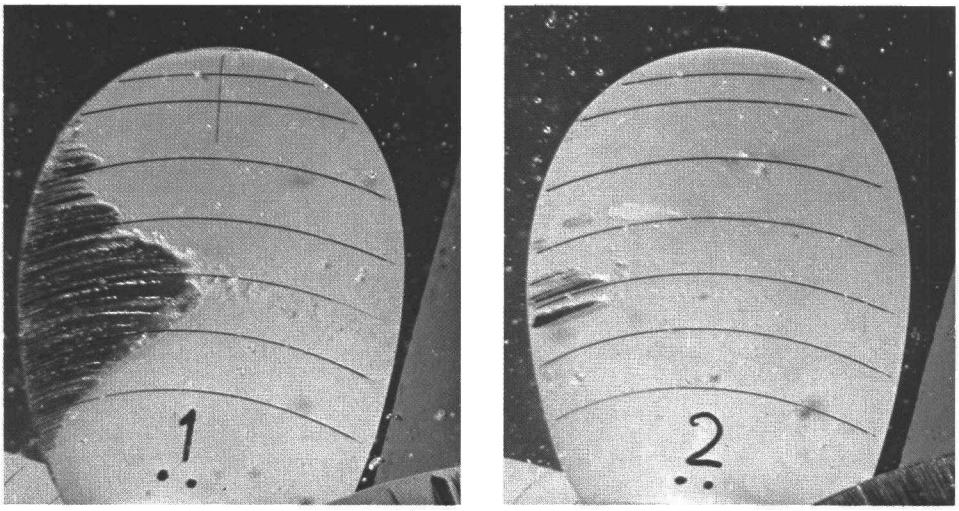

ROUGH SMOOTH

PLATE 7.10. CAVITATION OBSERVATIONS IN THE CAVITATION TUNNEL ON PROPELLER S AT J=0.6. (Re_n=2.11x10^6, σ_n=0.92).

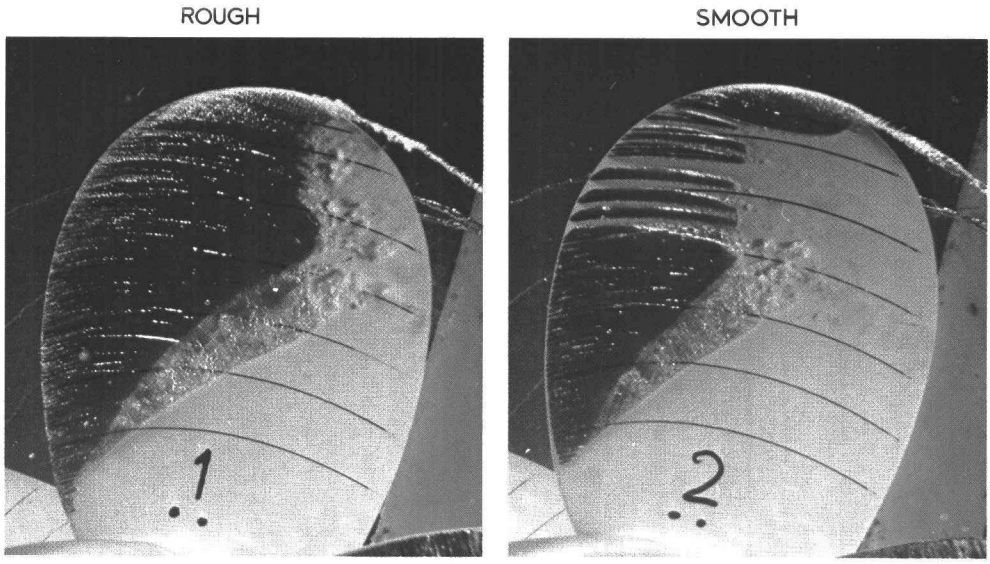

PLATE 7.5. CAVITATION OBSERVATIONS IN THE CAVITATION TUNNEL ON PROPELLER S AT J=0.4. (Re_n=1.78x10^6, σ_n=1.3).

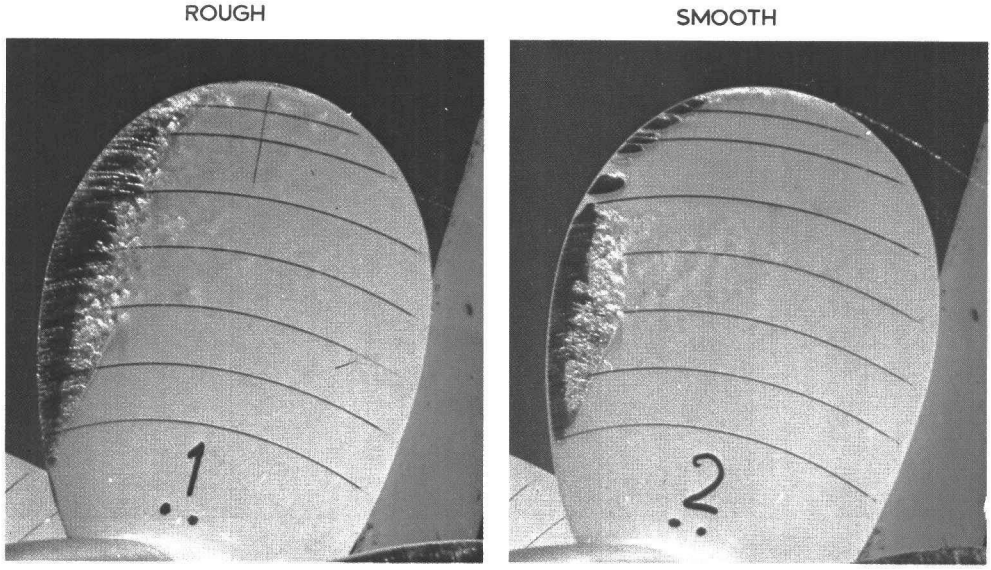

PLATE 7.6. CAVITATION OBSERVATIONS IN THE CAVITATION TUNNEL ON PROPELLER S AT J=0.4. (Re_n=1.36x10^6, σ_n=2.2).

Stellingen

1. Verbetering van het schroefontwerp, van de fabricagenauwkeurigheid van de modelschroef en van de beproevingscondities leiden alle tot vergroting van de schaaleffecten op cavitatie-inceptie.

2. Toepassing van ruwheid aan de intredende kant van de bladen van een modelschroef is een bruikbaar middel ter verkleining van schaaleffecten op cavitatie.

3. Bepaling van cavitatie-inceptie van een tipwervel kan worden gedaan door meting van de diameter van de tipwervel onder verschillende omstandigheden.

4. De bewering dat schaaleffecten bij het ontstaan van cavitatie in een vacuumtank belangrijk groter zijn dan in een cavitatietunnel is onjuist.

   E.A. Weitendorf, R.I.N.A. Symp. on Propeller Induced Vibration, discussion to paper 6, London 1979.

5. De tijdsduur nodig voor het maken van een computerprogramma is minimaal twee maal zo lang als een acceptabele schatting aangeeft.

6. De ideale werknemer lijkt voor veel bazen op een computer, hoewel niet beseft wordt dat dan zeer lange programma's nodig zouden zijn. Slechts programmeurs weten wat het zou inhouden wanneer werknemers uitsluitend precies zouden doen wat hun gezegd is.

7. Hoewel de techniek van wetenschappelijke methoden en resultaten gebruik maakt wordt het eigen karakter ervan ten opzichte van de wetenschap onvoldoende onderkend. Dit bemoeilijkt innovatie en versluiert het maatschappelijk karakter van de techniek. Wetenschapsbeoefening wordt daarentegen versmalt tot onderzoek waarvan de uitkomsten van te voren kunnen worden overzien.

8. Het bestaan van elkaar overlappende of zelfs van samenvallende onderzoekprogramma's, uitgevoerd in verschillende instituten, is productief in plaats van inefficient en doet recht aan de naam "research".